BSD-TR-67-140

[redacted]

7741-4-T
Copy 4

THE UNIVERSITY OF MICHIGAN

COLLEGE OF ENGINEERING
DEPARTMENT OF ELECTRICAL ENGINEERING
Radiation Laboratory

UNCLASSIFIED

(U) Investigation of Re-Entry Vehicle Surface Fields

Final Report
18 December 1965 - 18 December 1966

By

R. F. GOODRICH, B. A. HARRISON, E. F. KNOTT,
T. B. A. SENIOR, V. H. WESTON and L. P. ZUKOWSKI

January 1967

7741-4-T = RL-2164

Contract AF 04(694)-834

Contract With: Ballistic Systems Division
Deputy for Ballistic Missile Re-Entry Systems
Air Force Systems Command
Norton AFB, California

UNCLASSIFIED

Administered through:
OFFICE OF RESEARCH ADMINISTRATION • ANN ARBOR

[redacted]

THE UNIVERSITY OF MICHIGAN

7741-4-T

BSD-TR-67-140

(U) Investigation of Re-entry Vehicle Surface Fields

Final Report

18 December 1965 - 18 December 1966

AF 04(694) - 834

by

R. F. Goodrich, B. A. Harrison, E. F. Knott,
T. B. A. Senior, V. H. Weston and L. P. Zukowski

January 1967

Prepared for

BALLISTIC SYSTEMS DIVISION
DEPUTY FOR BALLISTIC MISSILE RE-ENTRY SYSTEMS
AIR FORCE SYSTEMS COMMAND
NORTON AFB, CALIFORNIA

In addition to security requirements which apply to this document and must be met, it may be further distributed by the holder only with specific prior approval of BSD/ BSOMS, Norton AFB, California 92409.

FOREWORD

(U) This report (BSD-TR-67-140) was prepared by the Radiation Laboratory of the Department of Electrical Engineering of The University of Michigan under the direction of Professor Ralph E. Hiatt, Head of the Radiation Laboratory, Burton A. Harrison, Program Manager and Raymond F. Goodrich, Principle Investigator. The work was performed under Air Force Contract Number AF 04(694)-834, "Investigation of Re-entry Vehicle Surface Fields." The work was administered under the direction of the Ballistic Systems Division, Deputy for Ballistic Missile Re-entry Systems, Norton AFB, California by Lt. James Wheatley, BSYDP, and was monitored by H. J. Katzman of the Aerospace Corporation.

(U) The studies presented herein cover the period 18 December 1965 through 18 December 1966.

(U) In addition to security requirements which apply to this document and must be met, this document is subject to special export controls and each transmittal to foreign governments or foreign nationals may be made only with prior approval of Ballistic Systems Division (BSOMS), Norton AFB, California 92409.

(U) Information in this report is embargoed under the Department of State International Traffic in Arms Regulations. This report may be released to foreign governments by departments or agencies of the U.S. Government subject to approval of Ballistic Systems Division (BSOMS), Norton AFB, California, or higher authority within the Department of the Air Force. Private individuals or firms require a Department of State export license.

This technical report has been reviewed and is approved.

Headquarters, Ballistic Systems Division
William C. Zeun, BSYDF
Contracting Officer

ABSTRACT

(S) This is the final report on Contract AF 04(694)-834, an investigation of re-entry vehicle radar cross section, the second phase of a program designated Project SURF. The objective of the SURF program is to achieve the capability to determine the radar cross section of metallic and coated re-entry vehicles which are sphere-capped-cones in shape, or modifications of that basic shape. The investigation reported here includes a determination of the effect on radar cross section of the plasma re-entry environment and of such perturbations as slot antennas, annular antennas, rocket motors and non-spherical terminations at the rear of the vehicle. The study is based upon the interpretation of surface field data obtained on models illuminated by radar in a specially designed experimental facility. Radar backscatter data and computer programs are used to check theoretical conclusions. The unperturbed metallic cone-sphere was investigated in the previous phase of the project. In this second phase, the metallic cone-sphere with antenna and termination perturbations and the coated unperturbed cone-sphere were studied. A report is given of the results of the experimental work, the interpretation of the measurement data, the theoretical work on plasma environment and such formulas for cross section as were developed and which extend the results previously reported.

TABLE OF CONTENTS

I

INTRODUCTION

1.1 Objectives and General Approach

(S) This is the final report on Contract AF 04(694)-834, an investigation of re-entry vehicle radar cross section, the second phase of a program designated Project SURF. The investigation reported here covers the 12-month period from 18 December 1965 to 18 December 1966. It was carried out at the Radiation Laboratory of the Department of Electrical Engineering of The University of Michigan. The investigation is part of the ABRES program and is sponsored by the Ballistic Systems Division of the Air Force Systems Command. It is monitored for the Air Force by the Aerospace Corporation.

(S) The objective of the SURF program is to achieve the capability to determine the radar cross section of metallic and coated re-entry vehicles which are sphere-capped cones in shape or modifications of this basic shape. The investigation includes a determination of the effect on radar cross section of the plasma re-entry environment and of such perturbations as slot antennas, annular antennas, rocket motors and non-spherical terminations at the rear of the vehicle. An understanding of the basic physics of the scattering of radar energy by these metallic bodies and the materials with which they are coated is the cost-effective means of designing re-entry vehicles and realistic decoy representations. Where this understanding does not exist, a guessing method or trial-and-error approach with its costly delays and uncertainties is the only alternative. A secondary objective is to program the more complex equations resulting from this investigation for large scale computer computation. This will provide a computational tool for the determination of the radar cross section of extremely low cross section re-entry vehicles without recourse to full-scale radar range measurements.

(S) Although at the initiation of the SURF investigation there existed a body of theoretical and experimental data on the radar scattering behavior of cones and sphere-capped cones, the theory was not sufficiently developed to handle cases of

current interest to the Air Force. This necessitated consideration of ablation coatings and the control of scattering behavior by the judicious application of radar absorbing materials. An adequate understanding of the physical phenomena did not exist and the necessity of using empirical methods limited the generality of the results obtained to the specific shape, frequency, absorber material and absorber location studied.

(S) Moreover, the use of scaled-down models (a measurement technique which is very useful for determining the radar reflection characteristics of relatively high cross section vehicles) is not practical with the very low radar cross section shapes it is now desirable to design. To determine the radar back scattering of low cross section shapes, it became necessary either to make full-scale measurements which are cumbersome and costly in time and funds, or to develop a new technique for achieving the same objective. The aim of the SURF program is to formulate a theory which would permit practical numerical computations to be made of the cross section of a class of re-entry vehicles without necessitating full-scale measurements and which could be used in the design phase of re-entry vehicle development to place absorber materials and such perturbations as antennas in locations which would give the lowest achievable radar cross section in the aspect angles of importance without compromising operational effectiveness.

(S) The SURF program is tentatively divided into three phases. The first phase which is complete is reported in Goodrich et al (1965) was concerned with the "clean" metallic cone-sphere. The cone-sphere is a mathematically precise shape which is a cone capped by a sphere with a continuous tangent at the join. The term "clean" is meant to include cone-sphere shapes in which the spherical cap may be modified (as for example in the Mark 12 re-entry vehicle) and the cone tip may be rounded, but not to include additions to the basic shape such as antennas and rocket motors. The latter shape which does include additions of this type and which may be coated with ablators and absorbers is being investigated in the subsequent phases of the program. The results of the work on the "clean" shape form a basis

for an understanding of the perturbed shape and the effect of radar absorber coatings. They were worked out with the assistance of surface field and back scatter experiments and through an extension of a body of prior work by many investigators. They are confirmed by comparison with such measurements as are available for the nose-on cross section of metallic models. In addition to being prerequisite to a study of coated perturbed vehicles, the results have an intrinsic value since they are immediately applicable to problems involving the radar cross section of the metallic cone-sphere.

(S) The second phase of the SURF program, the results of which are presented in this report, extended the investigation to consideration of (a) metallic cone-sphere vehicles with perturbations due to slot and annular antennas, rocket motors and modifications of the spherical cap, (b) the effect of the plasma re-entry environment, and (c) the effect of coatings on the metallic unperturbed cone-sphere. Unlike the case of the "clean" metallic cone-sphere, the coated cone-sphere does not have a comparatively long history of research behind it. Much of the prior work, e.g. study of electromagnetic radiation impinging at normal incidence on an infinite slab, was not directly applicable to the case of the coated cone-sphere. In attacking the problem of the coated cone-sphere, the surface field approach which had been developed in the previous phase of SURF was used experimentally and analytically.

(S) The technique of using surface field phenomena to study the radar cross section of extremely low cross section vehicles has been described in previous reports (see, for example, Senior and Zukowski, 1965). Briefly the concept is as follows:

(U) When an electromagnetic wave is incident upon a body, a surface distribution of fields or currents is set up which then radiates to produce the scattered field. The latter is expressible in terms of the former by a relatively simple integral in the far zone. For a given direction of incidence, the complete (monostatic and bistatic) field can be derived from the surface field by quadratures. The surface field is also more sensitive to minor changes in shape and material perturbations than

the scattered field and knowledge of its amplitude and phase on the surface of an object is an important tool in studying how shape and material changes affect the radar cross sections of a body.

(S) Thus, when faced with the problem of investigating the radar scattering from low cross section shapes, advantage was taken of the fact that

(a) although the cross section of an object may be small, the induced current may be large and therefore relatively easy to measure;

(b) there is a simple computational relationship between the currents induced on an object and the far zone scattered field;

(c) the feasibility of measuring the surface current by laboratory techniques had been demonstrated previously at the Radiation Laboratory in related studies; and

(d) it is a comparatively simple procedure to identify and analyze the contributions to the total cross section made by significant scatterers or by modifications and perturbations on the cone-sphere surface.

(S) To obtain data on the surface currents induced by incident radar waves on cone-sphere shapes, a measurement facility and electromagnetic probes were designed and constructed during the first phase of the investigation. The facility and its operation have been described in detail in Knott (1965). A brief discussion of it is also given in the next section of this report.

(S) In addition to the use of surface current measurements on cone-sphere models, another analytical tool is being developed to furnish data for cases in which experimental techniques have limitations which are best overcome by numerical methods. A computer program is being written to provide the surface currents (or radar back scatter) from rotationally symmetric metallic bodies. In the next phase of SURF, if the computer program for the metallic body proves to be effective, it can be extended to handle situations in which the vehicle is coated and has rotationally symmetric perturbations such as an annular antenna. The status of this work is discussed in Appendix B.

(U) Chapter II of this report details the experimental investigation. The construction and operation of the experimental surface field facility had been described in previous reports and is not repeated here. However, the description of the experiments is preceded by a discussion of measurement techniques. A list of all the measurements performed is given in tabular form. It will be seen that the list is extensive. Nevertheless, only those measurements were made which were believed to be necessary for understanding the physical phenomena and for studying the effect of local perturbations (such as antennas and nozzles) and coatings on the cone-sphere surface. Back scatter measurements were made to check the theoretical results or to check full-scale measurements made on related vehicles. The models which were constructed or coated during this phase are illustrated in this section. Only brief remarks are made here concerning the interpretation of the data. The detailed analysis and interpretation is discussed in the section which follows.

(S) Chapter III is a discussion of the analysis and particularly of the interpretation of the experimental data. The Introduction to this section discusses the physical picture on which the investigation is based. It identifies the local sources of energy which contribute to the total radar scattering of a cone-sphere body and shows how the modifications to the basic shape affect the radar cross section. The modifications which were studied are of the type found on test or operational missiles and re-entry bodies. Although this study is aimed at achieving general results which would be applicable to any combination of the perturbations studied, an attempt was made to model those antennas, cone angles, nose-tips and rear terminations found on vehicles of current interest to the Air Force. For this reason, modifications typical of the Rex, LORV and Mark-12 vehicles were studied.

(S) When the SURF program was initiated, little that could be generalized and applied to a wide class of problems was known about the behavior of coated re-entry vehicles. During the first year of SURF, experimental techniques were developed for measuring the surface currents on coated objects. This first necessary step was followed in this second year by a development of the theoretical conditions under

which these experimental techniques could give meaningful data. An exposition of this development is given in the introduction to Section 3.5. It is followed by a discussion of the analysis of the data on coated shapes and an interpretation of the data. The unperturbed coated cone-sphere was the object of study for this phase of the investigation. Important data was also obtained from a study of relatively simpler shapes such as the coated sphere and cylinder. The effect of variation in the coating thickness, of fairing the absorber coating and of using layers of different coating materials was also studied and is reported on in this section.

(U) Chapter IV is a report of the work on the radar cross section of re-entry vehicles in the plasma environment. The investigation is focussed on identifying those cases expected to have practical significance. It made use of electron density profiles in specific altitude bands tabulated in data sheets provided by the Aerospace Corporation. However, the equations developed in the study are general and not restricted to specific cases. Recommendations for effects to be studied in an experimental investigation which is to accompany the continuing theoretical study are given in Section 4.4 and are detailed in the Program Plan for the continuation.

(S) Chapter V gives the formulae developed in this phase of SURF. They carry forward the work on the uncoated metallic cone-sphere to include the effects of additional perturbations and they cover the case of the coated unperturbed cone-sphere. The perturbations include the effects of an indented rear termination such as is typified by the Mark-12 re-entry vehicle and the effect of flush mounted antennas. Appendix A gives additional detail on the creeping wave analysis which forms the basis for aspects of the formulas when the cone-sphere join is in the penumbra region.

(U) Chapter VI lists supporting technical studies.

II

EXPERIMENTAL INVESTIGATION

2.1 The Purpose of Experimental Work

(U) A major goal of this contract in this age of specialization and technical complexity is the production of mathematical expressions or other aids which may easily be used by personnel not intimately acquainted with electromagnetic scattering theory to accurately predict the radar cross sections of typical re-entry vehicles. Ideally, such expressions should accommodate the host of variables which characterize the vehicle and the radar system such as vehicle size, the wavelength, the surface composition, effects of antennas, rocket nozzles and other perturbations, the vehicle shape, viewing angle, etc., but an exact formulation including all of these does not, and will not, exist. Although the mathematician prefers an exact solution, the engineer who must make the actual prediction uses an approximation of stated accuracy.

(U) The production of an approximate expression which accounts for all the variables is in itself a difficult task. The electromagnetic scattering from an arbitrary body has its origin in the surface fields induced on the object by the incident wave and by reason of the complexities introduced by the shapes of typical re-entry vehicles and the materials covering them, the calculation of these fields over the entire surface is formidable. This, it turns out, is the core of the problem and at this point the approximation process begins. It is also the point at which actual measurements of the induced (or total) surface fields can be used either to verify approximate theoretical predictions of the fields or to merely provide data from which an electromagnetician may make an inspired guess. This chapter discusses the measurement program with only general remarks about the data. A discussion of the detailed interpretation of the data obtained under this program is given in Chapter III.

(U) For the purpose of acquiring surface field data, an experimental facility was conceived and constructed by the Radiation Laboratory during the winter of

1964-1965. Since the system is described in some detail by Knott (1965) we will present only its major features. The measurements are performed in an anechoic chamber which is tapered to provide lower reflection levels than found in more conventional chambers having parallel sides. A transmitting antenna at the apex of the tapered portion illuminates the room and the energy falls upon the obstacle to be studied. It is mounted on a foam column in the test region of the chamber. A motor-driven mechanism installed above the ceiling controls the position of a small probe resting on the surface of the obstacle. The probe lies at the end of a slender coaxial lead projecting downward from the traversing mechanism through a large hole in the chamber ceiling, and is supported by a balsa framework which minimizes the tracking error between the mechanism and the probe itself. The small signal sensed by the probe is piped to a superheterodyne receiver in a control room adjacent to the chamber and is amplified to a level which can be read from a bolometer detector.

2.2 Measurement Technique and Data Acquisition

(U) The operator of the measurement system aligns the test object in the incident field by using the traversing mechanism and his own unaided eye. For example, if the fields along a cone are to be probed, the probe is moved in a straight line by the positioning mechanism and its distance from the surface is observed during the traverse. Unless the alignment is perfect, the probe will move toward or away from the surface and the observation of this movement shows how the cone must be positioned to improve the alignment. We note that the position and orientation of the mechanism is well known because it has been often checked and calibrated, hence may be used as a standard for model alignment.

(U) After the model has been aligned to the satisfaction of the operator of the system, its surface fields may be probed. For cone-sphere objects, the measurements are usually begun at the tip; the probe is moved from tip to join along one side of the object, from join to join around the spherical portion, then from join to tip on the other side. The operator decides, before the measurements are begun,

how far apart the measured points will lie along the surface, and generally he selects ten or more points per wavelength. He prepares a data sheet by listing the points at which the probe will rest during the experiment, leaving room for entries of the observed field amplitudes at those points. If the measurements are to take place on an object for which the operator has no previous data, he also prepares a graph on which he plots the data as the experiment progresses. By plotting the data as he records it, the operator can observe the trend and thus can investigate immediately any anomolous behavior by moving the probe back to the questionable points. This tends to reduce the errors in the experiment. On the other hand, if he is probing an object he is familiar with, he does not plot the data as it is observed, but instead fills out his entire data sheet, recording the observed amplitudes as they are shown on the receiving equipment. The data are plotted immediately after the measurements have been performed.

(U) Both before and after the experiment, the operator notes pertinent measurement information on the raw data sheet as well as on the graph of the data. This entry consists of (not necessarily in the order listed) the model probed; the quantity probed (electric or magnetic field components); the probe used; the frequency; the model's electrical size (ka); the calibration level (and therefore the incident field level); the size of the calibration sphere; the date of the experiment and, when necessary, the probe orientation. The data sheets and plots of the data are backed with carbon which makes them masters for subsequent reproduction. Copies of both the raw digital data and the plots are made and distributed to the Project Manager and to the senior Data Analyst, while the originals (masters) are retained on file.

(U) The raw data and the corresponding plots are loosely bound in groups of two or three hundred sheets (occasionally more) so that each sheet can be easily removed, copies made, and be replaced. Such a collection is given a volume number and each sheet in the volume is assigned a page number. Each volume contains an index summarizing each sheet in the volume. The volumes of data have been

assembled chronologically, since this was the easiest and most appropriate way of classifying the information early in the contract. In hindsight, now that we have several kinds of measurements, a more logical grouping could have been selected, since, as it stands now, unrelated experiments lie side-by-side in the data volumes only because they were performed in that order. We have therefore assembled indexes which show where related experiments may be found.

(U) A summary of the pertinent experiments performed during this contract year are listed in Table II-1. The experiments are grouped according to model measured. A brief model description is given in Table II-2.

(U) The surface field data for the test object must be calibrated and this is usually done after (not before) the object has been measured. Ordinarily, one need only remove the target and expose the probe to the incident field but this is inadvisable for several reasons. Firstly, the anechoic chamber is filled with a three-dimensional standing wave pattern and in the volume normally occupied by the test obstacle, this pattern has a peak-to-peak variation, depending on frequency, of 0.2 to 0.8 db. Hence, if the naked probe happened to lie on one of the peaks of the pattern, the calibration could be in error by 0.1 to 0.4 db (approx.). Secondly, there are some probe orientations which must be used on the test object for which there is no component of the incident field exciting the loop when the target is absent. In this case, it is not possible to obtain an incident field calibration level without a target of some kind; therefore, a conducting sphere is used to calibrate all surface field data. Usually, the probe (if it is a magnetic one) is placed on the surface of the sphere at the specular point and since the fields on this object can be computed exactly, the sphere measurement gives a reference level. When the probe is used in unusual orientations on the target, the same orientation is used on the sphere, hence for this kind of calibration the probe is not placed at the specular point, but at some location such that the plane of the loop is perpendicular to the surface of the sphere at a known position.

(S) TABLE II-1

Model No.	Volume*	Page(s)*	Frequency GHz.	Field Probed	ka	Remarks
D-1	VI	303, 304	2.97	H_ϕ	1.6	A (see footnote)
D-1	VI	307, 308	2.97	E_ϕ	1.6	B (see footnote)
D-1	VI	301, 302	2.97	E_s	1.6	A
D-2	VI	319, 320	2.97	H_ϕ	1.6	A
D-2	VI	319, 320	2.97	H_ϕ	1.6	A - In front of model.
D-2	VI	315	2.97	E_ϕ	1.6	B
D-3	VI	321, 322	2.97	H_ϕ	1.6	A
D-3	VI	323	2.97	H_ϕ	1.6	A - In front of model.
D-3	VI	317	2.97	E_ϕ	1.6	B
D-4	VI	326, 327	2.89	H_ϕ	3.	A
D-4	VI	331	2.89	E_ϕ	3.	B
D-5	VI	332, 333	2.89	H_ϕ	3.	A
D-5	VI	330	2.89	E_ϕ	3.	B
D-6	VI	337, 338	2.00	H_ϕ	1.6	A
D-6	VI	339	2.00	E_ϕ	1.6	B
D-7	VI	353, 354	1.25	H_ϕ	1.	A
D-7	VI	355	1.25	E_ϕ	1.	B
D-7	VI	355	1.25	E_s	1.	A - On spherical part only.
D-7	VI	350, 351	3.76	H_ϕ	3.	A
D-7	VI	347	3.76	E_ϕ	3.	B
D-7	VI	348	3.76	E_s	3.	A - On spherical part only.
D-7	VI	357, 358	6.26	H_ϕ	5.	A
D-7	VI	359, 360	6.26	E_ϕ	5.	B
D-7	VI	359, 356	6.26	E_s	5.	A - On spherical part only.
D-8	VI	364-367	6.80	H_ϕ	8.	A
D-8	VI	361, 362	6.80	E_ϕ	8.	B
D-8	VI	361, 363	6.80	E_s	8.	A - On spherical part only.
D-9	VII	1 - 4	6.80	H_ϕ	8.	A
D-9	VII	5, 6	6.80	E_ϕ	8.	B
D-9	VII	7	6.80	E_s	8.	A - On spherical part only.
D-10	VII	13, 14	1.25	H_ϕ	1.	A
D-10	VII	15, 16	1.25	E_ϕ	1.	B
D-10	VII	15, 16	1.25	E_s	1.	A - On spherical part only.
D-10	VII	10 , 2	3.76	H_ϕ	3	A
D-10	VII	8	3.76	E_ϕ	3	B
D-10	VII	9	3.76	E_s	3	A - On spherical part only.
D-10	VII	19, 20	6.26	H_ϕ	5	A

(continued)

A = Trajectory in plane of model axis and incident field

B = Trajectory in plane of model axis and perpendicular to incident field.

*The volume numbers and page numbers refer to laboratory records. A description of the models is given in Table II-2.

(S) TABLE II-1 (continued)

Model No.	Volume	Page(s)	Frequency GHz.	Field Probed	ka	Remarks
D-10	VII	17, 18	6.26	E_ϕ	5.	B
D-10	VII	17, 18	6.26	E_s	5.	A - On spherical part only.
D-11	VII	27, 28	1.25	H_ϕ	1.	A
D-11	VII	25, 26	1.25	E_ϕ	1.	B
D-11	VII	25, 26	1.25	E_s	1.	A - On spherical part only.
D-11	VII	148, 149	1.25	E_s	1.	A - On conical part only.
D-11	VII	29, 30	3.76	H_ϕ	3.	A
D-11	VII	31, 32	3.76	E_ϕ	3.	B
D-11	VII	31, 32	3.76	E_s	3.	A - On spherical part only.
D-11	VIII	1, 2	3.76	H_ϕ	3.	A
D-11	VIII	3, 4	3.76	E_s	3.	A
D-11	VII	21, 22	6.26	H_ϕ	5.	A
D-11	VII	23, 24	6.26	E_ϕ	5.	B
D-11	VII	23, 24	6.26	E_s	5.	A - On spherical part only.
D-11	VIII	5, 6	6.26	H_ϕ	5.	A
D-11	VII	152, 153	6.26	E_s	5.	A - On conical part only.
D-12	VII	35, 36	6.80	H_ϕ	8.	A
D-12	VII	33, 34	6.80	E_ϕ	8.	B
D-12	VII	33, 34	6.80	E_s	8.	A - On spherical part only.
D-12	VIII	112, 113	6.80	E_s	8.	A
D-12	VIII	114, 115	6.80	H_ϕ	8.	A
D-12	VIII	110, 111	0.935	H_ϕ	1.1	A
D-12	VIII	98, 99	2.55	H_ϕ	3.	A
D-12	VIII	108, 109	2.55	E_s	3.	A
D-12	VIII	104, 105	4.25	H_ϕ	5.	A
D-12	VIII	106, 107	4.25	E_s	5.	A
D-12b	VIII	72, 73	0.935	H_ϕ	1.1	A
D-12b	VIII	74, 75	2.55	H_ϕ	3.	A
D-12b	VIII	76, 77	4.25	H_ϕ	5.	A
D-12b	VIII	61, 62	6.80	H_ϕ	8.	A
D-12c	VIII	84, 85	0.935	H_ϕ	1.1	A
D-12c	VIII	80, 81	2.55	H_ϕ	3.	A
D-12c	VIII	78, 79	4.25	H_ϕ	5.	A
D-12c	VIII	82, 83	6.80	H_ϕ	8.	A
D-12d	VIII	117, 118	0.935	H_ϕ	1.1	A
D-12d	VIII	119, 120	2.55	H_ϕ	3.	A
D-12d	VIII	121, 122	4.25	H_ϕ	5.	A
D-12d	VIII	123, 124	6.80	H_ϕ	8.	A

(continued)

A = Trajectory in plane of model axis and incident field

B = Trajectory in plane of model axis and perpendicular to incident field.

(S) TABLE II-1 (continued)

Model No.	Volume	Page(s)	Frequency GHz.	Field Probed	ka	Remarks
D-13	VII	71, 72	2.55	E_ϕ	3.	B
D-13	VII	71, 72	2.55	E_s	3.	A - On spherical part only.
D-13	VII	73 - 75	2.55	H_ϕ	3.	A
D-13	VII	76, 77	2.55	H_ϕ	3.	A - On conical part only.
D-13	VIII	29, 30	2.55	E_s	3.	A
D-13	VII	78, 80	4.25	H_ϕ	5.	A
D-13	VII	81, 82	4.25	E_ϕ	5.	B
D-13	VII	83	4.25	E_s	5.	A - On spherical part only.
D-13	VIII	27, 28	4.25	E_s	5.	A
D-13	VII	84, 85	6.80	E_ϕ	8.	B
D-13	VII	86	6.80	E_s	8.	A - On spherical part only.
D-13	VII	87 - 89	6.80	H_ϕ	8.	A
D-13	VIII	13, 15	6.80	E_s	8.	A
D-13	VIII	67, 68	0.935	H_ϕ	1.1	A
D-13	VIII	69, 70	0.935	E_s	1.1	A
D-14	VII	90, 91	6.26	H_ϕ	5.	A
D-14	VII	93, 94	6.26	E_s	5.	A -On spherical part only.
D-14	VII	93, 94	6.26	E_ϕ	5.	B
D-14	VII	124, 125	3.76	H_ϕ	3.	A
D-14	VII	119, 120	3.76	E_ϕ	3.	B
D-14	VIII	18, 19	1.25	E_s	1.	A
D-14	VIII	20, 21	1.25	E_s	1.	A
D-14	VII	103, 104	10.02	H_ϕ	8.	A
D-14	IX	42, 43	2.50	H_ϕ	2.	A - 7 1/2° oblique incidence.
D-14	IX	44, 45	2.50	H_ϕ	2.	A 32 1/2° oblique incidence
D-14	IX	46, 47	2.50	H_ϕ	2.	A 57 1/2° oblique incidence.
D-14	IX	48, 49	2.50	H_ϕ	2.	A 82 1/2° oblique incidence.
D-14	IX	26, 27	6.26	H_ϕ	5.	A 7 1/2° oblique incidence.
D-14	IX	38, 39	6.26	H_ϕ	5.	A 32 1/2° oblique incidence.
D-14	IX	28, 29	6.26	H_ϕ	5.	A 37 1/2° oblique incidence.
D-14	IX	40, 41	6.26	H_ϕ	5.	A 57 1/2° oblique incidence.
D-14	IX	30, 31	6.26	H_ϕ	5.	A 82 1/2° oblique incidence.
D-14	IX	10, 11	6.26	H_ϕ	5.	A 165° oblique incidence.
D-14a	VIII	126, 127	1.25	H_ϕ	1.	A
D-14a	VIII	136, 137	1.25	E_s	1.	A
D-14a	VIII	128, 129	3.75	H_ϕ	3.	A
D-14a	VIII	130, 131	3.75	H_ϕ	3.	A
D-14a	VIII	138, 139	3.75	E_s	3.	A

A = Trajectory in plane of model axis and incident field.
B = Trajectory in plane of model axis and perpendicular to incident field.

(S) TABLE II-1 (continued)

Model No.	Volume	Page(s)	Frequency GHz	Field Probed	ka	Remarks
D-14a	VIII	132, 133	6.26	H_ϕ	5.	A
D-14a	VIII	140, 141	6.26	E_s	5.	A
D-14a	VIII	134, 135	10.02	H_ϕ	8.	A
ID-1	VII	68 - 70	0.935	H_ϕ	1.1	A
ID-1	VII	65, 66	2.55	H_ϕ	3.	A
ID-1	VII	60 - 63	4.25	H_ϕ	5.	A
ID-1	VII	47 - 51	6.80	H_ϕ	8.	A
ID-2	VII	140-143	0.935	H_ϕ	1.1	A
ID-2	VII	114-116	2.55	H_ϕ	3.	A
ID-2	VII	132-134	4.25	H_ϕ	5.	A
ID-2	VII	135-139	6.80	H_ϕ	8.	A
ID-3	VIII	63, 64	0.935	H_ϕ	1.1	A
ID-3	VIII	45 - 47	2.55	H_ϕ	3.	A
ID-3	VIII	49 - 51	4.25	H_ϕ	5.	A
ID-3	VIII	53, 54	6.80	H_ϕ	8.	A
LSP	VII	144-146	0.935	H_ϕ	1.1	A
LSP	VII	107-109	2.55	H_ϕ	3.	A
LSP	VII	129-131	4.25	H_ϕ	5.	A
LSP	VII	39 - 41	6.80	H_ϕ	8.	A
LSH	IX	1 - 3	0.931	H_ϕ	1.1	A
LSH	IX	4, 5	2.54	H_ϕ	3.	A
LSH	IX	36, 37	2.54	H_ϕ	3.	A
LSH	IX	6, 7	4.23	H_ϕ	5.	A
Slotted	IX	13, 14	1.25	H_ϕ	2.	A - 1 1/2" lucite filled slot.
Slotted	IX	15, 16	1.25	H_ϕ	2.	B - 1 1/2" lucite filled slot.
Slotted	IX	17, 18	1.25	H_ϕ	2.	A 1/4" above center. 1 1/2" lucite filled slot.
Slotted	IX	19, 20	2.50	H_ϕ	4.	A 1 1/4" air filled slot.
Slotted	IX	19, 20	2.50	H_ϕ	4.	A 1/4" above center. 1 1/4" air filled slot.
Slotted	IX	22, 23	2.50	H_θ	4.	B 1 1/4" air filled slot.
Slotted	IX	21, 23	2.50	H_θ	4.	B 1 1/4" air filled slot.
Slotted	IX	24, 25	2.50	H_ϕ	4.	A 1/4" above center. 1 1/2" lucite filled slot.
Slotted	IX	24, 25	2.50	H_ϕ	4.	A 1 1/2" lucite filled slot.
-	-	-	-	-	-	- -

A = Trajectory in plane of model axis and incident field
B = Trajectory in plane of model axis and perpendicular to incident field.

(S) TABLE II-1 (continued)

Model No.	Volume	Page(s)	Freq. GHz.	Field Probed	ka	Remarks
7 1/2° 6" C-S	IX	12, 14	1.25	H_ϕ	2.	A - On conical part only.
7 1/2° 6" C-S	IX	24, 25	2.50	H_ϕ	4.	A - On conical part only.
7 1/2° 4.42"C-S	VIII	23, 24	0.935	H_ϕ	1.1	A
7 1/2° 4.42"C-S	VII	110-113	2.55	H_ϕ	3.	A
7 1/2° 4.42"C-S	VII	126-128	4.25	H_ϕ	5.	A
7 1/2° 4.42"C-S	VII	42 - 45	6.80	H_ϕ	8.	A
Abs. Sphere	VIII	34, 35	2.35	E_s	5.	A
Abs. Sphere	VIII	36, 37	2.35	E_s	5.	A 5/32" from surface.
Abs. Sphere	VIII	38, 39	2.35	H_ϕ	5.	A
Abs. Sphere	VIII	40, 41	2.35	H_ϕ	5.	A 5/32" from surface.
C-1	VI	125	3.38	H_ϕ	3.38	A
C-1	VI	126	3.38	E_s	3.38	A
C-1	VI	146	6.26	E_R	5.	A
C-1	VI	162	6.26	H_ϕ	5.	A
C-2	VI	128	3.38	E_s	2.7	A
C-2	VI	129	3.38	H_ϕ	2.7	A
C-2	VI	150	6.26	E_R	5.	A
C-2	VI	164	6.26	H_ϕ	5.	A
C-3	VI	130	3.38	H_ϕ	8.1	A
C-3	VI	131, 132	3.38	E_s	8.1	A
C-3	VI	247, 248	3.38	H_ϕ	8.1	A
C-3	VI	251, 252	3.38	H_R	8.1	A
C-3	VI	255, 256	3.38	E_R	8.1	A
Posts	B	3 - 9	3.13	H_s	5.	A
Posts	B	10 - 15	3.76	H_s	3.	A
Posts	B	16 - 21	3.76	H_s	8.	A
Rings	B	22 - 24	3.76	H_s	8.	A
Knobs	B	25 - 29	3.13	H_s	5.	A
Knobs	B	30 - 34	3.76	H_s	3.	A
Monopoles	B	35 - 59	3.13	H_s	5.	A
Loops	B	60 - 67	3.13	H_s	5.	A
Monopole	B	68 - 97	3.13	H_s	5.	A
Loop	B	98 -151	3.13	H_s	5.	A
-	-	-	-	-	-	-

End

A = Trajectory in plane of model axis and incident field.

THE UNIVERSITY OF MICHIGAN

7741-4-T

(S) TABLE II-2: KEY TO MODELS AND REMARKS IN TABLE II-1.

Model No.	Degrees Half-Angle	Diameter Inches	Comments
D-1	7 1/2	2.024	Lucite coating
D-2	10	2.024	Lucite coating
D-3	11 1/4	2.024	Lucite coating
D-4	12 1/2	3.852	Lucite coating
D-5	12 1/2	3.852	"3.01" coating
D-6	7 1/2	3.00	Air coating; simulated using styrofoam spacer.
D-7	7 1/2	3.00	LS-22 coating
D-8	7 1/2	4.42	LS-22 coating
D-9	7 1/2	4.42	LS-26 coating
D-10	7 1/2	3.00	LS-26 coating
D-11	7 1/2	3.00	LS-24 coating
D-12	7 1/2	4.42	LS-24 coating
D-12b	7 1/2	4.42	Partial LS-24 coating, orange peel fairing.
D-12c	7 1/2	4.42	Partial LS-24 coating, tapered fairing.
D-12d	7 1/2	4.42	Partial LS-24 coating, abrupt fairing.
D-13	7 1/2	4.42	RS-X coating.
D-14	7 1/2	3.00	Eccosorb CR coating (Fig. 2-8)
D-14a	7 1/2	3.00	Eccosorb CR coating and teflon sheath (Fig. 2-9).
ID-1	7 1/2	4.42	Indented rear radius 4.56" (Fig. 2-5).
ID-2	7 1/2	4.42	Indented rear radius=2.21" (Fig. 2-5).
ID-3	7 1/2	4.42	Indented rear radius=1.52" (Fig. 2-5).
LSP	7 1/2	4.42	1/4" lucite spacer 3 1/2" from tip (Fig. 2-11).
LSH	7 1/2	4.44	1/4" lucite spacer between hemisphere and cone (Fig. 2-12).
Slotted	7 1/2	6.00	4 1/2" x 1/4" slot, depth adjustable to 1 3/4" using inserts (Fig. 2-10).
7 1/2°4.42"C-S	7 1/2	4.42	Plain cone-sphere
7 1/2°6.00"C-S	7 1/2	6.00	Plain cone-sphere
Abs. Sphere		8.00	RS-X coated sphere
C-1		3.00	RS-S coated cylinder 26" long.
C-2		3.00	AN-73 coated cylinder 25 1/2" long.
C-3		9.00	AN-75 coated cylinder 30" long.
Posts			Cone-spheres w/posts on spherical part.
Rings			Cone-sphere w/rings on spherical part.
Knobs			Cone-spheres w/knobs or nozzles on spherical part.
Monopoles			3 or 5 monopoles on cone-sphere.
Loops			3 loops on cone-sphere.
Monopole			Single monopole on cone-sphere.
Loop			Single loop on cone-sphere.

(U) The indicating device which the operator observes, and whose values he records, displays amplitude information in decibels. The distance along the surface probed is recorded in inches and, when plotted, becomes the independent variable. The resulting curves of surface field intensity, in decibels, versus distance in inches is of use in quickly determining the gross behavior of the fields and for rapidly making a comparison of the field behavior on different, but related, targets. For the purpose of analysis, however, the amplitude data is removed from its logarithmic framework and the distance information is expressed in terms of the wavelength. There is, then, a data reduction process which occurs after data have been obtained, in addition to the plot provided at or near the time of the experiment. After the data have been reduced, they are replotted for analytic purposes. The data are plotted twice-the two plots serving different purposes. The plot of raw data is a check of the experiment; since the smoothness of the curve is a measure of random errors in the system, it serves as a basis of judgement as to whether or not the experiment, or parts of it, should be repeated. The refined plot, on the other hand, is constructed and smoothed in a way that removes random errors. The periodic nature (with distance) of the observed amplitude distributions is more easily analyzed by the use of this refined plot, since the periodicity in terms of wavelengths is easier to ascertain than it is from the raw data plot. In addition, if two objects are electrically the same size, the refined plots of the data can be directly compared as they share a common unit (wavelength) although their physical size, and the frequencies used for each object, may be grossly different.

2.3 Notable Experimental Results During the Year

(U) In this section we list some of the more important experimental results obtained during the period of the contract but will present little or no analysis of these results. Each of the topics below corresponds in a very approximate sense to the completion of one of the subtasks in the Statement of Work. The topics are discussed more or less in the chronological order in which they were investigated.

2.3.1 Phase Measurements (Task 2.1.9)

(U) The first task we addressed was that of evaluating our capability of measuring the relative phase of induced magnetic surface fields. The circuitry used to measure phase was conventional (Knott, 1965) and depended upon comparing the probe signal with a sample reference signal of known phase and amplitude. The surface of a test sphere was probed with the equipment and both the phase and the amplitude of the probe output signal were measured. The probe trajectory started at the specular point, passed through the shadow region and terminated at the starting point from the opposite side. The results of the phase measurement are shown in Fig. 2-1 and the maximum error is less than 20^{o}. The source of error was not determined and although 20^{o} may seem to be a rather large error, it is in fact quite reasonable when one considers that the physical probe diameter spans an electrical distance of about 10^{o}.

(U) We were convinced that the phase variation of surface fields could be measured with acceptable precision, but the extra preparation required for measurements was a distinct disadvantage. Not only was more equipment required for phase measurements than for amplitude alone, but the technique which was used required equipment tuning at each point along the probe trajectory. This meant a great deal of work would be expended in acquiring data. We therefore measured phase only as often as was required for the understanding of surface field behavior.

2.3.2 Measurements of Electric Fields (Task 2.1.9)

(S) Much of the second year's work involved the measurement of the surface fields on objects coated with radar absorbing materials. Since these coatings in general support tangential electric fields as well as tangential magnetic fields, and normal magnetic as well as normal electric fields, we were obliged to develop probes capable of measuring electric fields.

(U) It turned out that a monopole probe did an admirable job of measuring radial electric fields, as shown in Fig. 2-2. This probe was merely a short length of the exposed center conductor of a coaxial line and it functioned best when the outer

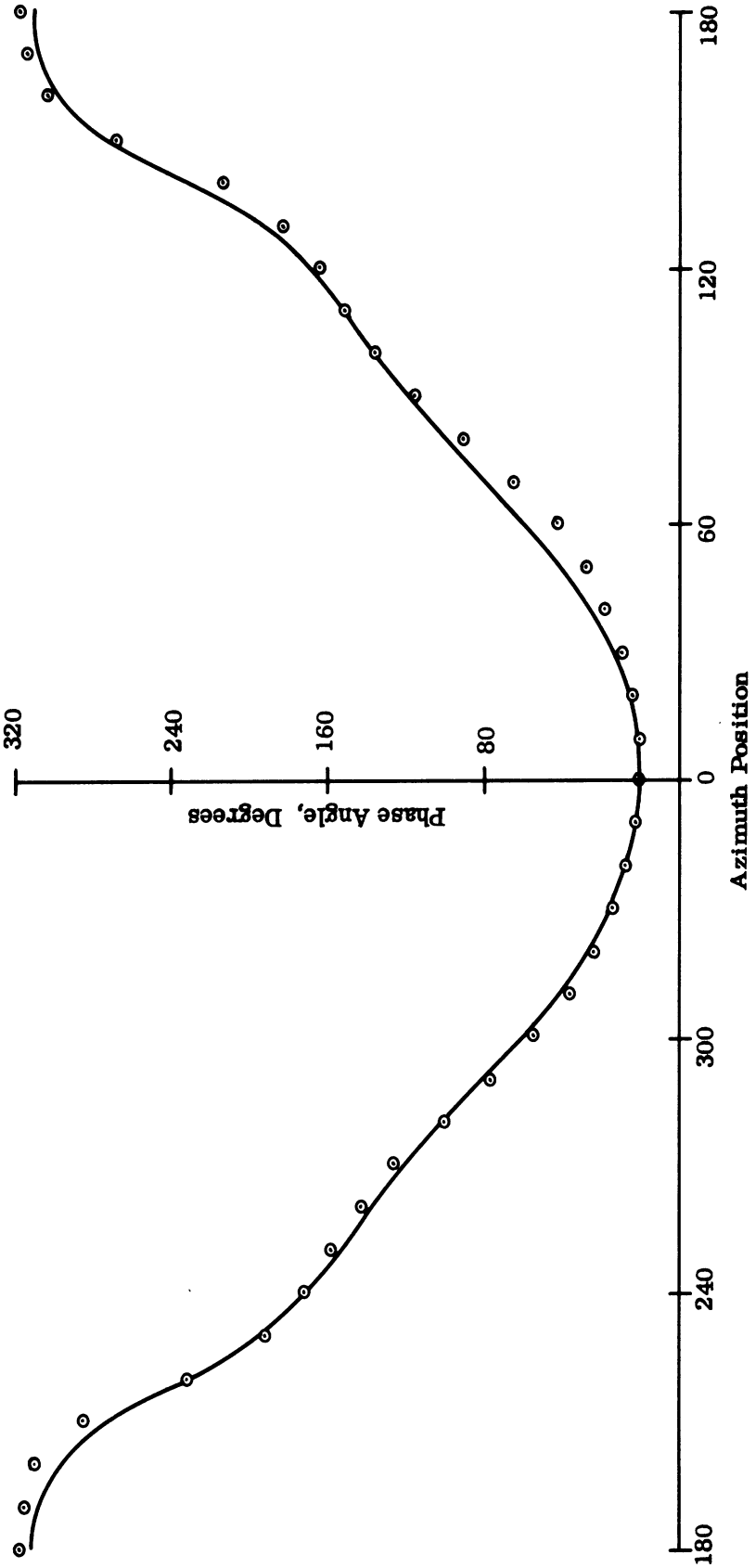

FIG. 2-1: THEORETICAL AND MEASURED PHASE OF MAGNETIC FIELD AROUND A CONDUCTING SPHERE. (——) THEORY, (o o o) EXPERIMENT. ka = 1.96, Sphere Dia. = 1.980", Frequency, 3.03 GHz.

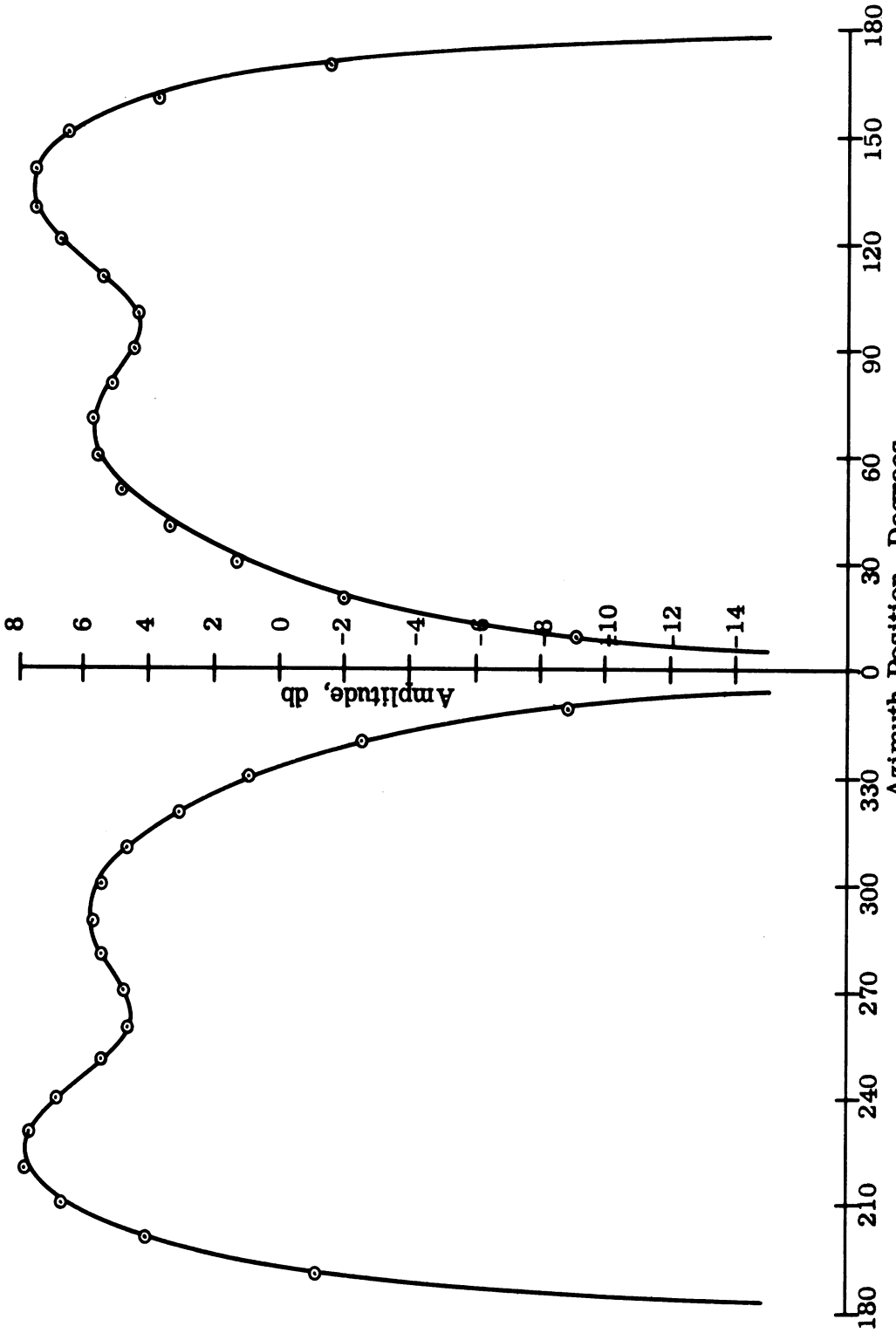

FIG. 2-2: THEORETICAL AND EXPERIMENTAL AMPLITUDE OF RADIAL ELECTRIC FIELD AROUND A CONDUCTING SPHERE. (—) THEORY, (● ● ●) EXPERIMENT, ka = 2.0, Sphere Dia. =2.945", Frequency, 2.505 GHz.

conductor was grounded to the test object (by physical contact), with the exposed center conductor pointed normally away from the surface. It was concluded that radial electric fields are easily measured with this kind of probe.

(U) The monopole electric probe is an unbalanced one and did not work when used to probe tangential electric fields. It turned out that a balanced probe made of two unbalanced ones mounted back-to-back worked best for this case. The testing of the balanced probe design was difficult, since for accurate evaluation, a surface had to be produced over which the tangential electric field distribution was known. A sphere coated with absorbing material of known properties was planned to be constructed (and is under construction) but was not completed in time for the evaluation. A test was therefore designed in which the probe was withdrawn radially from the surface of a metallic sphere at several stations. The experimental data were compared with theory and except near the surface, the probe responded quite well. The test was a severe one, however, since at the surface the field intensity theoretically falls to zero ($-\infty$ db) but our probe could not be placed close enough to the surface to register this level. The test of the probe showed that for most situations it could be trusted and the probe was later used for extensive measurements of coated cone-spheres.

2.3.3 Study of Materials (Tasks 2.1.1, 2.1.6, 2.1.6.1)

(U) Early in the investigation it was realized that more information was needed about the absorbing materials which were to be used than was specified by the manufacturers of the materials. About three man-months were expended testing various samples by means of transmission line techniques in an effort to compile descriptions of the materials. Several samples of each material were constructed and measured in a transmission line from 2.5 to 6.0 Gc., and from the measured data, the complex permeability and permittivity were ascertained. The results were reasonably uniform and were unquestionably useful in estimating impedance boundary conditions.

2.3.4 Absorber-Coated Cone-Spheres (Tasks 2.1.1, 2.1.2, 2.1.3, 2.1.6)

(S) Several grades of commercial absorber were obtained and applied to cone-spheres for study. The materials are listed in Table II-3. They were all of the order 3/8" thick and no attempt was made to vary the coating thickness. This was not critical, since the electrical thickness (in terms of the wavelength in the material) is the important parameter and this could easily be found from the study of material properties. A few cone-sphere models having a lossless coating were borrowed from the MIT-Lincoln Laboratory.

TABLE II-3: LIST OF ABSORBERS USED TO COAT CONE-SPHERES

Material	Type	Manufacturer
LS-22	Carbon-loaded flexible foam	Emerson and Cuming
LS-24	Carbon-loaded flexible foam	Emerson and Cuming
LS-26	Carbon-loaded flexible foam	Emerson and Cuming
RS-X RX-S	Thin flexible tuned absorber with magnetic loss	B. F. Goodrich
Eccosorb CR	Rigid cast-in-place absorber with with magnetic loss	Emerson and Cuming

(S) Both the electric and magnetic surface fields of the coated objects were probed for several values of ka (the distance around the maximum physical cross section of the metallic cone-sphere, expressed in wavelengths), ranging from ka=1 to ka=8. Only the tangential components of these fields were explored and for a few cases, the electric field was measured along two different trajectories. Most of the measurements were made with the target illuminated nose-on, but a few runs were performed for varying angles of incidence. By way of illustration, the behavior of the fields on a coated cone-sphere are compared with those on a bare object in Fig. 2-3. For the bare cone-sphere, the surface fields rapidly build up from the incident field level at the tip to a physical optics value approximately twice the strength of the incident field. This level is maintained all along the side of the cone

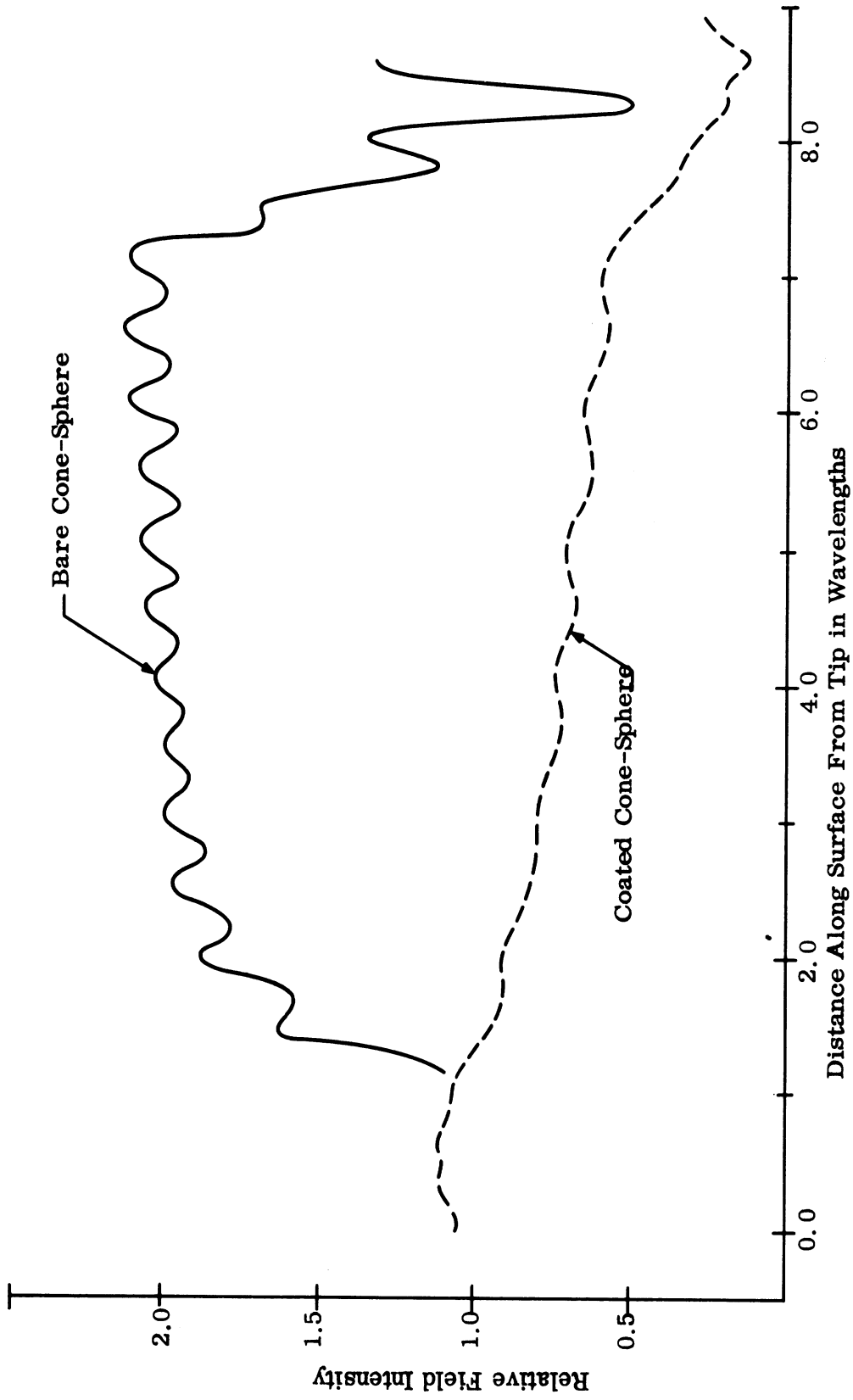

FIG. 2-3: COMPARISON OF SURFACE MAGNETIC FIELDS FOR COATED AND UNCOATED CONE-SPHERES (ka = 5.0).

up to the join and has perturbations which are due to the creeping wave which has traversed the rear of the spherical portion. From the join to the antipode the field decays rapidly and exhibits a series of peaks and nulls whose spacing and amplitudes depend on the electrical size of the object. The 'bright spot' at the antipode is a characteristic feature and its amplitude is a measure of the intensity of the creeping wave. The fields on the coated object, on the other hand, are quite different. In the region of the tip there is little difference between coated and uncoated surface field behavior, but in moving away from the tip, the fields on the coated object begin to decay, as opposed to the build-up and nearly constant level found on the bare object. The decay in the field intensity persists until the join is reached, where the intensity is of the order of one-third that of the bare model. From the join to the antipode, the amplitude falls off even faster, attaining the characteristic peak at the antipode, which is much lower than for the bare case. The total distance traversed in the measurements is much longer for the coated case than for the bare object by virtue of the coating thickness. The tangential electric field follows much the same decay as shown in Fig. 2-3 for the magnetic fields, with the exception that the tangential electric field is everywhere zero for the bare model.

2.3.5 Faired Coatings and Double Coatings (Tasks 2.1.6, 2.1.11)

(S) A study was made of the effects of an incomplete coating and in particular, of the effects of various ways of terminating the partial coating. Three distinct terminations were studied, all of which were at or near the join, and they are illustrated in Fig. 2-4. The terminations used were both abrupt and gentle and the material used was LS-24; the study was performed for ka values ranging from 1.1 to 8.0. The results showed that the surface fields decayed almost identically the way they would have had the model been totally covered. Although the creeping wave was different from that observed on the totally covered object (since the fields in the shadow were measured on the exposed metallic surface), the fields on the conical portion were practically unchanged. This was true for all three terminations studied, suggesting that once the fields have been suppressed along the side of the cone,

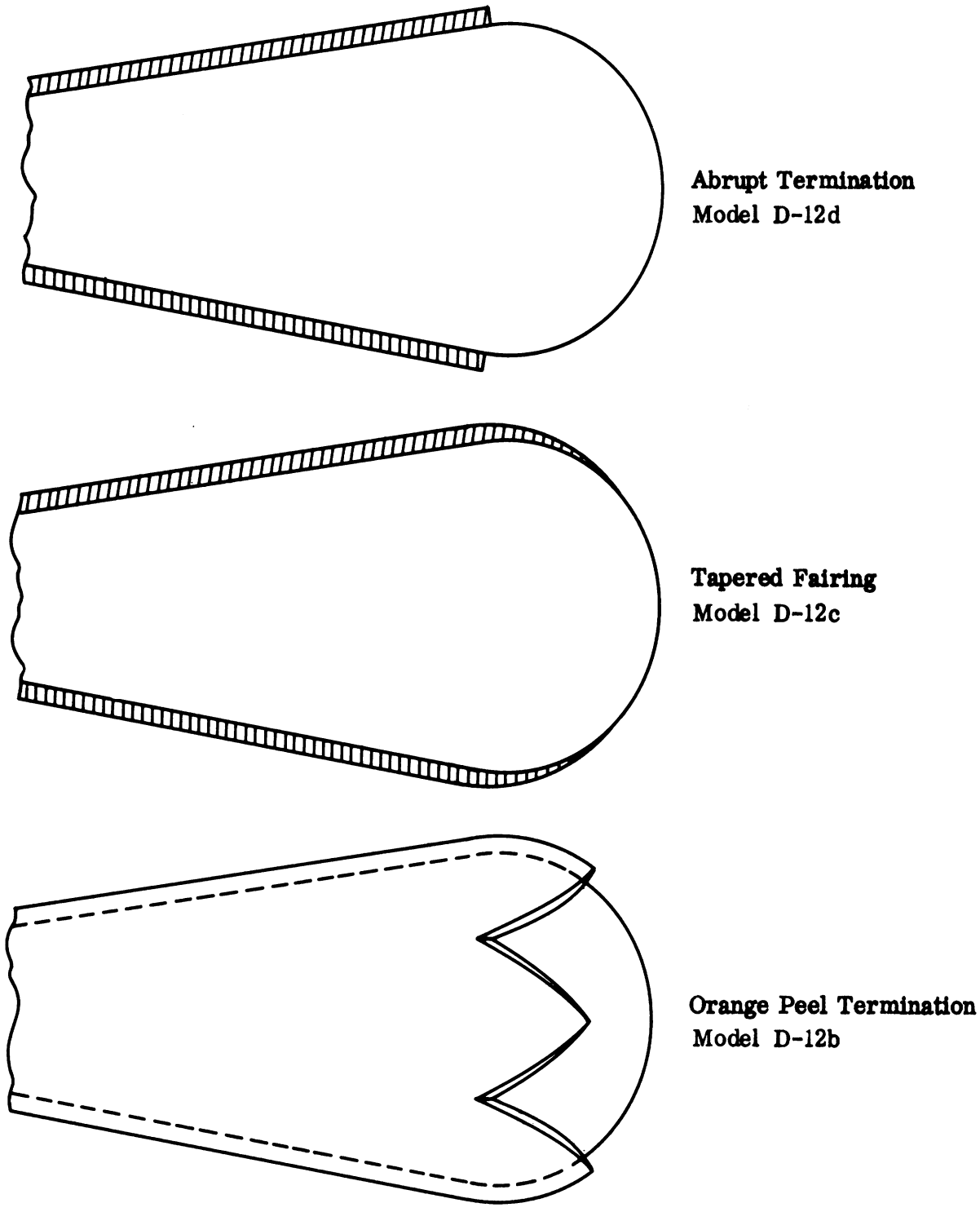

FIG. 2-4: THREE METHODS OF FAIRING LOSSY COATING TO CONE-SPHERE SURFACE. COATING WAS LS-24.

it matters little how a partial coating of good absorber is terminated.

(S) In the study of double coatings, a completely coated cone-sphere (this time with Eccosorb casting resin absorber) was partially coated with a thin teflon sheath (see Fig. 2-9). The sheath (or 'boot' as we call it) extended from slightly behind the tip all the way to the join; the material could not be curled around the small curvatures found near the tip, hence about 1 centimeter of the underlying coating of the tip was left exposed. The teflon was not carried beyond the join because it was very difficult to patch a sheet of this material to a double curved surface. Measurements of the surface fields with and without the sheath showed that its effect was small. The fields decayed practically the same way in both cases, suggesting that to all intents the presence of the thin lossless coating may be neglected when placed over an absorbing layer.

2.3.6 Indented Base Models (Tasks 2.1.6, 2.1.10, 2.1.5, 2.1.4)

(S) A series of three indented bases was constructed which approximated the terminations found on typical re-entry vehicles. The contour of the base of each was formed by two circles, the smaller of which had the same radius for all three terminations and the larger of which was varied. This resulted in a varying depth of indentation, as shown in Fig. 2-5, which was subsequently probed for each model. An ordinary magnetic probe was bent so that it could be inserted the required distance into the termination but the added horizontal length of the resulting probe lead picked up voltages due to the radial electric field. The resulting field distributions were asymmetrical about the center of the termination due to this voltage but when the results on either side of the symmetry plane were averaged, much of the error was removed. Only the base was measured with this probe while the conical portion of the model was measured with a more conventional probe. Since these objects were measured, and the resulting data normalized, in two separate steps, the field distributions had to match at the joins (the places where the two sets of measurements had common points). When the raw data are plotted, the field distributions do not match, because the error signal of the probe used for the

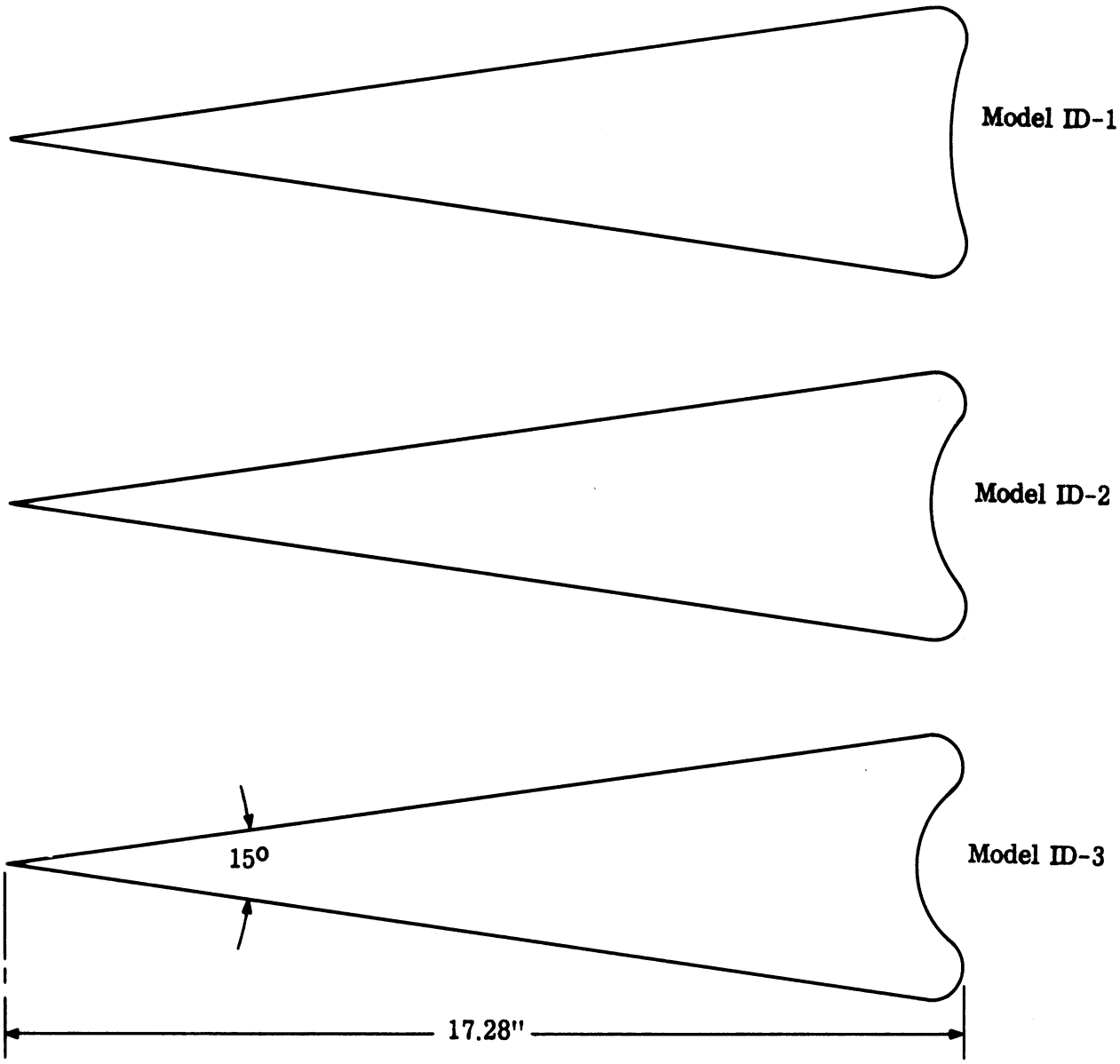

FIG. 2-5: THE THREE INDENTED BASE MODELS HAVE INDENTATION DEPTHS FROM MODEL TO MODEL WHICH VARY AS 1:2:3.

base. However, when the data are averaged (i.e. using the corresponding values on either side of the plane of symmetry) and plotted, the distributions on the conical part matched those on the indented base quite well at the one point in common, the join. Hence the measurements, when reduced and averaged, give a better picture of the behavior than one would suspect from a cursory inspection of the raw data.

(S) The results show that the fields around the rear of these terminations are smaller than for a cone-sphere. The distributions along the conical surface show a very slightly enhanced perturbation which, as will be seen in Chapter III, is related to the creeping wave and the radius of curvature near the join.

2.3.7 Perturbations (Task 2.1.8)

(S) The effects of three kinds of perturbations on the surface fields of a bare cone-sphere were examined. The perturbations were; a) small studs representing rocket nozzles protruding from the surface of the vehicle in the shadow region, b) loops and dipoles mounted on the conical portion to simulate slot antennas, and c) longitudinal and circumferential slots which were modeled from information furnished by Aerospace Corporation to simulate antennas found on full scale re-entry shapes. The effects of the above perturbations have been described in quarterly reports submitted during the course of the contract (see References).

(S) The rocket nozzle simulation was carried out for two frequencies, 3.13 and 3.76 GHz, and in comparison to the cone-sphere on which they were mounted, the simulated nozzles were quite small. Six nozzle ends were affixed to the spherical base of a cone-sphere, oriented as on a REX shape, see Fig. 3-16, and measurements of the surface magnetic fields with and without the small studs showed that their presence could not be detected. To all intents the object was a 'clean' one, as far as could be determined by surface field data.

(S) The perturbations produced on the surface field by a longitudinal slot was another study and rather than modify or destroy a model by cutting a slot in it, we chose to try to simulate the slot with dipole and loop elements. It was assumed that one or the other of these elements could simulate a slot and by mounting them on a

cone-sphere we would avoid mutilating a test object. It was discovered that a single element could not simulate the slot, but the data which was obtained gave considerable insight into the effect of these perturbations. Loaded monopoles, which were actually carbon resistors, were used for the elements and not unexpectedly some combinations of monopole length and load gave large surface field perturbations whilst others gave scarcely any. For example, a quarter wavelength long wire erected perpendicular to the cone surface, scarcely perturbs the surface field if it is not touching that surface, whereas the perturbation is locally very strong if it does contact the surface. A 3/8 wavelength long wire severely disturbs the surface fields, whether it contacts the surface or not. Wire loops behave in similar fashion; a loop 0.4λ in circumference has no effect of the surface fields, while one 0.8λ in circumference has a large effect.

(S) In addition to the simulation of a longitudinal slot with wires and wire loops a model with an actual slot in it was constructed (see Fig. 2-10). The slot was designed approximately to the same relative length as those found on REX or LORV vehicles; i.e., the total slot length when divided by the vehicle length results in the same ratio for our model and for the full scale object. A set of metallic and dielectric plugs was obtained so that the electrical depth of the slot was subject to control. It turns out that the slot is almost exactly 0.45λ wide (resonant) when the frequency of the illumination is such as to give ka=2.0 and is 0.90λ wide (anti-resonant) when ka=4.0. The object bearing the slot was illuminated nose-on for both these ka values and the local slot fields were probed for two different slot depths (provided by the dielectric loading); for the lower ka, the slot was examined in two orientations. The results showed that when the slot lay perpendicular to the plane of the electric polarization its effect was barely measurable and when it lay in the plane of the polarization the fields over its aperture fell by 0.5 db or so. However, the surface fields just adjacent to the slot seemed to be relatively unaffected. The experiment suggested, at least for the orientation examined (nose-on incidence), the slot has a relatively small effect.

(S) At the direction of Aerospace Corporation, two annular antennas were represented by taking out a transverse slice of the metal (of the cone-sphere) and replacing it with an equally thick slice of dielectric material (see Figs. 2-11 and 2-12). This electrically separated the model into two non-contacting parts. The first 'antenna' was about 3.5" from the tip and the second was just aft of the join; in each case the dielectric spacer was 0.25" thick and was made of lucite.

(S) Measurement of the surface fields showed that the first of these, the tip antenna (called lucite spacer point, LSP), could be a severe source of reflection for some frequencies. The electrical circumference of the spacer turned out to be the critical quantity and when the spacer was about a wavelength in circumference the reflections were particularly large. The second model, representing a ring antenna at the rear of a model, had the spacer near the join. It was called LSH (lucite spacer hemisphere). The spacer had a smaller perturbing effect on the surface fields than did that of model LSP. The measurement showed that a disturbance of this kind can have a large effect and it is probable that an internal load in these simulated annular antennas will further complicate the behavior.

2.3.8 Backscatter Measurements (Task 2.1.7)

(S) The backscattering patterns of some of the models described above were measured for selected frequencies. These far field measurements were made as required by the requirements of the analytic study and to confirm theoretical computations of radar cross section based upon formulas under development. The frequencies for which the measurements were meaningful and/or for which surface field data had been acquired were selected as far as was consistent with available equipment. Ideally, the radar cross sections (backscattering) should have been measured over a range of closely spaced frequencies in order to bring out their cyclical behavior but a program of this scope was not essential. The same frequencies as were used for the backscatter system could not always be used in the surface field facility by virtue of the fundamental differences in the equipment used for each system. As will be discussed in Chapter III, we did succeed in matching some

frequencies within one or two per cent, but these cases are relatively rare. It was not feasible to 'back up' after the backscatter data were obtained and measure the surface fields at the corresponding far field frequencies.

(S) Generally the measured radar cross sections of the absorber coated objects were smaller than that of a plain, bare model, but it is possible to find some frequencies for which there is an enhancement. This is because the returns of both the bare and coated objects are periodic in frequency and since the periods are shorter for the bare object, a minimum in its response may lie near a peak in the response of the coated object. This usually occurs only for low performance coatings.

(S) The radar cross section of the indented base model ID-1 was found in general to exceed that of a cone-sphere of the same base radius. The other indented base models were not measured, but the increase in the return measured for ID-1 can be attributed to the small radius of curvature just behind the join. Not enough frequencies were used in the backscatter measurements to permit a detailed analysis of this enhancement to be made from experimental work, but in general, the return was 6 to 8 db greater than a cone-sphere of comparable physical size. Further study of this Mk-12 type of termination will be made in a subsequent phase of SURF.

(S) The radar return of the tip antenna simulation model (LSP) showed that the surface field data interpretation was useful. Those data suggested an enhancement of several db would be observed and this was confirmed by the relatively few backscatter measurements to be of the order of 4 db.

2.4 Models (Task 2.1.13)

(U) During the course of the contract several models had to be constructed or modified to suit experimental needs. In this section photographs of some of the objects (Figs. 2-6 through 2-13) are presented along with a brief description of their purposes or features.

2.5 Re-entry Plasma Experiments (Task 2.1.12)

(S) Recommendations for experiments to investigate the effect of the re-entry plasma sheath on the radar cross section have been formulated. They are based

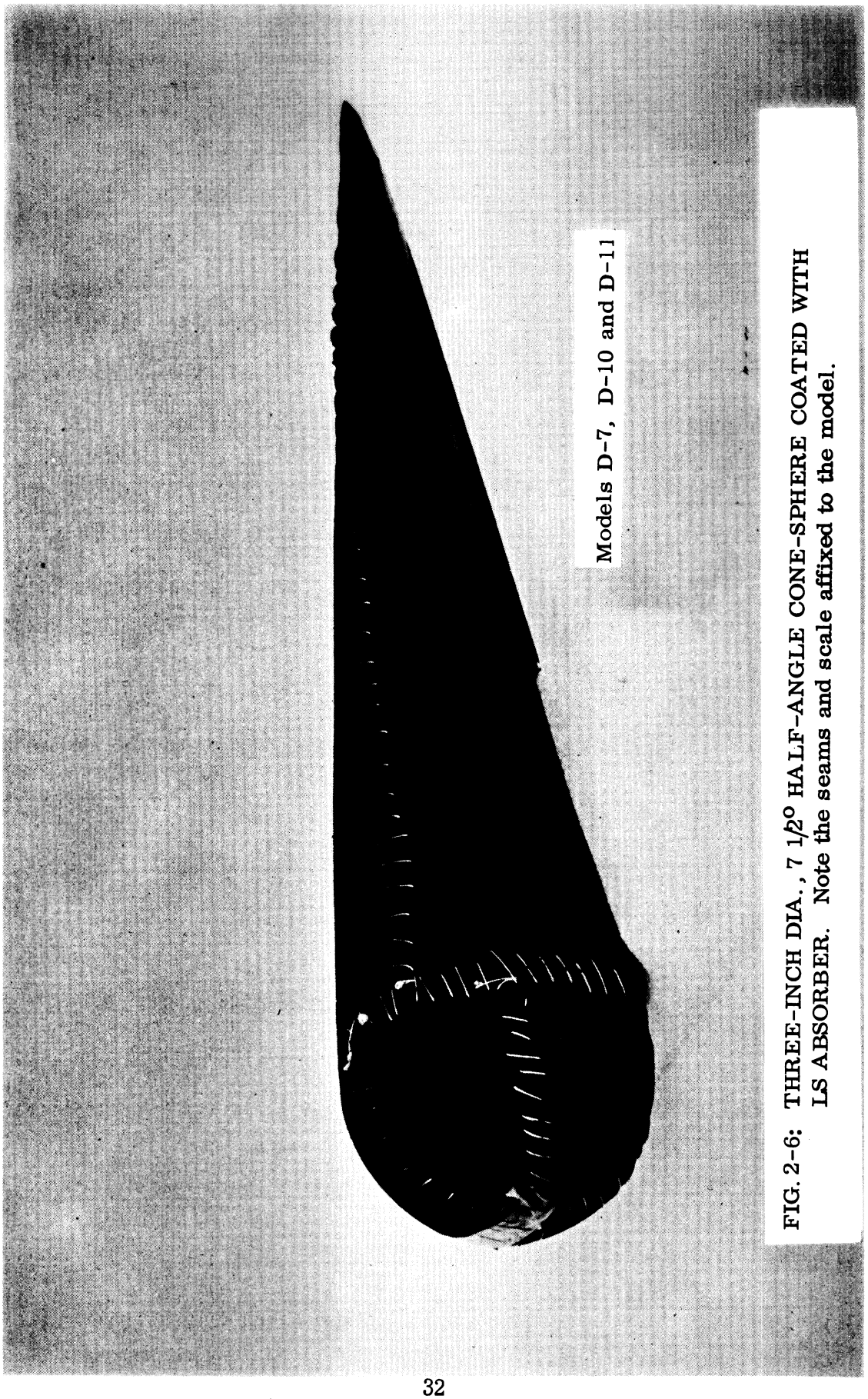

FIG. 2-6: THREE-INCH DIA., 7 1/2° HALF-ANGLE CONE-SPHERE COATED WITH LS ABSORBER. Note the seams and scale affixed to the model.

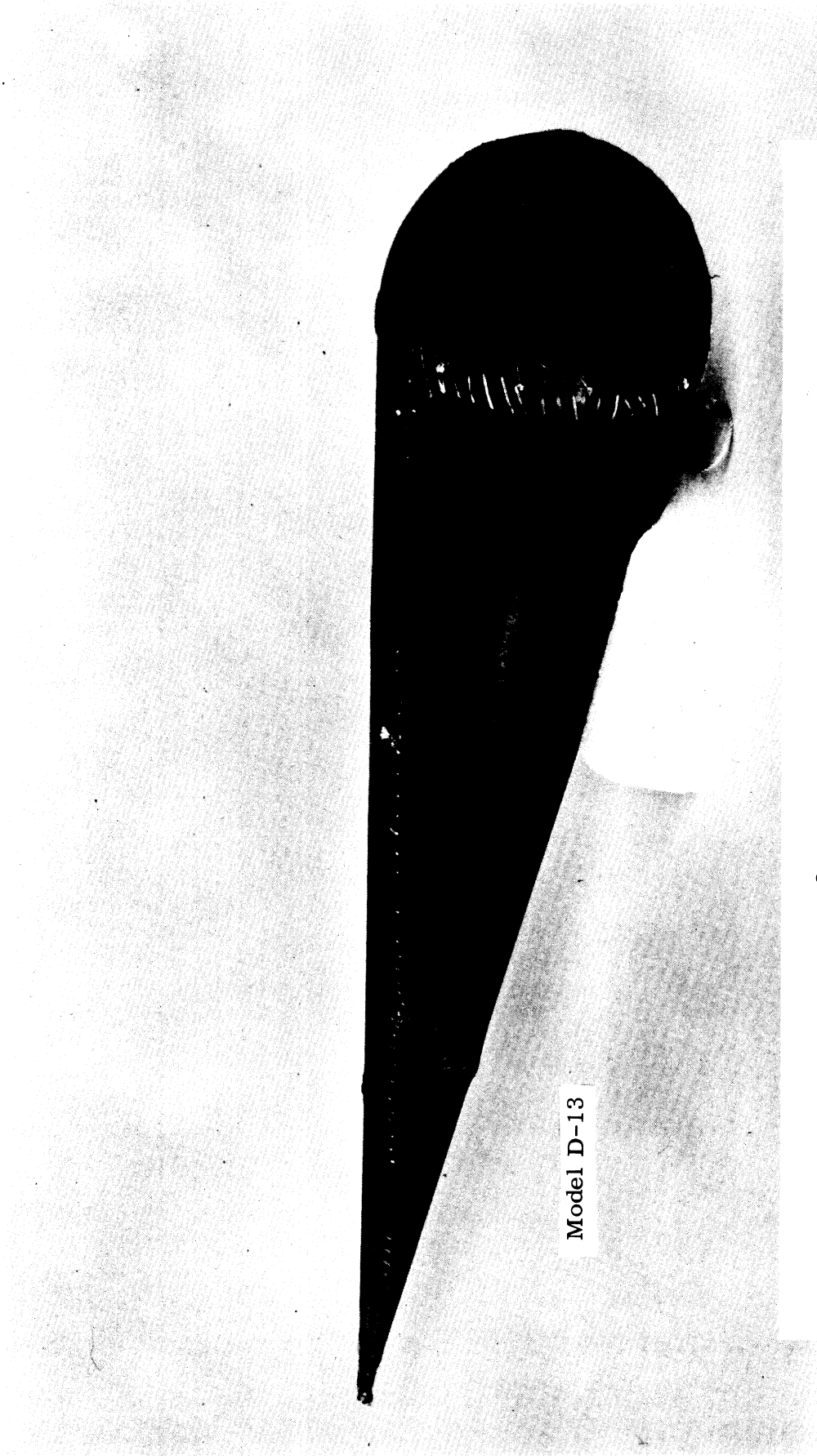

FIG. 2-7: 4.42" BASE DIA., 7 1/2° HALF-ANGLE CONE-SPHERE COATED WITH RS-X ABSORBER. The coating was difficult to apply, as the many seams attest.

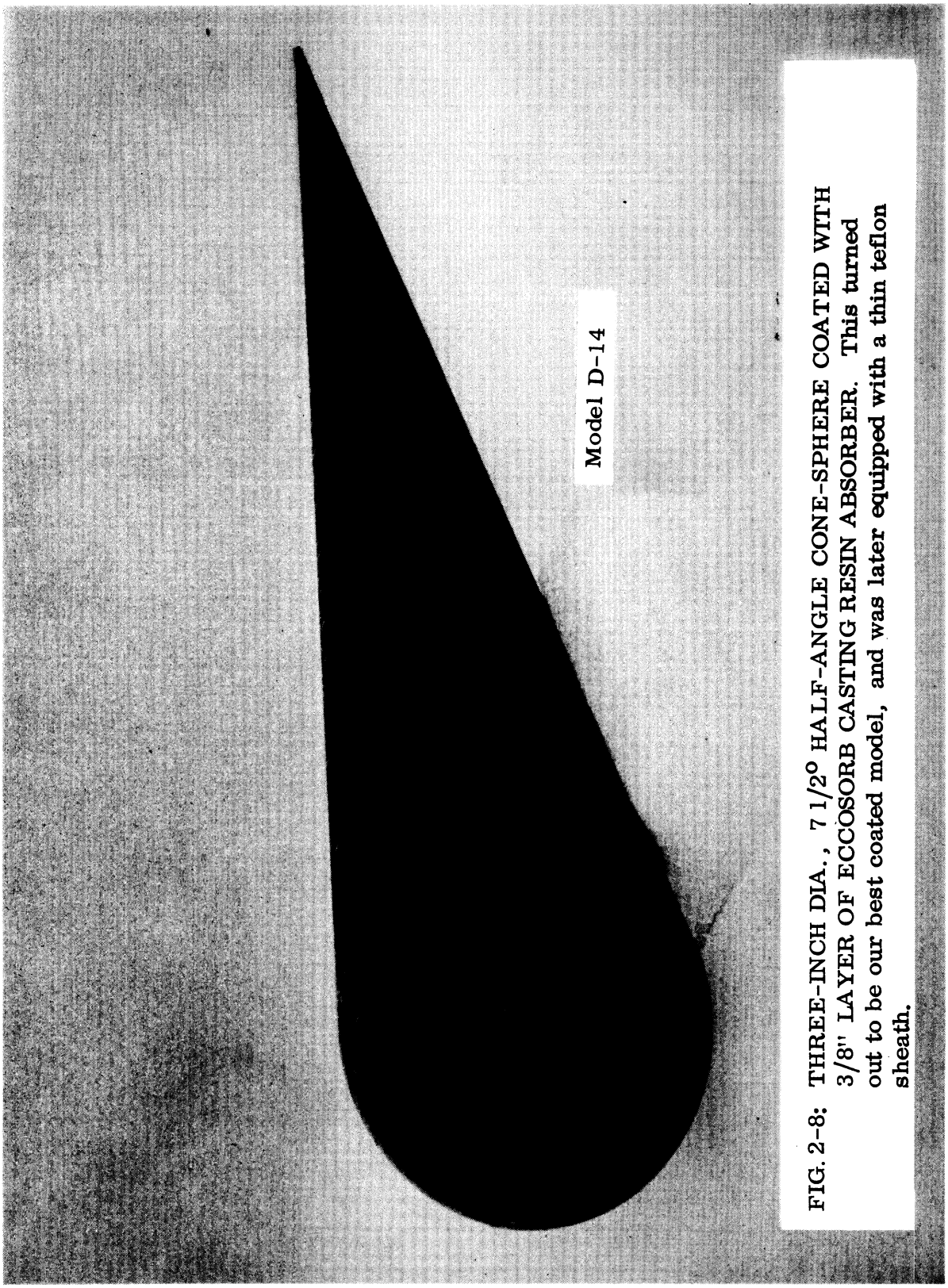

FIG. 2-8: THREE-INCH DIA., 7 1/2° HALF-ANGLE CONE-SPHERE COATED WITH 3/8" LAYER OF ECCOSORB CASTING RESIN ABSORBER. This turned out to be our best coated model, and was later equipped with a thin teflon sheath.

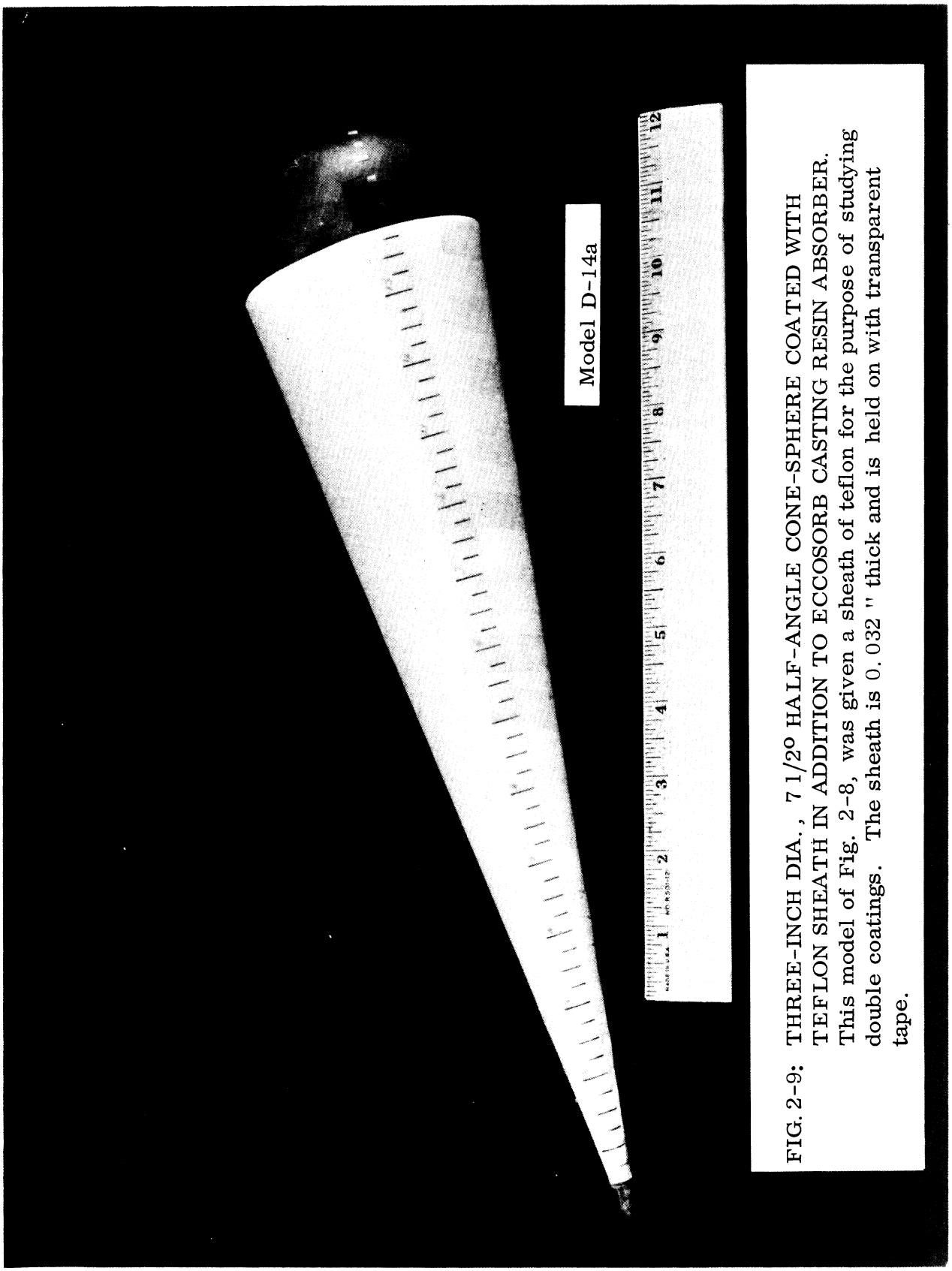

FIG. 2-9: THREE-INCH DIA., 7 1/2° HALF-ANGLE CONE-SPHERE COATED WITH TEFLON SHEATH IN ADDITION TO ECCOSORB CASTING RESIN ABSORBER. This model of Fig. 2-8, was given a sheath of teflon for the purpose of studying double coatings. The sheath is 0.032 " thick and is held on with transparent tape.

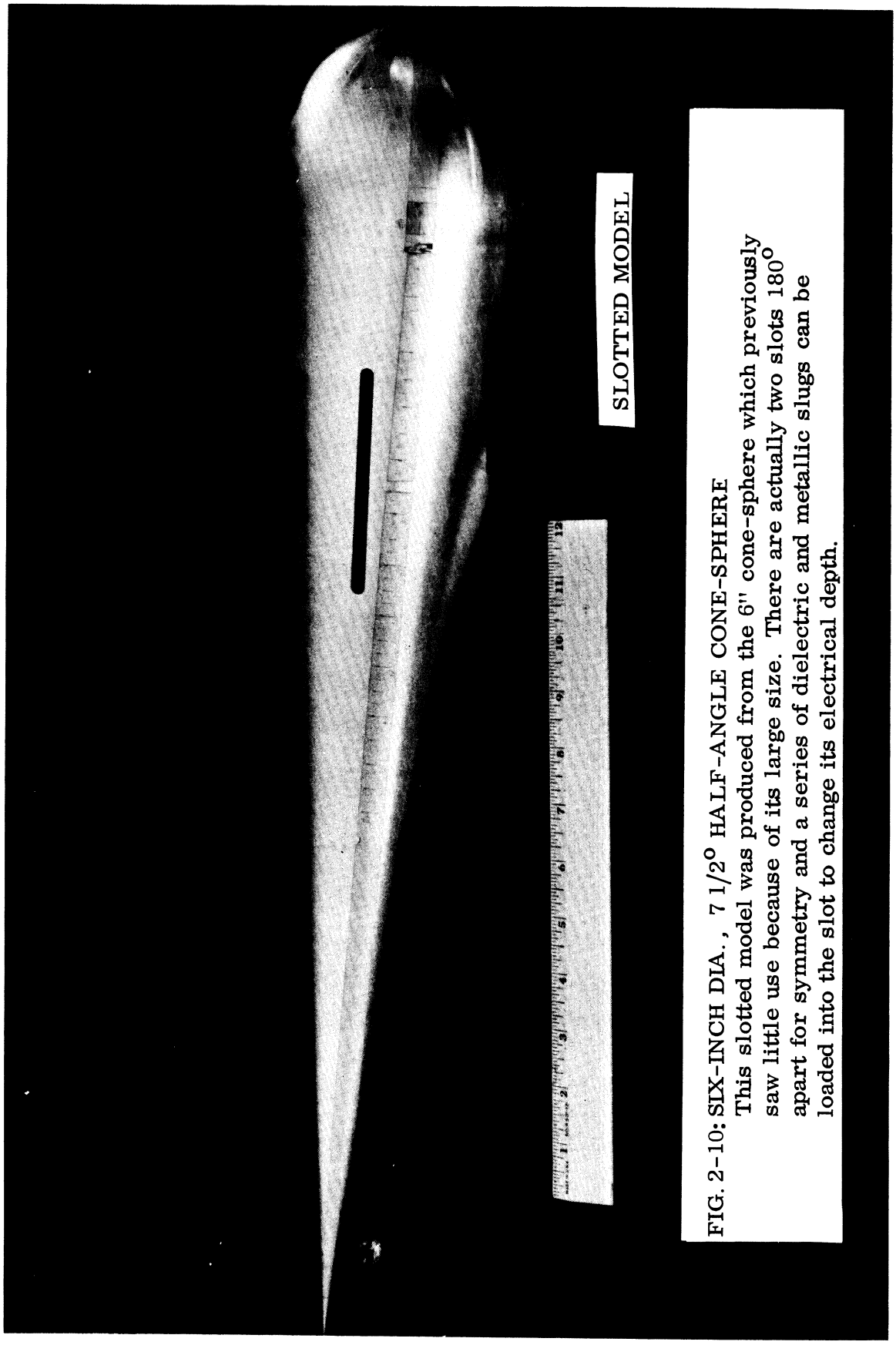

FIG. 2-10: SIX-INCH DIA., 7 1/2° HALF-ANGLE CONE-SPHERE
This slotted model was produced from the 6" cone-sphere which previously saw little use because of its large size. There are actually two slots 180° apart for symmetry and a series of dielectric and metallic slugs can be loaded into the slot to change its electrical depth.

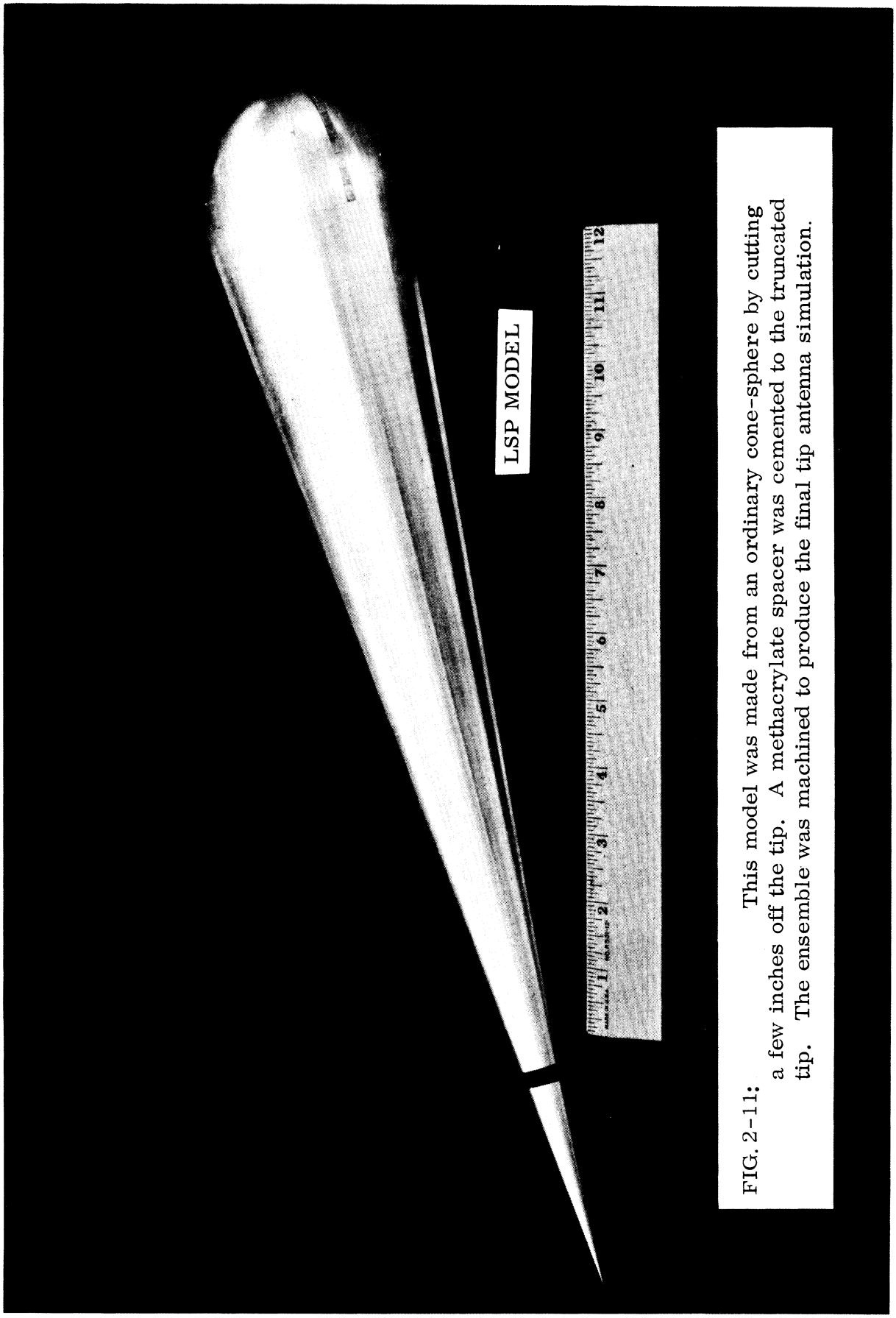

FIG. 2-11: This model was made from an ordinary cone-sphere by cutting a few inches off the tip. A methacrylate spacer was cemented to the truncated tip. The ensemble was machined to produce the final tip antenna simulation.

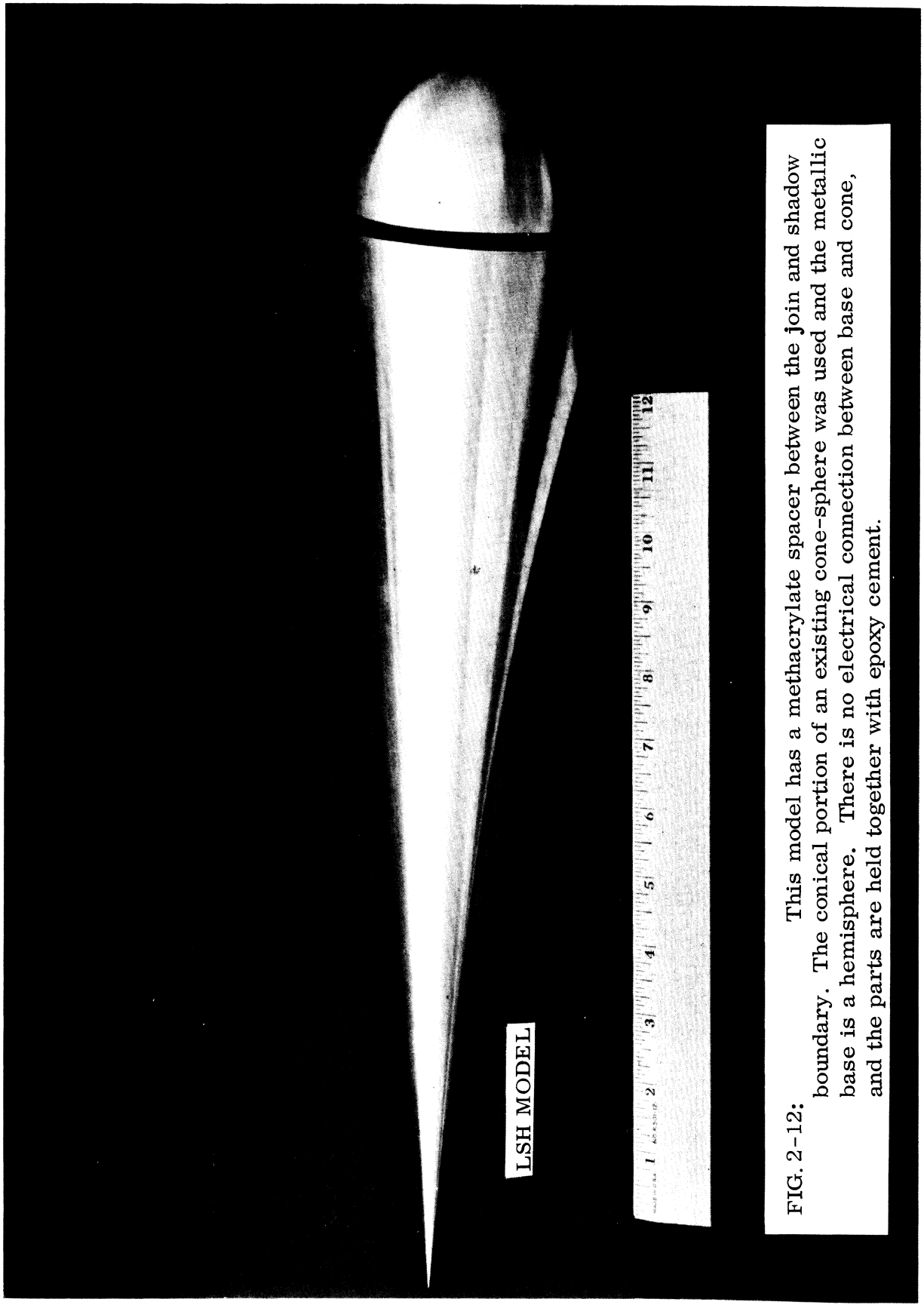

FIG. 2-12: This model has a methacrylate spacer between the join and shadow boundary. The conical portion of an existing cone-sphere was used and the metallic base is a hemisphere. There is no electrical connection between base and cone, and the parts are held together with epoxy cement.

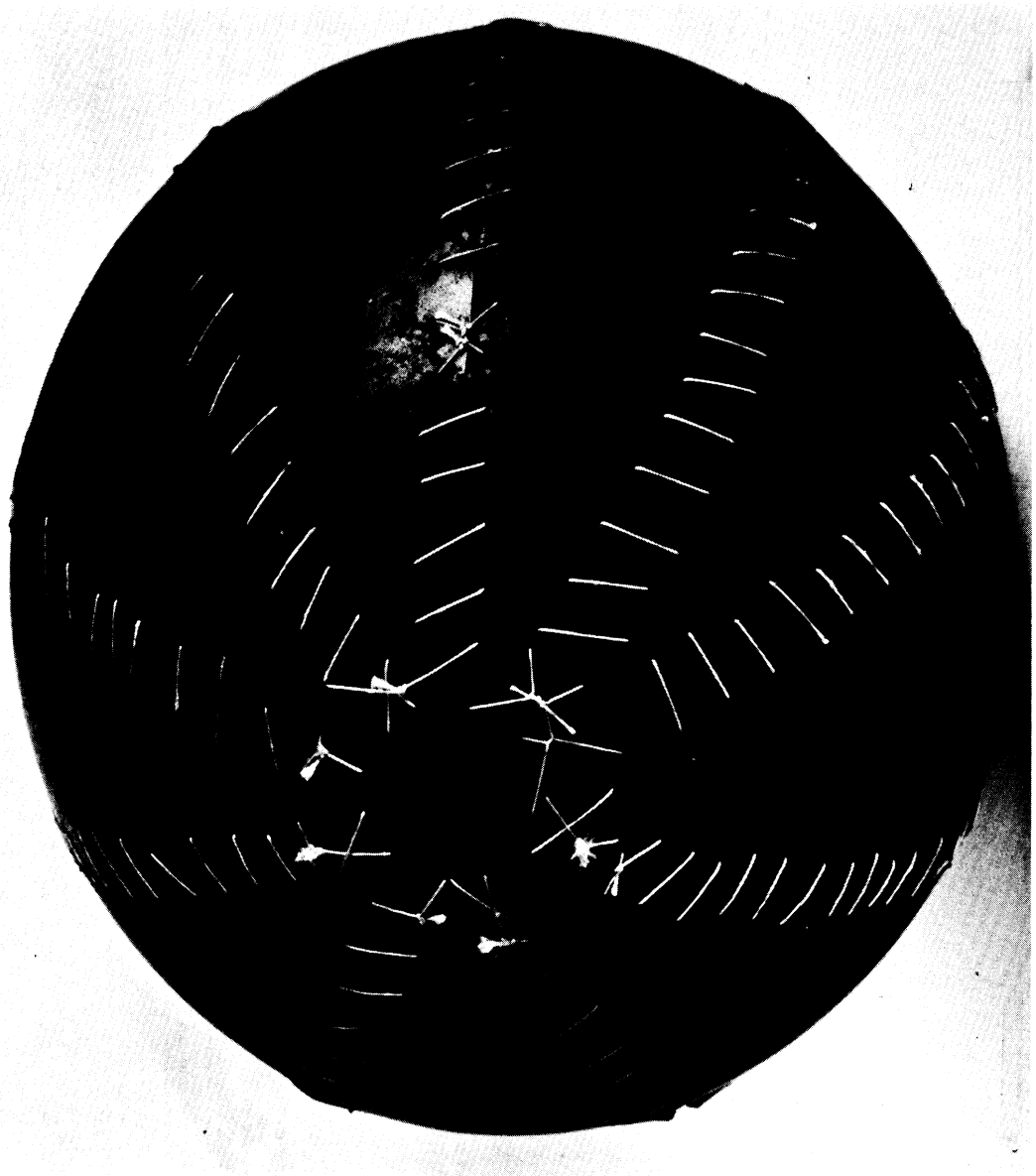

FIG. 2-13: EIGHT-INCH DIA., SPHERE COATED WITH RS-X.

upon the theoretical investigation made during this phase of SURF and are to be carried out in the subsequent phase of the program. The theoretical work was aimed at isolating those cases for which experimental investigations would be useful. The discussion of the recommendations is given in Chapter IV as part of the report on re-entry plasma studies.

III

INTERPRETATION OF EXPERIMENTAL DATA

3.1 Introduction

(S) As evident from the listing given in the preceding chapter, this program has generated a wealth of surface field data for bodies of a general cone-sphere shape, both metallic and otherwise, for a variety of additions and modifications to the basic configuration. Such data is of considerable value in and of itself, but because of the impossibility of investigating every situation of operational interest, it is necessary to draw from the data conclusions that can form the basis for cross section predictions in other and wider circumstances.

(S) Surface field measurements are a most valuable tool in this regard inasmuch as they can serve to pinpoint immediately the effects of perturbing a structure. Whereas the addition of a substantial source of scattering to the surface of a target may serve to reduce its far field scattering at some frequencies due to a fortuitous phase cancellation, and the true effect of the addition can only be judged by a substantial number of far field readings at a variety of closely spaced frequencies, a single set of surface field measurements has the capability of revealing immediately the scattering resulting from the perturbation for all directions of observation under the chosen illumination. To carry through this procedure in general would admittedly involve an integration over the surface of the body, both with and without the perturbation present, and would therefore demand that the surface field measurements include phase as well as amplitude. However, for almost all of the tasks of interest under this program, it is unnecessary to go through this procedure, and though the surface field facility has the ability to provide phase data, the measurements have usually been restricted to amplitude alone.

(S) It is legitimate to ask why it is that such restricted measurements are adequate for our program. The answer lies in the restricted class of bodies that we

are dealing with. These bodies have been selected for their low cross section behavior and have few (if any) surface singularities exhibiting marked resonances. The surface fields are also dominated by incident field and/or surface wave components, which further minimizes any complicated resonance or interaction effects, and because of this, the behavior of the surface field is substantially determined by the local characteristics of the body.

(S) The overriding role played by the local characteristics was clearly demonstrated for the metallic cone-sphere during the first year of this program. Even for cone-spheres which are not electrically large (ka as small as 0.8, where a is the radius of the base) an essentially local interpretation of the field distribution that is a logical extension of the high frequency approach is entirely appropriate, and on this picture only certain portions of the surface are responsible for generating the bulk of the back scattered return at any particular aspect. These 'sensitive' regions are located where the mathematical description of the surface profile (or one of its derivatives) is discontinuous (e.g. the base of a right circular cone or the join of a cone and spherical cap), or where an element of the surface is normal to the direction of illumination (e.g. the tip of a blunted cone, or the side of a cone for near-specular incidence), or where a surface wave is born or launched (e.g. a shadow boundary). Thus, for example, at nose-on incidence the cross section of a cone-sphere is made up of a join contribution determined by the geometry of the join and the strength of the local field there; a creeping wave return originating in the vicinity of the shadow boundary and modified by any (minimal) interaction between the join and shadow boundary fields (the creeping wave enhancement); and a tip return. This last contribution is quantitatively insignificant if the tip is pointed, and though it can be important for rounded or blunted tips, it can still be estimated by a substantially local analysis, with any interaction between the tip and rear regions being negligible providing their separation is more than a wavelength or two.

(S) As we go away from nose-on incidence, each of these contributions evolves in a relatively simple manner. The join contribution, for example, initially follows

the Bessel function behavior characteristic of a ring singularity. As the angle increases, the Bessel function can be split into two exponentials associated with returns from diametrically-opposed portions of the ring. Outside the backward cone, the further part of the ring is shadowed and its contribution is no longer present, whereas the exponential corresponding to the nearer part can be combined with the (growing) tip return, leading ultimately to the specular flash and its side-lobes as we approach an incidence angle normal to a generator of the cone.

(S) All this is, of course, fully described in the Final Report resulting from the first year's investigation, but the important point to be remembered is that with any modification to the original body shape or constitution it is only necessary to examine (a) the scattering or surface field perturbation attributable directly to that change, and (b) the effect (if any) on the other scattering contributions from the body. To achieve this end, it could be enough to sample the surface field only in the immediate vicinity of the perturbation, and to do so only for nose-on incidence. Even if we were to coat the original surface in its entirety with a non-metallic material, there may be no necessity to measure the surface field at all points (or, conversely, to be able to predict accurately the surface field everywhere) in order to produce an adequate prediction of the scattering. For example, with a pointed body viewed at or near nose-on, the only sensitive regions of the surface are the vicinity of the join and beyond, and this is still true in the presence of the coating. Hence, for prediction purposes at the above aspects, we only have to be able to predict how the coating affects the level of the surface field near the join, and how the creeping wave is modified. A knowledge of the field over the whole of the surface of the cone is not important unless we are also seeking to add perturbations (e.g. slots or antenna) there. This we shall be doing in the year to come

(S) In the following sections of this chapter we shall be presenting data, both surface field and (in some cases) back scatter, for a variety of modifications to the clean, metallic cone-sphere shape, and we shall interpret this data to produce an understanding sufficient for cross section prediction purposes. Space permits the

inclusion of only a small fraction of the data that has been obtained. It is our belief that the data shown is representative, and that the conclusions reached, based on an analysis of all the data, are well substantiated.

(S) The initial cone-sphere modification to be discussed (Section 3.2) is that of adding one or more external protuberances to the surface. The protuberances took the form of electric dipoles of variable impedance (small resistors), magnetic dipoles (wire loops) or metal studs. In the case of the first two categories, it was our intention to use them to simulate slots, thereby avoiding the destructive (and costly) modification to the body which results when slots are cut, and enabling us both to move the 'slots' and vary their loading in a relatively painless manner. The importance of the loading applied to the slot (or dipole) will be referred to again in a moment. In parallel with the measurements, a theoretical study of the equivalence of slots and dipoles was performed (Plonus, 1966), and this showed that not only were both an electric and a magnetic dipole necessary (in general) to simulate a slot, but, in addition, the dipoles may have to be placed at positions other than that of the slot. And, even then the simulation is not precise. The advantages of using external dipoles in place of slots are now minimal to say the least, particularly in view of the more complicated interpretational problem that results. For this reason, more attention was directed at slots as such (see Section 3.3), and the data obtained for the external dipoles was felt to be more obviously applicable to the simulation of external antennas. Detailed analysis of the data was therefore postponed, but a brief discussion is given in Section 3.2. In summary it turns out that for a single electric resistor or wire loop mounted on the conical portion of the body in a plane normal to its surface, the effect on the surface field when the body is illuminated at nose-on incidence is (a) confined to the fields or generators of the cone intersecting (or nearly intersecting) the protuberance (i.e. is mainly local), (b) is strongest ahead of the protuberance (i.e. on the tip side) and, in most cases, dies out rapidly (within a half wavelength at most) beyond the protuberance, and (c) is markedly dependent on the resistance value of the dipole or the diameter of the loop.

(S) To assess the effect of rocket nozzles on the surface field, experiments were also carried out with six small button-like studs symmetrically placed around the base of a cone-sphere, and the results are discussed in Section 3.2. Because of the small electrical size of the protuberances when scaled to represent nozzles, it was our expectation that the consequences of their presence would be small. In actual fact, no changes whatsoever in the surface fields could be found.

(S) Section 3.3 is devoted to slots, both longitudinal and azimuthal. The former were two in number, placed 180^{o} apart around the cone just forward of the join so as to simulate a telemetry antenna, and the latter was near to either the tip or join. All surface field measurements for these configuations were confined to nose-on incidence, but complete back scatter patterns at several frequencies were obtained for the aximuthal tip antenna. In the case of the longitudinal slot, the only significant change in the surface field occurred at the slot itself, and the field over the remainder of the body was unaffected. The modification to the back scattering cross section is therefore simply the additive one attributable to the slot return, and this is easily estimated on the basis of a radiating slot of the appropriate excitation placed in an infinite ground plane. Such a prescription should hold for all angles of incidence.

(S) For the azimuthal (ring) antenna the effect on the surface field is a good deal greater, but as with the dipole and loop protuberances, the main effect occurs forward of the ring and is identifiable as a backward traveling wave resulting from a reflection at the ring. When the ring is near to the tip, the field beyond it reverts to the values that it had on a 'clean' cone-sphere within a distance of a wavelength or so, and consequently the join and shadow boundary fields are unaffected by its presence. Once again, therefore, the modification to the scattering cross section is easy to determine, and by likening the ring antenna to the surface singularity at the rear of a flat backed cone (with the strength of the singularity deduced from the amplitude of the surface field oscillations), the additive contribution to the scattering can be found.

The estimates are consistent with the bounds derived from an examination of back scatter data.

(S) With the ring placed at the join of the cone and sphere, the field over the whole of the conical portion of the body is changed as a result of the reflection of the field at the ring, and, in addition there is a small but detectable modification of the field over the spherical cap. This last is due to the presence of the perturbation in the 'sensitive' region of the surface, and to the fact that the field no longer has sufficient time to regain its original value before the shadow boundary is reached (when it is deprived of the direct influence of the incident field). In practice, the modification to the creeping wave contribution is of no concern. Using the magnitude of the surface field oscillations ahead of the ring, the direct scattering can be estimated, and not surprisingly it turns out to be comparable to that which would be found were the body terminated with a flat back at this point. Such scattering is, in general (i.e. for ka greater than (about) unity), much greater than for the unperturbed cone-sphere, and by comparison, any creeping wave component is negligible even when enhanced.

(S) It is tempting to conclude from these results that a ring antenna near to the tip is superior to one placed further back, but such a conclusion would be hasty. Since the ring has, in practice, to operate as an antenna, it must be so excited as to give an acceptable signal over a specified angular range, and this is in turn related both to its radius and to its radiation impedance. The impedance presented by the antenna to the incident illumination is an important factor which was in no sense under our control in the experiments carried out. Indeed, the antenna was simulated by a simple lucite spacer only, and any discussion of the advantages of one positioning over another is of marginal validity unless the impedance of the antenna, subject to a design performance at its operating frequency, is taken into account.

(S) It is at once obvious that the modification to the scattering from the unperturbed shape is vitally affected by the impedance of the ring or slot, since this is the fundamental basis of the so-called reactive (or impedance) loading technique for cross section control. Detailed studies of this technique over the last five years

have shown that the method is capable of either increasing or reducing scattering from the original body, but that the resulting modifications to the surface field are often confined to the immediate vicinity of the load. Indeed, the method can be evaluated by a straightforward superposition process, with the ability to control the amplitude and (most essentially) the phase of the additive component being achieved through variations in the impedance applied to the load. Thus, for example, a body viewed at some aspect and loaded with a slot at some position may have its cross section reduced by 30 db or increased by 5 db by varying only the loading of the slot (see, for example, Liepa and Senior, 1965), and for this reason the cross sectional changes obtained with the passive slots considered in this program are not necessarily indicative of those that would occur with more realistically loaded slots, even when located at the positions we have used. On the other hand, the types of effect we have observed are believed to be typical.

(S) The next form of cone-sphere perturbation considered is the replacement of the spherical rear by an indented back, and the measured data is discussed in Section 3.4. Three variations of indentation were examined and the profiles are depicted in Fig. 2-5. In each case the linear profile of the cone was first joined to a spherical segment of radius 0.533", and thence to a concave spherical segment. The three models ID-1, ID-2 and ID-3 had different radii for the latter segment, with continuity of tangency preserved at the joins in all cases.

(S) For each model the surface field was measured at four different frequencies (0.935, 2.55, 4.25 and 6.799 Gc) with nose-on incidence. Comparison (see Figs. 3-25 through 3-27) with the data for a pure cone-sphere of the same cone dimensions shows that in the vicinity of the join of the cone and cap the field is not significantly changed by the different termination, but thereafter the field at any given distance back of the join of the ID models is substantially lower than at the same distance on a purely spherical cap. This does not, however, imply that the creeping wave contribution to the back scattering cross section is reduced. Indeed, along the sides of the cone, all three models show surface field oscillations of almost the

same amplitude, which would support the idea that the creeping wave 'skips across' the concavity, and these amplitudes are only slightly larger than for a cone sphere at the lowest frequency considered, and almost indistinguishable at the higher frequencies. Even so, the back scattering cross section of a cone-sphere at a single frequency will certainly be affected by the change in termination resulting from the different path length traversed by the creeping wave and, hence, by the different phasing of its contribution relative to that from the join, but there is no evidence to suggest that any one of the three terminations has raised the mean cross section (i.e. the cross section averaged over a range of frequencies) to any marked extent. Such a conclusion is not inconsistent with the back scattering patterns for the ID-1 model which were also obtained at four (unfortunately different) frequencies, namely 2.53, 3.37, 3.83 and 5.73 Gc.

(S) The final form of cone-sphere modification investigated is, perhaps, the most drastic of all and consists of the use of non-metallic surfaces. A wide variety of coatings was considered, including materials either lossy or lossless, double layerings, and both full and partial coverings, and when the variations of parameters inherent in these cases are combined with the variations such as frequency, aspect angle and body size implied by the base surface, it is obvious why the study of this cone-sphere modification was the most extensive of all. On the experimental side the task is complicated by the necessity of acquiring coatings having an adequate range of electrical properties so as to sample the differing ways in which the surface field can be affected. And having acquired the coatings, we must then physically apply them to the surface in a manner as uniform and devoid of irregularities as possible.

(S) Whereas with a metallic surface only the magnetic field has non-zero tangential components and, in practice, it is often sufficient to confine the measurements to one of these components alone, a non-metallic surface can support a non-zero tangential electric field as well. In some instances at least the electric field can be dominant, and it was therefore necessary to measure up to four individual

surface field components to give an adequate description of the surface field behavior. The measurements of the electric field required the development of new experimental techniques which are described elsewhere, but in spite of these complications, well over fifty different parameter combinations were investigated in complete detail. Space permits the inclusion of only a sampling of the data. This is given in Section 3.4, along with our interpretations of the data and a summary presentation of the theoretical picture of material effects that has evolved thereby. It would be foolish to pretend that the picture is complete, or that it is incapable of improvement. It may not even be sufficient to cope with all of the coatings of practical interest, but it does at least have the intuitive simplicity that is most desirable if the formulae are to be widely employed, and the picture is in general accord with all of the experimental surface field data acquired under this program.

(S) This single study of the effect of coatings on the back scattering behavior of a 'clean' cone-sphere has involved many sub-tasks, both theoretical and experimental. The way in which these tasks evolved, and the relation which they bear to the development of the overall study, are described in Section 3.5.1, but there are a few general comments that can be made here. Firstly, because of using the experimental data only to provide the basis for theoretical expressions that should describe the behavior of coatings in terms of their thickness and electrical properties, there is no requirement for the various coatings to simulate precisely those which are employed operationally. In consequence there is no need for our coatings to be exactly-scaled versions, in thickness and properties, of the full scale absorbers, and, in fact, the materials that we have used have been selected only to produce a reasonable variety of behavior. This has enabled us to profit from the materials readily available on the open market, but has carried with it the necessity of measuring carefully the electrical parameters of these materials at the frequencies we chose to use them. Such measurements, and the results obtained, are fully described in the Second and Third Quarterly reports and in Section 2.6 of this report.

(S) The most desirable outcome of any interpretational study applied to experimental data is a complete understanding of every single facet of every single curve. In the case of coatings, it was not our hope to realize this, and at the present stage we have certainly not achieved it. Rather have we concentrated on those portions of the surface which are known to be responsible for the bulk of the back scattered energy at the appropriate angles of incidence, and with a cone-sphere, our attention is therefore focussed on the portions of the surface near to and beyond the join. The present theoretical picture seems adequate for the prediction of the fields in these regions, although it is not sufficient to reproduce the measured data at positions nearer to the tip. In the continuation of this study when we may be concerned with protuberances, such as slots or antennas, added to the surface of the (coated) cone, it will be necessary to develop and improve the picture to encompass all portions of the cone.

3.2 Protuberances

(S) We here consider the effect of attaching three different types of external appendage to the surface of the cone-sphere. The three types investigated are wire loops of almost semicircular shape, monopoles of various lengths and loadings, and small metallic studs. The loops and monopoles were placed on the cone portion far from the tip, and orientated normal to the surface, and in addition, the loops were either perpendicular or parallel to the cone generator through their midpoints. The studs, on the other hand, were attached to the base of the cone-sphere and were intended as a simulation of rocket nozzles.

(S) As mentioned in Section 3.1, the original motivation for the study of loops and monopoles was the desire to simulate the effect of slots by external attachments only, thereby facilitating the movement and loading of the 'slots' without the costly destruction of models. In parallel to the experimental work, a theoretical examination of the simulation process was performed, and this soon revealed that not only were both loops and monopoles required for this purpose, but also these may have to be placed at positions other than the intended slot if the simulation was to be at all

precise. The complication associated with the interpretation and understanding of data obtained under these circumstances was now felt to be such that the time (and money) could be more appropriately committed to a somewhat enlarged program of actual slot investigations, and these results are presented in Section 3.3. In the meantime, however, certain measurements of loops and monopoles had been carried out, and in view of their quite extensive nature, a summary presentation of the data, along with some brief comments, will now be given; but since the data is more directly applicable to the effects of external antennas, conclusions and interpretations will be kept to a minimum.

3.2.1 Loops

(S) The effects on the surface field of wire loops placed on the cone portion of the cone-sphere were studied for three loop configurations. Four different loop sizes, ranging in 1/2" to 2" in diameter, were used in each experiment. The cone-sphere on which the loops were mounted had a half-angle of 7 $1/2^{o}$ and a base radius of 3". Each of the measurements of the azimuthal surface field component was made at a frequency of 3.13 Gc, corresponding to ka=5.0.

(S) The first arrangement consisted of a single wire loop located about 18 3/8" from the tip and placed so that the plane of the loop is perpendicular to the cone generator at that position. Part of the loop was removed, leaving slightly more than a semi-circular section, with the precise fraction determinated by the requirement that, at the points of contact with the cone sides, the wire ends be normal to the cone surface. For convenience the loop size is characterized by kr, where r is the loop radius. It should be kept in mind, however, that kr does not represent the actual circumference of the loop in wavelengths because of the portion deleted. This arrangement, as well as schematic representations of the other configurations, is depicted in Fig. 3-1. As usual, the incident field was horizontally polarized and measurements were taken along a portion of the trajectory formed by the intersection of a horizontal plane passing through the cone axis with the cone-sphere surface. In order to study the angular confinement of the loop-induced perturbations, the

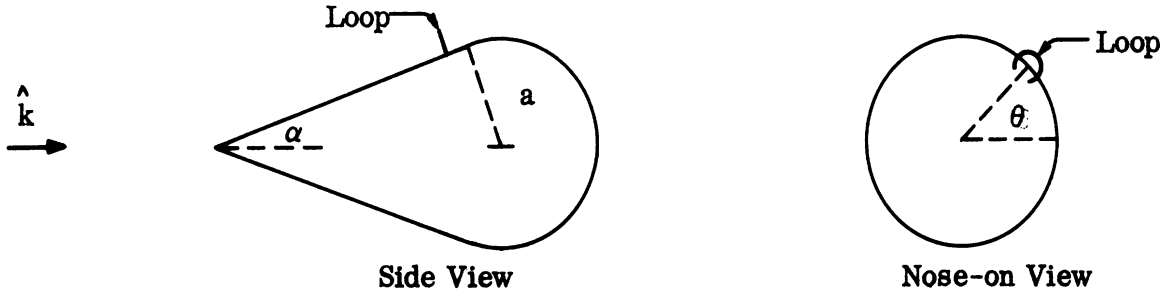

Set I: Plane of Loop Perpendicular to Cone Generator

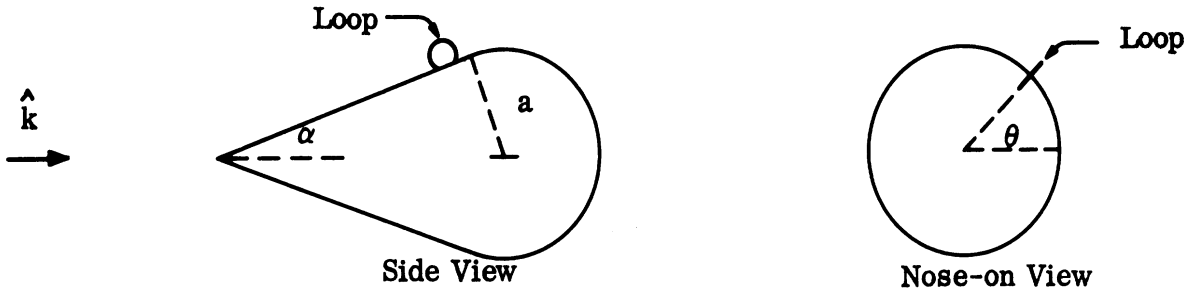

SET II: Plane of Loop Parallel to Cone Generator

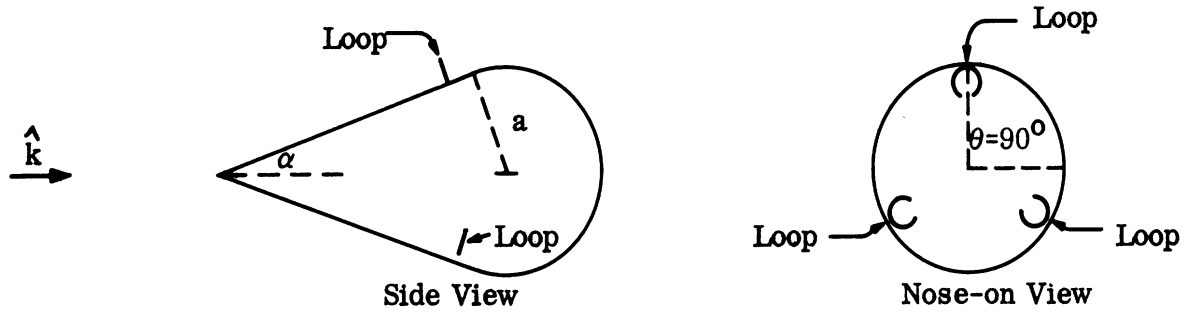

SET III: Three Loops with Plane Perpendicular to Cone Generator.

FIG. 3-1: GEOMETRY OF CONE-SPHERES MOUNTED WITH LOOPS.
($\alpha = 7\ 1/2^{\circ}$, a = 3")

cone-sphere (with the loop mounted) was also rotated through an angle θ about its own axis and the surface field remeasured along the horizontal trajectory.

(S) The second arrangement differed from the first only in the orientation of the plane of the loop: in this case the partially-clipped loop was placed so that its plane was parallel to the cone generator through which its two wire ends passed. Each of the four loops was again used and surface field measurements were obtained for various angular locations (θ) of the loop.

(S) In the final arrangement, three loops of the same truncated nature as in the first set, were placed at 120° intervals around the cone (about) 18 3/8" from the tip. The plane of each loop was perpendicular to the cone generator passing through it and the configuration fixed by the location of one loop at $\theta = 90^{\circ}$. A tabular summary of the measurements is as follows.

TABLE III- 1 :

Configuration	Loop Diameter (inches)	Loop Location
I: Plane of loop perpendicular to cone generator.	2	$\theta = 0^{\circ}$ (15°) 180°
	1 1/2 1 1/2	$\theta = 0^{\circ}(15^{\circ})\ 90^{\circ}$
II Plane of loop parallel to cone generator	2	$\theta = 0^{\circ}(15^{\circ})180^{\circ}$
	1 1/2 1 1/2	$\theta = 0^{\circ}(15^{\circ})90^{\circ}$
III Three loops with plane perpendicular to cone generator	2 1 1/2 1 1/2	$\theta = 0^{\circ}$

(S) The considerable amount of data obtained is represented here by the following selection: For a given loop diameter (2") surface field measurements are shown in Figs. 3-2 through 3-5 for each of the two orientations of the plane of the loop when it is placed at $\theta = 0^{o}$, 30^{o}, 60^{o} and 90^{o} with respect to a horizontal plane. The effects of loop size are considered (Figs. 3-6 through 3-8) by examination of the surface fields for both orientations with the loop placed at $\theta = 0^{o}$ for the various loop diameters. One example of the surface fields for the three-loop configuration is also given. In each case a comparison curve (dashed) shows the measured fields in the absence of the loop(s). In all succeeding figures for the loop-modified surface fields except the last (which refers to the three-loop configuration) the abscissae are given in inches from the tip in which each cm on the graph corresponds to one inch on the model. At the measured frequency of 3.13Gc, one inch is 0.26519λ, so that when s=15, 19 and 23 inches, the respective distances in wavelengths are 3.978, 5.039 and 6.099.

(S) Figures 3-2 and 3-3 contain the surface field data for perpendicular orientation of the 2" diameter loop (for which kr=1.67) with $\theta = 0^{o}$ (30^{o}) 90^{o}. At the cone surface the loop subtends a central angle of approximately 45^{o} and the finite size of the probe and its lead makes it difficult to sample the field in the immediate neighborhood of the loop for the $\theta = 0^{o}$ and $\theta = 30^{o}$ positions. This is the origin of the discontinuity in these graphs. The surface field is significantly altered forward of the loop where there is a 7 db difference in peak-to-trough moduli compared to a less than 0.8 db difference for a no-loop situation. Behind the loop the field drops 2 db below the plain cone-sphere values, but with some slight indication of a gradual recovery. As the angular position, θ, of the loop increases, both modifications diminish, with the 'shadowing' effects decreasing more rapidly than do the field perturbations in front of the loop. At $\theta = 90^{o}$ there is little evidence of any disturbance behind the loop, and even forward of the loop the amplitude of oscillation is only about 0.7 db greater than usual. Although the data for $\theta > 90^{o}$ is not shown here, the effects have become undetectable by the time θ has become this large.

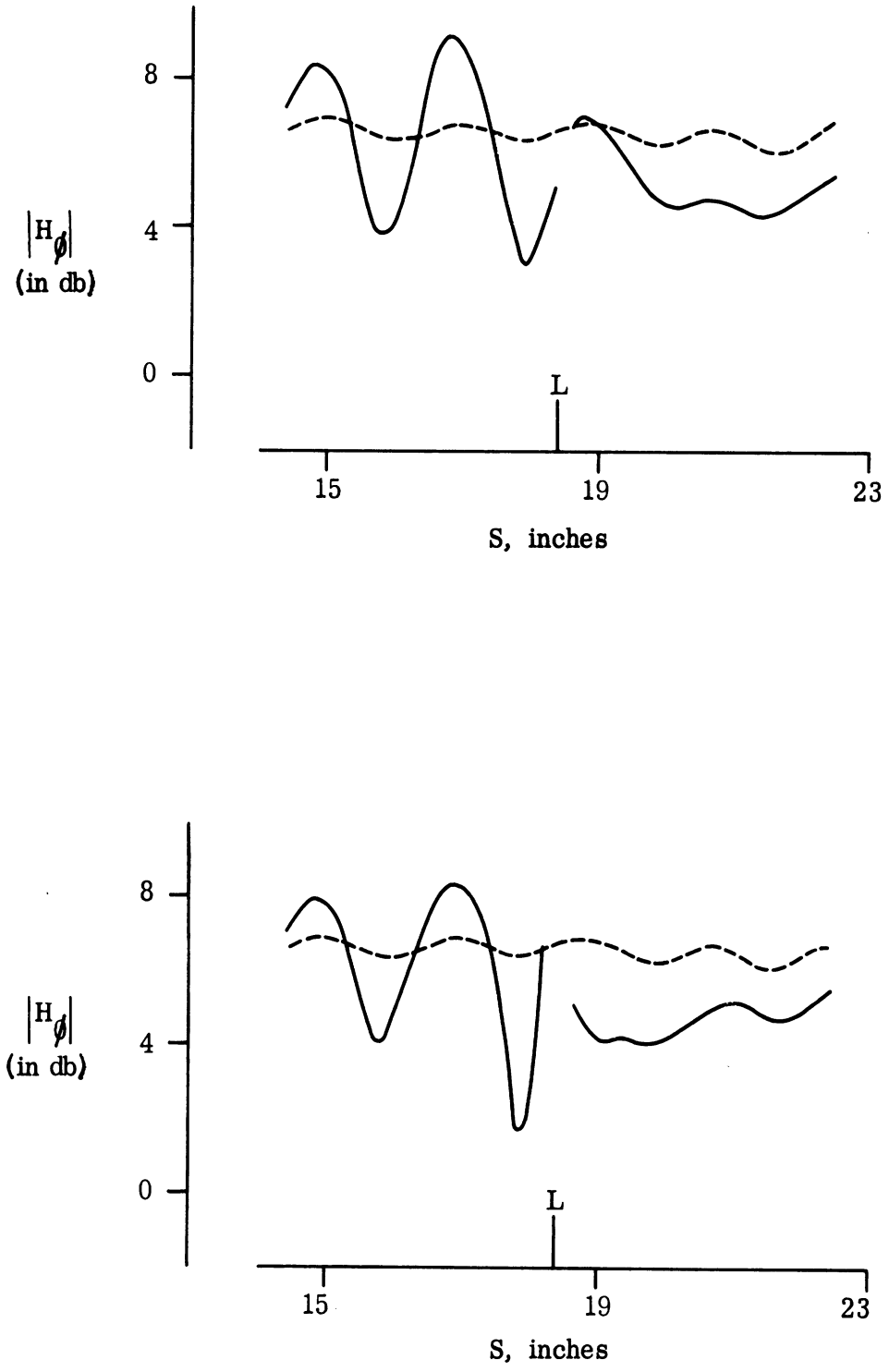

FIG. 3-2: SURFACE FIELD AMPLITUDES $|H_\phi|$ WITH (——) AND WITHOUT (– – –) A 2" DIAMETER PERPENDICULAR LOOP: UPPER CURVE $\theta=0^\circ$; LOWER CURVE $\theta=30^\circ$. ka = 5.0

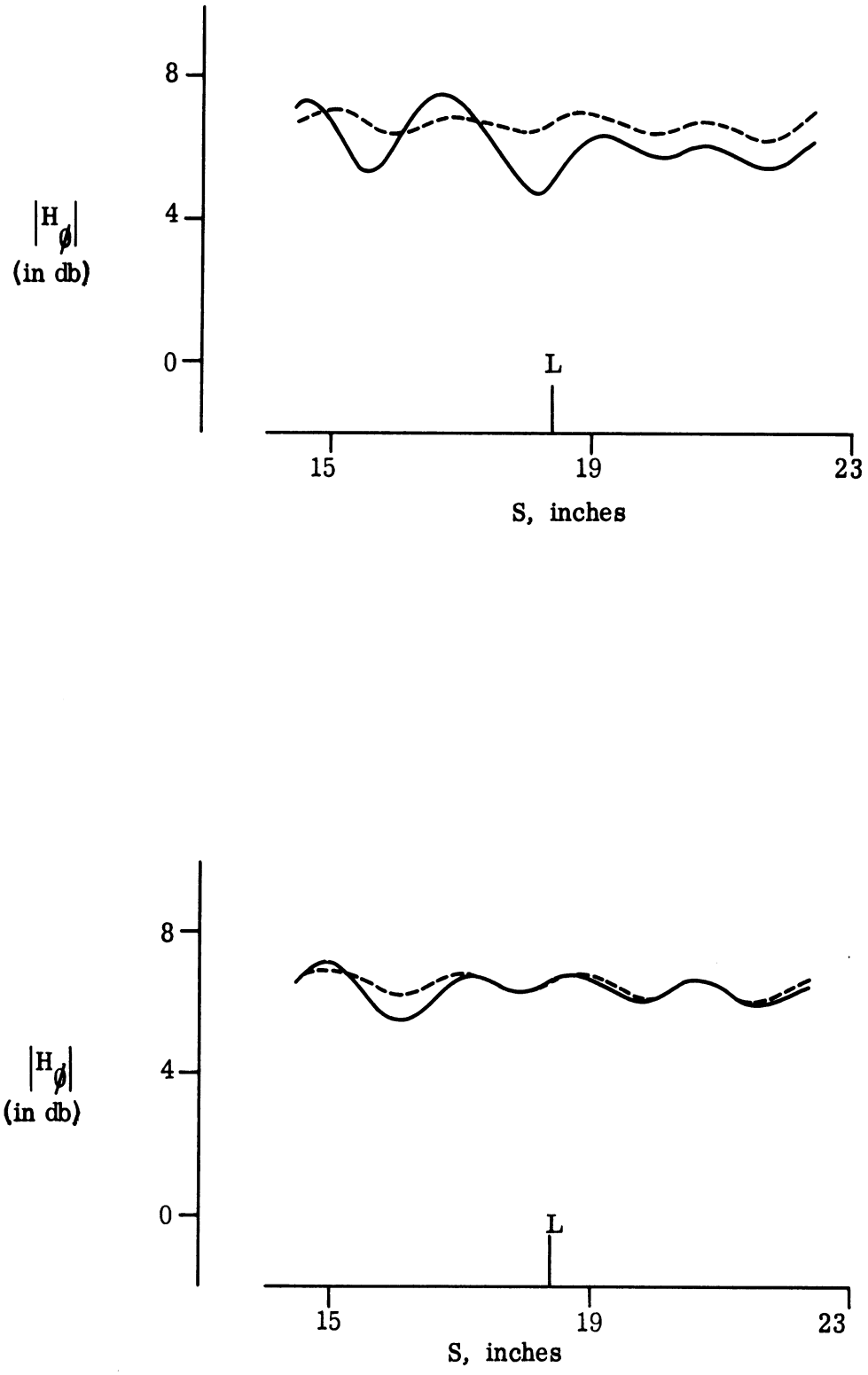

FIG. 3-3: SURFACE FIELD AMPLITUDES $|H_\phi|$ WITH (——) AND WITHOUT (- - -) A 2" DIAMETER PERPENDICULAR LOOP: UPPER CURVE θ =60°; LOWER CURVE θ = 90°. ka =5.0

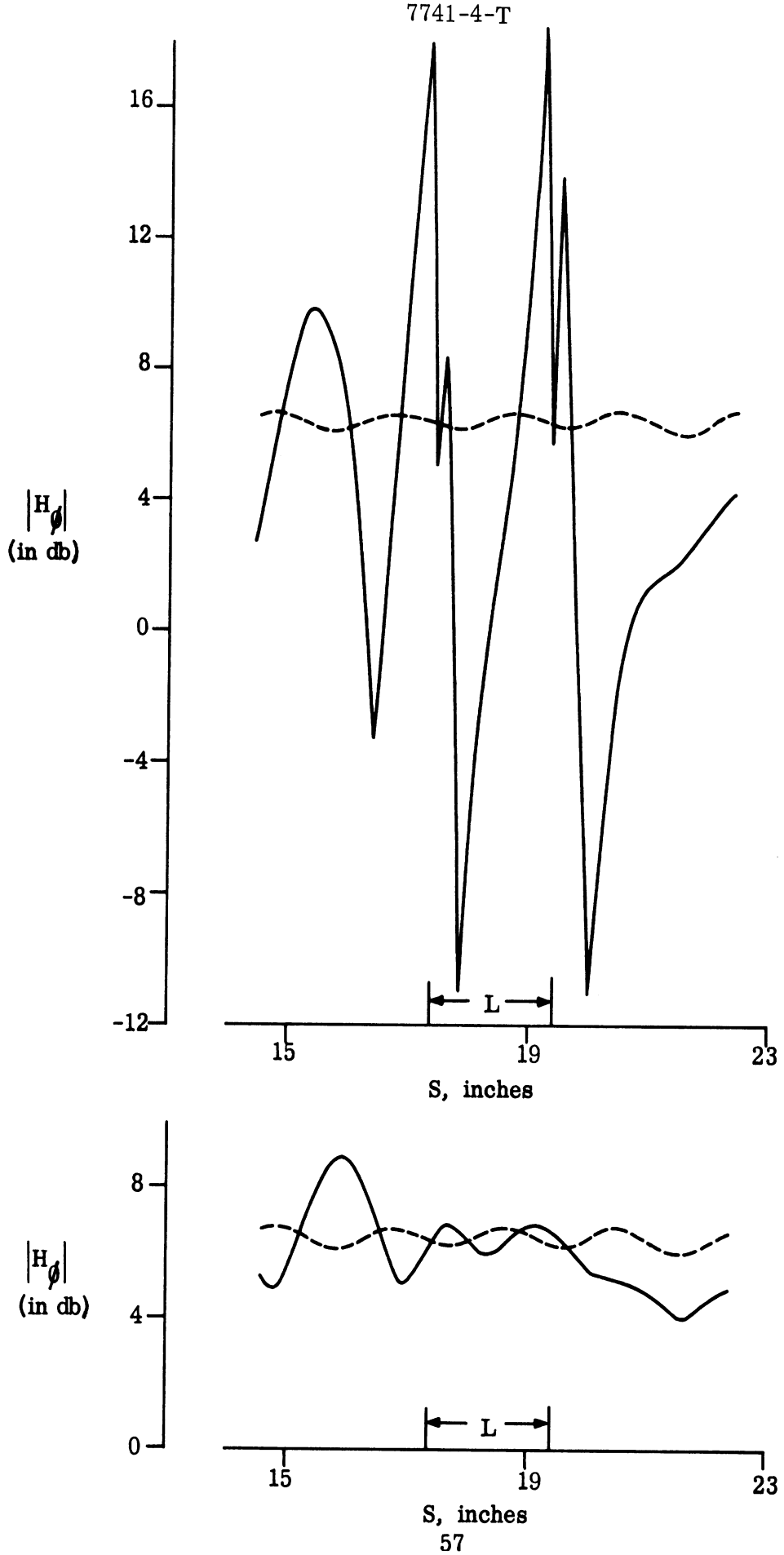

FIG. 3-4: SURFACE FIELD AMPLITUDES $|H_\phi|$ WITH (——) AND WITHOUT (- - -) A 2" DIAMETER PARALLEL LOOP: UPPER CURVE, $\theta = 0^\circ$; LOWER CURVE, $\theta = 30^\circ$. $ka = 5.0$

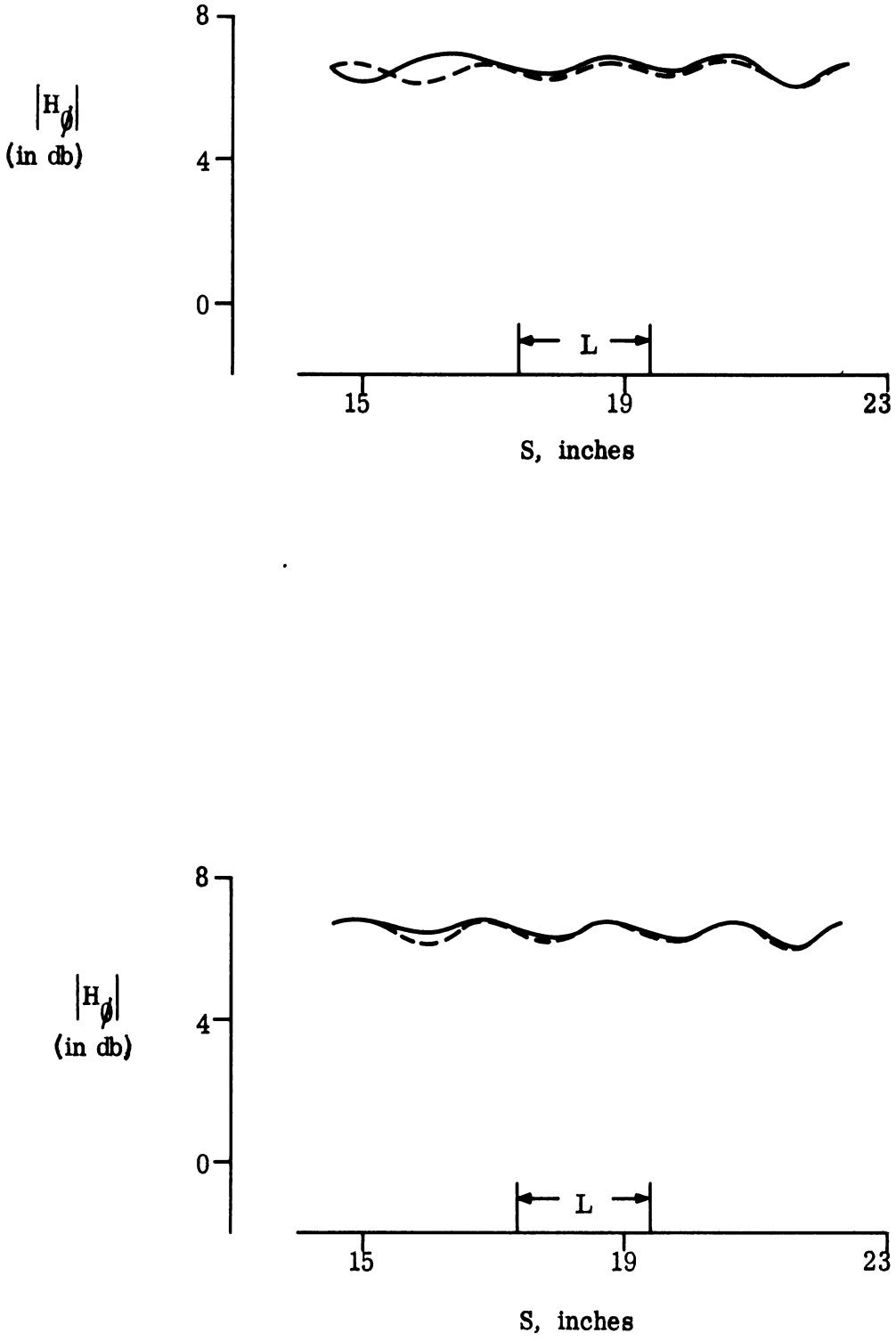

FIG. 3-5: SURFACE FIELD AMPLITUDES $|H_\phi|$ WITH (——) AND WITHOUT (- - -) A 2" DIAMETER PARALLEL LOOP. UPPER CURVE, $\theta = 60^\circ$, LOWER CURVE, $\theta = 90^\circ$. ka=5.0

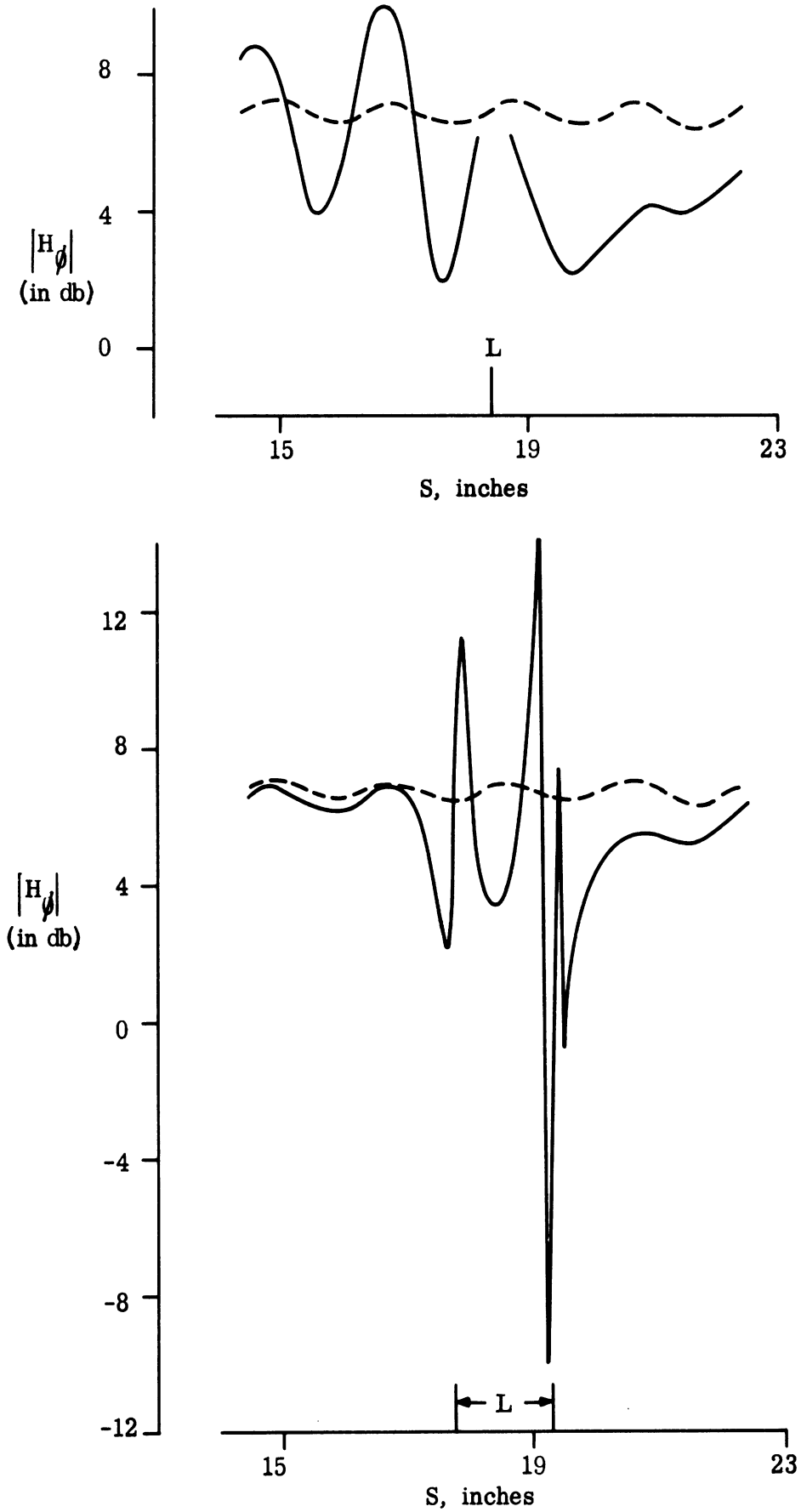

FIG. 3-6: SURFACE FIELD AMPLITUDES $|H_\phi|$ WITH (——) AND WITHOUT (- - -) A 1-1/2" DIAMETER LOOP AT $\theta = 0^o$: UPPER CURVE, PERPENDICULAR ORIENTATION; LOWER CURVE, PARALLEL ORIENTATION. ka=5.0

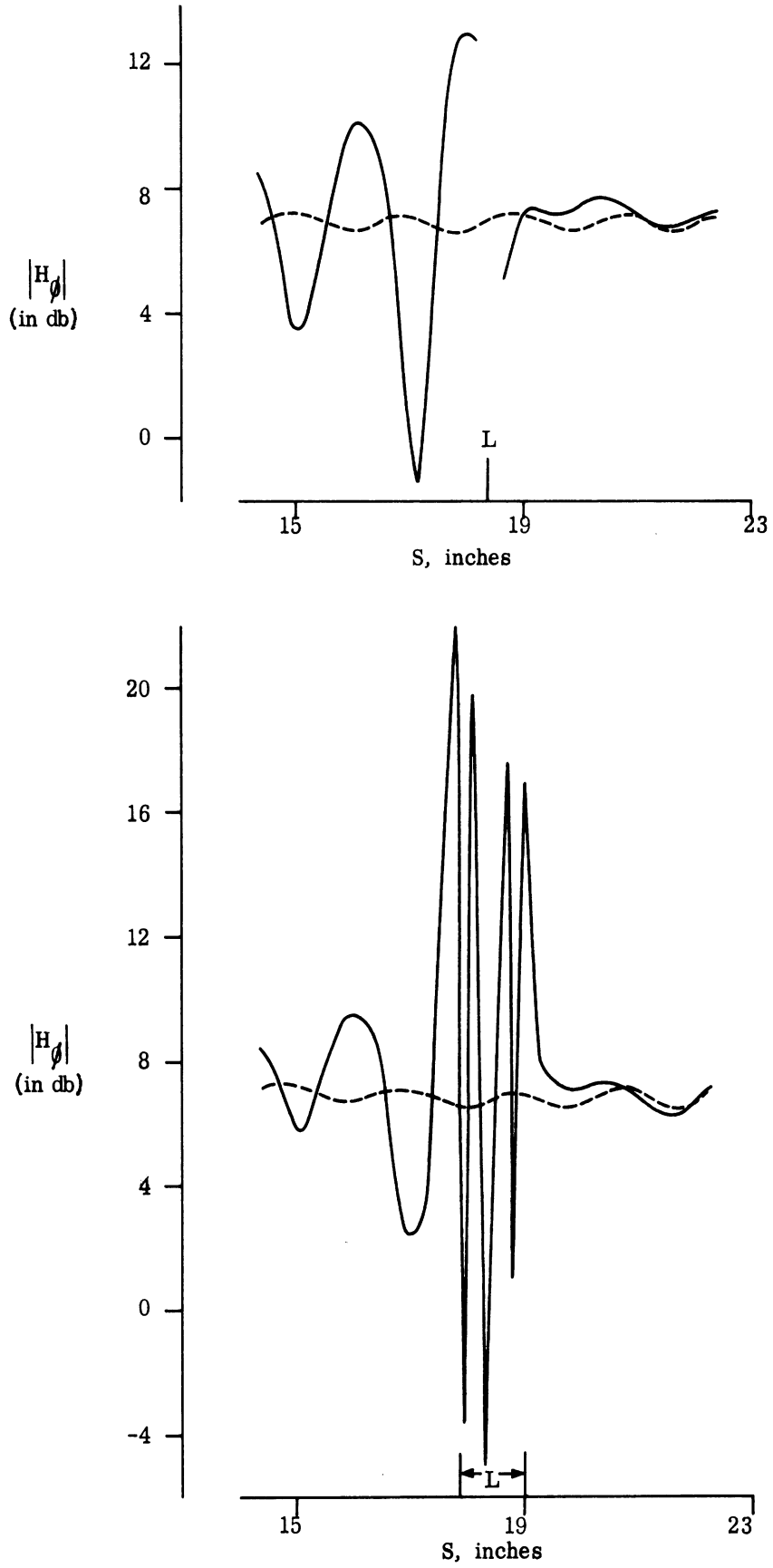

FIG. 3-7: SURFACE FIELD AMPLITUDES $|H_\phi|$ WITH (——) AND WITHOUT (– – –) A 1" DIAMETER LOOP AT θ=0: UPPER CURVE, PERPENDICULAR ORIENTATION; LOWER CURVE, PARALLEL ORIENTATION. ka=5.0

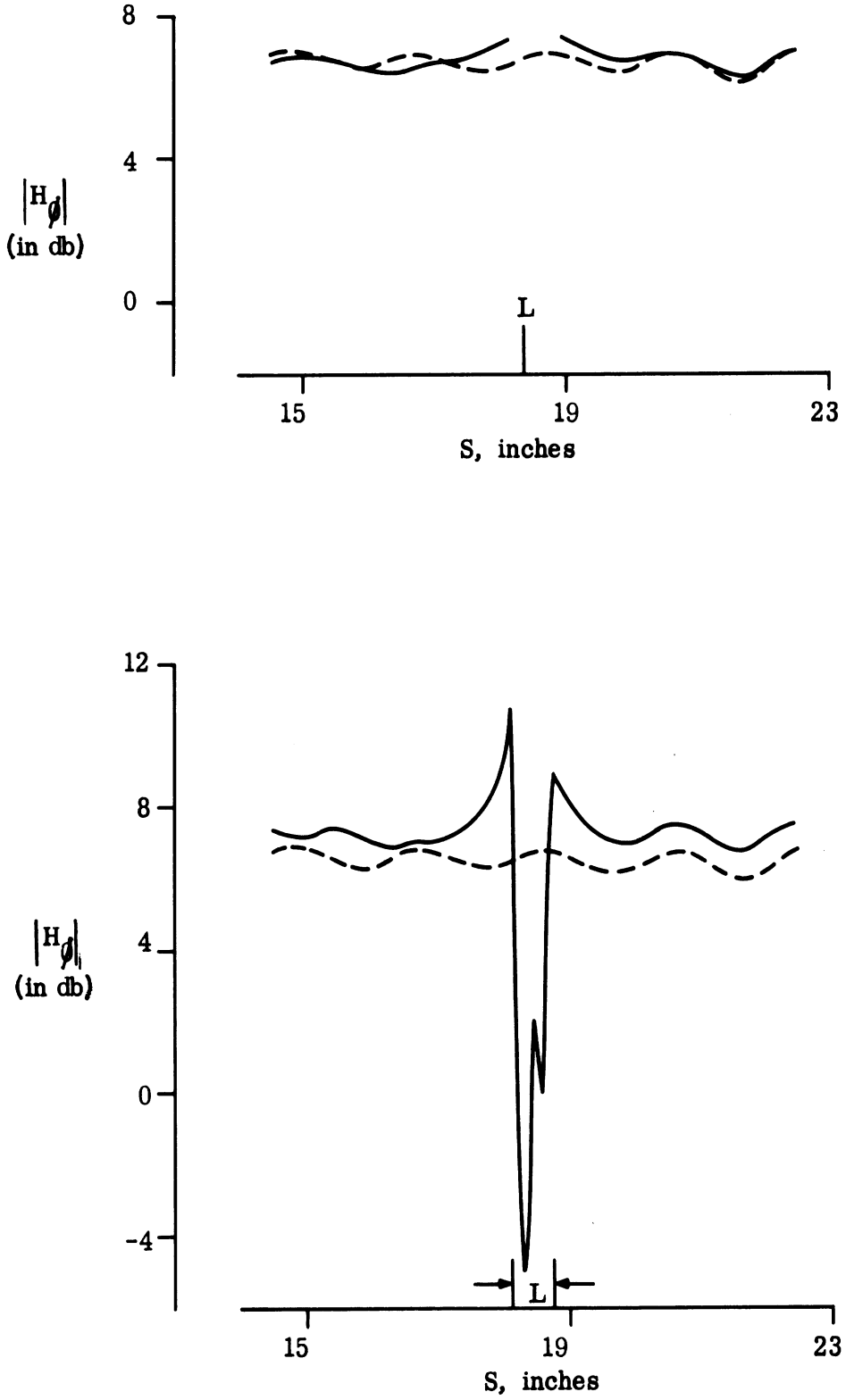

FIG. 3-8: SURFACE FIELD AMPLITUDES $|H_\phi|$ WITH (——) AND WITHOUT (- - -) A 1/2" DIAMETER LOOP AT θ=0: UPPER CURVE, PERPENDICULAR ORIENTATION; LOWER CURVE, PARALLEL ORIENTATION. ka=5.0

(S) In Figs. 3-4 and 3-5 the case of parallel orientation is considered and, in general, the effects are similar in character, but somewhat larger in magnitude. In front of the loop the oscillation amplitude increases to about 6.5 db; behind the loop the level drops about 4 db below the plain cone-sphere levels; and across the loop itself, the surface field is strongly perturbed, with an oscillation of amplitude 15 db appearing at both the leading and trailing edges of the loop. When $\theta = 30^{\circ}$ the perturbations across and in front of the loop decrease sharply, although a 2 db shadowing is still noted behind the loop. When $\theta = 60^{\circ}$ some small effects exist but are confined to positions forward of the loop, and for $\theta = 90^{\circ}$ even they have vanished.

(S) Figure 3-6 shows the measured surface fields for the 1 1/2" diameter loop placed at $\theta = 0^{\circ}$. The loop now subtends an angle of 34.5° at the axis of the cone, and is one for which kr=1.25.

(S) For the perpendicular orientation, the oscillations forward of the loop begin with an amplitude of about 4 db just in front and seem to decay slightly in the forward direction. Behine the loop the shadowing averages (about) 3 db. Although the data for $\theta \neq 0^{\circ}$ is not shown here, as θ increases, the shadowing decreases rapidly and has disappeared when $\theta = 45^{\circ}$, but the forward perturbations are still somewhat in evidence out to $\theta = 60^{\circ}$.

(S) For the parallel orientation the perturbations are much more local in character. Behind the loop shadowing is still present but it now amounts to about 1 db, while in front of the loop the oscillations are not significantly different from those on a plain cone-sphere. It is only in the immediate vicinity of the loop that severe modifications take place. Strong lobes serve to mark the position of the leading and trailing edges of the loop, but their moduli, which are (about) 5 db and 13 db respectively, differ appreciably from each other. As the angular position of the loop increases, the effects decrease: the shadowing is almost imperceptible for $\theta = 30^{\circ}$ and, for $\theta \geqslant 45^{\circ}$ the loop has ceased to have any measurable effect on the surface field.

(S) Figure 3-7 contains the surface field data for the 1" diameter loop (kr=0.833) placed at $\theta = 0^{o}$. The central angle which it subtends on the cone has now decreased to (approximately) 23^{o} and it is worth noting that for this loop kr is within 0.17 of an integral value.

(S) When the plane of the loop is perpendicular to a generator, modifications in the surface field are largely confined to positions forward of the loop, where the oscillation amplitude is 7 db immediately in front, but markedly decays towards the tip. Beyond about 0.5λ behind the loop the shadowing is barely detectable. The data for $\theta \neq 0^{o}$ is not shown but it reveals that for $\theta \geqslant 45^{o}$ the loop no longer causes any surface field perturbations.

(S) When the plane of the loop is parallel to a generator, the modifications of the surface field are again largely absent at positions behind the loop. Even for $\theta = 0^{o}$ very little shadowing is discernible. At the leading edge of the loop the oscillation amplitude is 4 db but this diminishes by 2 db within one wavelength in the forward direction. At positions across the loop, lobes whose amplitudes are each approximately 9 db do mark the leading and trailing edges of the loop but they are now separated by two additional lobes which have oscillation amplitudes greater by several db. When $\theta \neq 0^{o}$ (not shown) the behavior is similar to earlier patterns and even for $\theta = 15^{o}$ the complex lobe structure across the loop has been replaced by the simpler type of oscillations present in the forward direction. For $\theta \geqslant 45^{o}$ all enhancements of the oscillations in excess of plain cone-sphere values have disappeared.

(S) Figure 3-8 contains the surface field data for the 1/2" diameter loop when it is placed at $\theta = 0^{o}$. The central angle on the cone subtended by the loop is now only (approximately) 12^{o}. Since kr=0.417, it is doubtless because of the small electrical size of this loop that its effects on the surface field are smallest of all.

(S) For the perpendicular orientation of the loop the shadowing is insignificant, even for the loop at $\theta = 0^{o}$. In the immediate vicinity of the loop, and slightly forward of it, some increase in level (less than 1 db) is noted, but a half wavelength

forward there is no change from plain cone-sphere levels. For $\theta > 0^{o}$ (not shown) no effects are visible for $\theta \geqslant 15^{o}$.

(S) For the parallel orientation the surface field is more strongly affected. Behind the loop a 1 db shadowing takes place. At both the leading and trailing edges of the loop a noticeable (approximately 4.0 and 2.5 db respectively) rise can be seen, and forward of the loop this carries over as a 1 db increase in the mean surface field level but no substantial increase in oscillation amplitudes. For $\theta \neq \emptyset^{o}$ (not shown) the perturbations vanish rapidly and no effects are found for $\theta \geqslant 30^{o}$.

(S) From the preceding remarks certain conclusions may be drawn. The electrical size of the loop is an important parameter and there is some evidence to suggest that whether kr is an integral or half-integral has a marked effect on the perturbations. For a loop of fixed size the modifications of the surface field are, in general, greater when the loop is placed parallel to a cone generator than for the perpendicular orientation. These perturbations take three forms: forward of the loop the oscillation amplitudes are significantly increased by up to 7 db; behind the loop the surface field is shadowed (by several db) below its level on a pure cone-sphere; finally, for the parallel orientation, the leading and trailing edges of the wire are marked by sharp rises in surface field levels and a relatively complex lobe structure. These effects are most pronounced along the $\theta=0^{o}$ generator but are also observed for an angular span which increases with loop size. (One modification of this remark concerns the parallel orientation when, for $\theta \neq 0^{o}$, the complex lobe structure disappears and is replaced by the oscillation characteristic of the behavior forward of the loop.) This angular range depends on the loop orientation and is larger for the perpendicular case (as might be expected from a simple geometrical consideration); however, in no instance was an effect observable for $\theta > 90^{o}$.

(S) The last figure (Fig. 3-9) contains data for the third type of loop configuration in which three 2" diameter loops are spaced 120^{o} apart along the cone sides with their planes normal to their respective cone generators. The data is in agreement with that expected from the single loop measurements based on the assumption

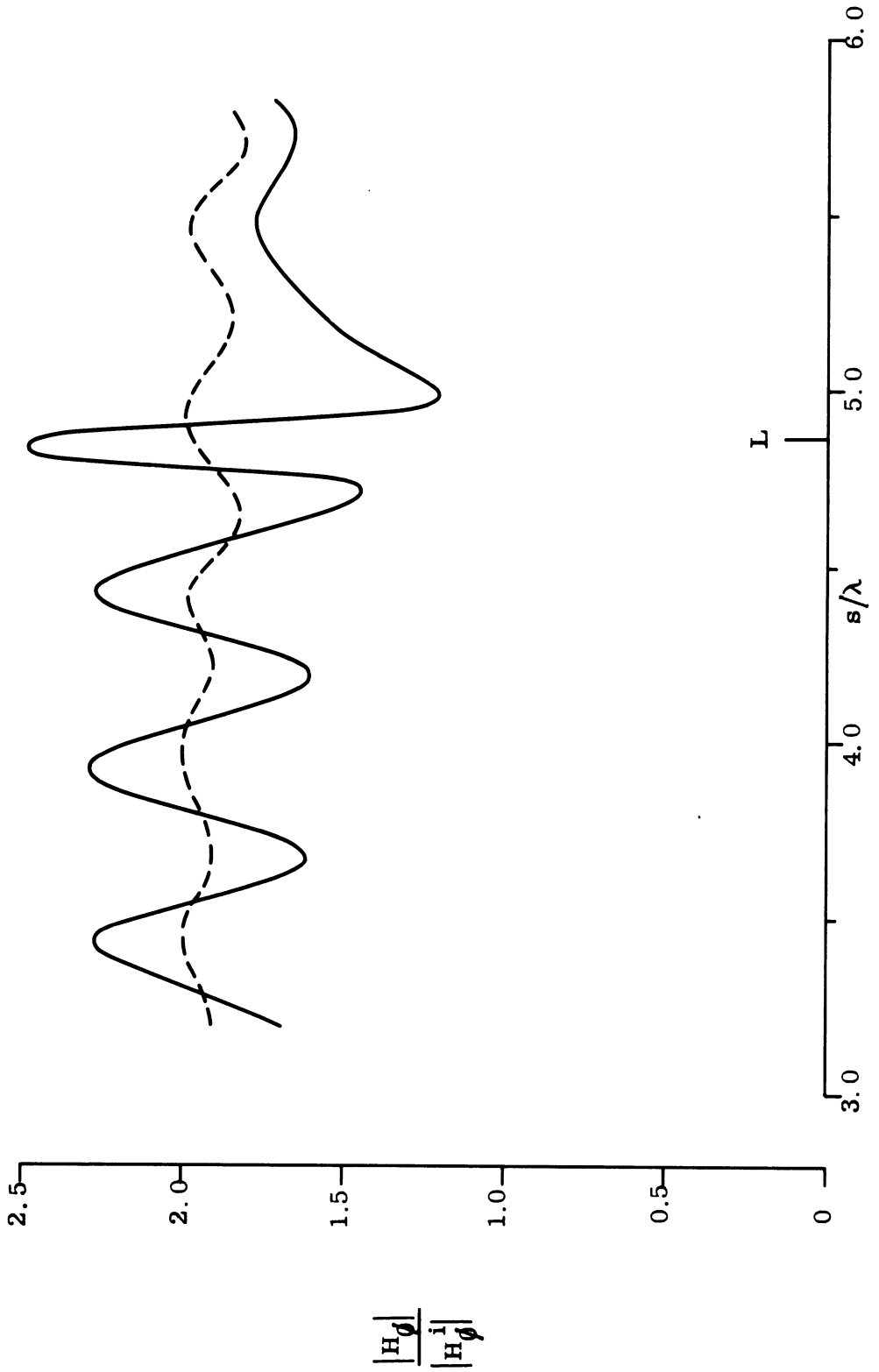

FIG. 3-9: SURFACE FIELD AMPLITUDES $|H_\phi|$ WITH (——) AND WITHOUT (- - -) THREE 2" DIAMETER PERPENDICULAR LOOPS SPACED 120° APART. ka=5.0

that, for a given loop size, the surface field should be similar to that for some $\theta \neq 0^{o}$ except for the possibility of more pronounced characteristics due to the presence of the two extra loops. The conclusion is clearly supported by the data: the oscillations forward of the loop are enhanced in amplitude and the behavior behind the loop shows the shadowing effect noted earlier.

(S) Although not shown here, the data for the other loop sizes, subject to modifications due to their electrical size, is similar. For the 1" diameter loop some resonance effects are evident, while for the 1/2" diameter loop almost no perturbations of the surface field are seen.

3.2.2 Monopoles

(S) For the reasons previously described, experiments were carried out to determine the perturbations of the surface fields produced by single monopoles of varying resistance mounted on the cone perpendicular to a generator at a distance of 18 1/2" from the tip. The cone-sphere was identical to that used for the loop experiments, and the frequency was again 3.13 Gc., for which ka=5.0. The measurements were confined to the azimuthal component H_{ϕ} and this was probed along a portion of the cone generator formed by the intersection of the surface with the horizontal plane through the cone axis. However, to find the extent to which fields along generators bordering that through the monopole are also affected, the measurements were repeated with the body and its monopole rotated through varying angles θ about its axis.

(S) The monopoles used were either $\lambda/4$ or $3/8\lambda$ in length and consisted of 1/4 watt carbon resistors whose leads were cut to the proper lengths, thereby enabling us to vary the electrical loads provided by these elements without changing their lengths. One end of the resistor body was coated with silver paint to improve contact with the cone surface, and the resistor was held in place with transparent tape of the office supply type. Although the rf resistances of these loaded monopoles are not the same as their nominal dc values, the data nonetheless displays a definite trend as the nominal resistance, R, is varied.

(S) For the $\lambda/4$ monopole with R=0 (short-circuited), the field was probed along the generators having $\theta = 0 (15^{o}) 180^{o}$, and a selection of the results is given in Figs. 3-10 and 3-11. Taking first the field behavior along the 'main' generator, $\theta = 0$, we observe that the main effect occurs forward of the monopole, i.e. toward the tip. Here there is a marked perturbation of the field with an oscillation indicative of reflection. The amplitude of the oscillation decreases with distance from the monopole, but is of sufficient magnitude to swamp the mild oscillations appropriate to a pure cone-sphere. At the monopole itself there is a 'swing' of almost 10 db (the discontinuity of the curve at this point is due only to the difficulty of probing here), and behind it there is some shadowing which produces a reduction in the field strength of at most 4 db. The reduction, however, decreases rapidly with increasing s: at a distance of $\lambda/4$ behind, it is down to a mere 1 db, and there is indication that, with a small increase in s, the shadowing will have disappeared entirely.

(S) All of these effects decrease with increasing θ. For $\theta = 30^{o}$ (see also Fig. 3-10), the maximum amplitude of oscillation ahead of the monopole is less than 2 db, and the swing at the monopole itself is now only 4 db. The shadowing beyond is also much less: the maximum reduction of field strength in only 1 db, and is zero at a distance of a wavelength away. For $\theta = 60^{o}$ (Fig. 3-11) the perturbations are hardly more than the experimental error, but even so there is some increase in the amplitude of the natural field strength oscillation ahead of the monopole, and because of the positioning of the monopole, the maxima and minima are shifted relative to where they were on a pure cone-sphere. When θ is increased to 75^{o} or greater, all evidence indicates that the field has recovered to the value that it had in the absence of the monopole by the time the shadow boundary is reached.

(S) With the monopole of length $\lambda/4$, increasing the loading via its nominal resistance decreases its effect on the surface field, and this is illustrated in Figs. 3-12 and 3-13 in which data for the generator $\theta = 0$ is presented for five values of R. The initial change in R from 0 to 100Ω has little effect on the behavior along the main generator, $\theta = 0$, and the curves in Fig. 3-12 are, indeed, almost indistinguishable.

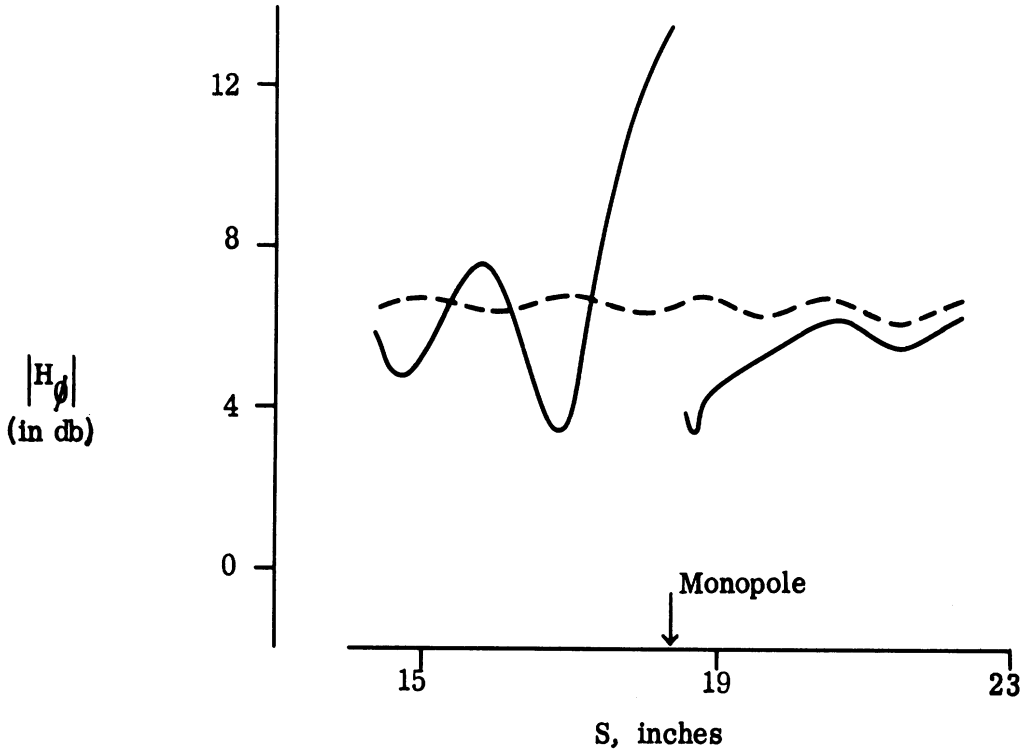

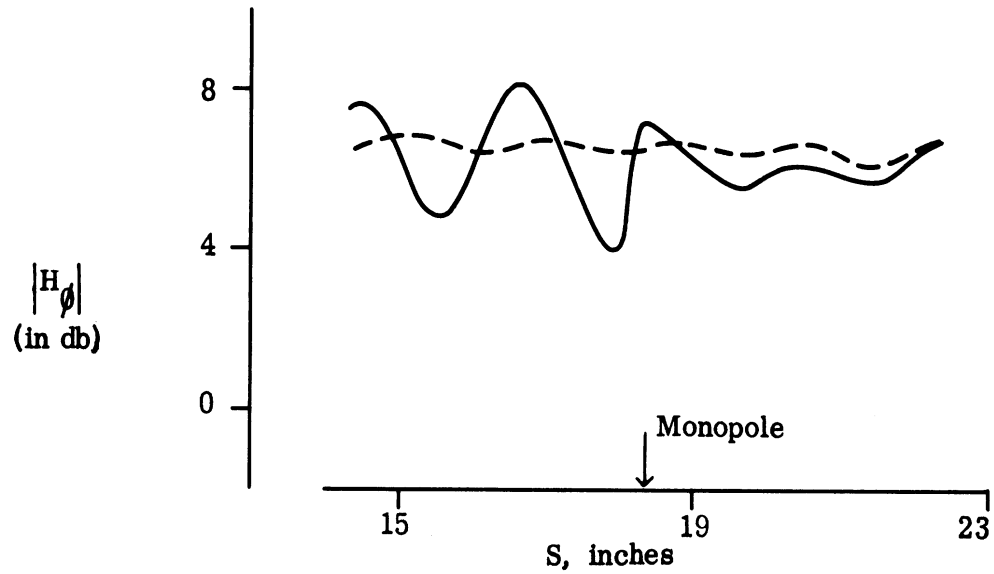

FIG. 3-10: SURFACE FIELD AMPLITUDES $|H_\phi|$ WITH (——) AND WITHOUT (- - -) 0 Ω, λ/4 MONOPOLE: UPPER CURVE $\theta=0^o$; LOWER CURVE $\theta = 30^o$. ka = 5.0

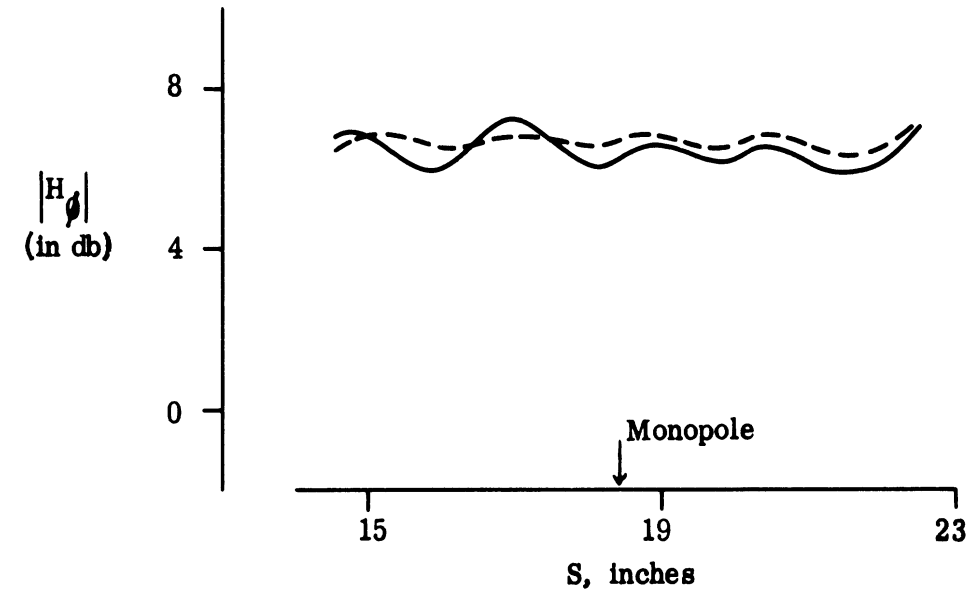

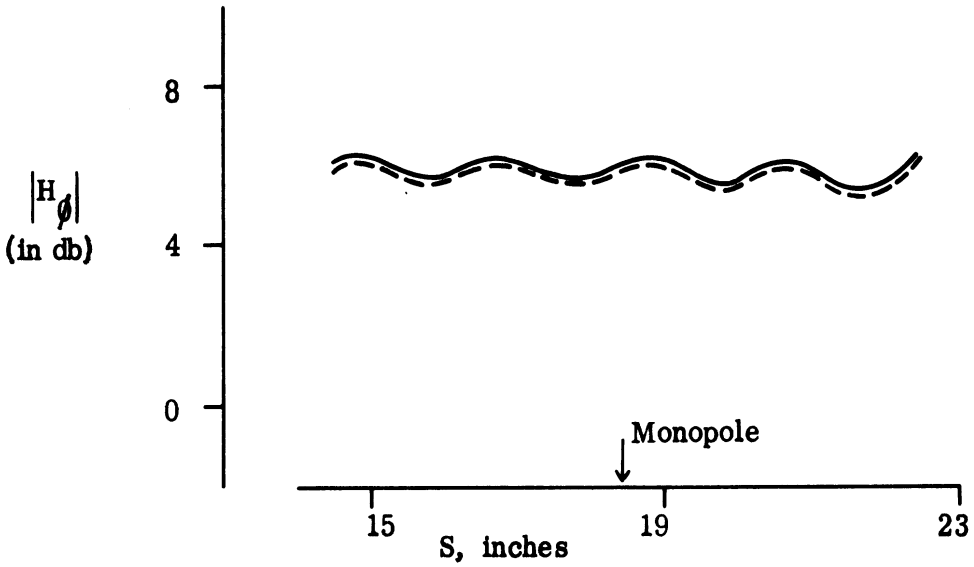

FIG. 3-11: SURFACE FIELD AMPLITUDES $|H_\phi|$ WITH (——) AND WITHOUT (- - -) 0 Ω, λ/4 MONOPOLE: UPPER CURVE, $\theta=60^o$; LOWER CURVE $\theta=90^o$. $ka = 5.0$

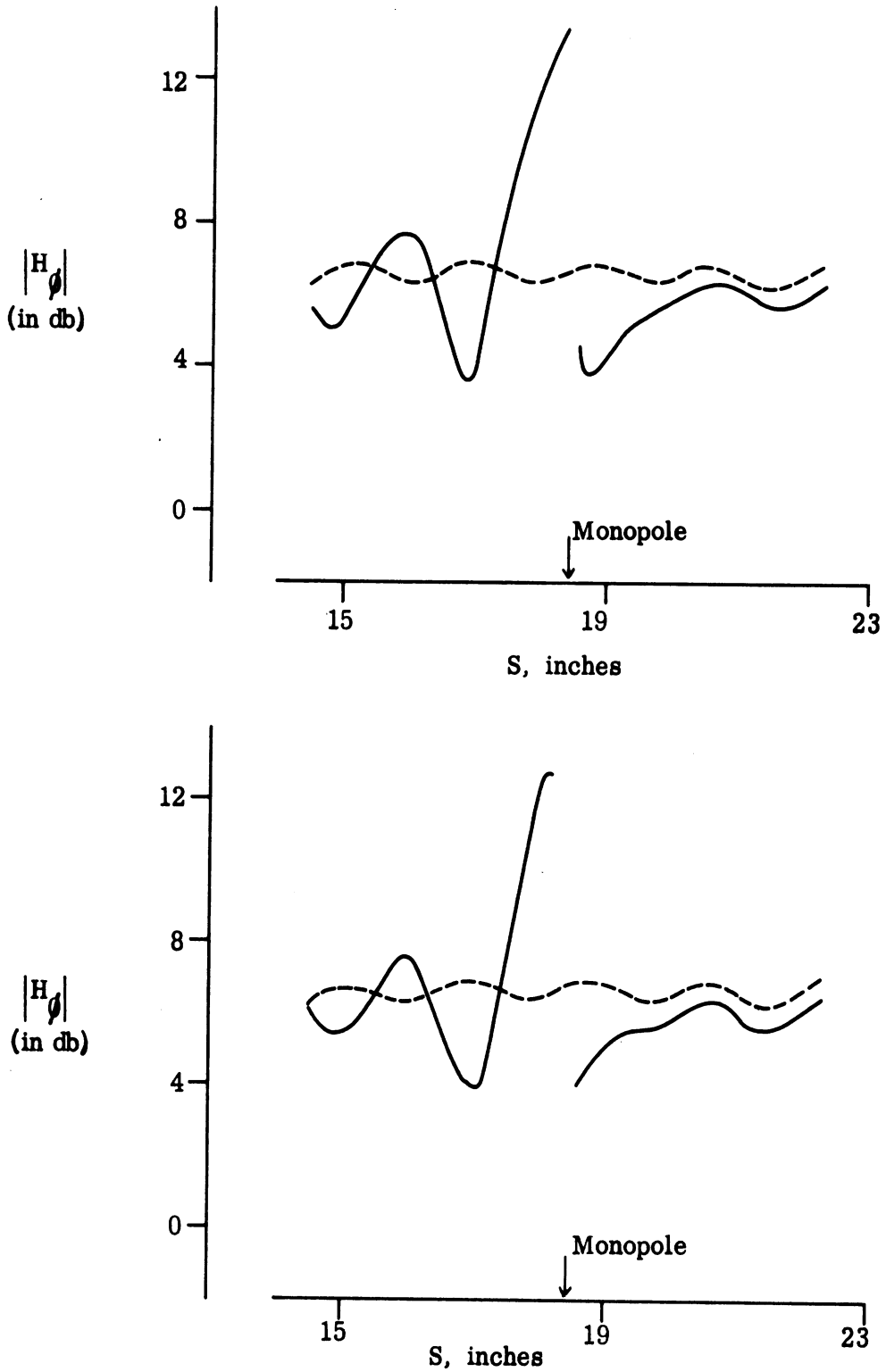

FIG. 3-12: SURFACE FIELD AMPLITUDES $|H_\phi|$ WITH (⟶) AND WITHOUT (- - -) $\lambda/4$ MONOPOLE, $\theta=0^o$: UPPER CURVE, R = 0 Ω; LOWER CURVE R= 100 Ω. ka = 5.0

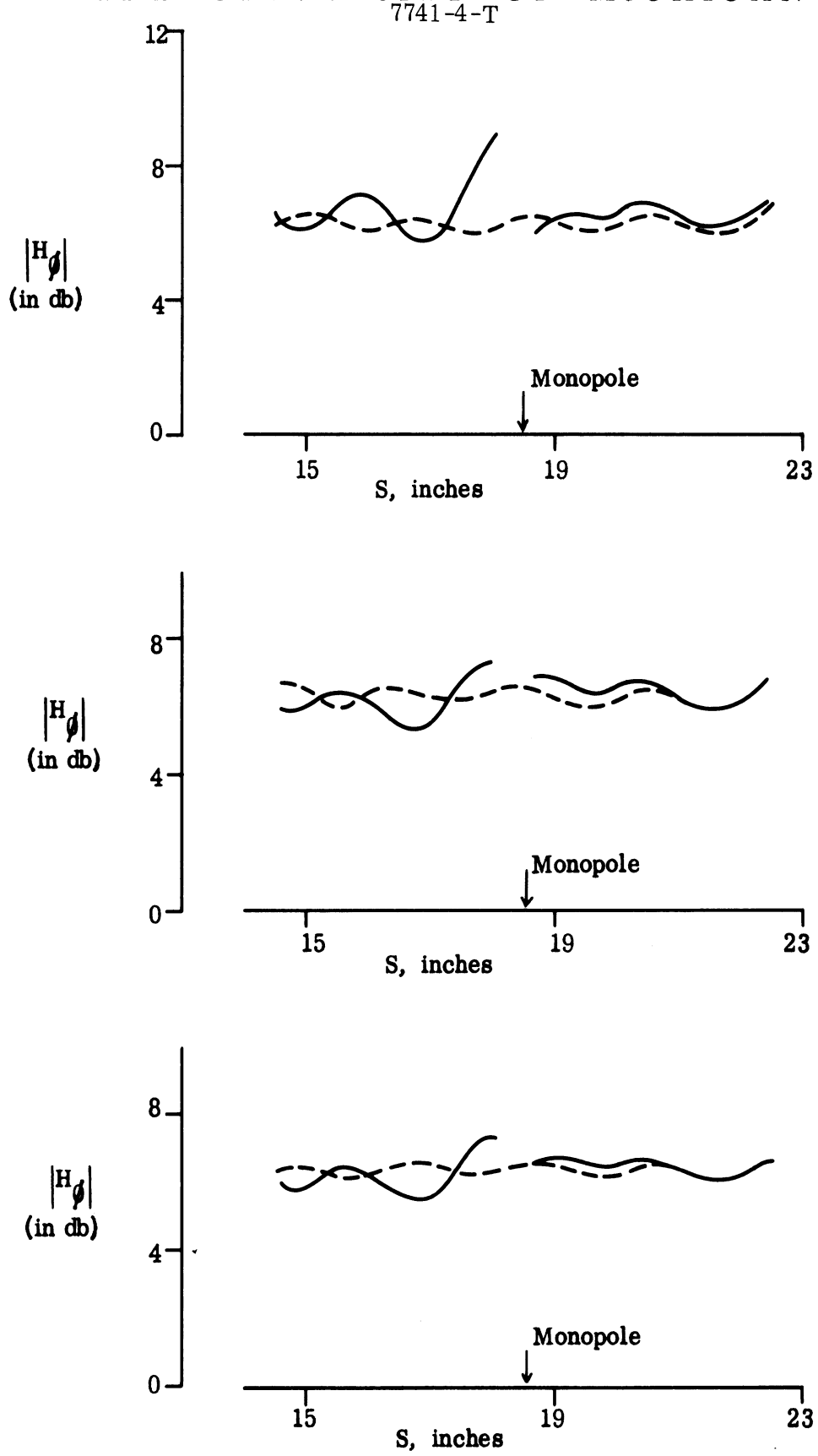

FIG. 3-13: SURFACE FIELD AMPLITUDES $|H_\phi|$ WITH (——) AND WITHOUT (– – –) $\lambda/4$ MONOPOLE, $\theta=0^o$: UPPER CURVE, R=1KΩ; MIDDLE CURVE, R=100KΩ; LOWER CURVE, R= $\infty\,\Omega$. ka=5.0

Nevertheless, there is some localizing of the perturbation, and the field strength curve for $\theta = 45^{\circ}$ and $R = 100\Omega$ is more akin to that for $\theta = 60^{\circ}$ and $R = 0$, than for $\theta = 45^{\circ}$ and $R = 0$. If the loading of the monopole is increased still more, a rapid reduction in the perturbation takes place, and this is seen as a decrease in shadowing and in the magnitude of the reflection along the main generator, and also as a confinement of the effects to this one generator. The curves in Fig. 3-13 show the perturbations for $\theta = 0$ and $R = 1K\Omega$, $100K\Omega$ and $\infty\Omega$ (open circuited). With $R = 1K\Omega$, there is no longer any shadowing behind the monopole, and though there is still a swing of about 4 db at the monopole itself, the amplitude of oscillation ahead of it is only about 1 db. Increasing R decreases somewhat both the swing and the amplitude of oscillation, and as $R \longrightarrow \infty$ it would appear that the magnitude of the wave reflected by the monopole along the main generator is asymptotic to (about) 10 per cent of the amplitude of the surface field on the pure cone-sphere. The confinement in azimuth is such that all effects have disappeared for $\theta \geqslant 30^{\circ}$.

(S) With the monopoles of length $\lambda/4$ it would be a straightforward matter to estimate the modification to the back scattering cross section of the cone-sphere as a function of the loading R. Since the field strength at the join (distance 22.79" from the tip) and beyond differs at most by a small fraction of a db from its values in the absence of the monopole, the modification to the scattering is essentially only the additive contribution provided by the monopole, and we can estimate this quite trivially by comparing the observed field perturbations with those which a radiating dipole would produce when mounted on an infinite ground plane. The technique is similar to that used in Section 3.3.2

(S) All of these results are, however, functions of the length of the monopole, and increasing the length changes the picture drastically. This is illustrated in Figs. 3-14 and 3-15 in which the curves for the trajectory $\theta = 0$ are shown for a $3\lambda/8$ monopole. Observe that the effects are now greatest for $R = \infty$ (open circuit). The amplitudes of the reflected wave increase with R, as do the swings at the dipole (for $R = 100K\Omega$, the measured swing is in excess of 20 db, but experimental errors due to

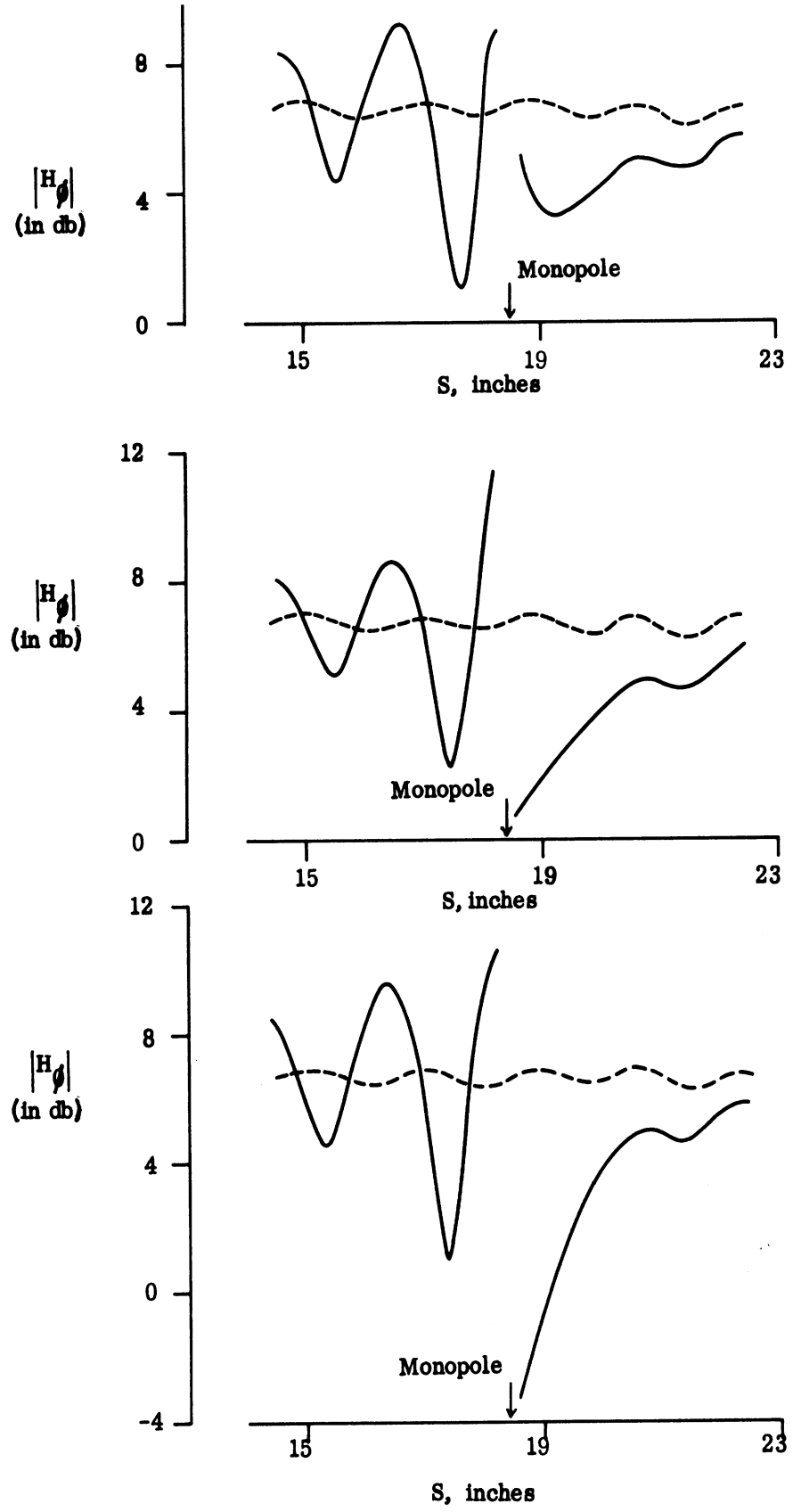

FIG. 3-14: SURFACE FIELD AMPLITUDES $|H_\phi|$ WITH (——) AND WITHOUT (- - -) 3λ/8 MONOPOLE, θ = 0: UPPER CURVE, R=0 Ω; MIDDLE CURVE, R=100 Ω; LOWER CURVE, R = 1K Ω ka=5.0

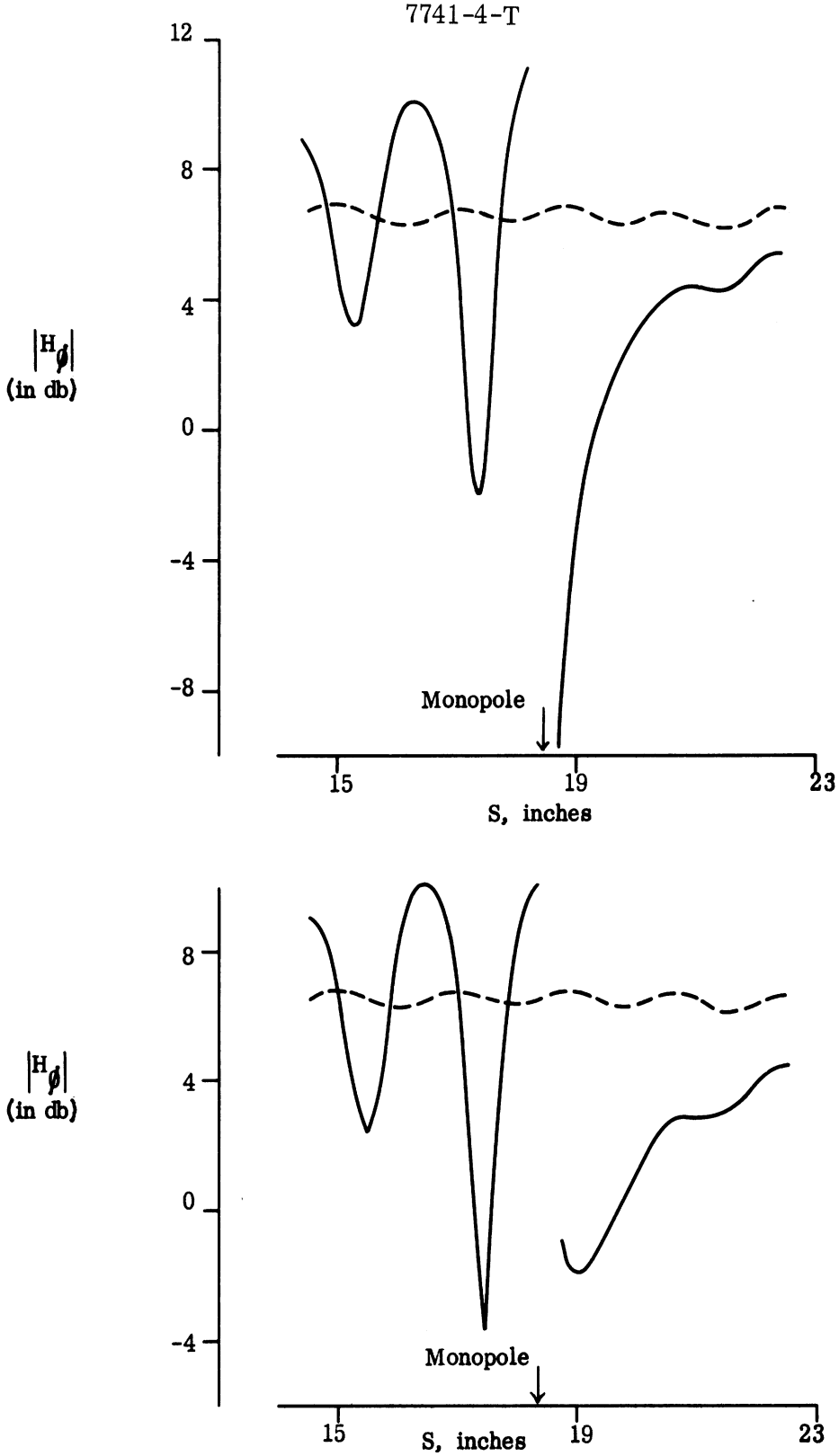

FIG. 3-15: SURFACE AMPLITUDES $|H_\phi|$ WITH (——) AND WITHOUT (- - -) $3\lambda/8$ MONOPOLE, $\theta=0$. UPPER CURVE, R=100K Ω; LOWER CURVE, R= ∞ Ω . ka=5.0

the small signal strength could be a factor here) and the extent of the shadowing. Regardless of the resistance of the monopole, some reduction (at least 1 db) in the field strength is evident at the join. This increases to as much as 2 db for the open-circuited case, and will produce a corresponding reduction in the contribution to the scattering of the pure cone-sphere.

3.2.3 Studs

(S) From a consideration of their sizes on full scale vehicles, the exposed portions of typical rocket nozzles were modelled by six cylindrical metallic studs placed on the rear cap and spaced equally apart around a circle perpendicular to the cone axis, the diameter of the circle being equal to two-thirds of the cap diameter.

(S) Two types of studs were used. For each the essential shape is that of a cylinder whose base diameter is 1/8" and whose height is 1/16". In Type A the lower base is slightly curved to ensure a smooth fit with the spherical surface and the cylinder axis is then parallel to a normal through the common spherical surface element. In Type B the lower base has a curved cylindrical addition so that the exposed base is aligned parallel to the cone-sphere axis. The accompanying diagrams (not to scale) illustrate the geometry of the nozzle simulation (Fig. 3-16).

(S) Surface field measurements were made for nose-on incidence with ka=5.0 and 3.0, in the presence of each type of stud as well as in their absence. At ka=5.0 the cone-sphere model used had a spherical cap radius of 3" while for ka=3.0, the model was smaller with a radius equal to 1.5". Since the physical size of the studs remained the same, their electrical size was relatively larger at ka=3.0 and hence their effects on the surface fields should be larger for this case.

(S) Examination of the experimental data revealed no perceptible differences between the surface fields measured for studs of Type A or B and this was true for both cone-sphere sizes. Moreover, the presence of either form of stud had no measurable effect on the surface field supported by a pure cone-sphere except in such cases when the probe was actually placed on one of the studs. Differences of about 1 db were then observed, but even this was felt due mainly to the fact that the probe

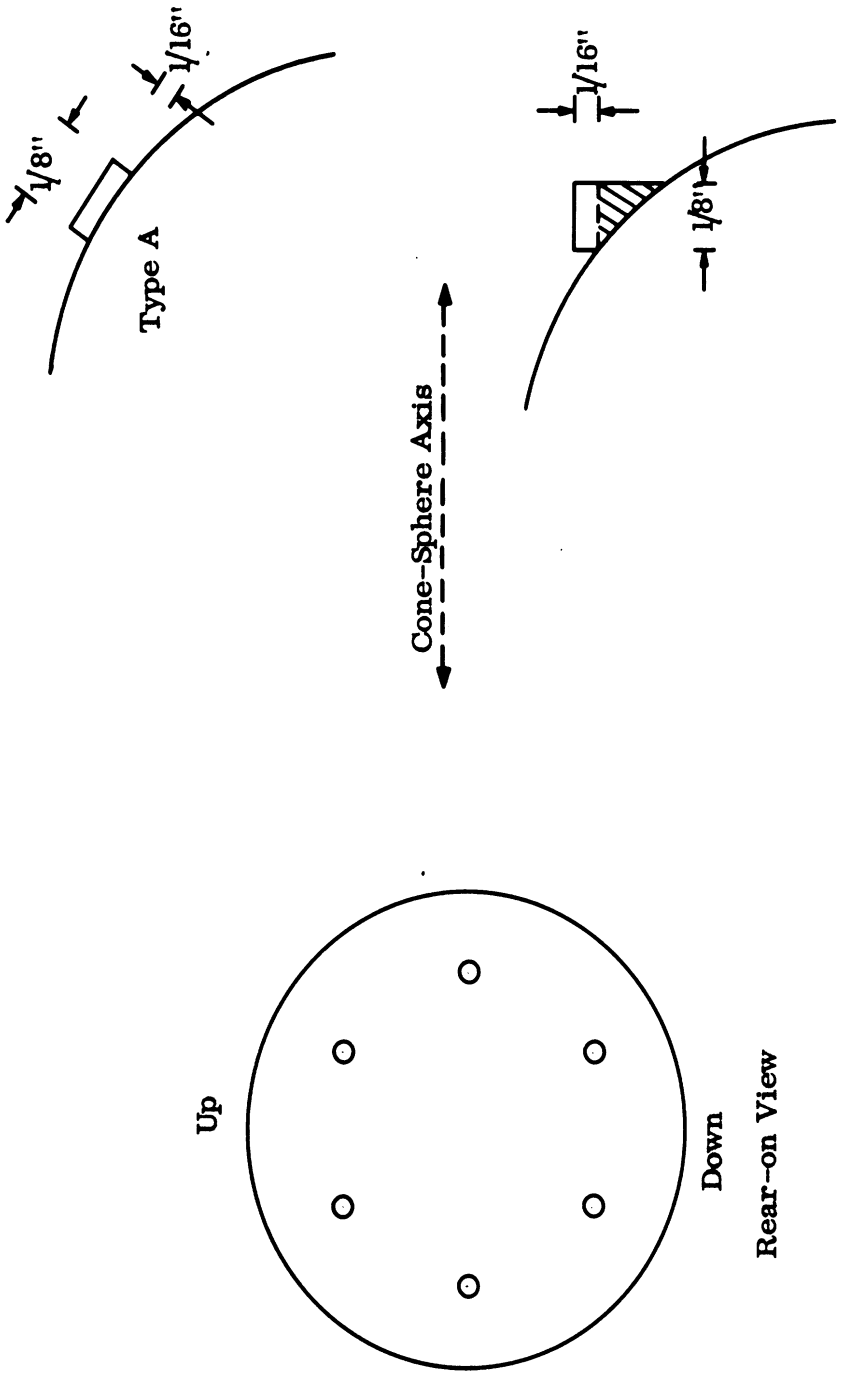

FIG. 3-16: GEOMETRY OF NOZZLE SIMULATION.

axis was not now normal to the surface where the measurement was being made. On the base surface itself there was no disturbance whatsoever created by the studs, a result which was expected in view of their small electrical size. Typical of the data obtained is that in Fig. 3-17 for ka=3.0, in which the surface field curve can be regarded as appropriate to either the unperturbed cone-sphere, or to the body with studs of either type. Only a partial scan is shown here, starting about 0.8λ short of the join with the abscissa representing the distance in wavelengths from the tip.

(S) It is thus safe to conclude that these rocket nozzle simulations can have no discernible far field effect.

3.3 Slots

(S) Two types of slots have been considered in the investigations: longitudinal and annular. In models with longitudinal slots one slot is cut along a portion of a cone generator just forward of the shadow boundary; similarly, a second is cut and symmetrically placed along a cone generator on the opposite side of the model. The arrangement of the two slots is meant to simulate a telemetry antenna. In models with annular (azimuthal) slots a thin segment of the metallic model perpendicular to the cone axis is removed and replaced by a non-metallic insert of the same dimensions. When placed near the tip, this type of annular slot simulates a nose-tip antenna, while if placed near the join, it simulates a ring antenna.

3.3.1 Longitudinal Slots

(S) To provide some direct information about the affect of longitudinal slots such as might be used for a telemetry antenna, a cone-sphere of half angle $\alpha = 7\ 1/2^{\circ}$ and base radius 3.00" was modified in the manner shown in Fig. 2-10. Two slots were cut into the surface of the cone along generators 180° apart and starting 2" forward of the join. Each slot was of width 0.25" and length 4.25" and their depths could be varied up to a maximum 1.75". By varying the depth and, at the same time, inserting materials of different electrical properties, it was our hope that at least a small range of impedance values could be simulated. In all the experiments performed, however, the slots have had a minimal effect on the surface field outside the

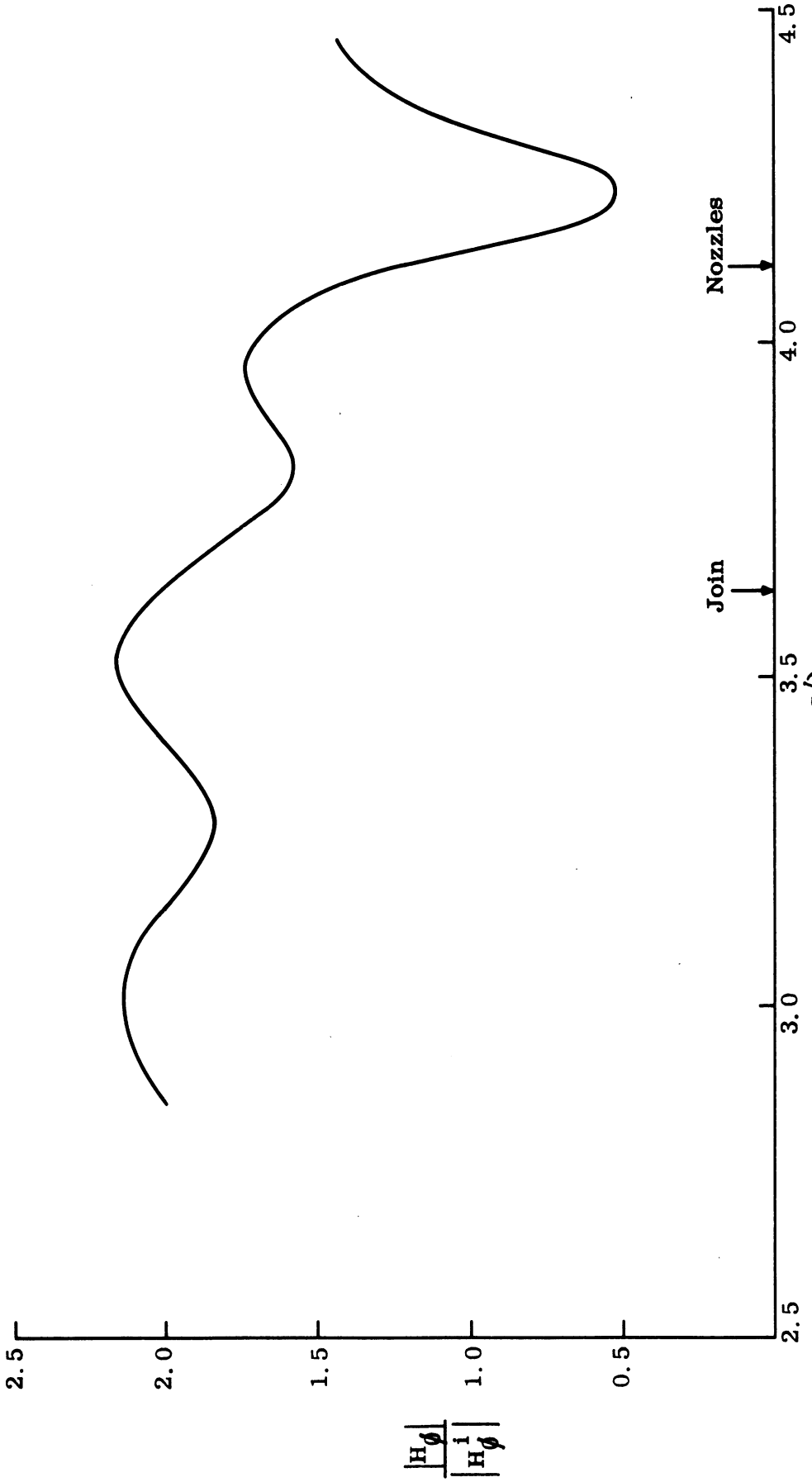

FIG. 3-17: MEASURED SURFACE FIELD COMPONENTS $|H_\phi|$ FOR ka=3.0.
PURE CONE-SPHERE (α=7-1/2°, a=1.5"); TYPE A AND TYPE B NOZZLES.

slot itself. Inasmuch as the direct scattering from the slot will be shown to be small, the far field scattering is unaffected by the presence of the slots used here.

(S) Measurements were made of the surface field component H_ϕ for nose-on incidence, and in each case a parallel experiment was carried out with aluminum (conducting) tape over the slots to show the corresponding surface field behavior for the unmodified cone-sphere, i.e. without the slots present. The frequencies used were 1.25 and 2.50 Gc, for which ka = 2.0 and 4.0 respectively, where a is the radius of the spherical base. Typical of the results obtained are those shown in Fig. 3-18, in which the slot was 1.5" deep and filled with lucite. At this frequency (1.25 Gc) the electrical depth of the slot is approximately $\lambda/8$.

(S) The horizontal scale in Fig. 3-18 is the distance, in wavelengths, along the surface forward of the join, and with the slots taped the surface field behavior is characteristic of a pure cone-sphere. With the slots open the field over the slot is lower by about 25 per cent, but shows the same oscillation there as was the case when the slot was taped. The drop into the 'well' occurs abruptly at the ends of the slot, and outside the slot the field reverts to the value that it had on the unmodified body within a distance of only a small fraction of the wavelength. The results obtained were unaffected by the removal of the lucite, leaving the slots filled with air alone.

(S) Since the introduction of the slots destroys the rotational symmetry of the body, it no longer follows that the surface field component H_ϕ must be a sinusoidal function of the azimuthal angle ϕ and measurements along a single probe trajectory (e.g. $\phi = 0$ in Fig. 3-18) are not then sufficient. The body was therefore rotated through an angle 90° about its axis, and the loop probe bent so as to permit the measurements of H_ϕ along the top (and bottom) sides of the body. By virtue of the body's rotation, such a trajectory still passes through the slots, but in the absence of the slots, no field component should be detected. In practice, a small signal was found when the slots were taped, and this is shown as the lower broken line in Fig. 3-18.

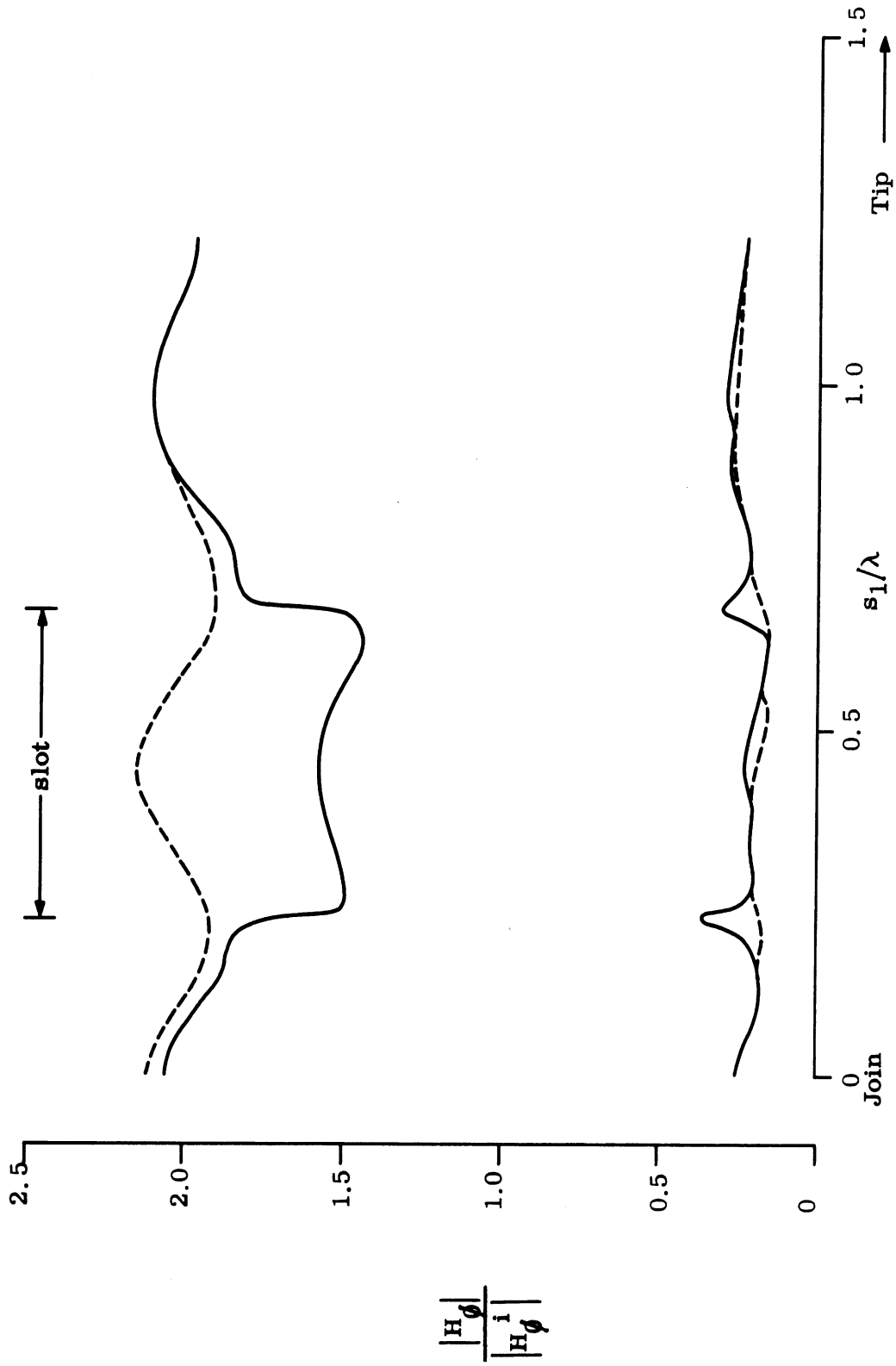

FIG. 3-18: MEASURED SURFACE FIELD COMPONENT $|H_\phi|$ FOR ka=2.0 WITH SLOTS TAPED (- - -) AND LUCITE FILLED TO DEPTH OF 1.5" (——). LOWER CURVES ARE FOR BODY ROTATED 90°.

It is, presumably, due in part to a slight residual asymmetry resulting from the taping, and to a stray pick-up of other fields (e.g. H_z) by the probe. Such a component would serve to generate a cross polarized contribution to the back scattered field, but its measured surface field amplitude is smaller than that along the (main) generators displaced 90^o by at least 20 lb. With the slots open and filled with lucite, the lower (solid) curve in Fig. 3-18 is generated, and it is interesting to note that the field variation near to the ends of the slot is characteristic of the expected edge behavior.

(S) The extent to which the influence of the slots is confined to their immediate vicinity was further demonstrated by probing the fields along trajectories adjacent to that passing through the slots when the model was oriented such that the slots were along the sides. At a frequency of 2.50 Gc with the slots 1.25" deep and air filled, the fields measured along a trajectory 1/4" above the slot (approximately 0.053λ) are shown in Fig. 3-19. The values are indistinguishable from those for the taped (unmodified) object, and differ markedly from the readings over the slot itself.

(S) In view of the fact that the fields outside the slot are sensibly unaffected by the presence of the slots, it follows that we can treat a slot as merely an additive contributor to the scattering. Using the expression for the radiated field of a single slot in a ground plane, with excitation strength given by the difference between the measured fields with the slot taped and open, and phase appropriate to the incident field over the cone, we are led to the following formula for the contribution to the back scattered field provided by the two slots on the body:

$$\frac{\sigma}{\lambda^2} = \left\{ 4\sqrt{\pi}\, A \frac{\ell}{\lambda}\frac{w}{\lambda} \sin\alpha \cdot \frac{\sin(k\ell\cos\alpha)}{k\ell\cos\alpha} \right\}^2 \qquad (3.1)$$

where ℓ and w are the length and width of each slot, and A is the effective amplitude of excitation, i.e. the amplitude of the field which must be subtracted from the

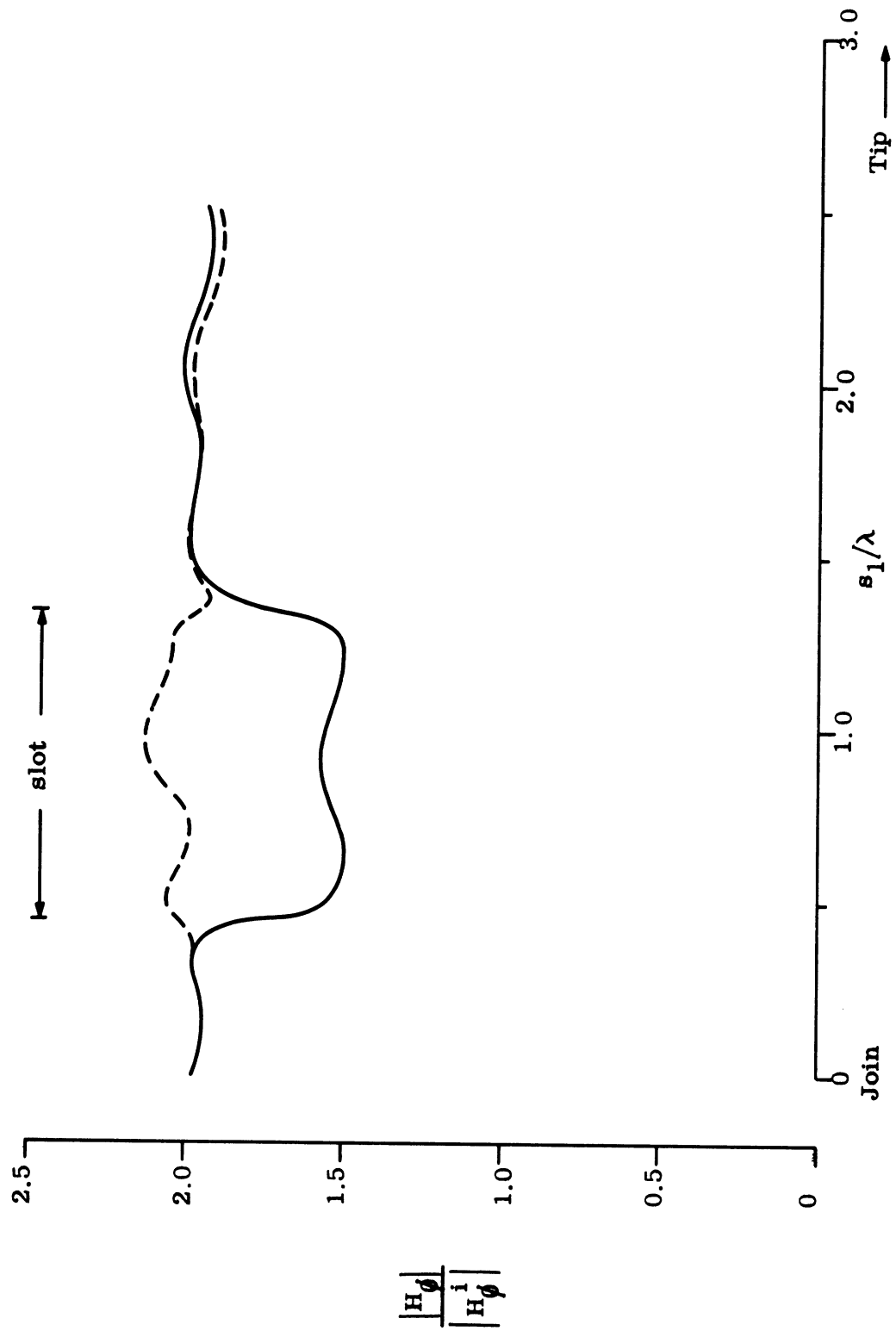

FIG. 3-19: MEASURED SURFACE FIELD COMPONENT $|H_\phi|$ FOR ka=4.0 WITH AIR-FILLED SLOTS OF DEPTH 1.25". PROBE TRAJECTORY 0.25" ABOVE SLOTS (— — —) AND THROUGH SLOTS (——).

field on the unslotted body to give the measured amplitudes in Figs. 3-18 and 3-19.

$$\frac{\sigma}{\lambda^2} = 1.73 \times 10^{-5} \quad , \qquad (3.2)$$

which is approximately 40 db below that of the unslotted body.

(S) A similar analysis is, of course, appropriate to scattering in directions other than nose-on, but in spite of the fairly extensive study of this particular slotted model, the limited variety of impedances that can be simulated is a possible reason for caution in extrapolating the results to more practical antennas.

3.3.2 Azimuthal Slots

(S) The two types of azimuthal slots which were studied are distinguished by the location of the slot in the cone-sphere. In one case the slot is placed near the tip and in the second it is found in the vicinity of the join.

(S) The first of these, Model LSP (lucite spacer point), consists of a metallic cone-sphere of base radius 2.210" and half angle $7\text{-}1/2^{\circ}$. A segment 1/4" thick and centered 3-3/8" from the tip is removed and replaced by a lucite insert of the same dimensions. The resulting tip and spacer are meant to simulate a nose-tip antenna.

(S) On a body whose surface is predominantly metallic, the azimuthal component of the surface magnetic field is the more important one for far field considerations. For nose-on incidence the modulus of H_ϕ was measured for plane wave illumination along the entire cone-sphere surface of Model LSP from the tip to the antipode. The available measurements are summarized in Table III-2, where the last column lists the circumference at the midpoint of the lucite spacer (the lengths of the two edges of the spacer are lesser and greater by 3.7 per cent). Two samples of the LSP surface field data have been included (see Figs. 3-20 and 3-21) and are compared with those for a pure cone-sphere.

(S) Except for some small differences in mean level (which may simply be caused by problems of normalization and are less than 1 db at most), beyond the spacer the surface field on Model LSP rapidly reverts to the values that it would have

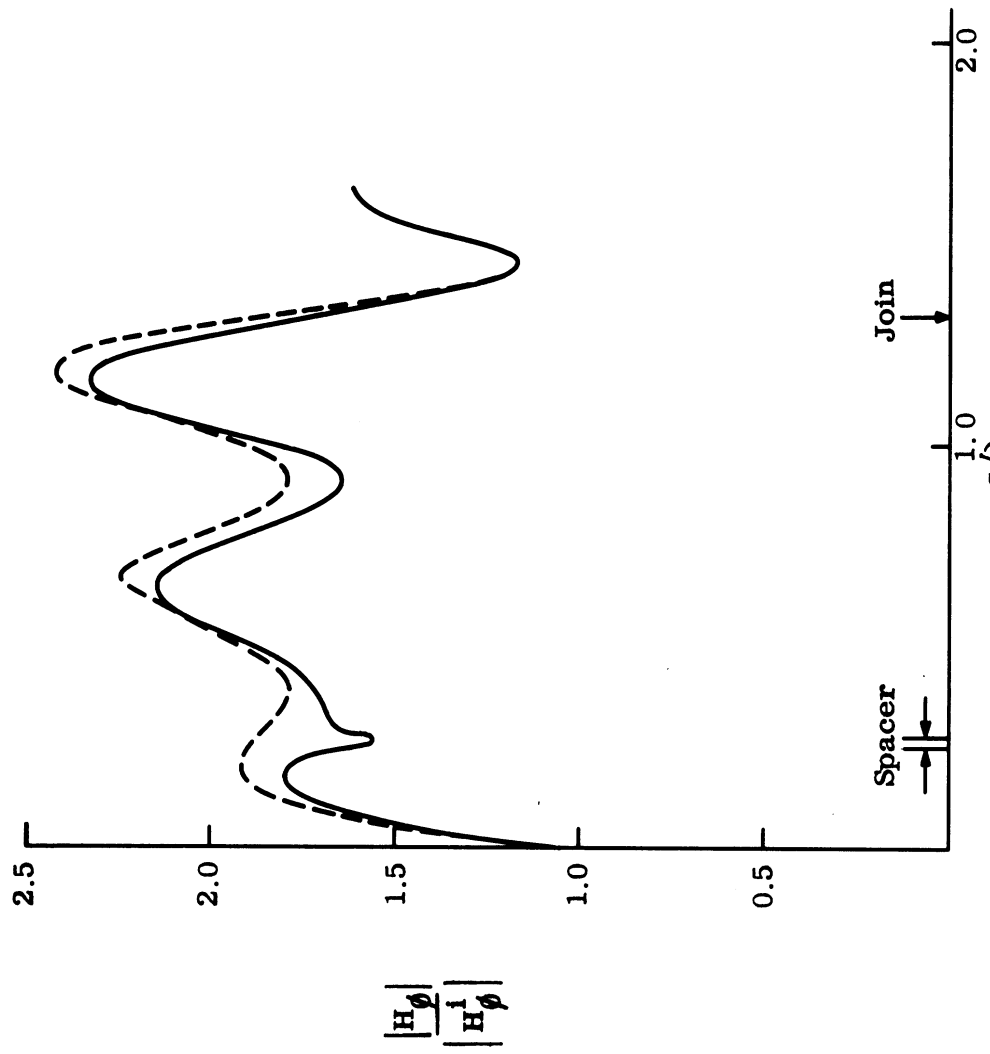

FIG. 3-20: SURFACE FIELD AMPLITUDE $|H_\phi|$ WITH (——) AND WITHOUT (---) LSP, ka = 1.1.

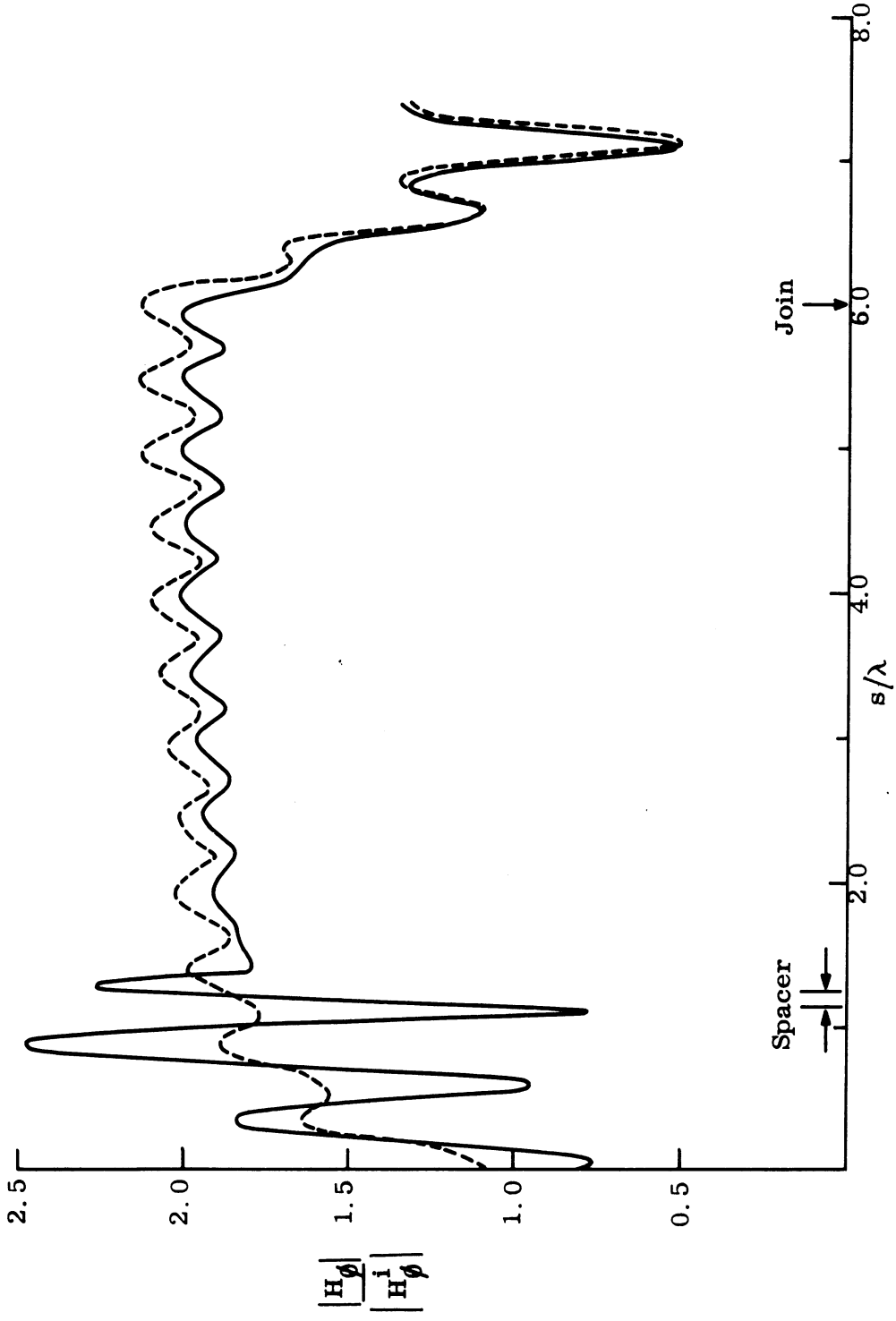

FIG. 3-21: SURFACE FIELD AMPLITUDE $|H_\phi|$ WITH (——) AND WITHOUT (- - -) LSP, ka = 5.0.

TABLE III-2: Model LSP MEASUREMENT SUMMARY

Frequency Gc	ka	Spacer Location (s/λ from tip)		ka_s
0.935	1.100	0.255	0.275	0.219
2.55	3.000	0.702	0.756	0.598
4.25	5.000	1.170	1.257	0.997
6.799	7.999	1.858	2.013	1.595

if the spacer had not been present. In particular, the surface fields in the vicinity of the join and shadow boundary are unaffected by the spacer, and, in consequence, the join and creeping wave contributions to the scattering are identical to those for a pure cone-sphere with this value of ka. The back scattering from the LSP model at nose-on incidence should thus differ from that of the pure cone-sphere only by the addition of a contribution from the vicinity of the spacer itself, and any coupling between the spacer and base regions of the body is negligible in its effect.

(S) It is possible to estimate the contribution to the back scattering cross section provided by the spacer and deduced from the relation

$$\frac{\sigma_{sp}}{\pi a_s^2} = \frac{16}{27} \Gamma^2 \qquad (3.3)$$

where the effective strength of the spacer is obtained by regarding it as a ring source, and Γ denotes the ratio of the mean amplitude of the measured oscillations of the surface field on Model LSP ahead of the spacer to the corresponding amplitude of oscillation on a half plane (Bowman and Senior, 1966, Fig. 8-12) inclined at the appropriate angle. The resulting estimates at the frequencies for which LSP surface field data was obtained are listed in Table III-3.

TABLE III-3
ESTIMATE OF SPACER BACKSCATTERING CONTRIBUTION

Frequency	ka	Γ	$\sigma_{sp}/\pi a_s^2$
0.935	1.1	0	0
2.55	3.0	1	0.59
4.25	5.0	3	5.3
6.799	8.0	1.29	0.98

(S) For Model LSP back scattering patterns were obtained for a 360^{o} span of incident angles as the model was rotated about a vertical axis. Unfortunately, however, the four frequencies of the far field measurements do not correspond to the four frequencies of the surface field measurements because the different equipment required for the two kinds of measurements made such coordination inconvenient. Back scattering patterns for a plain metal cone-sphere of the same ka and half angle were also obtained and by comparison of the nose-on back scattering cross sections of Model LSP with those of the corresponding cone-sphere, it is possible to deduce the minimum and maximum values of the additive cross section attributable to the spacer on the assumption that the other major contributions to the cone-sphere return are unaffected. The resulting bounds on σ_{sp} are shown in Table III-4 where a_s is now the radius of the tip side of the lucite spacer insert and the asterisk for the cone-sphere measurements indicates an average of two measured nose-on cross sections.

(S) Examination of Table III-3 shows that one of the frequencies is almost common to both the far and surface field measurements. For this case (ka=3.0) the estimate for $\sigma_{sp}/\pi a_s^2$ computed from the surface field measurements is certainly within the bounds deduced from the back scattering data. Thus for ka=3.0 the cross

TABLE III-4
EXPERIMENTAL SPACER BACK SCATTERING CONTRIBUTION

Freq. (Gc)	ka	ka_s	$\frac{\sigma_{LSP}}{\sigma_{CS}}$ (db)*	A	$\sigma_{sp}/\pi a_s^2$ min.	max.
2.53	2.98	0.60	-2.4	(0.241, 1.759)	(0.388,	20.62)
3.37	3.96	0.79	+3.6	(0.514, 2.514)	(0.273,	6.53)
3.83	4.51	0.90	+7.1	(1.265, 3.265)	(4.07,	28.8)
5.73	6.74	1.35	+2.5	(0.334, 2.334)	(0.262,	12.8)

section attributable to the spacer itself is

$$\frac{\sigma_{sp}}{\lambda^2} = -17.7 \text{ db}$$

and this may be compared with an experimentally measured nose-on cross section for the pure cone-sphere:

$$\frac{\sigma_{cs}}{\lambda^2} = -7.6 \text{ db} \quad .$$

At 2.55 Gc, therefore, the additive cross section associated with the spacer is small compared with the cross section of the unmodified body.

(S) The region between the tip and the spacer is not important for far field considerations but is of some interest in its own right. Ahead of the spacer a significant modification of the surface field may occur, but this seems to depend on ka. For example, at the two highest frequencies the amplitudes of the oscillations forward of the spacer are increased several times over their pure cone-sphere values. When ka = 5 the field is a maximum across the spacer and it is interesting to note that ka_s for this case is 0.997 which almost exactly corresponds to a resonant

situation if the spacer is treated as a ring singularity. When ka= 8 the field is a minimum across the spacer.

(S) At the two lower frequencies the situation is somewhat different. When ka = 3 there is no marked change in the surface field at the spacer itself, and ahead of the spacer the field is oscillating with a relatively small amplitude which is no longer consistent with an interference between forward and backward traveling waves. This is not surprising in view of the fact that the center of the spacer is only 0.729λ along the surface from the tip. At the lowest frequency, corresponding to ka=1.1, there is a slight dip in the amplitude at the position of the spacer but otherwise the build-up away from the tip is characteristic of a pure cone-sphere.

(S) The second type of azimuthal slot is one located near the join: Model LSH (lucite spacer hemisphere) consists of a metallic cone-sphere of half angle $7\text{-}1/2^{o}$ and base radius 2.2195". Its rear hemisphere is separated from the cone forward of the join by the removal of the original metallic spherical segment between the join and the hemisphere and its replacement by a correspondingly shaped insert consisting of two layers: a 0.040" thick aluminum spacer followed by a 0.250" thick lucite spacer so that the lucite borders the hemisphere and the resulting figure is again a cone-sphere with the originally quoted dimensions. The location of the lucite just beyond the cone-sphere join is meant to simulate a ring antenna.

(S) Measurements were made at three frequencies, 0.93, 2.54 and 4.23 Gc for which the corresponding ka are 1.099, 3.001 and 4.999 respectively. Since the angular width of the lucite spacer is (about) $6^{o}28'$ and its one side borders the hemisphere, the circumferential distance in 2π multiples of the wavelength at the center of the lucite is very nearly equal to the above values of ka, which are almost integers except at the lowest frequency. In the case of model LSP when the lucite circumference was an integral multiple of the wavelength a sharp peak was observed in the surface field amplitude across the lucite spacer and in the oscillations forward of the join. Inspection of representative curves of the experimental data (shown in Figs. 3-22 and 3-23) reveals that this is also true for Model LSH.

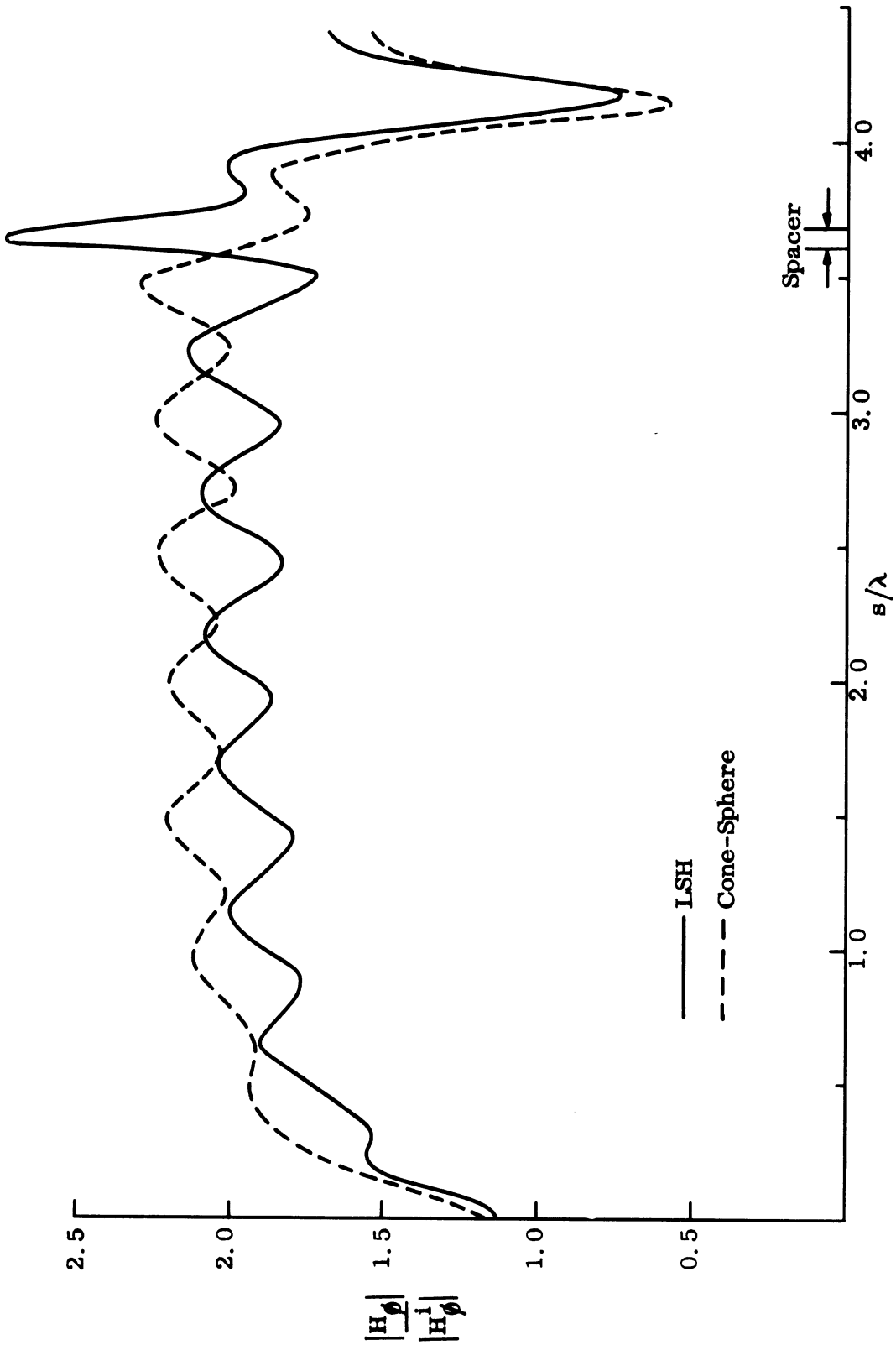

FIG. 3-22: SURFACE FIELD AMPLITUDE $|H_\phi|$ FOR ka = 3.0.

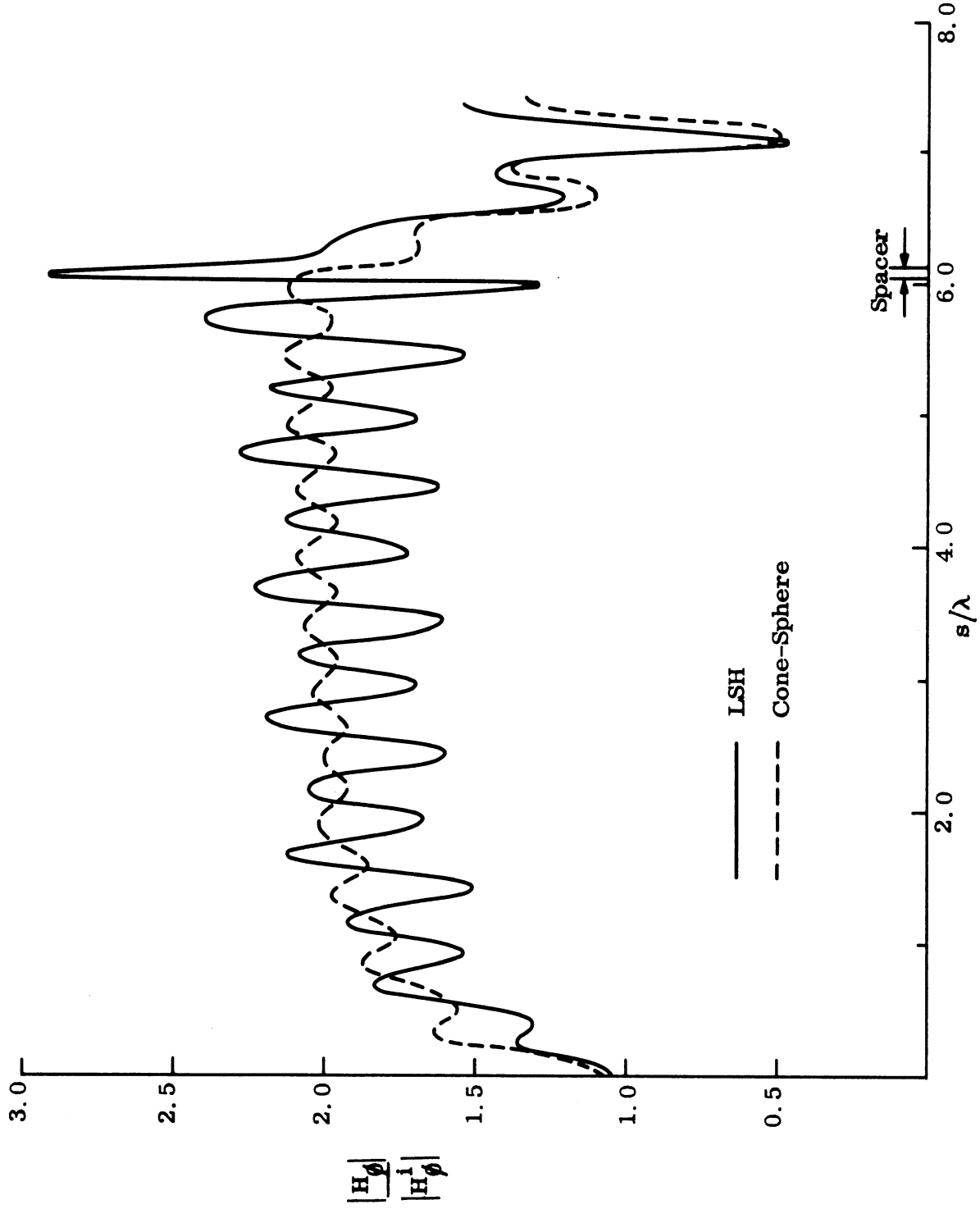

FIG. 3-23: SURFACE FIELD AMPLITUDE $|H_\phi|$ FOR k a = 5.0.

(S) No back scattering measurements are available for Model LSH but it is possible to anticipate some of the behavior from a further consideration of the measured surface fields. The mean level of the surface field displays two types of behavior. Forward of the join it is slightly below, while over the rear hemisphere it is slightly above, the mean on a pure cone-sphere. In addition, the LSH and the cone-sphere surface fields, which are in phase over the rear cap, are 180^{o} out of phase (with respect to the location of minima and maxima) forward of the join. Across the lucite spacer itself there is a pronounced increase in the surface field modulus in each case (including the non-integral ka=1.1). Part of this augmentation leads to an increase in the amplitude of the oscillations (compared to those on pure cone-spheres) forward of the join. This suggests that the creeping wave contribution to the nose-on back scattering cross section will be increased and that Model LSH should possess a larger cross section than a pure cone-sphere of the same ka.

(S) However, following the reasoning previously employed in estimating the return from the lucite spacer, the creeping wave contribution can be seen to be swamped by the greater contribution from the spacer itself and, in practice, even the enhanced creeping wave contribution may be ignored. Estimates of the additional contributions to the cross section from the lucite spacer in Model LSH are listed in Table III-5 and are compared with the standard theoretically-computed cross sections for a pure cone-sphere. As the last column shows, the spacer contribution is now large, both in comparison with the return from the cone-sphere, and also relative to its value when placed near the tip. However, as noted in the beginning of this chapter, there is a danger in attempting to deduce an optimum position for a practical azimuthal antenna from these results, not least because of the uncontrollable impedances presented by the slots.

TABLE III-5
ESTIMATES OF LSH BACK SCATTERING CONTRIBUTIONS

Freq. (Gc)	ka	Γ	$\sigma_{sp}/\pi a_s^2$	σ_{sp}/σ_{cs} (db)
0.93	1.1	5.72	19.4	12.1
2.54	3.0	1.79	1.9	9.6
4.23	5.0	2.84	4.8	17.3

3.4 Non-Spherical Rear

(S) A further type of modification of the pure cone-sphere shape is that provided by a concave spherical indentation of the rear spherical cap. Three distinct models were used, the basic shape of each being represented by the following diagram (Fig. 3-24) which has rotational symmetry with respect to the z axis. For each of the three models the cone half angle α is $7\text{-}1/2^{\circ}$, the original cap radius a is 2.210", the radius b of the spherical segment is 0.553", and the tangent to the surface is continuous at j_1 and j_2. The radius c of the concave spherical indentation is 4.558", 2.212" and 1.519" for Models ID-1, ID-2 and ID-3, respectively.

(S) Measurements of the azimuthal H_ϕ component of the surface field for the case of plane wave illumination at nose-on incidence were made at four frequencies spanning the range from 1.1 to 8.0 Gc, for each model and are summarized in Table III-6.

(S) Typical experimental results, one for each model, are presented here (Figs. 3-25 through 3-27). Examination of the entire set of available data suggests that, in the vicinity of the join, the surface field is not significantly changed from its pure cone-sphere levels by any of the indentations. Moreover from the graphical data it is possible to estimate the creeping wave component of the surface field

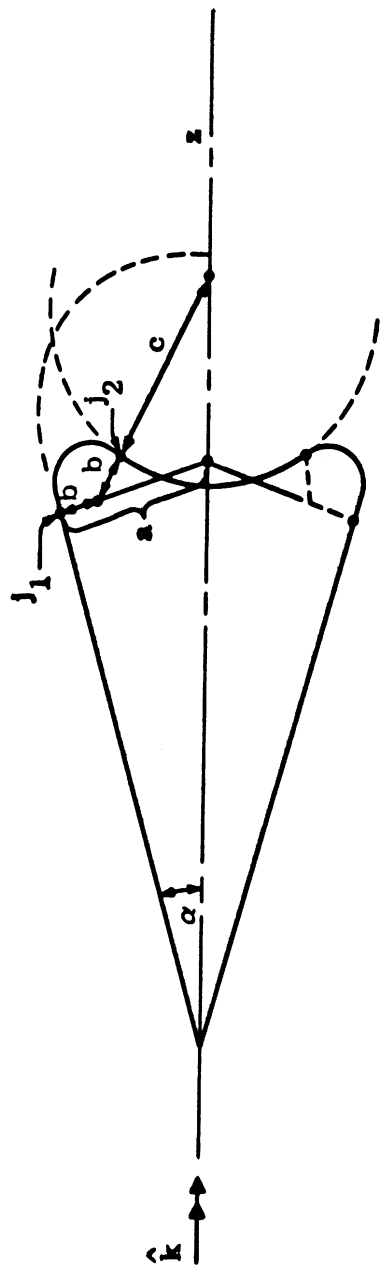

FIG. 3-24 : GEOMETRY FOR INDENTED BACK MODELS.

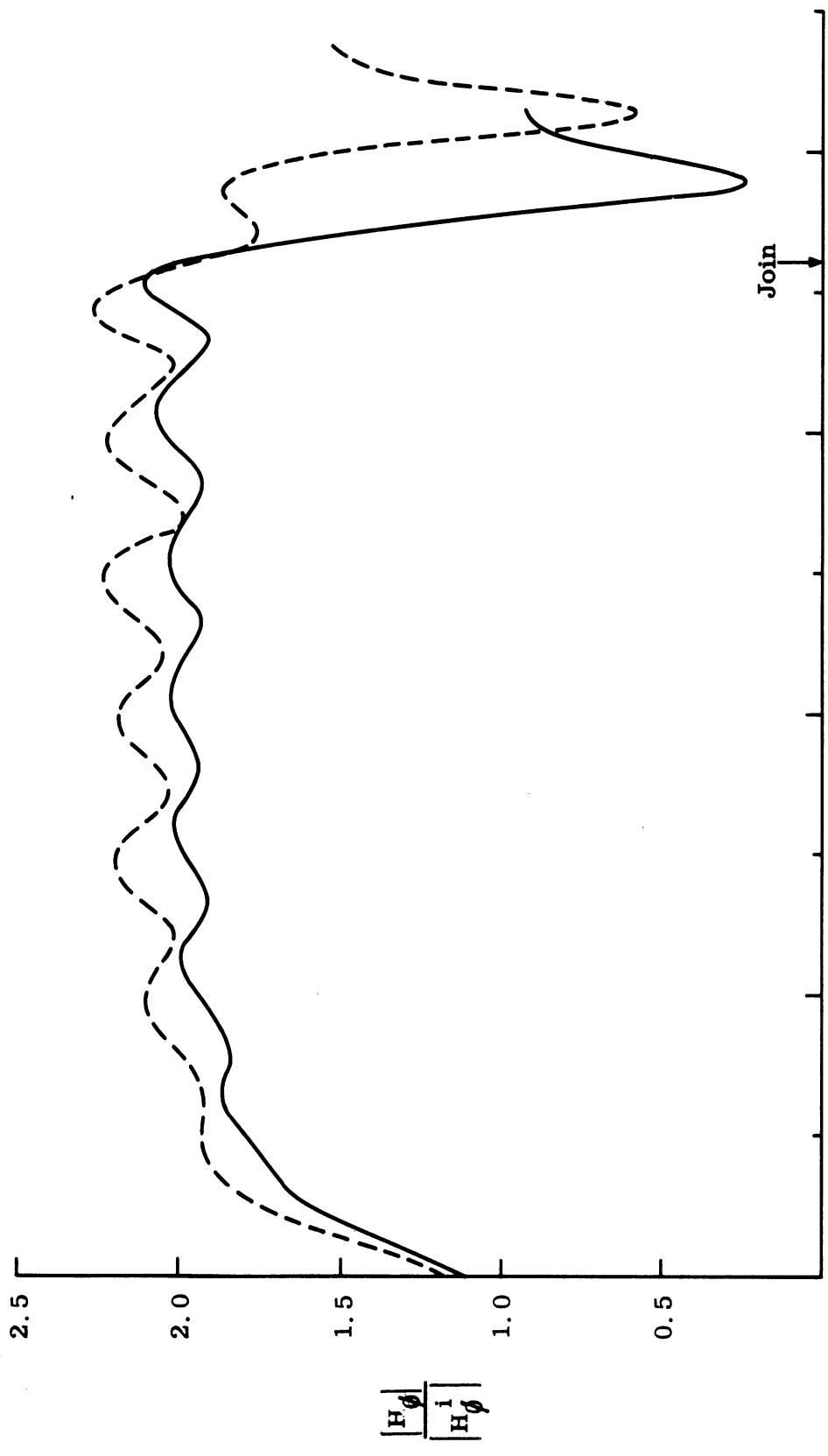

FIG. 3-25: SURFACE FIELD MEASUREMENTS $|H_\phi|$ (——) MODEL ID-1, (---) CONE-SPHERE. ka = 3.0, Frequency 2.55 Gc.

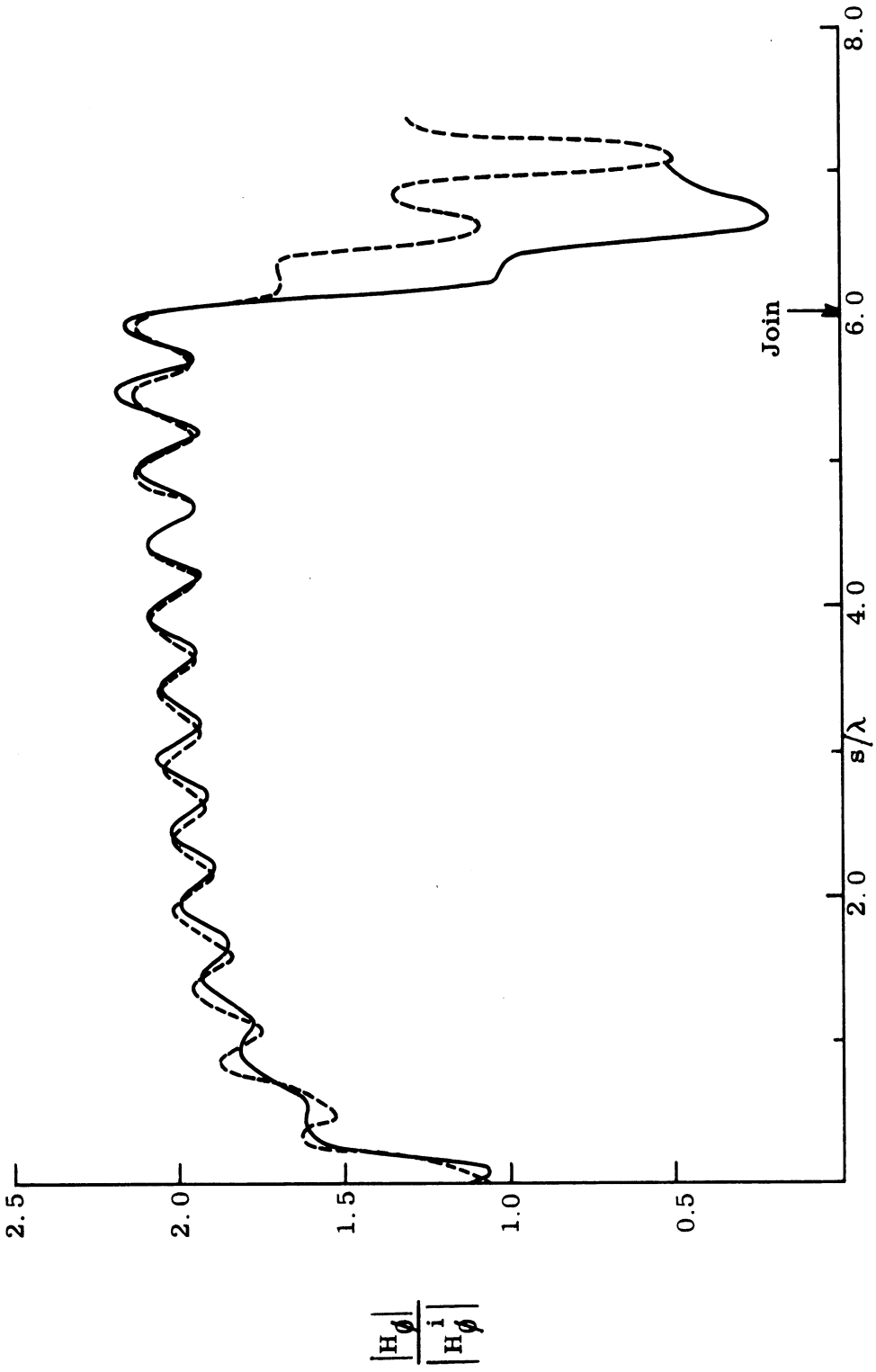

FIG. 3-26: SURFACE FIELD MEASUREMENTS $|H_\phi|$ (——) MODEL ID-3 (---) CONE-SPHERE. ka = 5.0, Frequency 4.25 GHz.

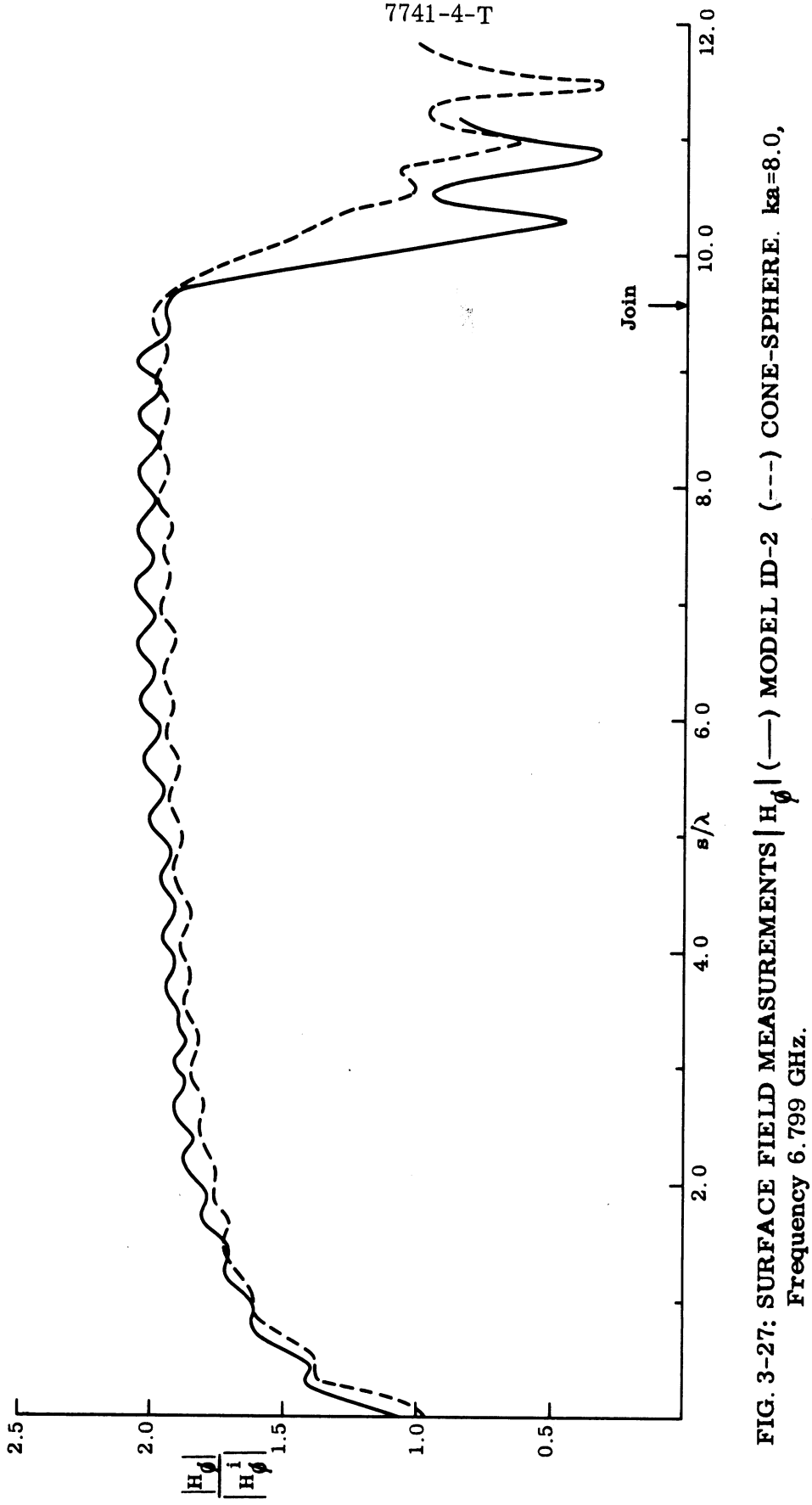

FIG. 3-27: SURFACE FIELD MEASUREMENTS $|H_\phi|$ (——) MODEL ID-2 (---) CONE-SPHERE. ka=8.0, Frequency 6.799 GHz.

TABLE III-6
SUMMARY OF SURFACE FIELD MEASUREMENTS
ON MODELS WITH INDENTED REAR

Frequency (Gc)	ka	Models Measured		
0.935	1.100	ID-1	ID-2	ID-3
2.55	3.000	ID-1	ID-2	ID-3
4.25	5.000	ID-1	ID-2	ID-3
6.799	7.999	ID-1	ID-2	ID-3

according to the analysis given in Senior and Zukowski (1965). A tabulation of these results is given in Table III-7.

TABLE III-7
ESTIMATES OF CREEPING WAVE COMPONENT

Measurement or Method of Estimation	$\|J\|_{c.w.}$ Component of Surface Field			
	ka=1.1	ka=3.0	ka=5.0	ka=8.0
ID-1 Data	.35	.09	.08	.04
ID-2 Data	.43	.10	.075	.035
ID-3 Data	.41	.07	.08	.04
Unenhanced Theoretical (Senior, Zukowski, 1965)	.40	.12	.055	.02
Enhanced Theoretical	.41	.13	.07	.03

(S) For Model ID-1, $|J|_{c.w.}$ is somewhat below the enhanced theoretical moduli at the two lowest frequencies and slightly above at the two highest. However, in view of the difficulty of accurately determining a creeping wave modulus which is less than (about) 0.04 by graphical means, the slight changes at the two highest frequencies may not be significant - at least insofar as changes in contributions to the back scattering cross sections are concerned. Bearing in mind this comment, the values of $|J|_{c.w.}$ deduced for both Models ID-2 and ID-3 are reasonably the same as those supported by a pure cone-sphere at three of the four measured frequencies. Only for ka=3.0 does there appear to be a decrease in the creeping wave strength.

(S) If the mean level of the surface field, as well as the creeping wave strength, for the indented back models is substantially the same as for a pure cone-sphere, the nose-on back scattering cross sections for an indented back model should not be altered to any significant extent from the cone-sphere value. For this conclusion to be valid it is necessary to consider the cross sections averaged over a range of frequencies in order to take into account the fact that the indentations cause a differing path length for the creeping wave contribution, and thus a different phase relative to the join contribution. Since the surface field data for the indented back models shows no noticeable change in the mean level of the field, the creeping wave contribution becomes of decisive importance. If the creeping wave strength is changed relative to that on a pure cone-sphere, a corresponding change is to be expected in the back scattering cross section. For the back scattering patterns made for Model ID-1 this conclusion seems to be supported by the experimental evidence.

(S) One of the frequencies (2.53 Gc) for which far field data was obtained with Model ID-1 is very nearly the same as the second lowest frequency (2.55 Gc) for which surface field measurements were made. The reduced creeping wave amplitude (0.09) relative to that of a cone-sphere (0.13) for ka=3.0 leads to the estimate

$$\frac{\sigma_{ID-1}}{\sigma_{cs}} = \left|\frac{0.09}{0.13}\right|^2 = 0.48$$

which is in good agreement with the measured ratios of 0.59 and 0.25 deduced from the back scattering patterns. The next highest frequency (3.37 Gc) for the far field measurements corresponds to ka= 3.96 and is very near a relative minimum in the standard theoretical cone-sphere cross section. Hence any difference in relative phase of the contributions is likely to result in an increase in the cross section and, in fact, an 8 db rise was experimentally observed. At the two highest frequencies, 3.83 and 5.73 Gc, no surface field data is available, but in this general range there is some indication of an increase in creeping wave strength, although, as indicated, it is difficult to obtain accurate estimates graphically when the strength is small. Experimentally, about a 4 db increase in cross section was found, at these two frequencies.

3.5 Coatings

(S) We shall here consider the effects of coatings of various types, lossy and lossless, full and partial, on the surface fields supported by a cone-sphere, with particular emphasis on the behavior in those regions of the surface which are known to be responsible for the bulk of the back scattered return.

3.5.1 Evolution of the Program

(U) It is not surprising that in a task as complicated as this, where there is little or no reliable information about the surface field behavior available at the outset, the lines of investigation that were followed have evolved and expanded as the work progressed. With the development of the experimental techniques necessary to provide accurate data for all of the surface field components in the presence of coatings, results became available which, in large measure, indicated the type of mechanisms responsible for the observed field behavior, and dictated the theoretical analyses required. It is therefore appropriate to review the steps that were taken to build up the picture as it now exists, and to indicate the philosophy that lay behind these steps.

(S) At the beginning of the task it was our hope (and reasonable expectation) that for many of the coatings of interest a form of impedance boundary condition

would be satisfied to an adequate extent at the surface. In other words,

$$\underline{E} - (\hat{n} \cdot \underline{E})\,\hat{n} = \eta Z (\hat{n} \wedge \underline{H}) \qquad (3.4)$$

where $(\underline{E}, \underline{H})$ is the total field, $\hat{n}$ is a unit vector normal drawn outwards to the surface, Z is the intrinsic impedance of free space, and η is a relative impedance indicative of the electrical properties of the surface. For a 'body' occupying the entire half-space $z < 0$ of a Cartesian coordinate system (x, y, z), Eq. (3.4) reduces to

$$E_x = -\eta Z H_y , \quad E_y = \eta Z H_x , \qquad (3.5)$$

at the interface $z=0$, and for a semi-infinite cone,

$$E_\phi = -\eta Z H_s , \quad E_s = \eta Z H_\phi$$

where E_ϕ and E_s are the azimuthal (circumferential) and longitudinal (along the generator) components of the surface electric field. H_ϕ and H_s are defined similarly, and at a perfect conductor (for which the boundary condition follows from (3.4) on putting $\eta=0$) only these components are non-zero. More generally, however, the tangential components of both $\underline{E}$ and $\underline{H}$ can be non-zero at the surface, and just as we define an electric current by the relation

$$\underline{J} = \hat{n} \wedge H ,$$

so that

$$J_\phi = H_s , \quad J_s = -H_\phi$$

on the cone, so it is convenient to conceive of a magnetic current

$$\underline{J}^* = \hat{n} \wedge \underline{E} .$$

(S) If an impedance boundary condition is satisfied at the surface, a knowledge of the tangential magnetic field immediately determines the tangential electric field there, and vice versa. In particular, $\underline{J}$ and $\underline{J}^*$ are directly related via the surface impedance, and measurements of the tangential magnetic field are now sufficient to specify the surface fields in their entirety. The situation is then comparable to that for a metal. On the other hand, if a boundary condition of the form (3.4) is not fulfilled, both the magnetic and electric fields must be considered.

(S) From the theoretical standpoint, it is extremely desirable to postulate an impedance boundary condition whenever this is appropriate. The properties of the coating are then incorporated into one parameter alone, which shows at once the role played by the thickness of the coating in relation to the bulk parameters of the material. It becomes obvious that coatings with quite different thicknesses and electrical parameters can produce effects which are in all respects identical, and in addition, the extension to multiple layers is simplified. These are certainly good reasons for hoping that Eq. (3.4) may be adequate. Equally important, however, is the fact that there are available exact solutions of the scattering problem for a few simplified shapes obtained subject to an impedance boundary condition. Even when the solutions could still have been obtained on the basis of an actual layered or homogeneous structure (as with a sphere or right-circular cylinder), the former solutions are relatively more simple, and this eases the problem of applying the results in the analysis of more general shapes.

(S) For extreme values of $|\eta|$ an impedance boundary condition has an additional advantage. If $|\eta| \ll 1$, Eq. (3.4) is but a simple perturbation of the boundary condition for a perfect conductor, and we may then use the results of either exact or intuitive analyses for the tangential magnetic field $\hat{n} \wedge \underline{H}$ to deduce the corresponding tangential electric field. A further perturbation then gives the effect of the non-zero η on the magnetic field itself. Similarly, if $|\eta| \gg 1$ we may perturb about a solution for a 'perfect' ferrite (i.e. a material for which $\hat{n} \wedge \underline{H} = 0$ at the surface) to deduce the effect of a large but finite $|\eta|$, a fact which is evident on writing (3.4) in

its alternative form (Senior, 1962)

$$\underline{H} - (\hat{n} \cdot \underline{H})\,\hat{n} = -\frac{1}{Z\eta}(\hat{n} \wedge \underline{E}) \quad .$$

Either approximation enables us to profit from the understanding gained from the study of 'perfect' surfaces, either metals or (by interchanging $\underline{E}$ and $\underline{H}$) ferrites, and opens up a wider variety of shapes amenable to analytical solution. When all is said and done, it is the nuggets of information gleaned from the solutions of these 'canonical' problems that constitute the building blocks out of which our edifice must be constructed.

(U) In recent years several studies of the applicability and limitations of an impedance boundary condition have been performed (see, for example, Senior, 1960; Weston, 1963; Bowman and Weston, 1966), and these have reinforced our belief in the validity of this condition under a wide variety of circumstances. Given a body composed of a homogeneous isotropic material having* (complex) permittivity ϵ_1 and (complex) permeability μ_1, the condition is applicable with

$$\eta = \sqrt{\frac{\mu_1 \epsilon}{\mu \epsilon_1}} \qquad (3.6)$$

providing all radii of curvature R are such that

$$|k_1|\ R >> 1 \qquad (3.7)$$

where k_1 (= Nk) is the propagation constant in the material. The surface impedance given in (3.6) will be recognized as simply the bulk impedance of the material relative to that of free space. The consequences of small variations in the impedance

*Parameters without suffix denote the corresponding quantities for free space.

from point to point in the body have been considered by Rytov (1940) and Senior (1960), and, in particular, it can be shown that the variations in the tangential direction have only a second order effect on the boundary condition.

(S) A specific type of normal variation - that of layering - is, however, of great concern to us, and if the material is confined to a layer of thickness δ backed by a metal, the required surface impedance for use in (3.4) is, under the same conditions as above,

$$\eta = -i\sqrt{\frac{\mu_1 \epsilon}{\mu \epsilon_1}}\ \tan N k \delta \quad , \tag{3.8}$$

where a time factor $e^{-i\omega t}$ has been assumed. Since $\tan N k_1 \delta \longrightarrow i$ as $\mathrm{Im}\, N k \delta \longrightarrow \infty$, the impedance in (3.8) reduces to that in (3.6) if the attenuation within the layer is sufficiently rapid. On the other hand, for a very thin layer, such that $\left| N k \delta \right| \ll 1$,

$$\eta \simeq -i \frac{\mu_1}{\mu} k \delta \quad . \tag{3.9}$$

If more than one layer is present, the generalization of the above results is quite straightforward.

(S) If the surface impedance to be used in (3.4) is defined appropriately as indicated in the above examples, the only significant limitation on the applicability of the boundary condition is that imposed by (3.7). This is, of course, a mathematically sufficient condition, and amounts to the requirement that the field behave locally as though it were impinging on an infinite plane tangential to the surface. We are aware of circumstances under which the impedance boundary condition retains its effectiveness even though (3.7) is violated locally, and two such cases are scattering by an impedance half-plane (Senior, 1952, 1959a) and by an impedance wedge (Senior, 1959b). The restriction (3.7) cannot therefore be regarded as a necessary one, but

even so analyses of the scattering by homogeneous and/or layered cylinders and spheres indicates that the local curvature of the surface can play a role. Bowman and Weston (1966) have, for example, considered the exact solution for a plane wave at normal incidence on a layered cylinder, and have shown that if the radius a is not so large as to satisfy (3.7), the surface impedances that are required for the two scalar equations making up the vector equation (3.4) are

$$-i\sqrt{\frac{\mu_1 \epsilon}{\mu \epsilon_1}}\left(1 \pm \frac{\cot Nk\delta}{2Nka}\right)\tan Nk\delta \quad . \tag{3.10}$$

It is therefore necessary that

$$\left|2Nka \tan Nk\delta\right| >> 1$$

(a less severe condition than (3.7)) if the impedance (3.5) is to be rigorously applicable to this case, and in a subsequent analysis of a layered sphere, Bowman and Weston have also shown that the transverse curvature can play a role.

(S) Although it is obvious that for an entirely arbitrary body with any type of coating, impedance boundary conditions cannot be assumed to be universally applicable no matter how the surface impedance η is defined, there are certain factors going for us in the present investigation that give grounds for believing that a condition of this type may be adequate for most purposes. In the first place, our analyses of the metallic nose-cones, either with or without perturbations of the basic cone-sphere shape, have proved that the surface field effects are predominantly local in character, and that local analyses are sufficient for their understanding. Over the surface of the cone, the incident field is the dominating influence, with subsidiary effects produced by the creeping wave contribution attributable to the base (a purely additive effect) and by the rapid field transition across the reflected wave boundary which, for a narrow cone, is in the near vicinity of the surface. This last effect is small, but does serve to produce a long period cyclical variation about

the optics value. Such a mechanism was postulated in Appendix C of Senior and Zukowski (1965) on the basis of the two-dimensional analogue of a wedge, and is strikingly confirmed by the recent exact analysis and computation (Senior and Wilcox, 1967) of the surface fields on a semi-infinite cone. For each of these contributors, the modifications resulting from a coating that can be represented by an impedance boundary condition are feasible to determine; and the fact that, with the study at its present stage, the portions of the cone near to the tip are of little concern in comparison with those near to the join (where the transverse radius of curvature is, of course, relatively larger) lends credence to the general adequacy of an impedance boundary condition for the estimation of the scattering.

(S) If the radius of curvature at the join is large enough (greater than λ, say) the field amplitudes there in the absence of any cap effect (equivalent to treating the cone as semi-infinite in extent) should have attained their limiting values appropriate to a planar surface. Locally, at least, an impedance boundary condition must then be valid, and the limiting field amplitudes for the special case of nose-on incidence on the cone are as follows.

$$\left|H_\phi\right| = \left|\frac{Y}{\eta} E_s\right| \sim \left|\frac{2\sin\alpha}{\eta+\sin\alpha}\right|$$

$$\left|H_s\right| = \left|\frac{Y}{\eta} E_\phi\right| \sim \left|\frac{2\sin\alpha}{1+\eta\sin\alpha}\right| .$$

If the transverse dimensions of the cone at the join are not quite as large (or, equivalently, further back toward the tip), the field amplitudes will depart from the above limits, but we may still hope to reproduce the correct qualitative behavior by the analysis of an appropriate canonical problem in which an impedance boundary condition is applied to some shape whose transverse dimensions are no longer infinite. For this purpose, the fact that each generator of the cone is at constant inclination to the illuminating field is a simplifying feature. We can therefore adopt as our model either a wedge subject to an impedance boundary condition, or a circular cylinder of

infinite extent (either layered or with an impedance condition at the surface) inclined at the approptiate direction to the field. For the first of these models, an exact solution is already available (Senior, 1959b) for arbitrary incidence and wedge angle. The solution is, however, of complicated form, and is not (as yet) well-suited to numerical computation. Instead, the simpler model of the cylinder was adopted. The surface field is then a function of the radius, a, the angle of incidence and the surface properties. Expressions were derived for the field both for a layered cylinder (exact analysis), and for a cylinder whose surface properties were incorporated in an impedance boundary condition. Both expressions were programmed for digital computation, and even for quite small radii of cylinder, the impedance boundary condition gave results which closely approximated those provided by the more complicated model. Knowing, then, the surface field as a function of ka for given incidence angle and surface properties, we can relate these to field values on a cone as a function of distance from the tip using, for example, the relation

$$\frac{s}{\lambda} = ka \cdot \frac{\cot \alpha}{2\pi} \quad . \tag{3.11}$$

(S) Inasmuch as this picture is predicated upon the surface field being determined only by the local geometry of the surface and the presence (or absence) of the direct illumination produced by the incident plane wave, it is clear that it would be placed in jeopardy were there any surface waves of significant amplitude excited on the cone itself. In our initial approaches to this problem, such a wave was, indeed, postulated as one of the decisive factors in creating the observed behavior of the surface fields on the cone. Using again the analogy with a circular cylinder, the excitation strength and decay rate of the corresponding surface wave were determined, but these were found to be irrelevant to the measured data for the surface field. It was therefore concluded that the incident field locally, rather than a surface wave launched elsewhere (as, for example, at the tip), was the dominating influence, and some evidence in support of this is (i) with a metallic cone the surface field does

not reveal any evidence of a spherical disturbance originating at the tip (Senior and Wilcox, 1967), (ii) measured surface field data for coated cone-spheres have shown no features readily identifiable with surface or trapped waves excited on the cone itself, and (iii) the measured field behavior on the cone portion of a cone-sphere illuminated at an angle near rear-on incidence ($\theta = 180 - 2\alpha$) is in general agreement with that expected based on the dominating effect of the local geometry.

(S) Turning now to the base of the cone-sphere, our aim is to determine the strength of the creeping wave that has circumscribed the rear and, hence, the corresponding contribution to the back-scattered field. Since the base is spherical, we have at our disposal an almost exact model in the form of a complete sphere, coated in whatever manner is appropriate. We can therefore compare the measured surface field values on the back of the cone-sphere with computed data for the field in the rear of the sphere; and in addition, we can decompose numerically data computed for the back scattering and extract from this the portion attributable to the creeping wave contribution. Such a procedure is in no way dependent on the assumption of an impedance boundary condition, though the assumption would, of course, simplify both the analysis and computation. It is, however, dependent on the rear being spherical, and is not therefore applicable to more general forms of termination. Partly for this reason, but also because (i) if an impedance boundary condition must be postulated on the higher reaches of the cone, it is logical to maintain this postulate over the base (and with a spherical base, should be at least as valid there), (ii) our aim is primarily the estimation of the net creeping wave amplitude after the rear has been traversed, rather than the detailed prediction of the field at all points of the rear; and (iii) this type of estimate is amenable to asymptotic computation, and any marginal (or local) failure of an impedance boundary condition would not be expected to create a large error, attention has been directed mainly at the asymptotic approach. This has enabled us to profit from earlier computations (e.g. by Streifer, 1964) of the decay rates of creeping waves in the presence of an

impedance boundary, and from the work of Logan (1965) on the birth rates. The appropriate formulae are given in Chapter V.

(S) In the preceding pages we have endeavored to give something of the reasoning and philosophy that have motivated us in the approaches that we have followed. Initially at least, the experimental program was pursued in parallel to the theory, with the object of ascertaining practically the conditions under which an impedance boundary condition was fulfilled. To this end, measurements of all tangential field components were made for coated spheres and cylinders, as well as for a variety of cone-sphere models at primarily nose-on incidence, and in each case the ratios of the cross-coupled surface field amplitudes (e.g. $|E_s| / ZH_\phi$) were of as much concern as were their individual amplitudes. Typical results for a few of these bodies are presented in the next section. Under a wide range of circumstances, the data obtained supported the 'regional' effectiveness of an impedance boundary condition, e.g. over the upper reaches of the cone and over the base, or over the illuminated portion of a sphere and over the rear, but with some evidence of differences between the (constant) field ratios over the first part of the complete body as compared with the second. This is no real embarrassment in view of the separation of these regions inherent in the analytical treatment of their contributions.

(S) As more surface field data was accumulated, the general picture of the surface field behavior evolved, and then indicated the theoretical studies that were required. Meanwhile, the experimental program concentrated more on a cone-sphere with the cone half angle $\alpha = 7\text{-}1/2^{\circ}$, but with any of several different coatings. Multiple coatings as well as oblique angles of incidence were examined, and a selection of these results will be shown in Figs. 3-53 and 3-54 for a double coating and in Figs. 3-55 through 3-58 for oblique incidence.

3.5.2 Presentation and Discussion of Experimental Data

(S) As evident from the preceding discussion, the practical validity of any form of impedance boundary condition was a question whose answer was of some importance to the direction that the theoretical studies were to take, and at the

beginning of the experimental program, several sets of measurements were carried out to determine the extent to which ratios of field components at the surface were sensibly constant for the types of coatings of interest in this investigation. For purposes of such testing, spheres and cylinders are convenient shapes to use, and thus, for example, the surface fields were measured on a metallic sphere of radius 4.00" coated with a layer of RS-X absorber 1/16" thick, and illuminated by a plane wave at a frequency 2.348 Gc. This frequency corresponds to ka=5.000 for the bare metal alone, but 5.078 if the coating is taken into account.

(S) Although the tangential components of the electric field are zero at a metal surface, this is no longer true when the surface is coated, and measurements of four components (e.g. E_θ and E_ϕ, H_θ and H_ϕ) are now necessary for the complete determination of the surface field. Figure 3-28 shows the measured data for the amplitudes of the azimuthal magnetic (H_ϕ) and circumferential electric (E_θ) field components for the RS-X coated sphere. For a metallic sphere, the surface fields are, of course, known exactly, and using the values computed by Ducmanis and Liepa (1965), the curve for the dominant magnetic component $T_2(\theta)$ (equivalent to H_ϕ) with ka=5.0 has been superimposed on Fig. 3-28.

(S) The satisfaction of an impedance boundary condition uniformly over the surface requires that the ratio $|E_\theta| / |H_\phi|$ be constant, and if the radius of curvature of the surface is large enough ($> \lambda$, say) this constant should equal $|\eta|$, where η is the relative impedance of the bulk material of which the coating is composed or, if the thickness of the layer is not large, the constant should be as indicated in Eq. (3.8). Inspection of the measured data for E_θ and H_ϕ shows that the ratio of their moduli is, in fact, approximately constant. When the ratio is computed directly for $\theta = 0^\circ (10^\circ) 180^\circ$ from the curves in Fig. 3-28, two distinct (but only slightly different) numerical constants are obtained: for the illuminated portion $0^\circ \leqslant \theta \leqslant 90^\circ$ of the sphere the ratio is 0.432 ± 0.025, and over the shadowed region the ratio drops to 0.369 ± 0.022. If the distinction between regions is dropped, the overall ratio is

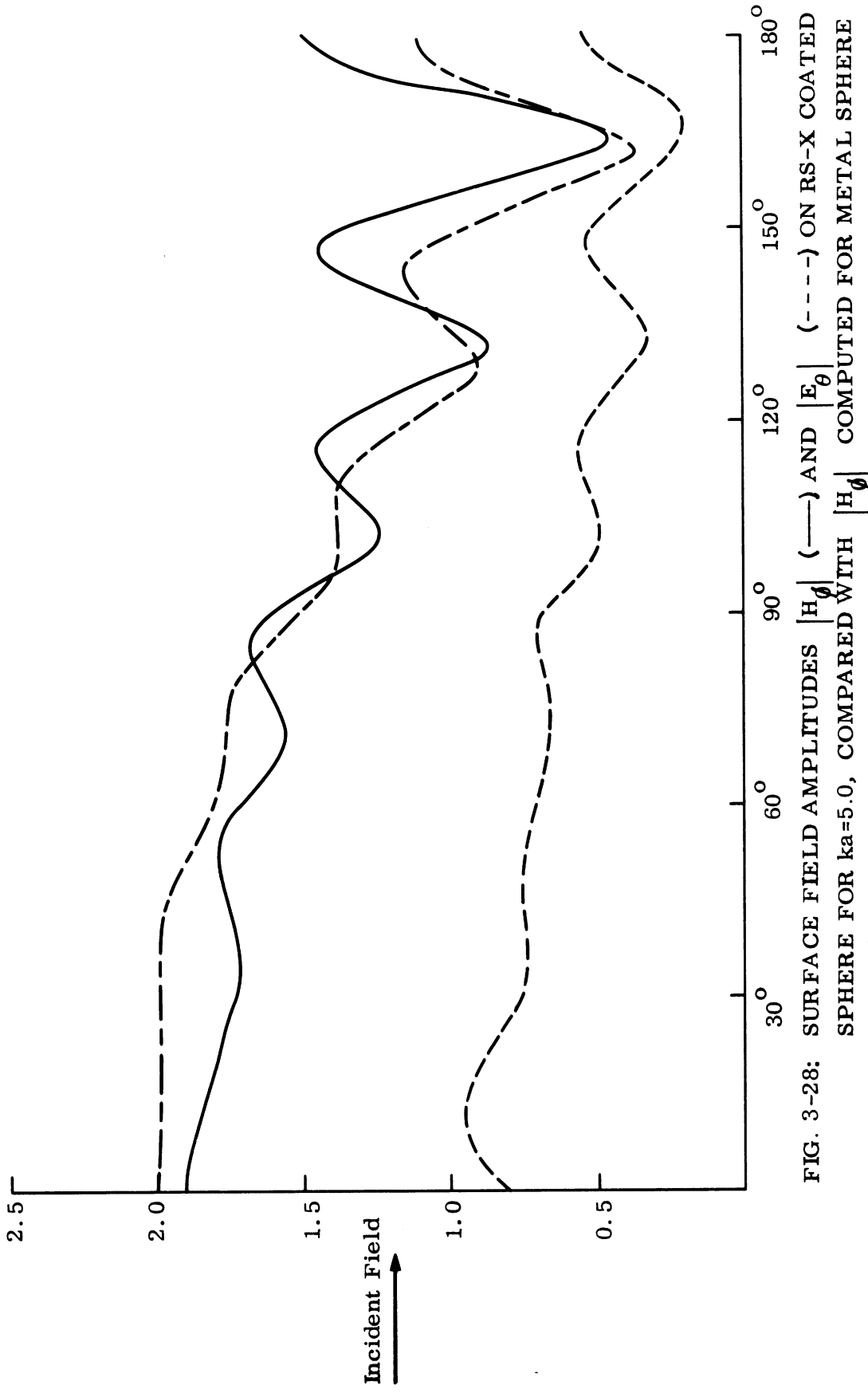

FIG. 3-28: SURFACE FIELD AMPLITUDES $|H_\phi|$ (——) AND $|E_\theta|$ (- - - -) ON RS-X COATED SPHERE FOR ka=5.0, COMPARED WITH $|H_\phi|$ COMPUTED FOR METAL SPHERE (.....).

0.402 ± 0.040, which is intermediate to the theoretical values 0.245 and 0.579 deduced from the measured impedance of the coating material with (see Eq. 3.8) and without (see Eq. 3.6) the thickness of the layer taken into account.

(S) We also observe from Fig. 3-28 that on the coated sphere $|H_\phi|$ is generally smaller than for a metal sphere throughout the illuminated region, but is somewhat larger in the shadow. Although the curve on the shadowed side has the same structure as, and tends to parallel, the curve for the bare sphere, there is a systematic displacement of the maxima and minima towards to rear. The displacement is larger than can be attributed to the increase in outer radius resulting from the coating, and is indicative of the change in phase velocity of the creeping wave on the coated body.

(S) As a further test of an impedance boundary condition, surface field measurements were made for a metal cylinder of length 24" and radius 1.500" coated with a 'home-made' S-band absorber of nominal thickness 0.140". With the cylinder mounted vertically on the support pedestal, the amplitudes of the tangential magnetic and electric surface fields were measured at the frequencies 3.381 and 6.262 Gc at points approximately 0.25" apart around a circumferential trajectory midway between the ends. Since the incident magnetic vector was along the axis of the cylinder (horizontal polarization), the components measured were, in fact, H_z and E_θ where (r, θ, z) are cylindrical polar coordinates. The measured length of the circumference was 10.273", corresponding to an outer radius b=1.635". The average thickness of the coating was therefore 0.135", and whereas the values of ka for which the measurements were made were 2.700 and 5.000, the values of kb were 2.943 and 5.451.

(S) When the measured data was examined it was found that the coating had indeed reduced $|H_z|$ relative to the values that it had on a bare cylinder, with the reduction being somewhat larger at the lower frequency. On the other hand, the coating had raised $|E_\theta|$ (which is zero at a metallic surface) to values in excess of those for $|H_z|$ at 3.381 Gc, but to values less than $|H_z|$ at 6.262 Gc. Rather than

present this data, we show instead (Fig. 3-29) the ratio of the measured amplitudes at each of the two frequencies. At the lower frequency we observe that the ratio is reasonably constant at about 3 db (=1.4) out to $\theta = 105^{\circ}$ (approx.), but then rises rapidly to a maximum of 8 db near $\theta = 150^{\circ}$ before falling to almost unity. It would therefore appear that at this frequency some form of impedance boundary condition is reasonably fulfilled over the illuminated region, though not in the deep shadow. At the higher frequency the region of fulfillment embraces almost the whole circumference of the cylinder, and out to $\theta = 160^{\circ}$ the ratio differs from -8 db (=0.40) by no more than $\pm$ 1 db. Within the next 20°, however, there is a marked change, with the ratio dropping to almost -16 db at $\theta = 166^{\circ}$, but because of the minima in the field components occurring near this angle, at least a portion of the drop in ratio could be due to experimental error.

(S) By virtue of the normalization of the experimental data, the measured ratio of the field components should be $|\eta_{eff}|$, and it is of interest to compare its values with those deduced from the electrical constants and thickness of the coating. Using conventional transmission line techniques, the relative permittivity and permeability were measured in real and imaginary parts at 8 frequencies in the range 2.5-6.0 Gc, and from these values it is possible to compute the bulk impedance $|\eta|$ of the layer at frequencies corresponding to those used in the surface field experiments. Almost no variation in $|\eta|$ between the two frequencies is found ($|\eta| = 0.549$ at 3.381 Gc, compared with 0.542 at 6.262 Gc), but because of the small electrical thickness of the coating η_{eff} is expected to show a frequency dependence through its tangent factor. In fact, from Eq. (3.8), we have

$$|\eta_{eff}| = 1.23 \qquad \text{at } 3.381 \text{ Gc}$$

$$= 0.432 \qquad \text{at } 6.262 \text{ Gc},$$

and these not only explain the qualitative behavior of the measured ratio $|E_{\theta}/H_{z}|$ at the two frequencies, but are also in excellent agreement with the numerical constants deduced from the data. Figure 3-29 therefore supports the validity of the

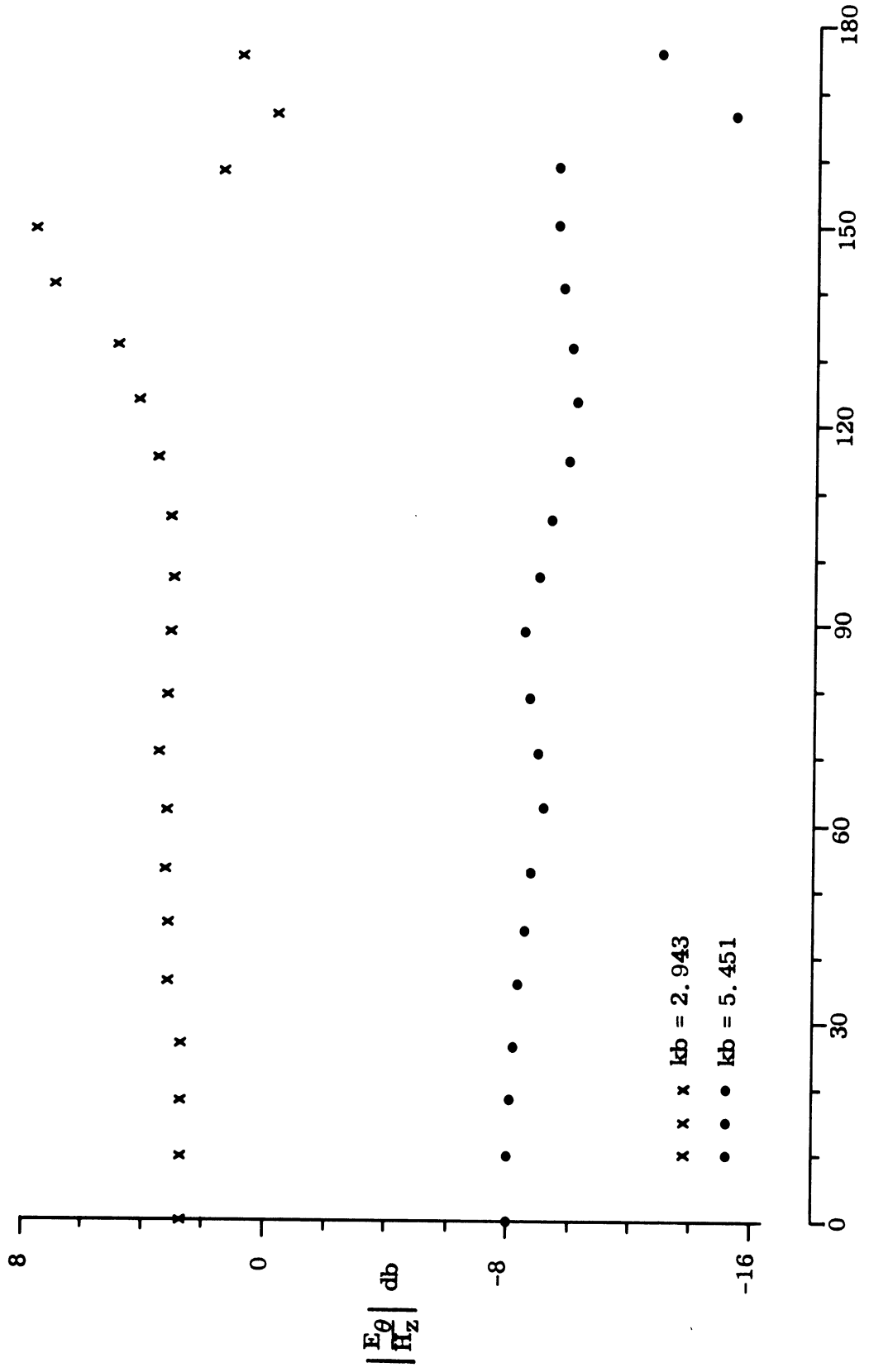

FIG. 3-29: MEASURED RATIO OF SURFACE FIELD AMPLITUDES ON S-BAND COATED CYLINDER FOR TWO FREQUENCIES.

theoretically-derived impedance boundary condition for this coating over almost the entire surface at the higher frequency and over the illuminated region at the lower frequency. This is in spite of the fact that at 3.381 Gc the cylinder is less than $\lambda/2$ in radius, and because of the relatively small radius of curvature, it is not surprising that the coating affects the creeping wave (or shadow field) component in a different way to the optics (or illuminated) one.

(S) Since the configuration of prime interest is the cone-sphere rather than a sphere or cylinder alone, attention was now directed at this shape and a series of measurements was undertaken to determine the fields on variously-coated cone-spheres with half angles in the range $7\text{-}1/2^{\circ} \leqslant \alpha \leqslant 12\text{-}1/2^{\circ}$. As a result of these investigations, a general picture of the surface field behavior was built up that is independent of the half angle α in all its major features. It was therefore sufficient to concentrate on a single cone angle, and use this as the vehicle to study in detail the varying effects of coatings as functions of their material constants, thickness and frequency. The case chosen was $\alpha = 7\text{-}1/2^{\circ}$, a choice that was convenient not only because of the considerable amount of data for uncoated cone-spheres and near cone-spheres of this half angle available through the first year's program, but also because the required models were on hand and the coatings could be readily applied. It should be emphasized, however, that this subsequent restriction to $\alpha = 7\text{-}1/2^{\circ}$ in no sense limits the validity of the conclusions reached from the interpretation of the surface field data: as the selection of data presented in this section shows, the results for $\alpha = 7\text{-}1/2^{\circ}$ are typical of those for any cone-sphere of small cone-angle.

A selection of the surface field data obtained for lucite-coated cone-sphere is given in Figs. 3-30 through 3-33, and some of the corresponding parameters are listed in Table III-8.

(S) The general nature of the surface field is not dissimilar from that found on a pure metal cone-sphere, a fact which is readily seen in Fig. 3-31 where the azimuthal magnetic field component on a plain cone-sphere with ka=2.2 is also shown for comparison.

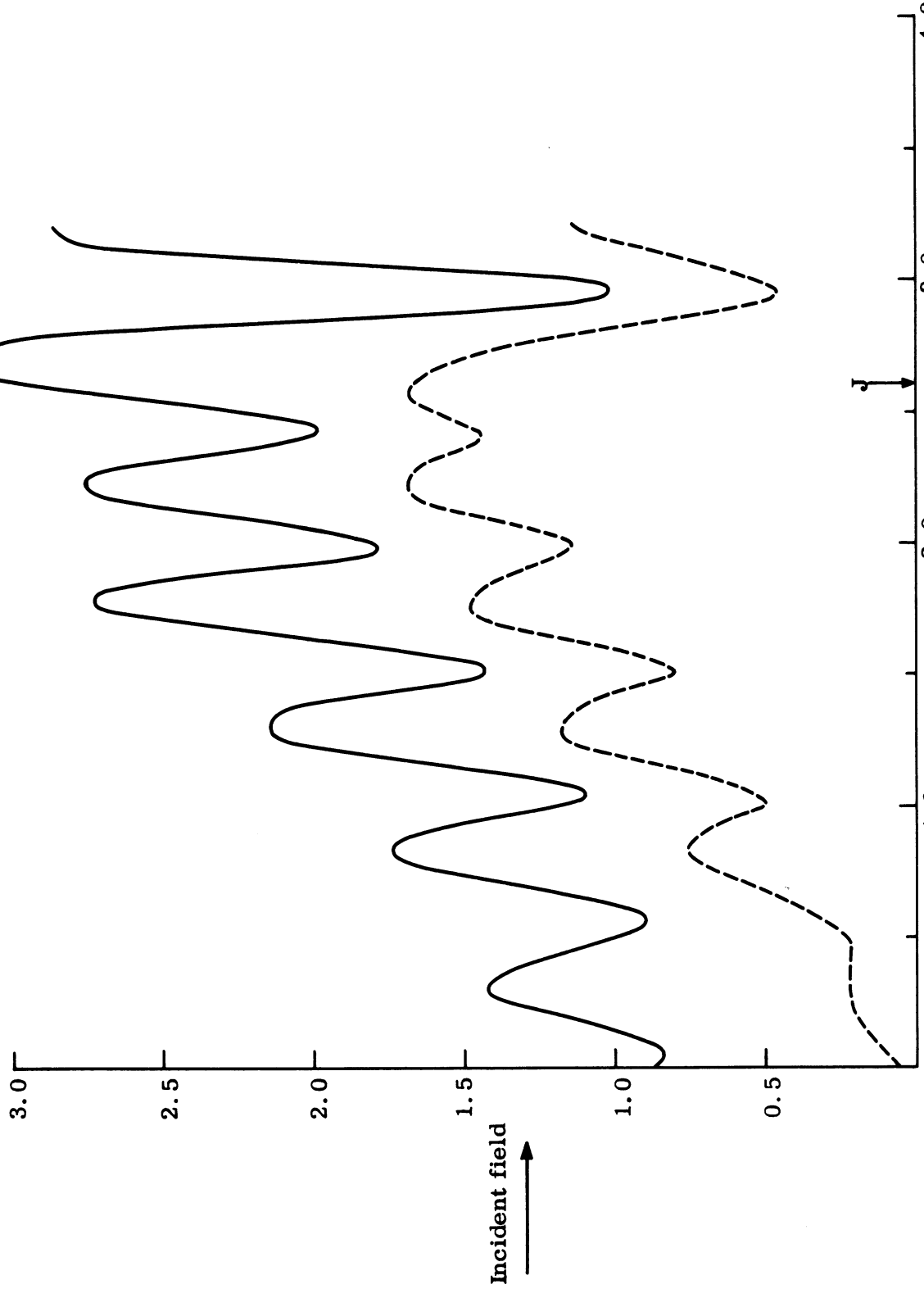

FIG. 3-30: SURFACE FIELD AMPLITUDES $|H_\phi|$ (—) AND $|E_s|$ (---) ON LUCITE-COATED CONE-SPHERE WITH $\alpha = 7\text{-}1/2^\circ$ AND ka=1.600 (ka=2.193).

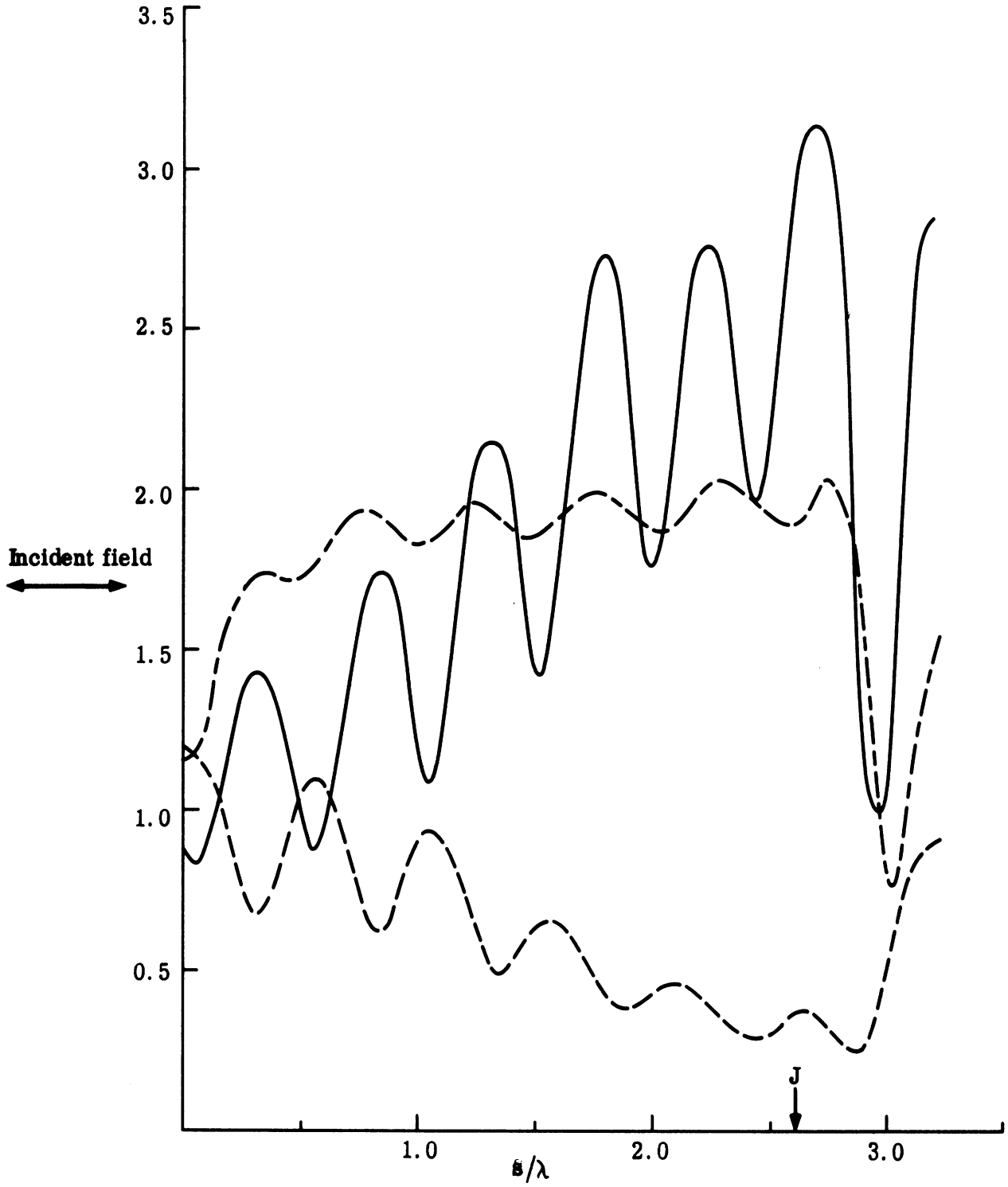

FIG. 3-31: SURFACE FIELD AMPLITUDES $|H_\phi|$ (—) AND $|E_\phi|$ (---) ON LUCITE-COATED CONE-SPHERE WITH α=7-1/2° AND ka=1.600 (kb=2.193); (—·—) INDICATES $|H_\phi|$ FOR UNCOATED CONE-SPHERE WITH α=7-1/2° AND ka=2.2 .

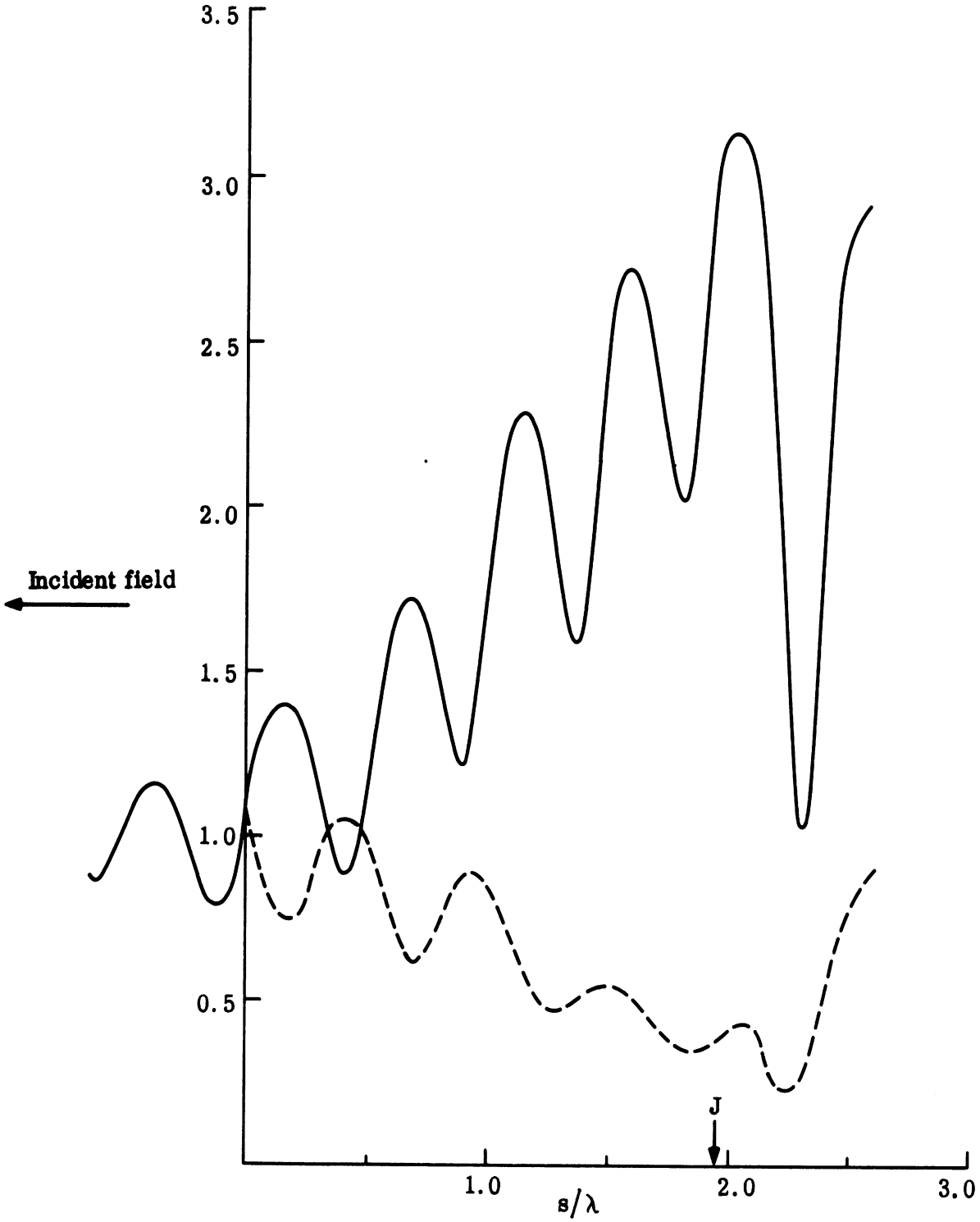

FIG. 3-32: SURFACE FIELD AMPLITUDES $|H_\phi|$ (—) AND $|E_\phi|$ (---) ON LUCITE-COATED CONE-SPHERE WITH $\alpha = 10^o$ AND ka=1.600 (ka=2.193).

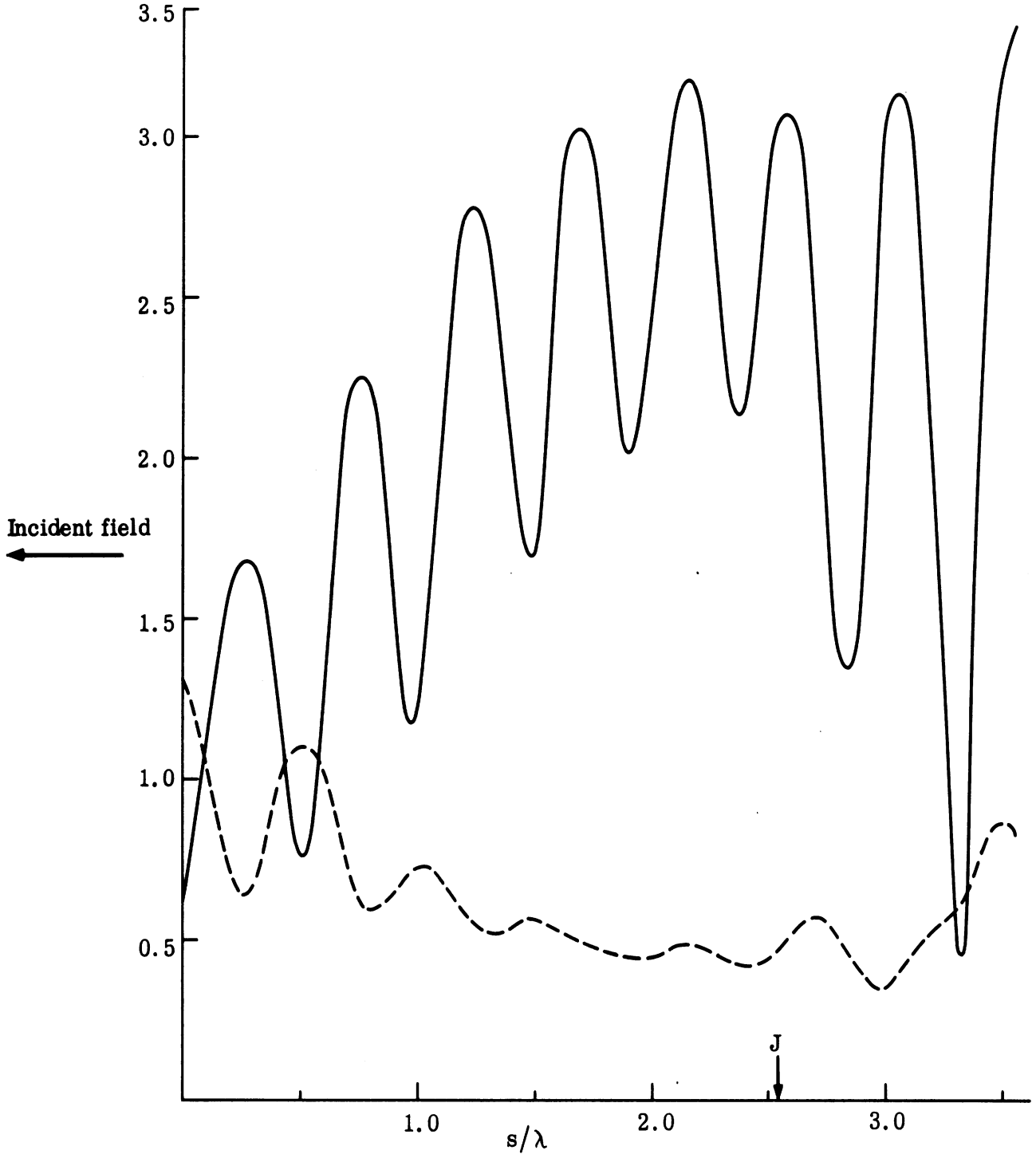

FIG. 3-33: SURFACE FIELD AMPLITUDES $|H_\phi|$ (—) AND $|E_\phi|$ (---) ON LUCITE-COATED CONE-SPHERE WITH $\alpha = 12\text{-}1/2^\circ$ AND ka = 2.963 (ka = 3.540).

TABLE III-8
REPRESENTATIVE MODEL CHARACTERISTICS

Half-Angle (degrees)	Coating	Cap Radius (inches)	Frequency Gc	ka	kb	Component Measured
7 1/2	3/8" lucite	1.012	2.9699	1.600	2.193	H_ϕ, E_s, E_ϕ
10	3/8" lucite	1.012	2.9699	1.600	2.193	H_ϕ E_ϕ
12 1/2	3/8 " lucite	1.926	2.8896	2.963	3.540	H_ϕ E_ϕ

(S) Over the rear spherical cap the field on the lucite-coated model almost parallels that which is supported by a pure cone-sphere. The slight shift in the location of the relative minimum in this region is due in part to the change in the phase velocity of the creeping wave relative to its value on a metal, and also to the size difference (ka=2.193 compared with ka=2.2). Forward of the join the field is characterized by oscillations superimposed on a mean level which falls as the tip is approached. Near the join this mean level is as much as 25 per cent higher than the corresponding cone-sphere level but it decreases so that within a wavelength or so of the tip it reaches the metallic cone-sphere value after which it continues to fall as the tip is approached. There is some evidence to suggest that, at the join, the mean level of $|H_\phi|$ increases with half angle; this agrees with observations on metallic cone-spheres.

(S) The oscillations are quite regular in period and reasonably regular in amplitude and may be identified with the strength of a creeping wave contribution. Although the lucite coating raises the creeping wave strength in all cases, the increase (even for a fixed ka) no longer simply decreases with increasing half angle, as in the case of a pure cone-sphere, but also depends on the relative thickness of the coating. When ka and kb are both fixed, however, the creeping wave strength does increase with decreasing half angle.

(S) On one of the graphs (Fig. 3-30) the moduli of the H_ϕ and E_s components are shown and, even though the frequency is relatively low (ka=2.2), it can be verified that an impedance boundary condition is satisfied to a surprisingly large extent.

(S) There are three general features of the above data that should be noted: (1) the enhanced mean level of $|H_\phi|$ at the join, together with the increased creeping wave strength, indicate that in far field measurements, the backscattering from the coated models will be larger than from the pure metal models; (2) an impedance boundary condition is still approximately satisfied in spite of the low value of the refractive index for this coating; and (3) the dependence of the surface field amplitudes on the cone half-angle is not one whose character changes radically as α varies, and is at most a smooth and slowly varying function of this parameter.

(S) With emphasis thus placed on cone-sphere models whose half angle is $7\text{-}1/2^\circ$, a variety of coatings was applied and the resulting surface fields measured. In the remainder of this section, attention will be directed at the results for three coating materials which are representative of the entire collection.

(S) The first absorber is a 1/16" layer of RS-X material applied to a metallic cone-sphere whose half angle and base radius are $7\text{-}1/2^\circ$ and 2.210" respectively. The cases studied are summarized below and portions of the data are presented in Figs. 3-34 through 3-36.

TABLE III-9
SUMMARY OF RS-X SURFACE FIELD MEASUREMENTS

Frequency (Gc)	ka	kb	Component Measured
0.935	1.100	1.131	H_ϕ, E_s
2.55	3.000	3.085	H_ϕ, E_s, E_ϕ
4.25	5.00	5.141	H_ϕ, E_s, E_ϕ
6.80	8.000	8.226	H_ϕ, E_s, E_ϕ

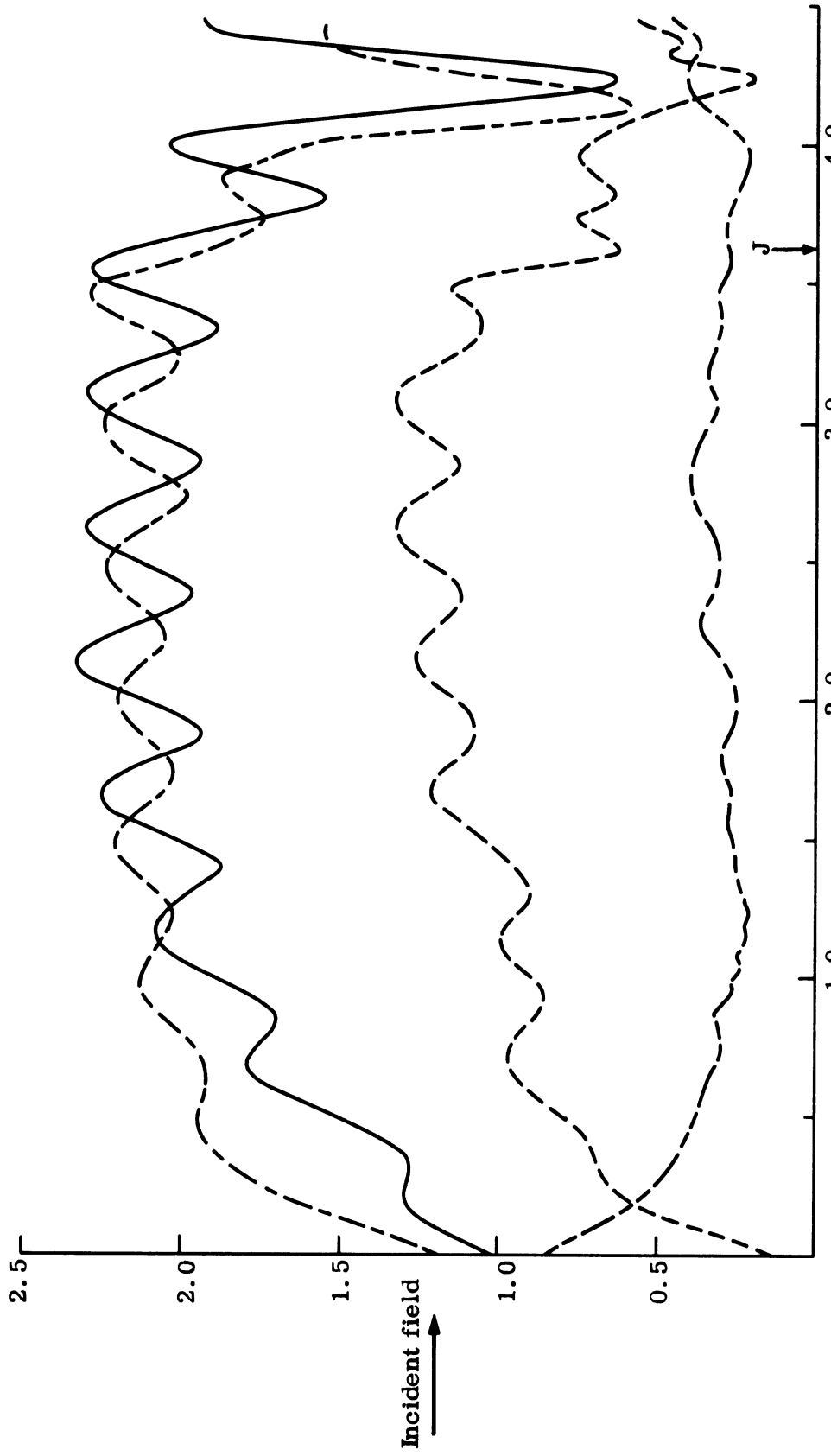

FIG. 3-34: SURFACE FIELD AMPLITUDES $|H_\phi|$ (—), $|E_s|$ (---) AND $|E_\phi|$ (- - - -) ON RS-X COATED CONE-SPHERE FOR ka=3.0; (— — —) INDICATES $|H_\phi|$ FOR BARE MODEL.

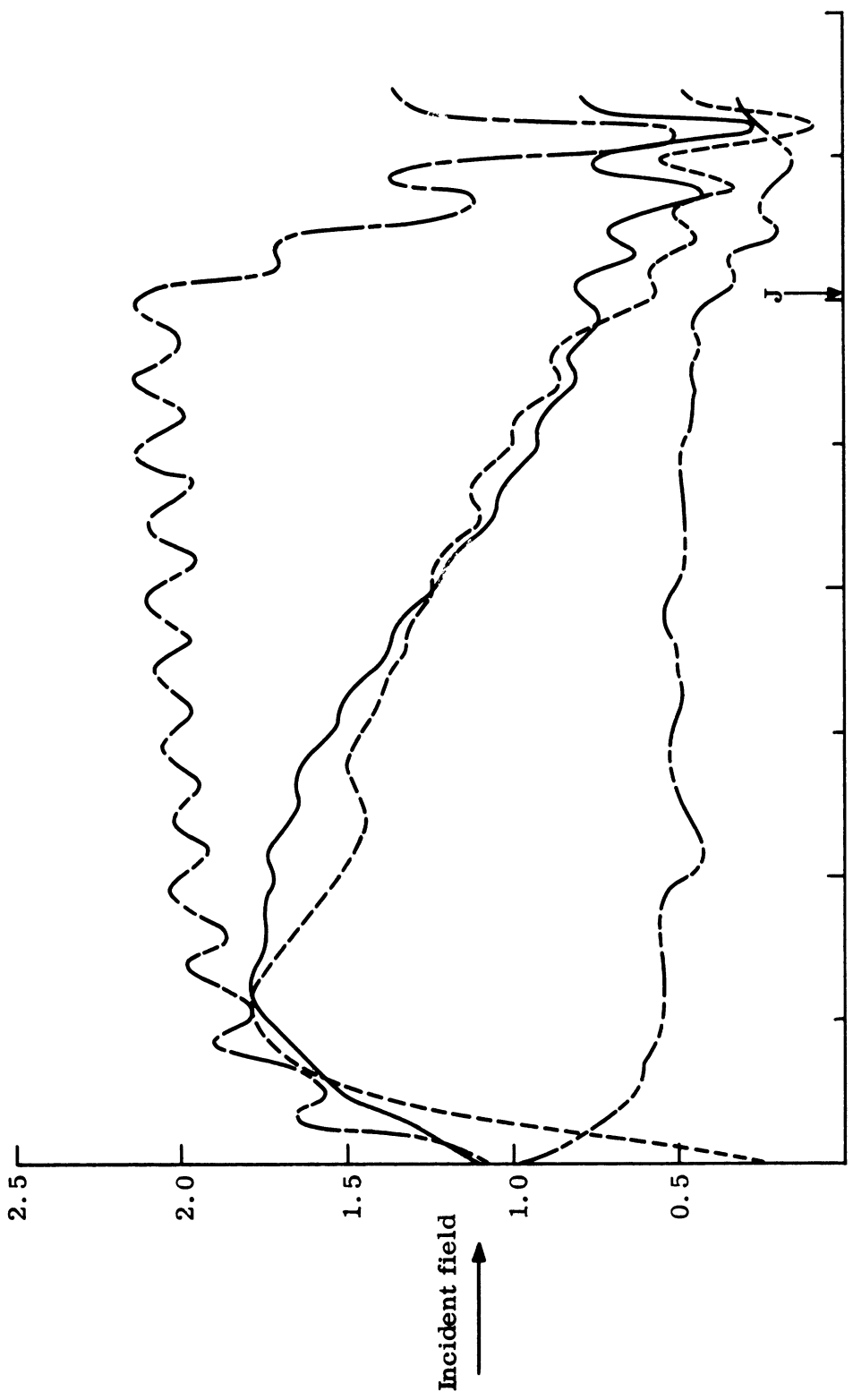

FIG. 3-35: SURFACE FIELD AMPLITUDES $|H_\phi|$ (—), $|E_s|$ (---) AND $|E_\phi|$ (-·-·-) ON RS-X COATED CONE-SPHERE FOR ka=5.0; (-·-·-·-) INDICATES $|H_\phi|$ FOR BARE MODEL.

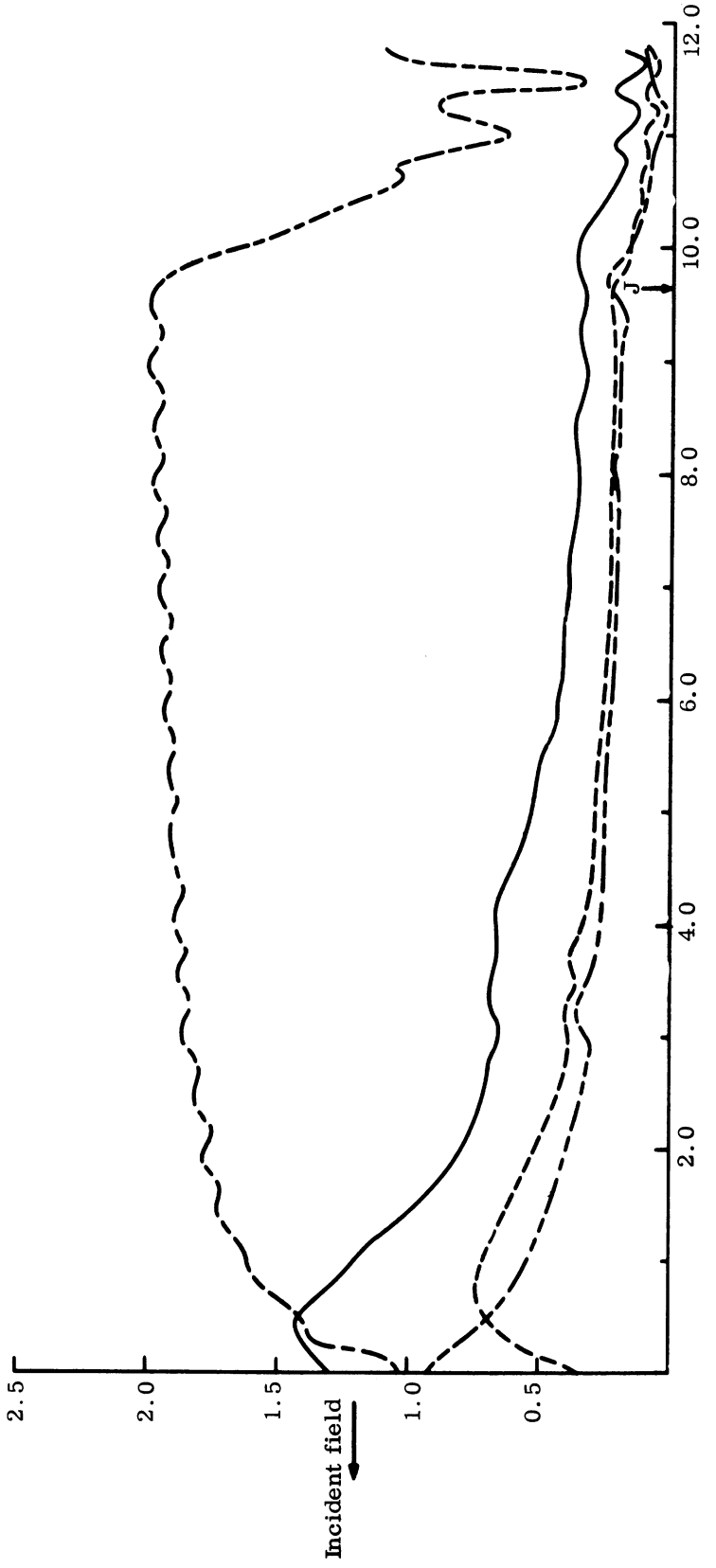

FIG. 3-36: SURFACE FIELD AMPLITUDES $|H_\phi|$ (—), $|E_s|$ (---) AND $|E_\phi|$ (-·-·—) ON RS-X COATED CONE-SPHERE FOR ka=8.0; (-·-·—) INDICATES $|H_\phi|$ FOR BARE MODEL.

(S) Before examining each of the figures in detail, it is desirable to gain an overall impression of the nature of the surface field variation over the cone portion as the electrical size of the body changes.

(S) On a metallic cone-sphere only a radial (normal) electric field can be supported, but on the coated body both an azimuthal and a longitudinal component exist. From a value near unity at the tip, $|E_\phi|$ falls off rapidly and within a short distance reaches a mean value which is almost constant. This distance increases with frequency, but even at the highest frequency, it is less than 2λ compared to a total cone length of (about) 9.6λ.

(S) As the frequency increases there is a marked change in the behavior of the dominant surface field component H_ϕ on the coated body. At the lowest frequency the mean level of $|H_\phi|$ is very similar to that on an uncoated model, at least for distances greater than about 1.5λ from the tip. However, at the next higher frequency the mean of the curve for $|H_\phi|$ on the coated body is similar to that for the uncoated one when $s/\lambda \lesssim 1.0$, but levels out for s/λ around 1.75 and then, for $s/\lambda \gtrsim 2.0$, falls rapidly. At the highest frequency 6.80 Gc, for which ka=8.0, the field component H_ϕ on the coated body is even more suppressed. Though the component starts with a value in excess of that on the uncoated body at the tip, it rises more slowly with increasing s, and its magnitude is comparable to that on the uncoated body for s/λ=0.4. Thereafter, it decreases rapidly out to a distance of 3 wavelengths from the tip. Beyond this, the rate of fall-off is somewhat less, and for $s/\lambda \gtrsim 5$ the field component H_ϕ is almost constant even to the shadow boundary.

(S) The longitudinal electric component E_s parallels the azimuthal magnetic component at each of the frequencies measured. At the tip the modulus of this component seems to increase with frequency, but even for ka=8.0, it is less than a third of the incident field value.

(S) A more precise comparison of E_s and H_ϕ is provided by Figs. 3-37 and 3-38 which show the graphically-deduced ratios of $|E_s/H_\phi|$. For ka=3.0 the ratios are plotted in quarter wavelength intervals for the cone portion forward of the join

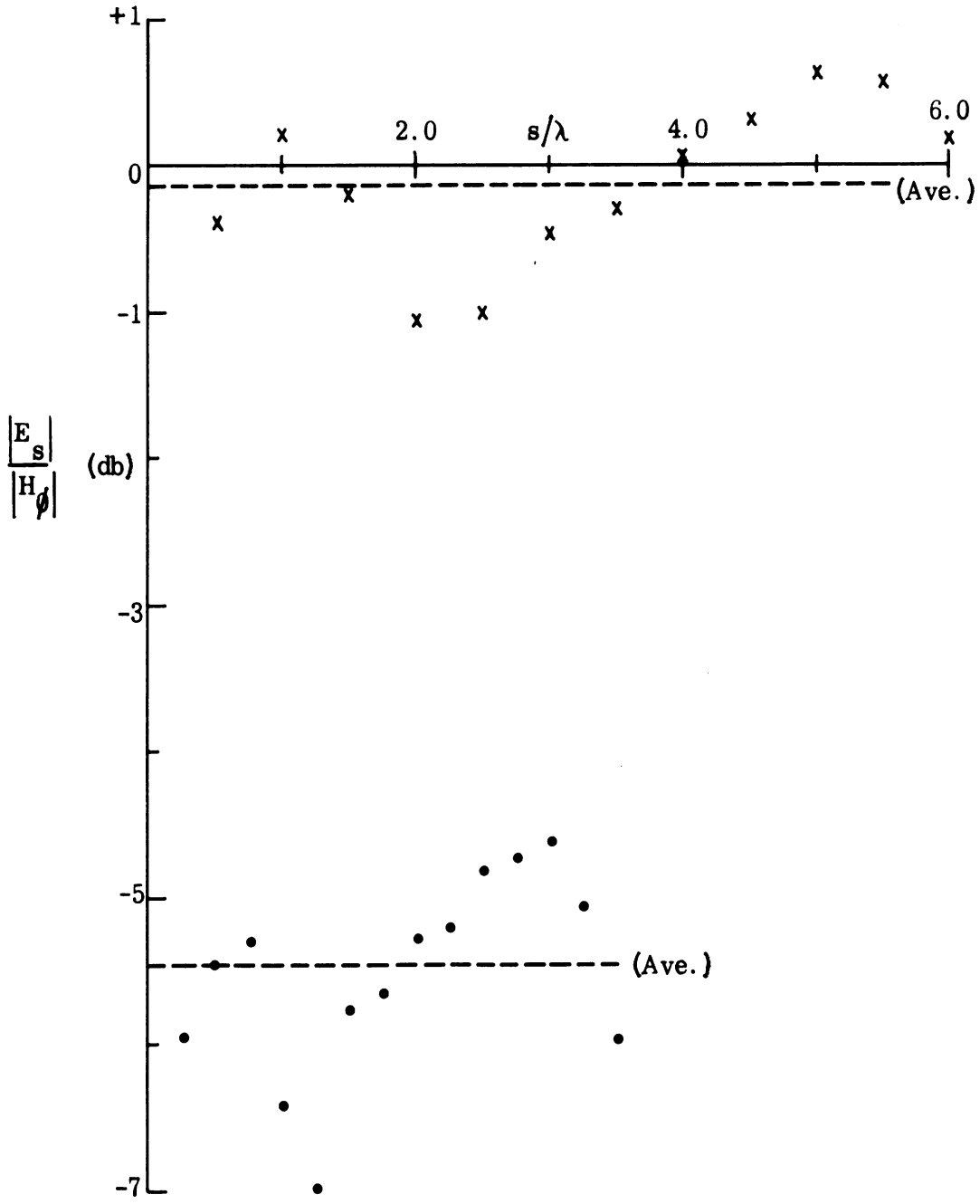

FIG. 3-37: MEASURED RATIOS OF SURFACE FIELD AMPLITUDES ON RS-X COATED CONE-SPHERES FOR ka=3.0 (···) AND ka=5.0 (xxx).

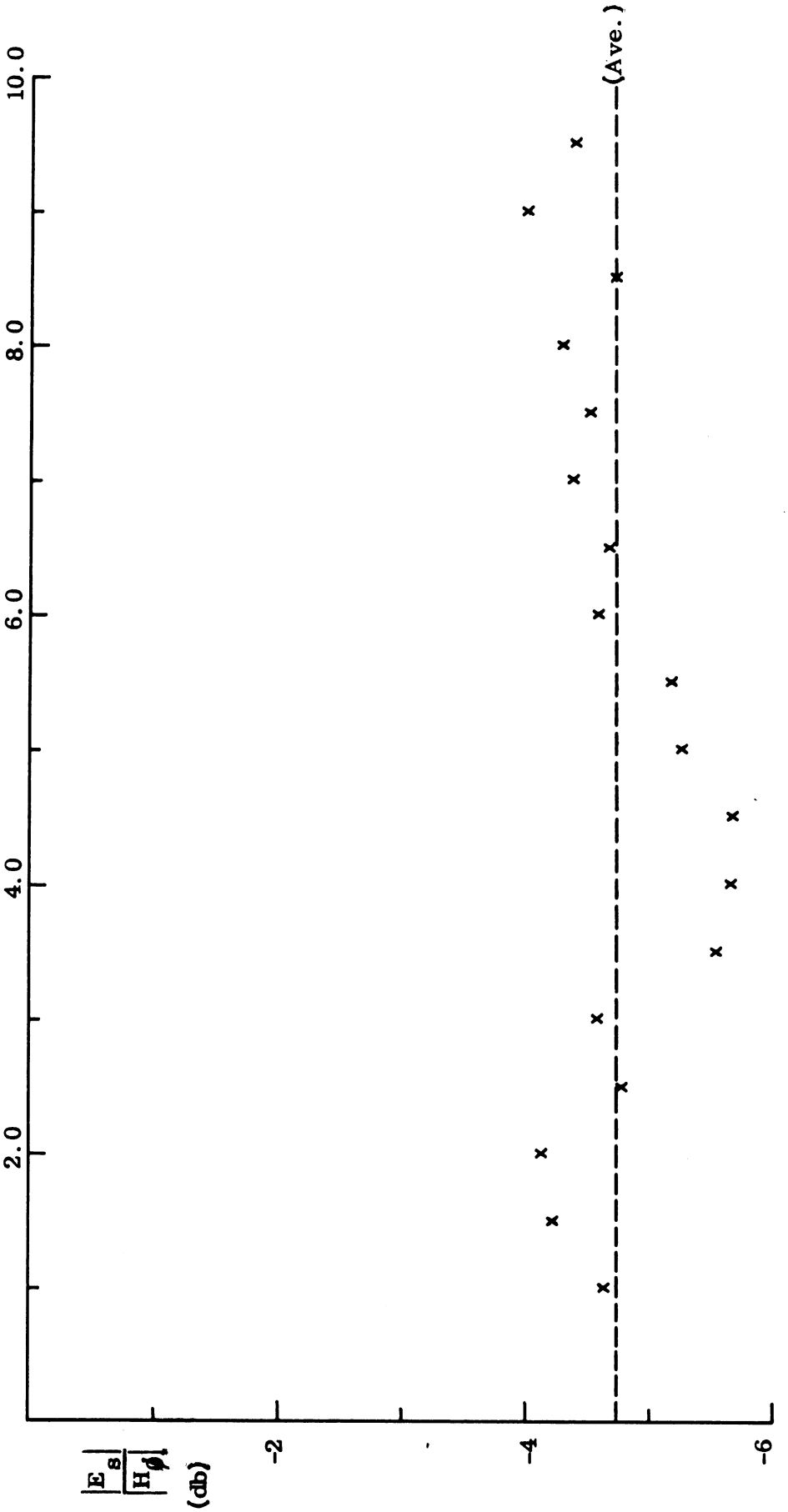

FIG. 3-38: MEASURED RATIOS OF SURFACE FIELD AMPLITUDES ON RS-X COATED CONE-SPHERE WITH ka=8.0.

and not too near the tip. For this region the ratios oscillate within $\pm$ 1 db of the average value -5.46 db (= 0.533). It is interesting to compare this average with the one obtained earlier from the surface field measurements on the illuminated side of an RS-X coated sphere at 2.348 Gc, namely 0.432 ± 0.025. Figure 3-37 also shows the ratio at a frequency of 4.25 Gc plotted in half-wavelength intervals. For this case the numerical values have less than 1 db spread about the average -0.14 db (= 0.984). Figure 3-38 contains the ratio determined for the highest frequency (6.8 Gc) in half wavelength intervals for $0.5 \leqslant s/\lambda \leqslant 9.5$. The spread is again less than 1 db about the average -4.72 db (= 0.581).

(S) The moduli of the bulk impedance obtained from transmission line measurements of the RS-X material at the above three frequencies are (respectively) 0.580, 0.520 and 0.549, but because of the small electrical thicknesses of the coatings, it is expected that Eq. (3.8) rather than (3.6) must be used to compute the expected surface impedance. The resulting values for $|\eta_{eff}|$ at the three frequencies are 0.250, 0.374 and 0.636, and though these are not in particularly good agreement with the measured ratios, some general comments are in order: (1) the agreement is best at the highest frequency (as expected), but the fact that the bulk impedances give almost as close a fit as the ones in which the layer thickness is taken into account suggests some non-uniformity of the coatings in depth; (2) the failure is inexplicably marked at the middle frequency, and (3) the small amplitude oscillations of the measured ratios are indicative of a transverse curvature effect.

(S) A considerable number of coatings were investigated (a complete list of which appears in Table II-1) and the general features of the surface fields found for other coatings exhibit correspondences with two prominant RS-X coating characteristics:

(1) The dominant H_ϕ component gradually changes from a behavior similar to that on an uncoated cone-sphere at low frequencies, to a component which is still dominant, but which decreases away from the tip, at intermediate frequencies. At

still higher frequencies the decrease in $|H_\phi|$ is rapid within a few wavelengths of the tip, but thereafter it maintains an appreciably constant value below which it does not fall. It is this fact that suggests that the mechanism responsible for the decay of $|H_\phi|$ with both frequency and s/λ is not a progressive energy absorption on the cone sides, but is instead intrinsically related to the transverse radius of curvature.

(2) The longitudinal electric field component is roughly proportional to the azimuthal magnetic component, with a proportionality factor which is substantially independent of s at distances of more than one or two wavelengths from the tip. With most coatings the factor is in satisfactory agreement with that computed from the known properties of the coating, but there are individual cases (e.g. the RS-X coating at 4.25 Gc) where marked (and so far inexplicable) discrepancies appear.

(S) Two sets of surface field data measured on a metallic cone-sphere with half angle $7\text{-}1/2^{\circ}$ and base radius 1.500", coated with a 3/8" layer of Eccosorb-CR (casting resin) absorber, serve to illustrate the behavior of some of the other coatings. The remarks made concerning the important characteristics of coated surface fields are borne out by an inspection of Figs. 3-39 and 3-40 which contain the data for frequencies 3.757 and 6.26 Gc, corresponding to ka=3.0 and 5.0 respectively. We note in passing that at the lower frequency the average ratio $|E_s| / |H_\phi|$ at distances of more than 1.25λ from the tip is about 0.8, compared with the value 0.611 computed from Eq. (3.8), but at the higher frequency, the measured value is in excellent agreement with the computed one of 0.455.

(S) The surface field data for the two models shown is typical of the results of all our other coated cone-sphere measurements. It will be noted in particular that beyond a certain distance (of order λ) from the tip, the field diminishes with increasing distance and then, if the cone is long enough, levels out. Such a decrease would occur were the field on the surface similar to a surface wave which is progressively attenuated as it proceeds up the sides of the cone. The measured rates of attenuation are, however, incompatible with those expected from the known electrical constants of the surface, as is the fact that the decrease does not continue

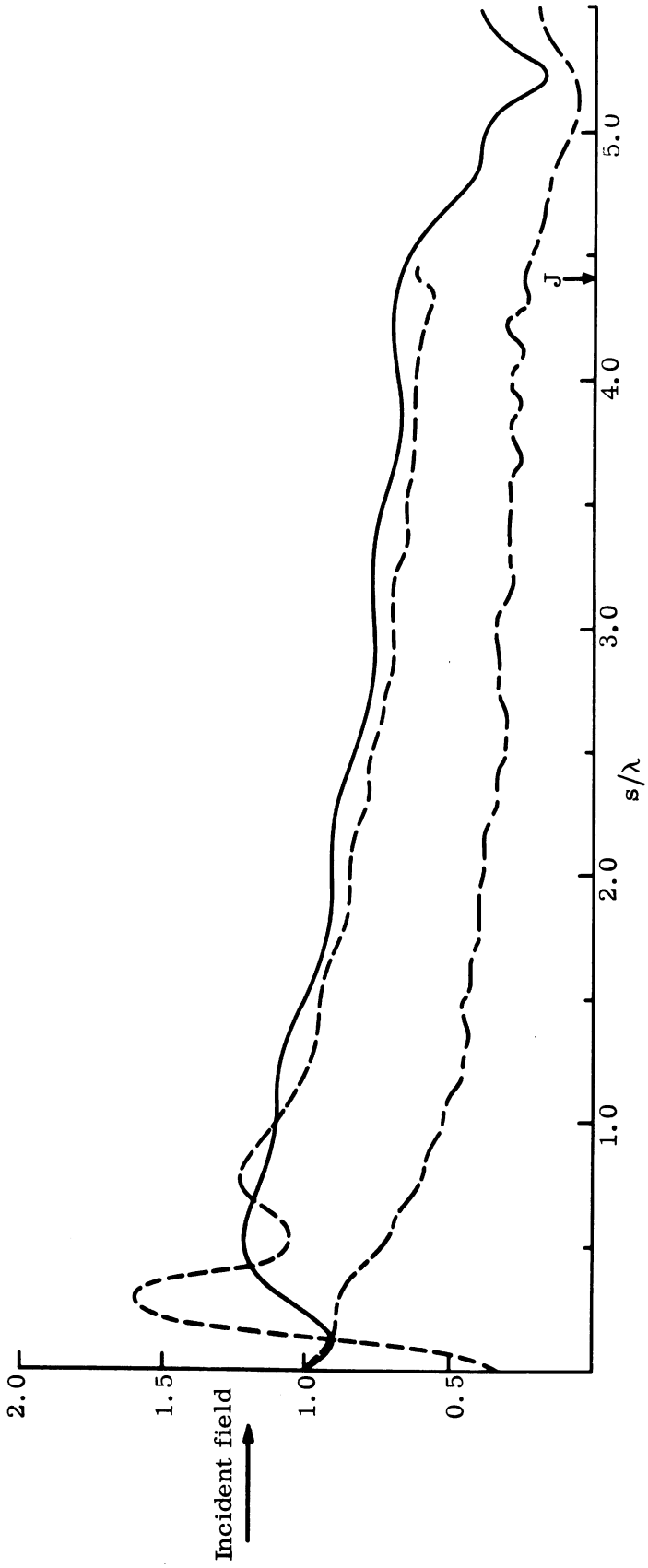

FIG. 3-39: SURFACE FIELD AMPLITUDES $|H_\phi|$ (—), $|E_s|$ (- - -) AND $|E_\phi|$ (—·—) ON ECCOSORB COATED CONE-SPHERE FOR ka=3.0.

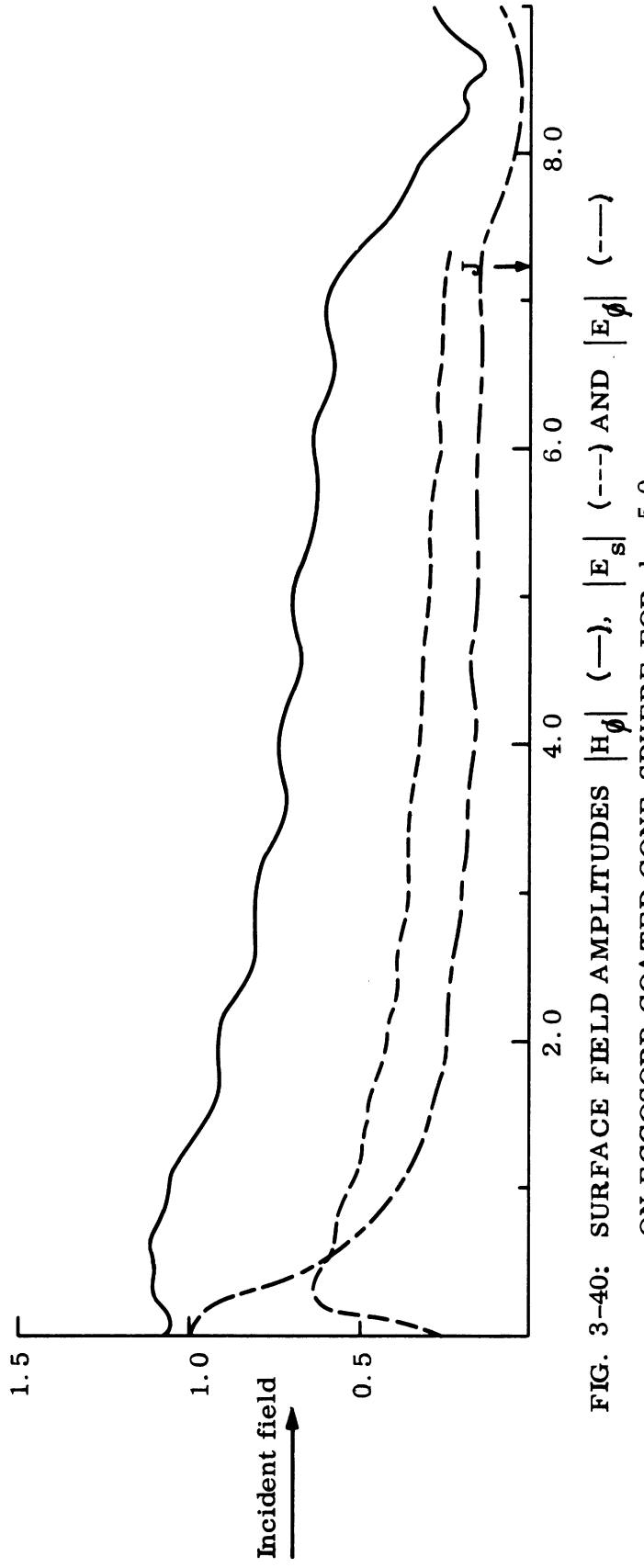

FIG. 3-40: SURFACE FIELD AMPLITUDES $|H_\phi|$ (—), $|E_s|$ (---) AND $|E_\phi|$ (—·—) ON ECCOSORB COATED CONE-SPHERE FOR ka=5.0.

indefinitely. Indeed, the levelling-out that occurs was one of the items that led us to conclude that any surface wave attentuation was irrelevant as regards the bulk of the surface field reduction observed, and to hypothesize that the transverse radius of curvature of the surface was the most important factor affecting the field behavior.

(S) A test of this hypothesis was provided by an experiment involving oblique, rather than nose-on, incidence, the geometry of which is shown in Fig. 3-41. The model was a cone-sphere with half angle $7\text{-}1/2^{o}$ and base radius 1.500", covered with a 3/8" layer of Eccosorb-CR coating. Measurements were made of the modulus of the H_{ϕ} component along the illuminated and shadowed sides at a frequency 6.26 Gc (corresponding to ka=5.0), and the data is shown in Fig. 3-42 as a function of the distance s/λ measured from the tip.

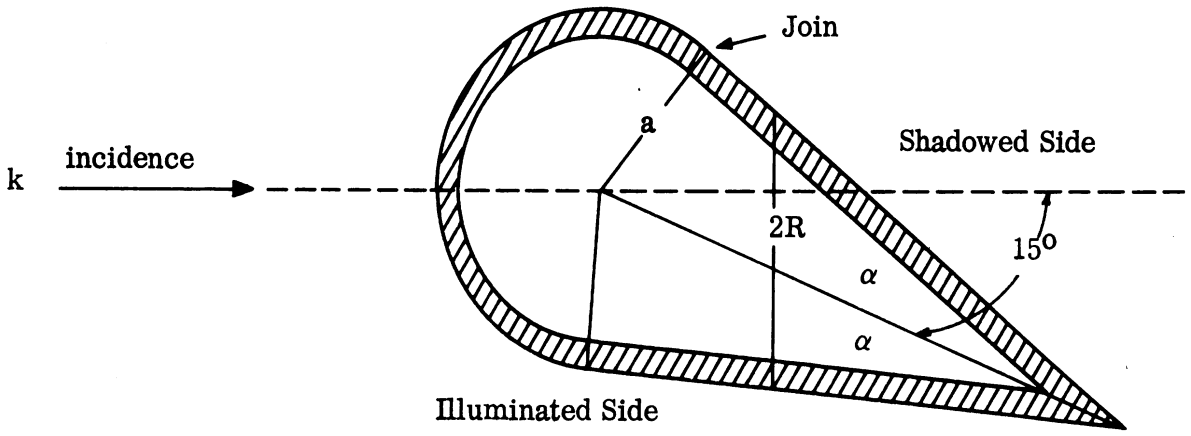

FIG. 3-41: OBLIQUE INCIDENCE GEOMETRY (TOP VIEW)

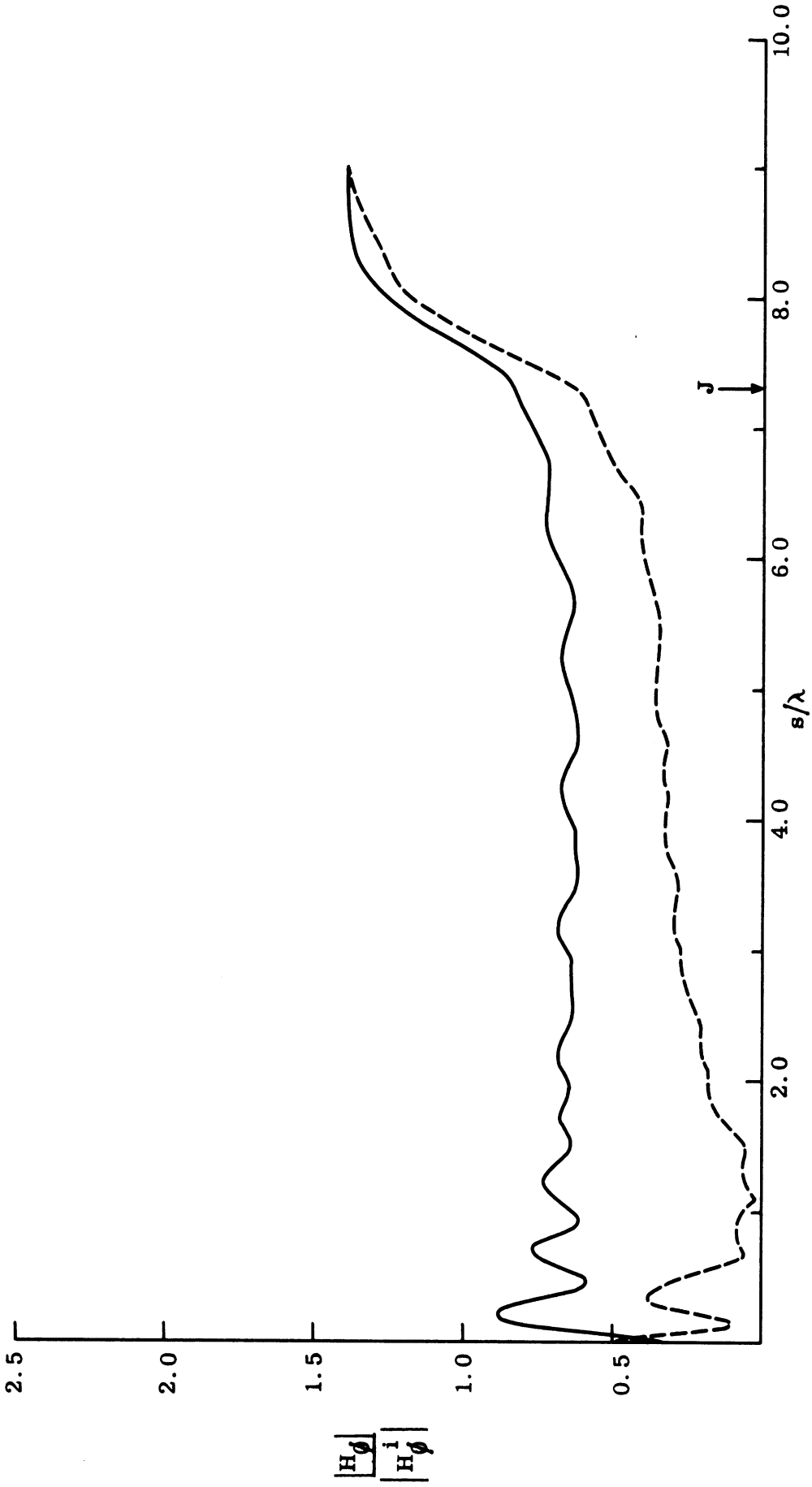

FIG. 3-42: MEASURED SURFACE FIELD COMPONENT $|H_\phi|$ FOR OBLIQUE INCIDENCE (θ=82-1/2°) ON ECCOSORB-CR COATED CONE-SPHERE WITH ka=5.0: ILLUMINATED SIDE (—) SHADOW SIDE (---).

(S) From Fig. 3-41 it is evident that on the illuminated side of the cone the angle between the surface and the direction of incidence for oblique illumination is the same ($7\text{-}1/2^{o}$) as that between a tangent to the surface and the incident field for the case of nose-on incidence. Hence, if the assumption regarding the effect of the transverse curvature is correct, the field on the illuminated side and just beyond (i.e. on the tip side) of the join should have the same amplitude as it had at that same point when the incidence was nose-on, and as we move toward the tip, that amplitude should not show any of the progressive reduction typical of the attenuation of a surface wave. Were the amplitude to re-trace the curve appropriate to nose-on incidence, it would, of course, increase with increasing distance of travel (i.e. decreasing s/λ), but since that would imply an increase of energy, our expectation was that the amplitude would remain sensibly constant. Figure 3-42 shows this to be true, and if we discount the small initial decrease within a wavelength of the join (almost certainly due to the local effect of the discontinuity), the field shows only a small amplitude oscillation about a mean level which is independent of s/λ, and indistinguishable from that at which the amplitude for nose-on incidence 'bottomed-out'. Even the oscillations are predictable in terms of a traveling wave reflection at the tip.

(S) The qualitative agreement between the surface field data for cone-spheres and the behavior expected on the basis of the local dependence on transverse curvature led to a search for an appropriate mathematical model from which to determine the quantitative dependence of the surface field amplitude on radius and coating parameters. As indicated in Section 3.5.1, several models were considered, from which two were singled out for detailed study. Both involved right circular cylinders of infinite length illuminated by a plane wave at oblique incidence, but whereas the first one had an impedance boundary condition imposed at its surface, the second was a metallic cylinder coated with a layer of material whose electric constants and thickness were arbitrary. In each case an exact solution for the boundary value problem was obtained, and the resulting expressions for the amplitudes and phases

of the field components at the surface were programmed for digital computation, thereby permitting the rapid calculation of the fields as function of the radius of the cylinder for specified values of the parameters governing the nature of the surface.

(S) The ultimate goal of these investigations was, of course, the quantitative determination of the surface fields as a function of position along the sides of a coated cone-sphere. To use the cylinder computations for this purpose requires us to relate the local curvature of the cone to that of the cylinder. One possible* geometrical identification is shown in Fig. 3-43, from which we have

$$\frac{s}{\lambda} = \frac{1}{2\pi} \cot \alpha \, kR \, , \qquad (3.12)$$

where R is the radius of the cylinder appropriate to the local geometry of the cone at a distance s from its tip.

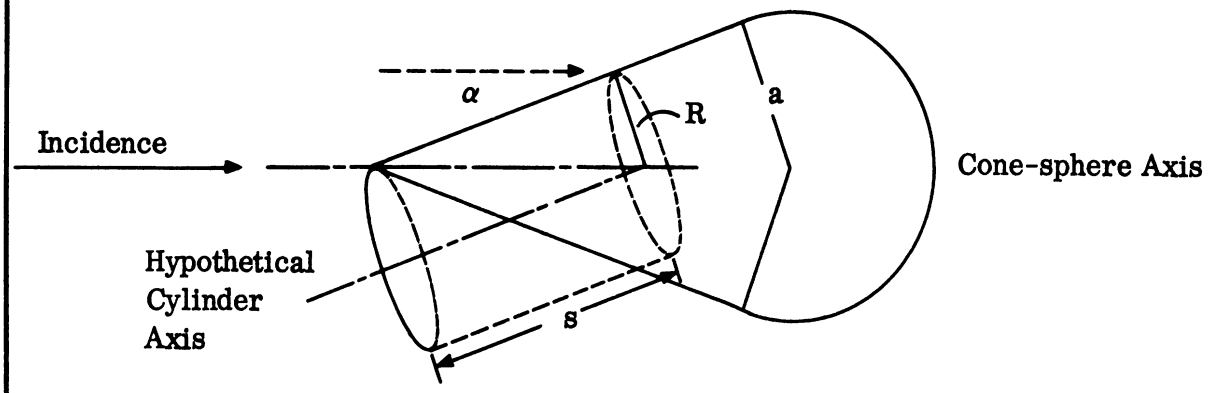

FIG. 3-43: GEOMETRY OF CYLINDER IDENTIFICATION

*When α is small, the numerical relation between s/λ and kR is almost the same regardless of the particular identification chosen.

(S) Typical of the cylinder data obtained is that shown in Fig. 3-44 in which $|H_\phi|$ is plotted as a function of kR for a layered cylinder illuminated at an angle $7\text{-}1/2^\circ$ from grazing. The thickness and electrical parameters of the layer are those corresponding to the Eccosorb-CR coating at a frequency of 6.0 Gc. The curve shown as a broken line in Fig. 3-44 is a 'graphical' mean through the oscillations of the exact values, and by virtue of its averaging over adjacent values of the cylinder radius, it could well be more appropriate to a body, such as the cone, whose radius changes continuously.

(S) With the identification shown in Eq. (3.12), the exact computed data in Fig. 3-44 can be used to predict the amplitude of the surface field component H_ϕ on the Eccosorb coated cone-sphere viewed at nose-on incidence or, alternatively, on the illuminated side when viewed at $82\text{-}1/2^\circ$ from nose-on. For convenience the latter case has been chosen, and in Fig. 3-45 we have superimposed the computed points on the experimental curve taken from Fig. 3-40. Quantitatively, the comparison is not an advantageous one, as is otherwise evident from the fact that the theoretical curve has the features appropriate to nose-on incidence on the cone, and the experimental curves for $\theta = 0$ and $\theta = 82\text{-}1/2^\circ$ are quite distinct in character. Thus, for example, the theoretical curve has two marked oscillations (which are, however, somewhat suppressed if the empirical 'mean' curve in Fig. 3-44 is employed) and rises to a peak value 1.86 for s just less than $\lambda/2$, whereas the experimental values are almost constant apart from the smaller oscillations attributable to a traveling wave reflection. On the other hand, the theoretical values close to the join of the cone and sphere are quite remarkably accurate. This is typical of most of the comparisons that have been carried out and, as remarked earlier, this is one of the more important regions for estimating the back scattering behavior.

(S) In Fig. 3-45, the region $s/\lambda \geqslant 7.3$ corresponds to the spherical portion of the body. This is entirely illuminated when $\theta = 82\text{-}1/2^\circ$, and in the expectation that the component H_ϕ will behave as a constant multiple of its amplitude on a metallic sphere of the same radius, values taken from the computations of Ducmanis and

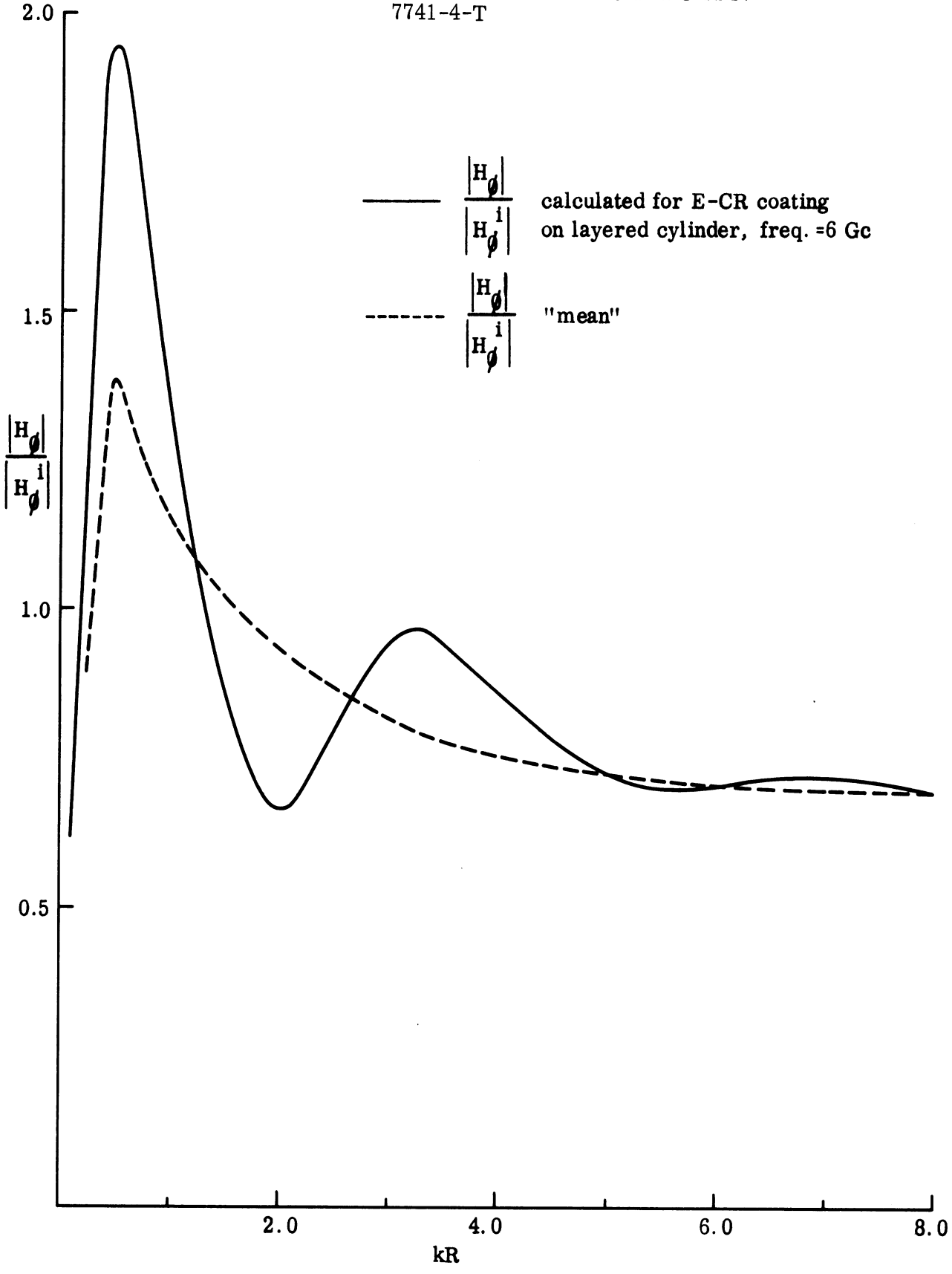

FIG. 3-44: COMPUTED SURFACE FIELD COMPONENT $|H_\phi|$ FOR ECCOSORB-CR LAYERED CYLINDER AT 6.0 Gc, WITH INCIDENCE 7-1/2° FROM GRAZING.

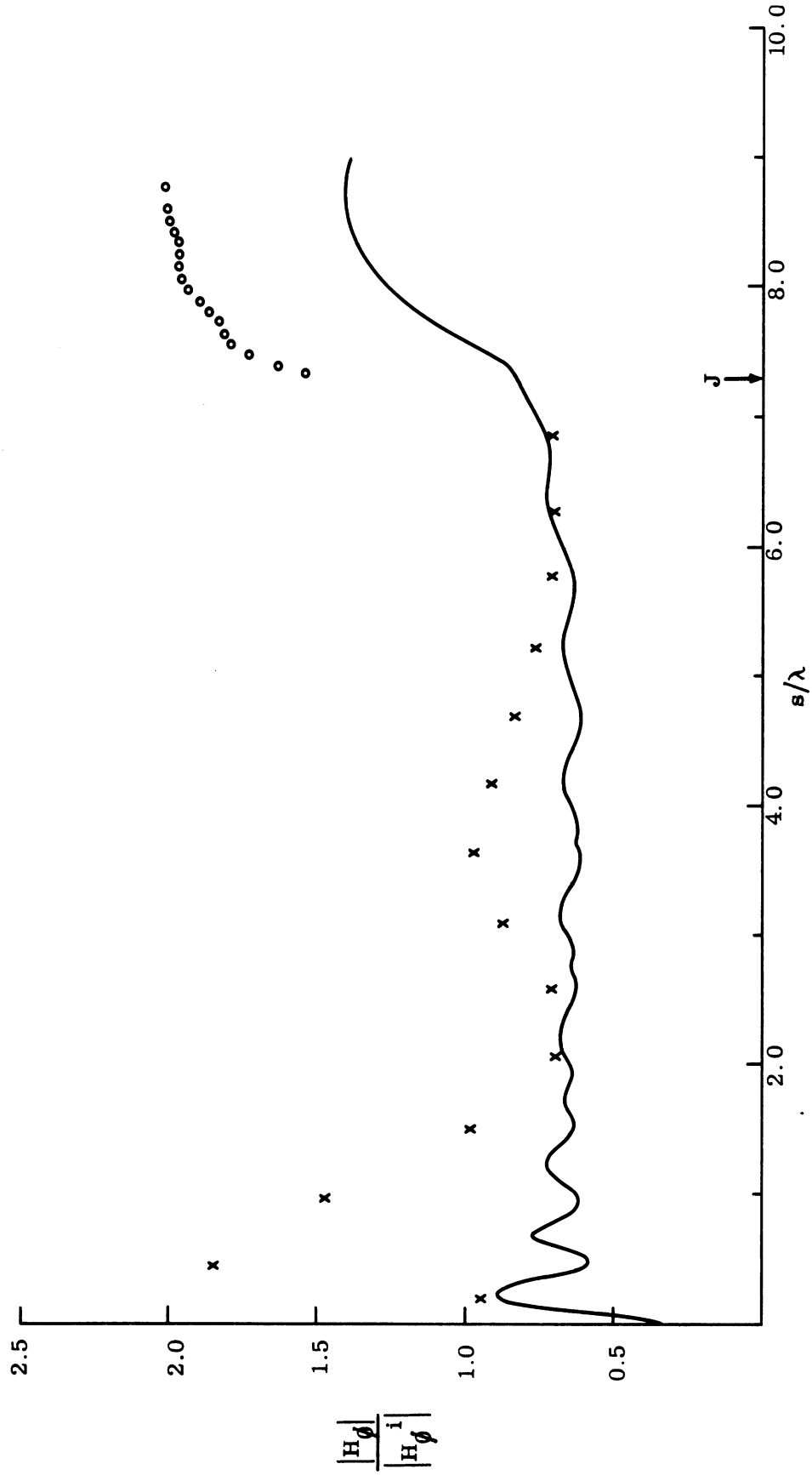

FIG. 3-45: MEASURED AMPLITUDE OF COMPONENT H_ϕ (—) ON ECCOSORB-CR COATED CONE-SPHERE FOR ka=5.0 AND θ=82-1/2° COMPARED WITH THEORY: CYLINDER PREDICTIONS (xxx), METALLIC SPHERE VALUES (θoo). (see text)

Liepa (1965) have been included. If, following our original notation, we denote the metallic sphere component by T_2, we observe that the experimental curve follows closely the trends indicated by T_2 and, indeed, the ratio of the two at corresponding points is relatively constant over the spherical portion of the cone-sphere. This is expected based on the elementary concept of the reduction of the field amplitude by the Fresnel reflection coefficient of the surface. Since $|\eta_{eff}| = 0.4563$ for the Eccosorb-CR coating at 6 Gc, the factor by which $|T_2|$ is reduced should be 0.69, which is in good agreement with the value 0.62 obtained from the average ratio of the two curves in Fig. 3-45.

(S) The mean surface field levels predicted on the basis of a layered cylinder model (an infinite metallic cylinder coated with a single finite layer of non-metallic material) have been computed for various coatings and frequencies. The results are generally in good agreement with the moduli actually observed for positions on the coated cone-sphere in the vicinity of the join. Figures 3-46 through 3-48 contain typical examples.

(S) In Fig. 3-46 are shown the results of calculations for the RS-X coated cone-sphere at a frequency =4.25 Gc. The mean modulus of the dominant H_ϕ component measured at the join is (about) 0.75 while that computed on the basis of the layered cylinder model is 0.72 which is within 4 per cent of the former. Even away from the join there is some qualitative agreement between the shape of the experimental and computed curves. The same qualitative shape similarity is found for the E_s component, but the calculated value near the join is about half the measured modulus.

(S) Figure 3-47 contains the surface field data for the RS-X coating at 6.8 Gc. Away from the tip the dominant H_ϕ component is modelled with considerable accuracy, and even near the tip, the shape of the calculated curve is similar to that of the measured one. The same remarks apply to the E_s component.

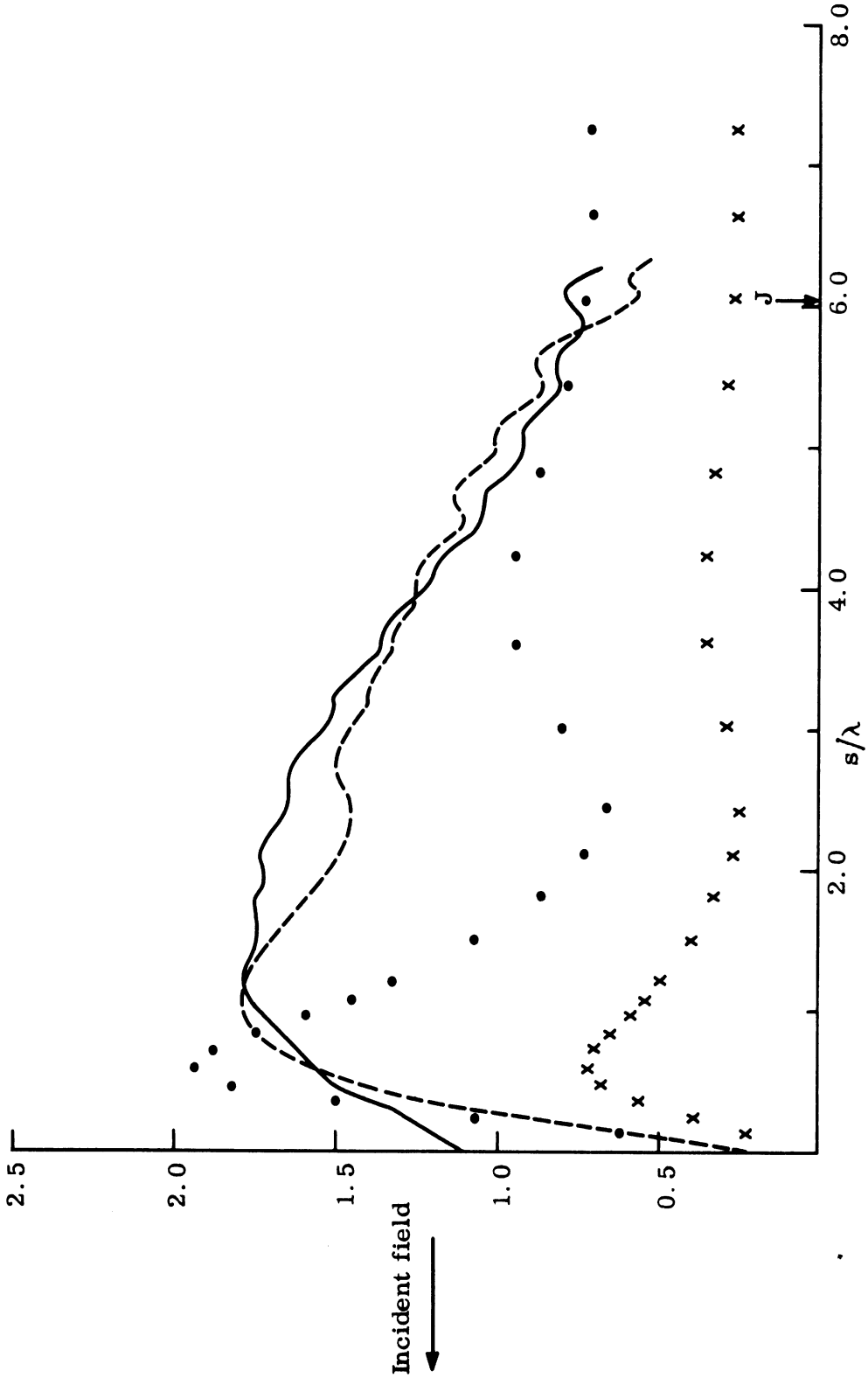

FIG. 3-46: MEASURED AMPLITUDES OF SURFACE FIELD COMPONENTS H_ϕ (—) AND E_s (---) ON RS-X COATED CONE-SPHERE FOR ka=5, COMPARED WITH LAYERED CYLINDER PREDICTIONS (•••, xxx).

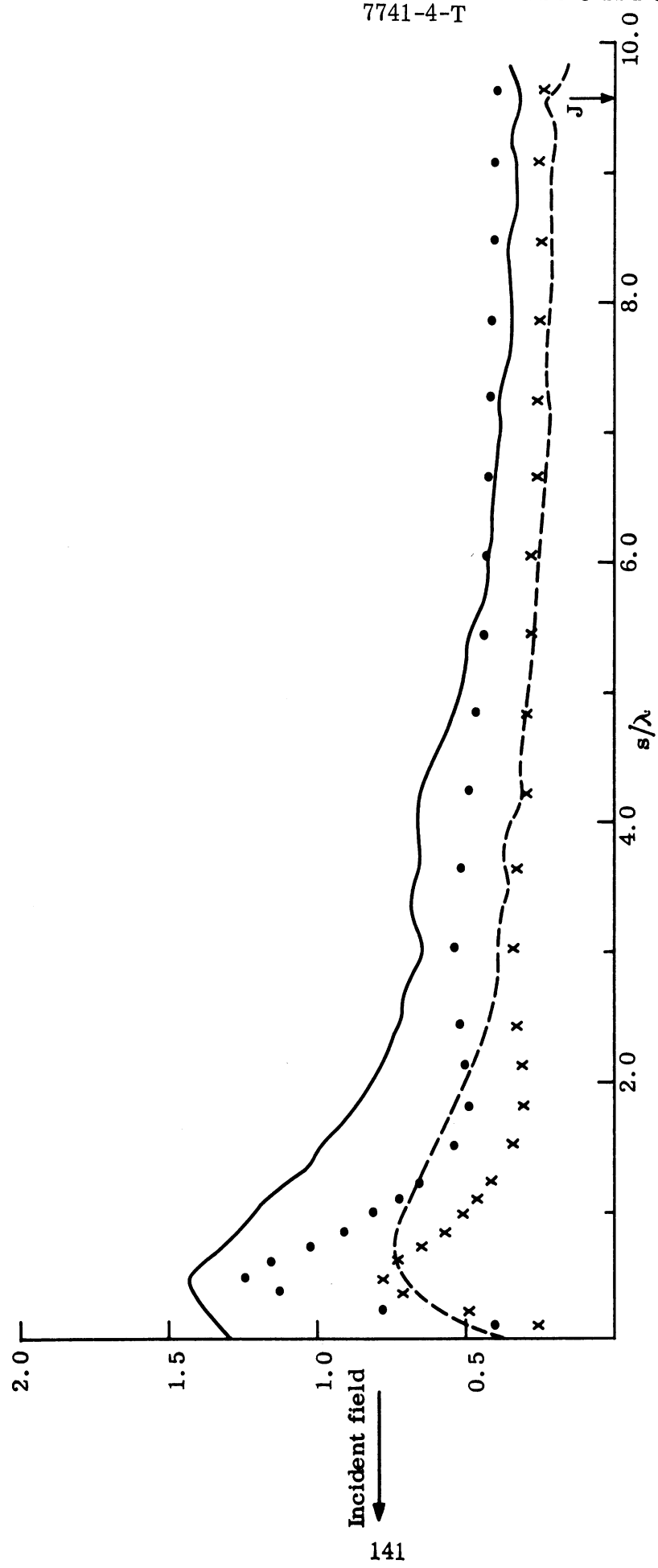

FIG. 3-47: MEASURED AMPLITUDES OF SURFACE FIELD COMPONENTS H_ϕ (—) AND E_s (---) ON RS-X COATED CONE-SPHERE FOR ka=8.0, COMPARED WITH LAYERED CYLINDER PREDICTIONS (•••, xxx).

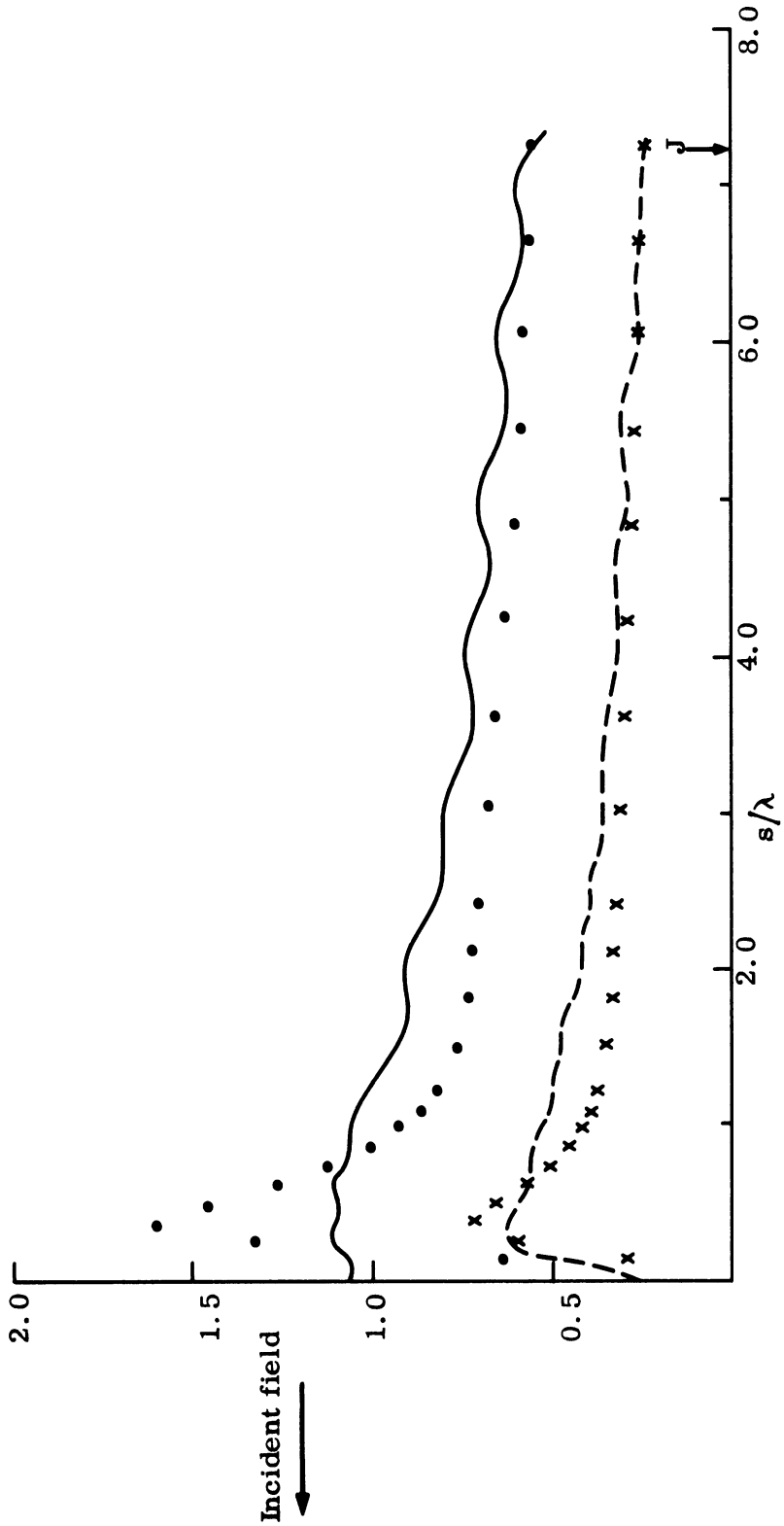

FIG. 3-48: MEASURED AMPLITUDES OF SURFACE FIELD COMPONENTS H_ϕ (—) AND E_s (---) ON ECCOSORB-CR COATED CONE-SPHERE FOR ka=5.0, COMPARED WITH LAYERED CYLINDER PREDICTIONS (•••, xxx).

(S) Figure 3-48 illustrates the data for the Eccosorb-CR coating at 6 Gc. Just as for the RS-X coating at the higher frequency, the agreement between the measured and calculated H_ϕ and E_s components is substantially better at the higher frequency, especially for distances greater than a wavelength from the tip. In fact, at the join, the calculated moduli ($|H_\phi| = 0.57$, $|E_s| = 0.25$) virtually coincide with the measured values.

(S) From the RS-X and Eccosorb-CR calculations shown here, as well as from the applications of the theoretical model to other coatings, certain general features are found: (1) Calculations of the surface field components based upon a layered cylinder model are virtually indistinguishable from those determined from a simulation in which an effective impedance (i.e. Eq. 3.8) boundary condition holds on the surface of a metallic cylinder. (2) For the dominant H_ϕ component on coated cone-spheres, the layered cylinder model generally gives good results for the mean level at sufficient distances from the tip. As the incident frequency increases, the calculated moduli of H_ϕ reproduce the measured values for increasingly larger segments of the cone portion. (3) The relation of E_s to H_ϕ through an impedance boundary condition has its experimental counterpart and the same remarks apply for calculations of the E_s coated cone-sphere component by means of a layered cylinder model as obtain for calculations of the H_ϕ component. (4) Calculated values of the E_ϕ component are often somewhat below those actually measured but since this component is important only for the cross-polarized contribution to the back scattering cross section, the underestimate is not regarded as serious.

(S) Estimates of the surface field based on a layered cylinder model involve extensive computations. When the effective impedance can be simply represented by Eq. (3.8) it is possible to obtain asymptotic estimates for the surface field components from consideration of the limiting case $ka \longrightarrow \infty$. This corresponds to a situation in which the radius of curvature becomes so large that the surface may be locally approximated by a plane. The case of an infinite conducting plane, illuminated

obliquely, and subject to an impedance boundary condition is readily solved and yields algebraic expressions for the surface field components (see p. 3-68, Section 3.5.1). From its asymptotic nature, these estimates should improve with increasing frequency. However, for the cone-sphere investigations, even in the vicinity of the join where the local radius of curvature is greatest, the estimates thus deduced can be expected to be inferior to those obtained from the layered cylinder model.

(S) A third model coating considered in this section is provided by a 0.249" layer of LS-24 absorber which covers a metallic cone-sphere whose half angle is $7\text{-}1/2^{o}$ and whose base radius is 2.210". Surface field measurements were made for this model (called D-12) at four frequencies, for two of which the data is shown in Figs. 3-49 and 3-50. At the lower frequency (2.549 Gc, corresponding to ka=3.0) the behavior is characteristic of other low frequency measurements for coated bodies, viz. the H_{ϕ} component is similar to that found on a pure metal cone-sphere of the same size and the E_s component runs considerably below, but generally parallel to, the H_{ϕ} component along the cone sides. At the higher frequency (4.25 Gc, corresponding to ka= 5.0) the typical decay in modulus of the H_{ϕ} component relative to its pure metal cone-sphere levels can be seen along the cone sides. The E_s component again follows a similar pattern and, though smaller in amplitude, also decreases as the join is approached.

(S) The purpose of including those two otherwise ordinary experimental patterns is to provide a basis for comparison when the coating over the rear spherical cap is not uniform. Three different terminations (D-12a, D-12b and D-12c) were constructed from the basic D-12 model and their geometry is shown in Fig. 2-4.

(S) Models D-12b and D-12c each have a 0.249" thick coating of LS-24 absorber along the cone portion out to the join. Over the spherical cap, the coating on Model D-12b continues out to a distance of 1.5" beyond the join, after which it ceases. The termination is not a smooth one, but consists of an indented (with

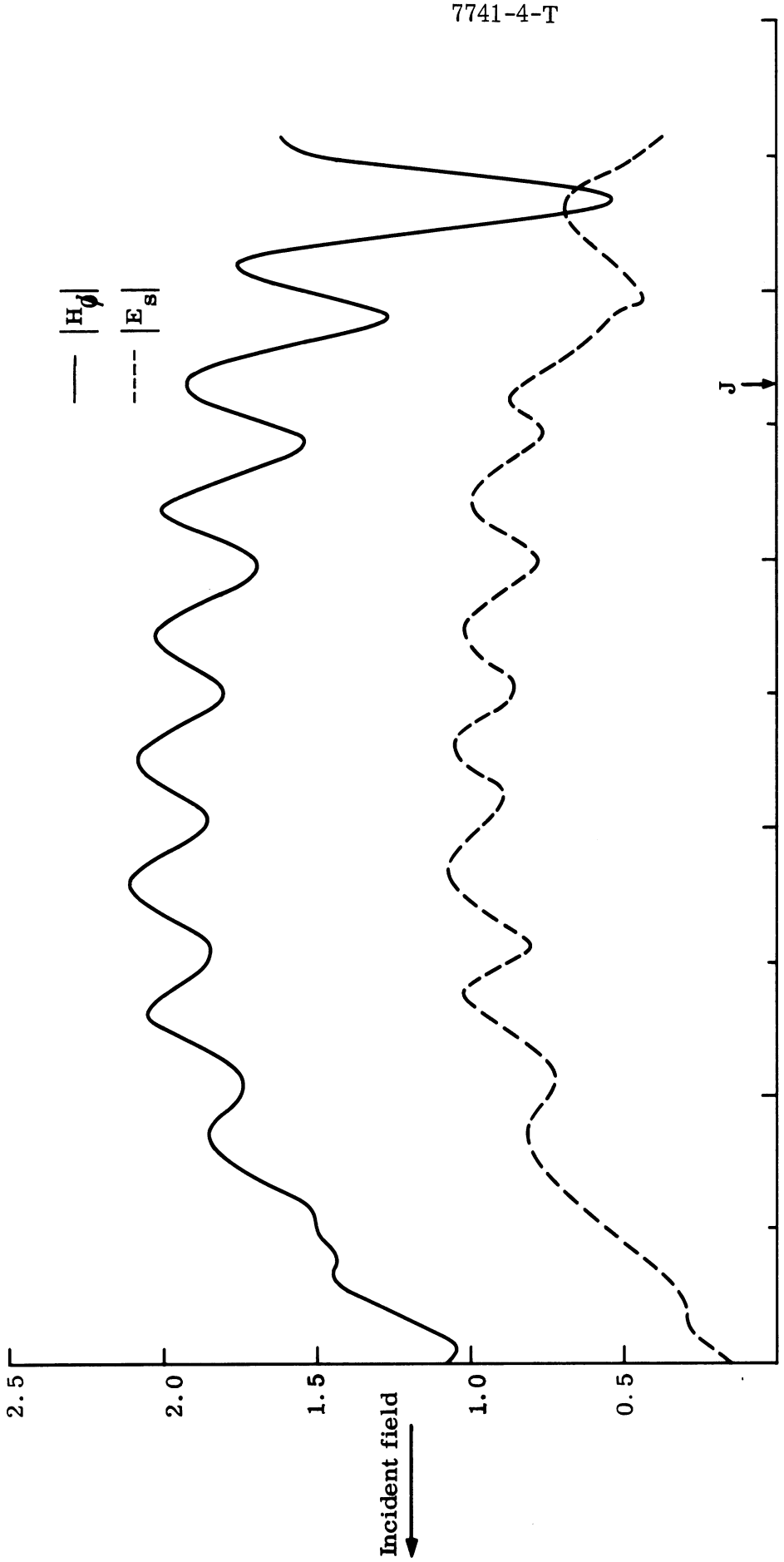

FIG. 3-49: SURFACE FIELD AMPLITUDES $|H_\phi|$ (—) AND $|E_s|$ (---) ON LS-24 COATED CONE-SPHERE FOR ka=3.0.

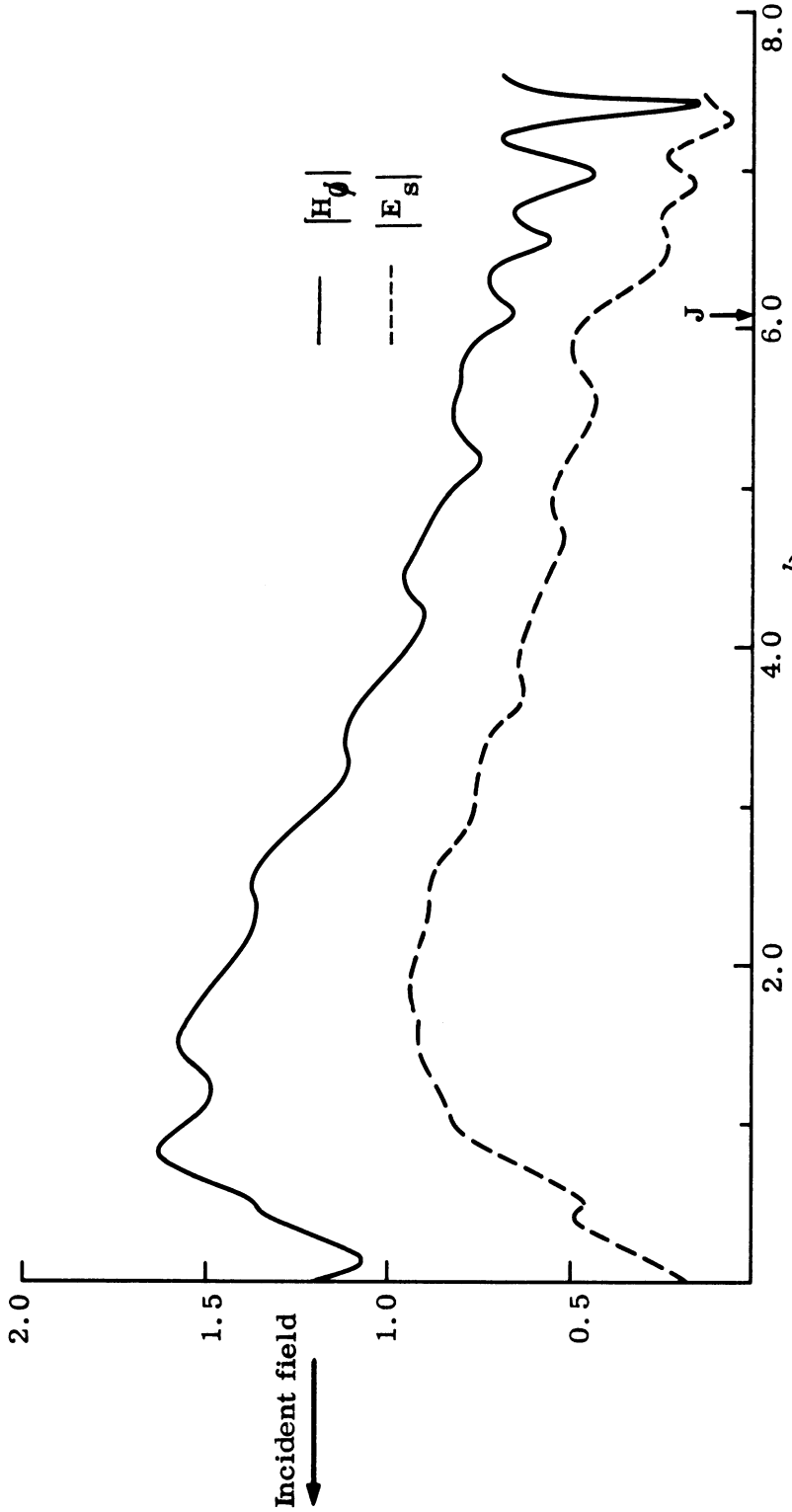

FIG. 3-50: SURFACE FIELD AMPLITUDES $|H_\phi|$ (—) AND $|E_s|$ (---) ON LS-24 COATED CONE-SPHERE FOR ka=5.0.

respect to the maximum 1.5" extension) serrated edge - much in the manner of a partly-peeled orange. On the other hand, for model D-12c, the termination of the coating 1.5" beyond the join is not only smooth, but is also tapered so that its thickness diminishes as the coating termination is approached. Model D-12a has the same coating characteristics as D-12b with one exception: instead of a pointed tip, the coating is rounded so that the nose is a portion of a sphere whose radius is equal to that of the coating thickness (approx. 1/4").

(S) The data for the azimuthal magnetic field component on Models D-12b and D-12c is shown for a frequency 2.55 Gc (ka=3.0) in Fig. 3-51 and for a frequency 4.2499 Gc (ka=5.0) in Fig. 3-52. Although not included, the data for D-12a is quite similar. The experiments indicate that as long as the coating is present on the cone sides, modifications to the coating over the rear cap have little effect on the surface field except on the rear cap itself. Whatever differences do exist in the surface fields do not appear to be systematic and are more naturally attributable to slight changes in calibration and/or positioning. Moreover, a comparison with the data for the fully-covered Model D-12 (see Figs. 3-49 and 3-50) shows that none of these terminations changes to any significant extent the field supported by the portions of the body covered by the absorber, and consequently the back scattering cross sections for the three modified models investigated here should be indistinguishable from the cross section for the original Model D-12.

(S) Yet another investigation was concerned with the surface field supported on a metallic body with a multi-layered coating. In this case the object consisted of a pure metallic cone-sphere with half angle $7\text{-}1/2^{\circ}$ and base radius 1.500" covered by a 3/8" coating of Eccosorb-CR absorber. An additional 1/16" layer of Teflon covers the cone portion and provides a double layer in this region.

(S) Measurements of the azimuthal magnetic and longitudinal electric surface field components were obtained at four frequencies spanning the range 1.25 to 10.02 Gc. This corresponds to ka between 1.0 and 8.0.

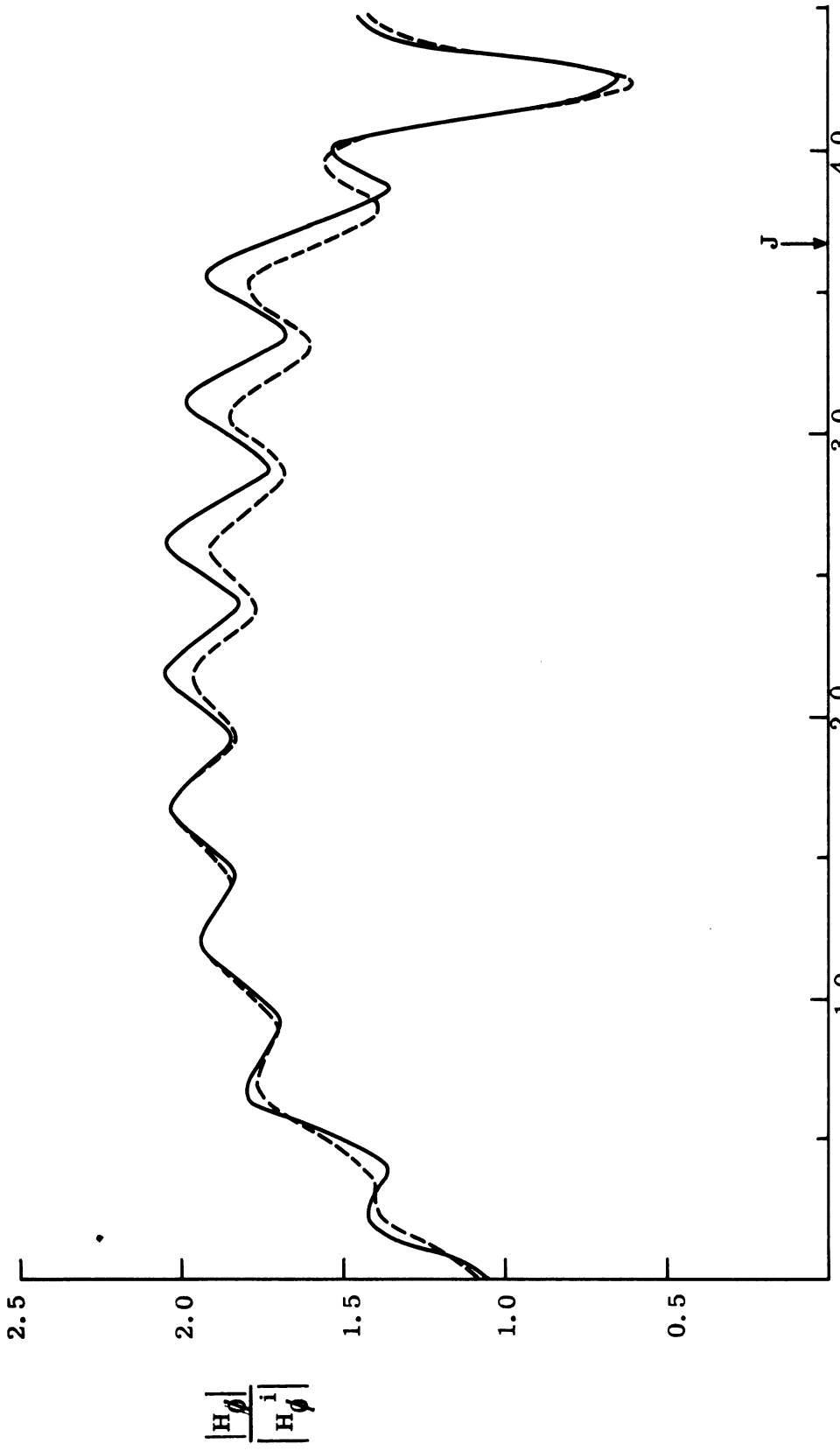

FIG. 3-51: SURFACE FIELD AMPLITUDES $|H_\phi|$ FOR D-12b (—) AND D-12c (---) ON LS-24 COATED CONE-SPHERE FOR ka=3.0.

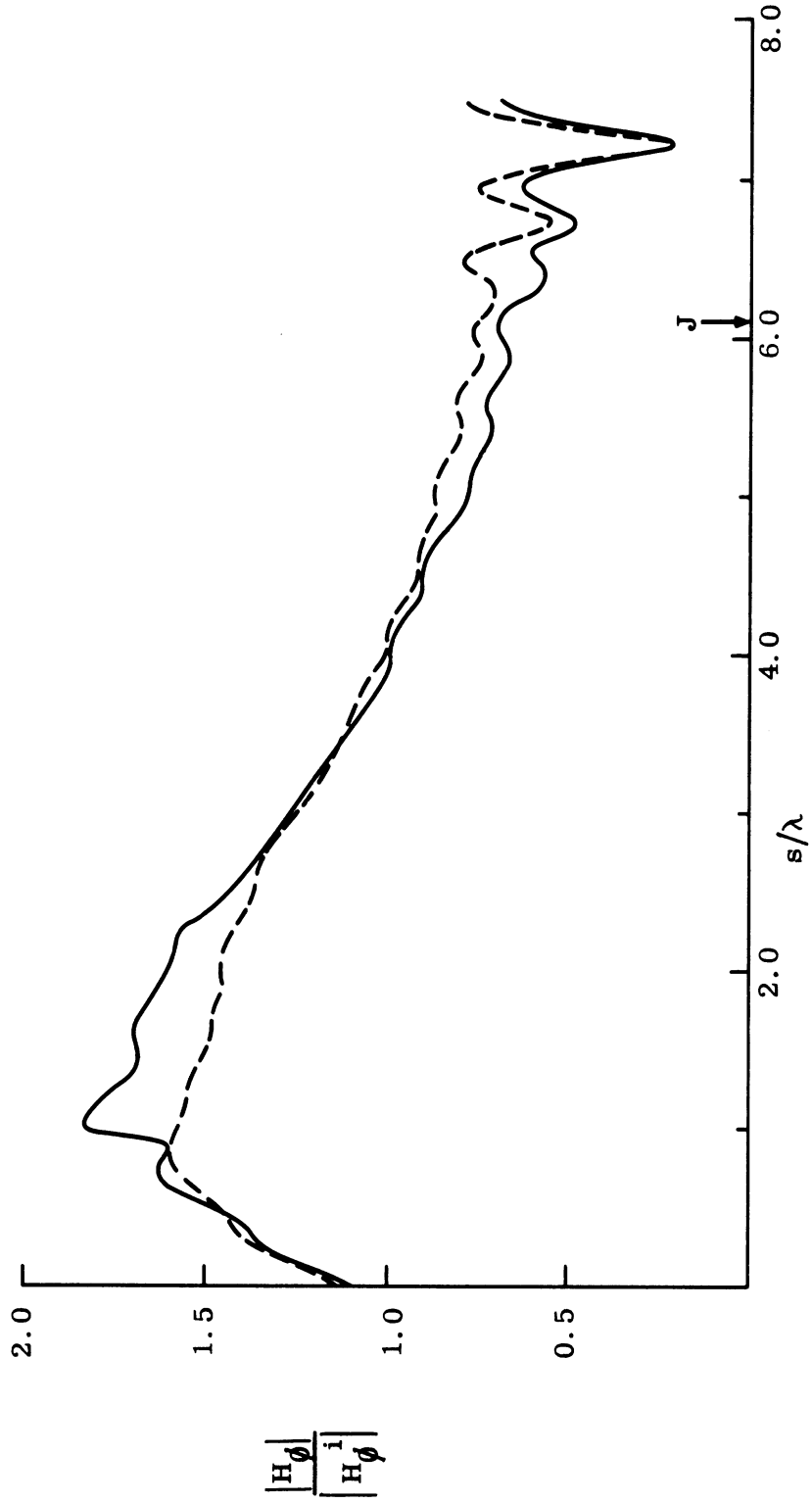

FIG. 3-52: SURFACE FIELD AMPLITUDES $|H_\phi|$ FOR D-12b (—) AND D-12c (---) ON LS-24 COATED CONE-SPHERE FOR ka=5.0.

(S) Typical of the data obtained is that for the H_ϕ and E_s components shown in Figs. 3-53 and 3-54 respectively. For comparison, the corresponding surface field components for the case of a single layer of Eccosorb-CR coating are included. Over the cone portion, the additional layer of teflon produces no systematic differences from the corresponding single layer behavior. Although the illustrated data for ka=5.0 indicates that, over the cone portion, the H_ϕ component is somewhat larger (and the E_s component smaller) for the double as opposed to the single coating, the differences are no more than can be ascribed to calibration. Over the rear spherical cap, there is some evidence that the double coating can produce a slight increase in field strength in certain cases: no such increase is, however, visible in the data presented here.

(S) Except for one case in which the direction of illumination was near rear-on, our discussion has so far centered on the surface field measurements for coated cone-spheres at nose-on incidence. Other directions are of interest, however, and a systematic study of the effects of changes in the dominant azimuthal magnetic surface field component was now undertaken as the angle of incidence changes. Measurements were carried out on each side of the cone-sphere along a horizontal trajectory from tip to antipode. The direction of incidence was fixed so that $\theta = 0^\circ$ refers to nose-on illumination while $\theta \neq 0^\circ$ refers to the angle through which the entire cone-sphere is rotated about a vertical axis through its tip. Since such a rotation inclines one side of the cone-sphere toward (and the other side away from) the direction of illumination, it is convenient to specify the former as the illuminated, and the latter as the shadowed, side.

(S) Measurements were made on a metal cone-sphere (with base radius 1.500" and half angle $7\text{-}1/2^\circ$) covered by a 3/8" layer of Eccosorb-CR absorber. From the table below, which summarizes the cases investigated, representative data has been selected.

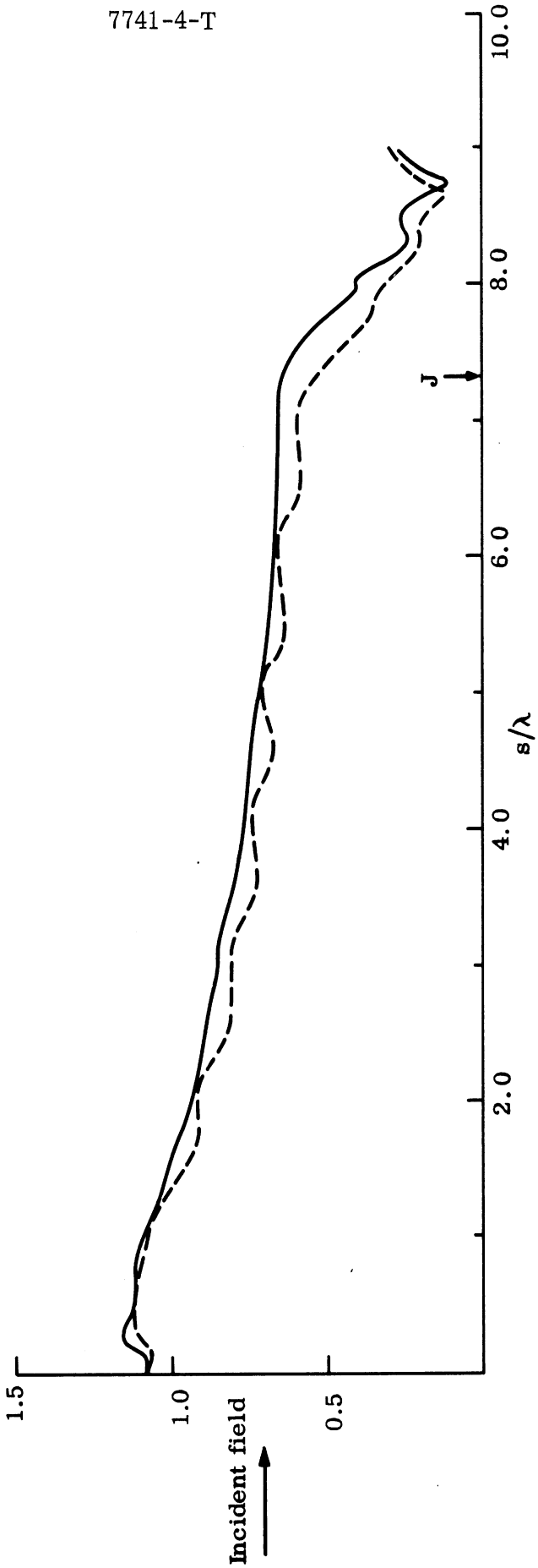

FIG. 3-53: COMPARISON OF $|H_\phi|$ SURFACE FIELD AMPLITUDES ON DOUBLE-COATED (—) WITH ECCOSORB-COATED (---) CONE-SPHERE FOR ka=5.0.

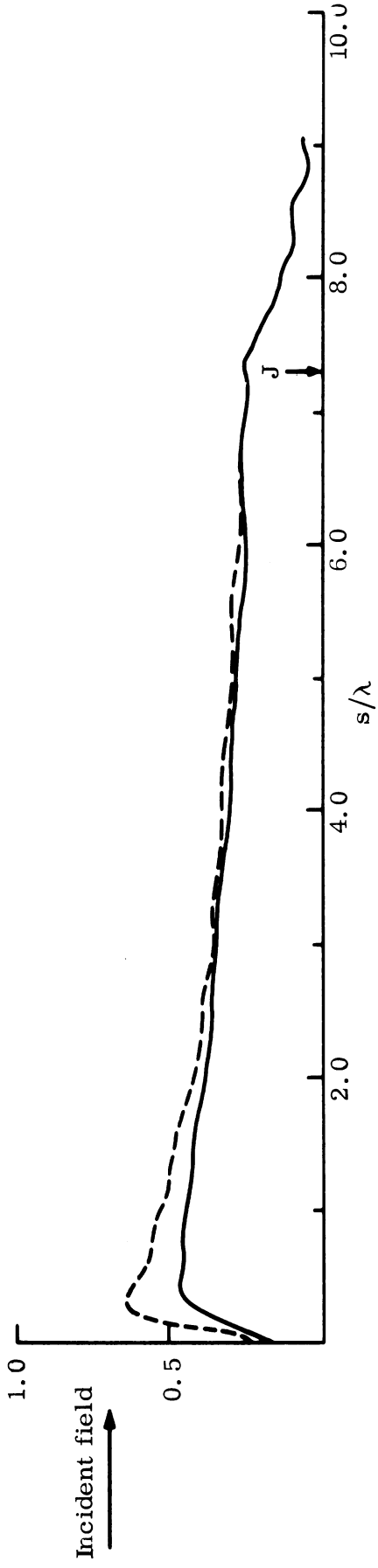

FIG. 3-54: COMPARISON OF $|E_s|$ SURFACE FIELD AMPLITUDES ON DOUBLE-COATED (—) WITH ECCOSORB COATED (---) CONE-SPHERE FOR ka=5.0.

TABLE III-10

ECCOSORB-COATED CONE-SPHERE MEASUREMENTS
FOR OBLIQUE INCIDENCE

Frequency (Gc)	2.5	6.26
ka	2.0	5.0
kb	2.5	6.25
Direction of Incidence (degrees)	7.5	7.5
	32.5	32.5
		37.5
	57.5	57.5
	82.5	82.5
		165.0

(S) Figures 3-55 and 3-56 illustrate the data for the E-CR coated cone-sphere at 2.5 Gc (which corresponds to ka=2.0) for $\theta = 32.5^{o}$ and 82.5^{o}, respectively.

(S) The data shows that on the illuminated side the azimuthal magnetic field component quickly rises to a maximum near the tip and then falls to a mean value which is approximately level and maintained out to the join. Both the location of the maximum (at about $s/\lambda = 0.4$ from the tip) and its amplitude (about 1.9) are independent of θ although the shape of the peak does show dependence on the angle of incidence. This is true for all angles of incidence outside the backward cone. With respect to this mean level the surface field, after decreasing from the initial peak, exhibits oscillations whose amplitude increased with increasing θ for θ up to 82.5^{o} (broadside to cone) and persists for greater s/λ as θ increases. Moreover, as the angle of incidence increases, so does the mean level near the join.

(S) On the shadowed side, for θ small (so that the shadowed side is still illuminated) the field parallels that on the illuminated side, but it lies somewhat below the latter (for example, 1.5 db for $\theta = 7.5^{o}$). As the side becomes more deeply shadowed, the field falls initially from the tip to a minimum near the same position at which the field on the illuminated side has its maximum. It then rises to a

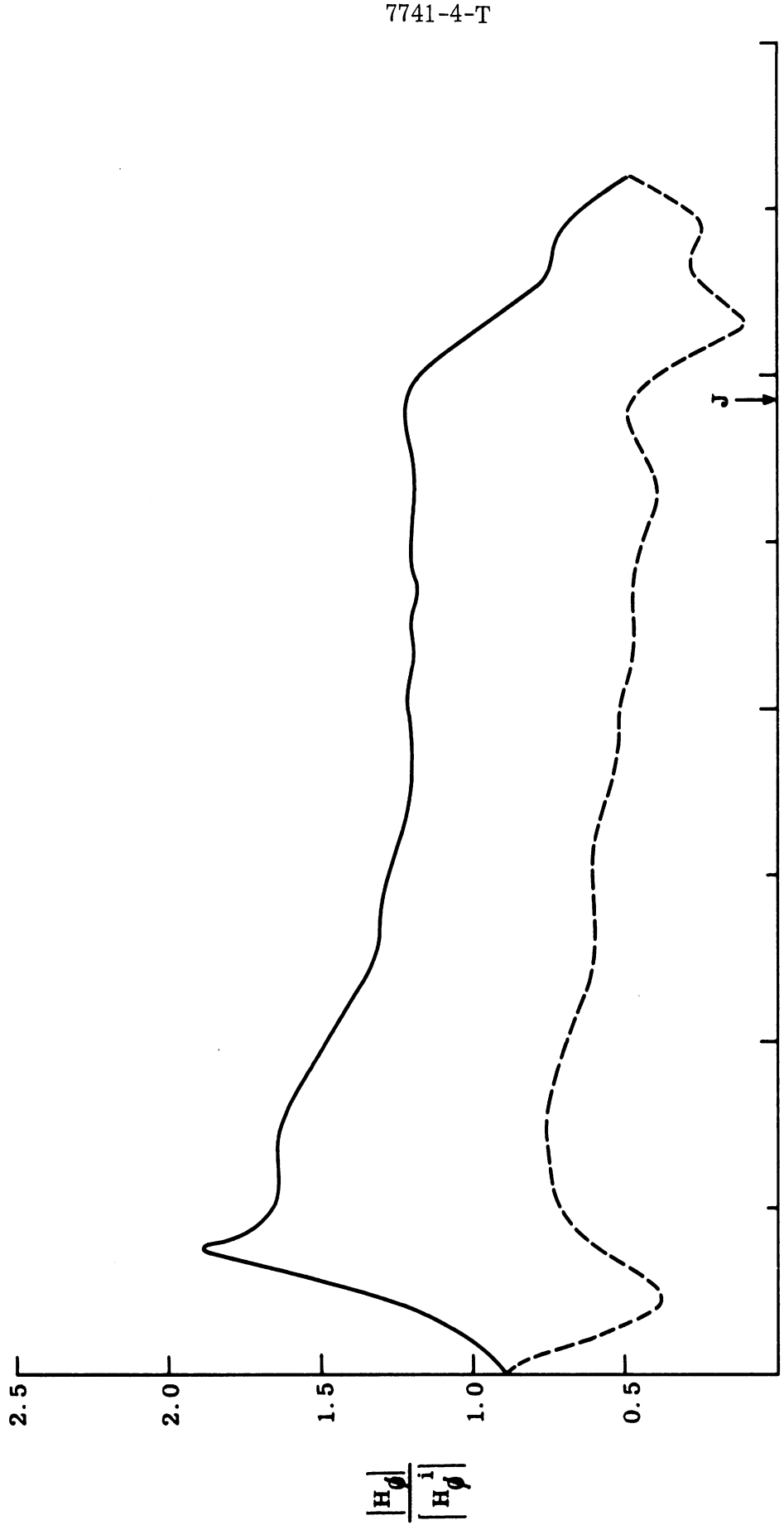

FIG. 3-55: MEASURED SURFACE FIELD COMPONENT FOR AN ECCOSORB-CR COATED CONE-SPHERE WITH ka=2.0 AT OBLIQUE INCIDENCE, θ=32-1/2°: (—) ILLUMINATED SIDE, (---) SHADOW SIDE.

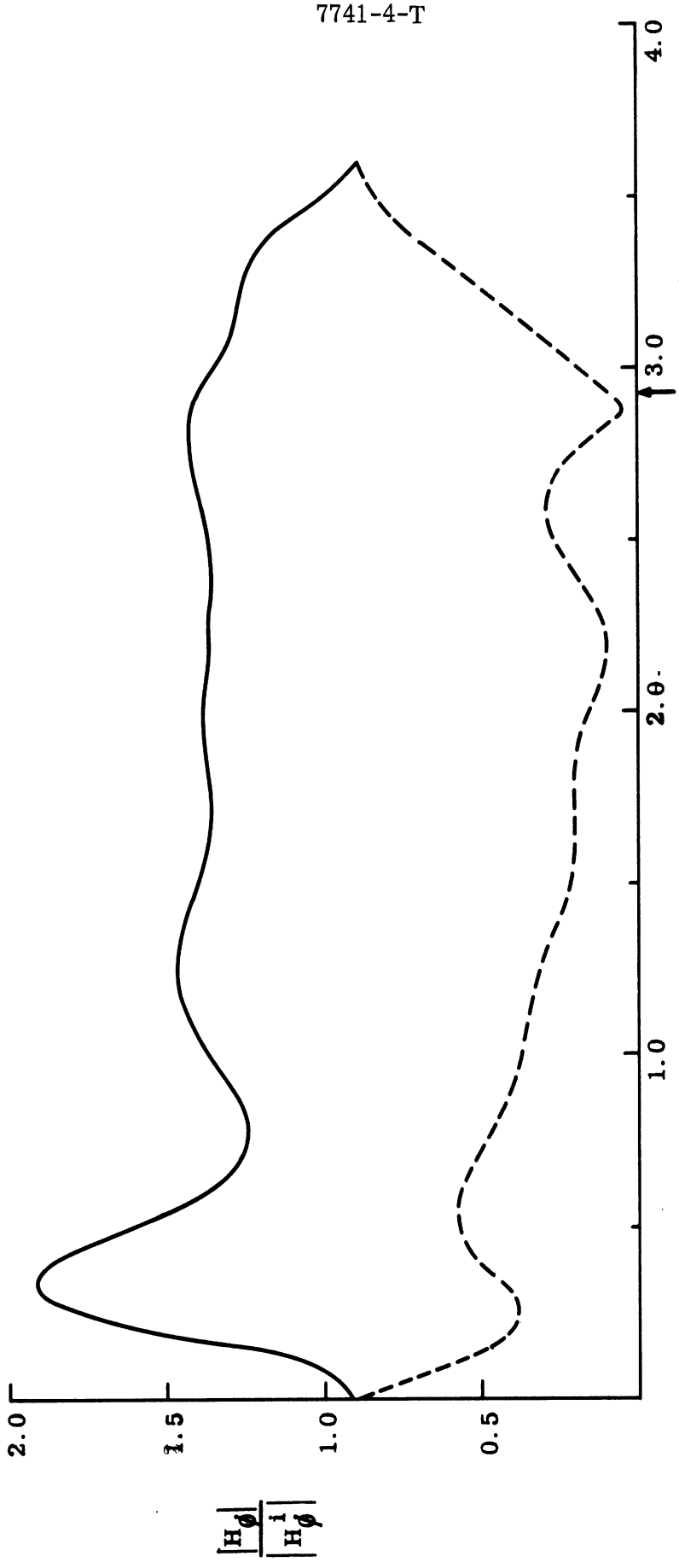

FIG. 3-56: MEASURED SURFACE FIELD COMPONENT $|H_\phi|$ FOR AN ECCOSORB-CR COATED CONE-SPHERE WITH ka=2.0 AT OBLIQUE INCIDENCE, θ=82.5°: (—) ILLUMINATED SIDE, (---) SHADOW SIDE.

maximum after which it decays with only slight oscillations. The field on the shadowed side falls progressively below the level on the illuminated side as θ increases and the levelling in the mean value near the join is not so evident as for the illuminated side.

(S) Measurements of the $|H_\phi|$ surface field component on a pure metal cone-sphere (also for ka=2.0) are shown in the next two figures (Figs. 3-57 and 3.58) for the same two directions of incidence and are included for purposes of comparison. The presence of the coating increases, of course, the trajectory on the coated body even though the metal cone-sphere has the same electrical size; this is the reason for differences in corresponding tip-to-antipode distances.

(S) Two selections of the data for the surface field measurement on the E-CR coated cone-sphere at the higher frequency (ka=5.0) have also been included and are given in Fig. 3-59 ($\theta = 32.5^\circ$) and Fig. 3-60 ($\theta = 82.5^\circ$). In general, the same remarks concerning the qualitative surface field characteristics that held for the lower frequency also hold for the measurements at the higher frequency. One exception is the existence of a minimum in the field modulus near the tip on the shadowed side which is not so well pronounced as at the lower frequency.

(S) For the illuminated side on the coated cone-sphere, the modulus of H_ϕ at the join increases from (approximately) 0.95 to 1.40 as θ increases from 7.5° to 82.5° for the lower frequency; at the higher frequency the corresponding increase is from 0.87 to 1.47. On the uncoated cone-sphere, on the other hand, the corresponding modulus is (about) constant. Thus, although the coating lowers the average field, as the angle of incidence increases, the ratio (at the join) of the coated to uncoated field moduli itself increases.

(S) This increase in mean field strength near the join is not only compatible with the increasing strength of illumination as θ increases, but quantitative estimates of the field at the join are in good agreement with those observed. In the following table the moduli of $|H_\phi|$, measured at the join, are compared with estimates of the surface field for a given angle of incidence made using the effective

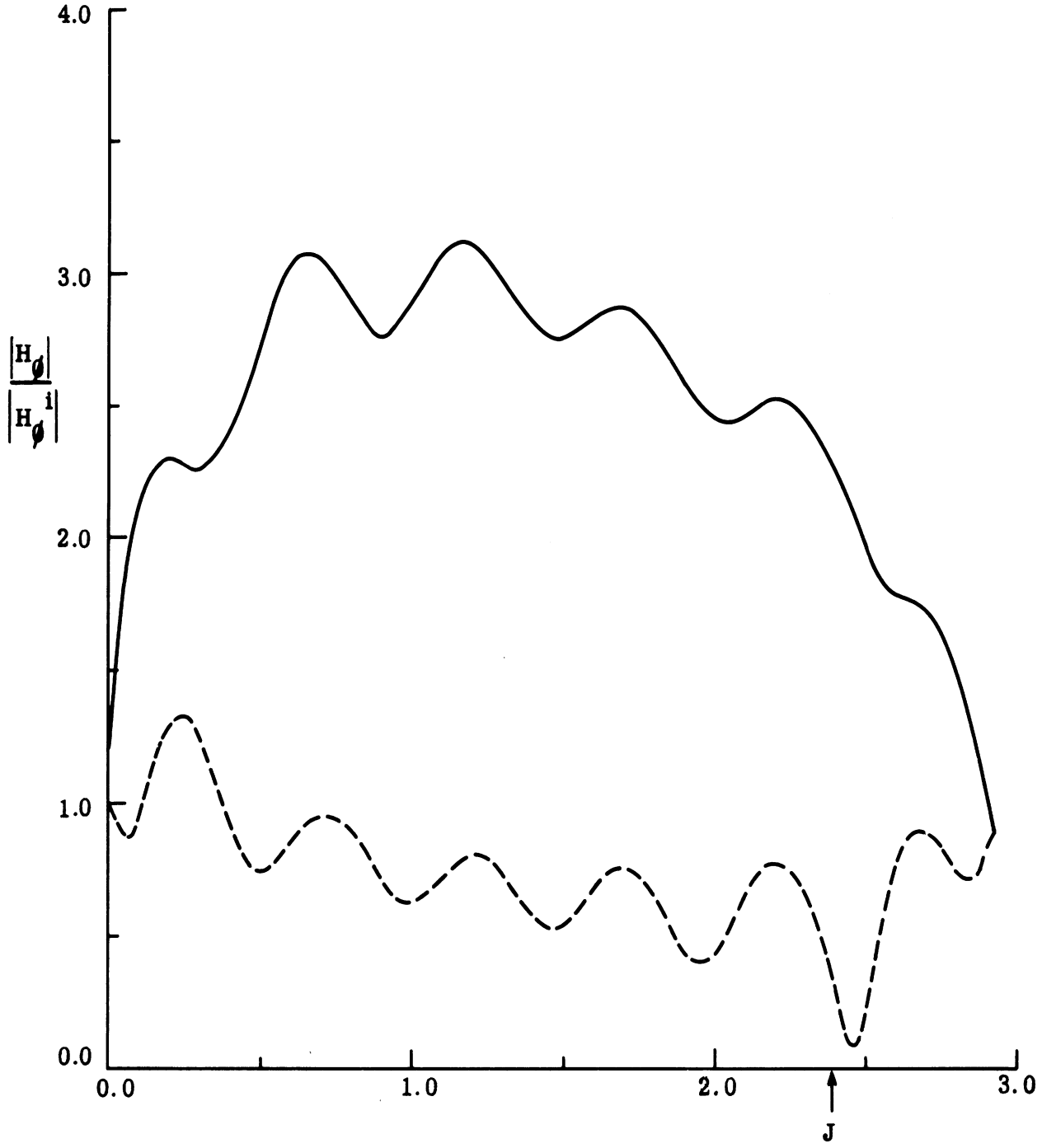

FIG. 3-57: MEASURED SURFACE FIELD COMPONENT $|H_\phi|$ ON A METALLIC CONE-SPHERE WITH ka=2.0, AT OBLIQUE INCIDENCE, θ=32.5°: (—) ILLUMINATED SIDE, (---) SHADOW SIDE.

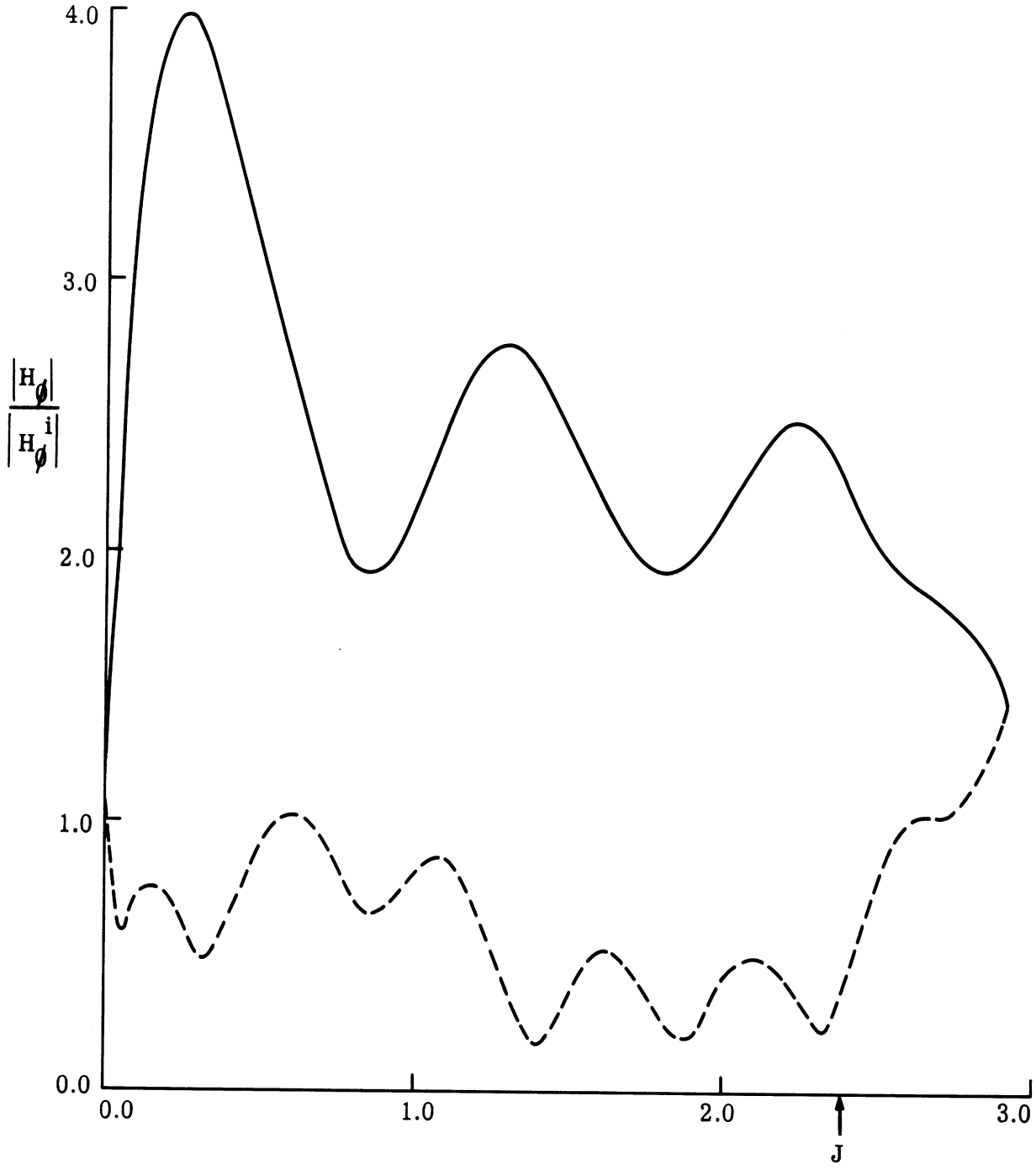

FIG. 3-58: MEASURED SURFACE FIELD COMPONENT $|H_\phi|$ ON A METALLIC CONE-SPHERE WITH ka=2.0 AT OBLIQUE INCIDENCE, θ=82.5°: (—) ILLUMINATED SIDE, (---) SHADOW SIDE.

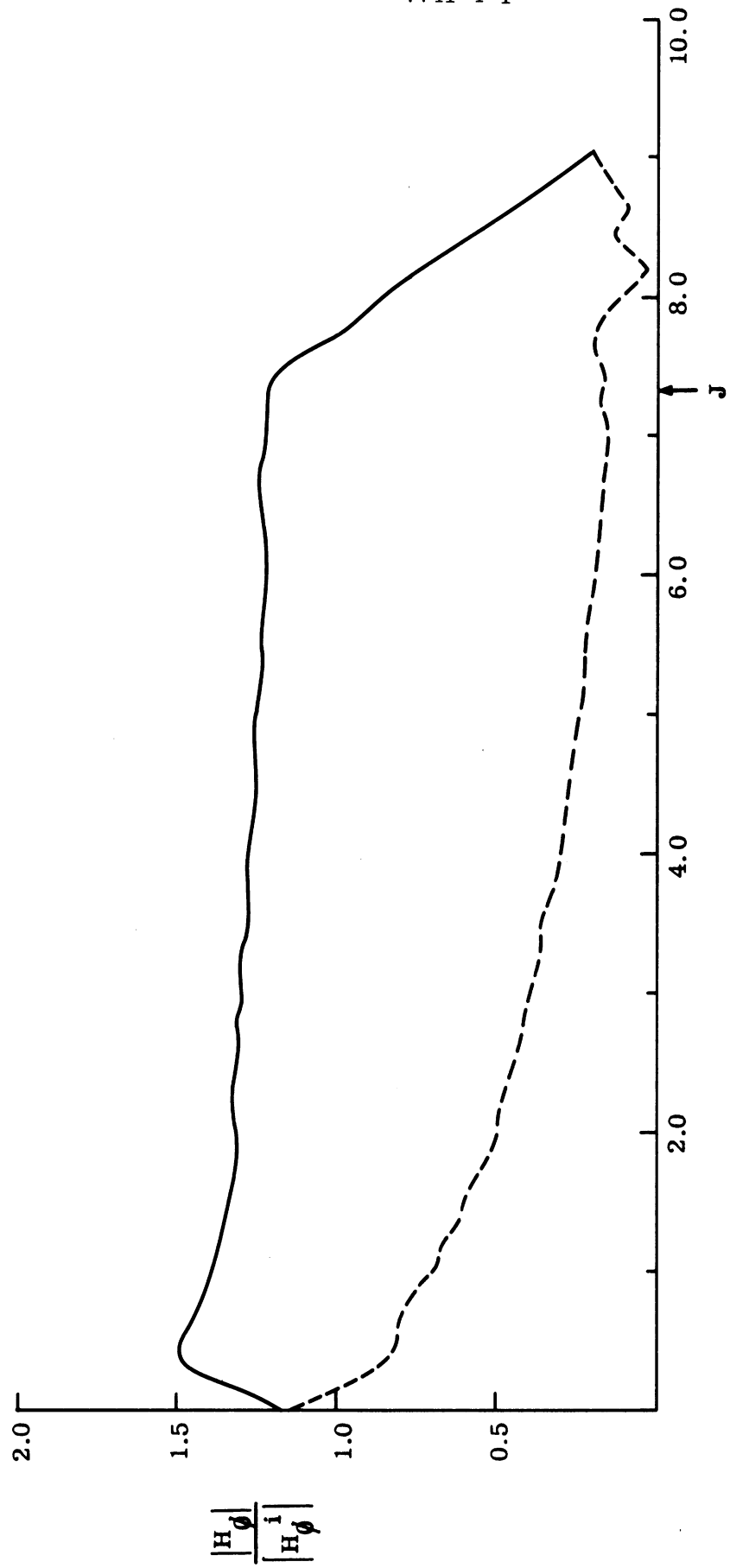

FIG. 3-59: MEASURED SURFACE FIELD COMPONENT $|H_\phi|$ FOR AN ECCOSORB-CR COATED CONE-SPHERE WITH ka=5.0 AT OBLIQUE INCIDENCE, $\theta = 32.5^\circ$: (—) ILLUMINATED SIDE, (---) SHADOW SIDE.

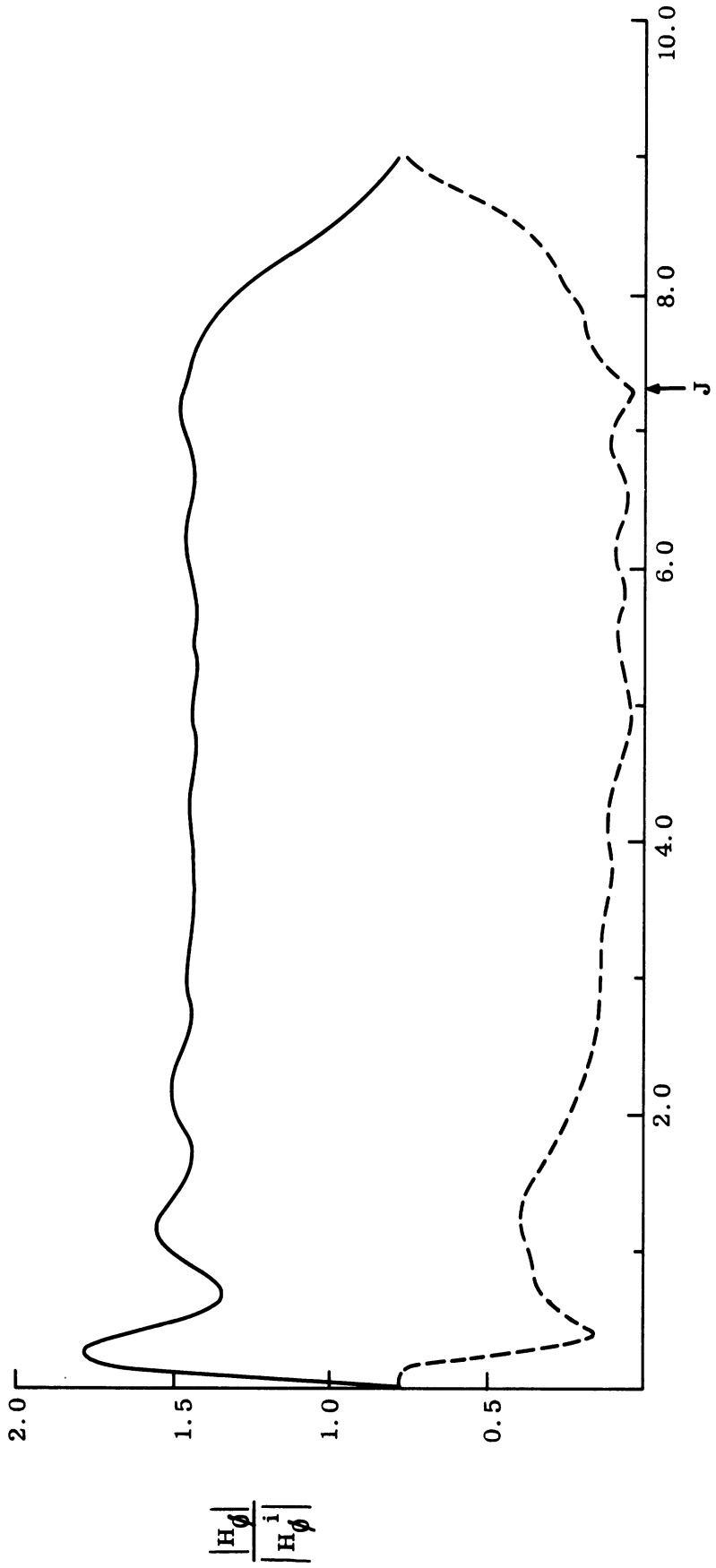

FIG. 3-60: MEASURED SURFACE FIELD COMPONENT $|H_\phi|$ FOR AN ECCOSORB-CR COATED CONE-SPHERE WITH ka=5.0 AT OBLIQUE INCIDENCE, θ=82.5°: (—) ILLUMINATED SIDE, (---) SHADOW SIDE.

TABLE III-11
COMPARISON OF $|H_\phi|$ AT JOIN
ON E-CR COATED CONE-SPHERE FOR OBLIQUE INCIDENCE

	$\|H_\phi\|$ Surface Field Amplitudes for Oblique Incidence			
	ka = 2.0		ka = 5.0	
θ	Meas.	Asympt. Est.	Meas.	Asympt. Est.
32.5^o	1.20	1.18	1.22	1.29
82.5^o	1.40	1.32	1.47	1.42

impedance (Eq. 3.8) in the asymptotic expression discussed in Section 3.5.1. It should be noted that, for the case of oblique illumination on a cone-sphere side, the effective angle of incidence is given by $\theta + \alpha$ when oblique illumination on a plane surface is considered.

IV
RADAR CROSS SECTION OF THE CONE-SPHERE IN A RE-ENTRY ENVIRONMENT

4.1 Introduction

(S) The objective of this task is to compute the back scattered field produced by an electromagnetic wave incident upon a plasma coated re-entry vehicle. The approach that has been followed this last year has been limited to the consideration of gross effects determined by the physical optics integral representation of the scattered field. Such an approximation ignores a number of phenomena which could be significant. These will be investigated in next year's program, and some further discussion on this subject is given at the end of this chapter.

(S) Calculations were carried out for a number of different sheaths, enclosing a cone of 11^{o} half-angle, corresponding to different altitudes. For computational purposes each case was given a profile number as follows:

Profile Number	Altitude (K ft)	Collision Frequency
3	150	2.06×10^{9}
4	100	1.87×10^{10}
5	80	4.67×10^{10}
6	60	1.16×10^{11}
7	30	3.46×10^{11}

The electron density profiles of these sheaths at a station 13 inches from the tip of the cone are given in Fig. 4-1. At other positions along the surface, the profiles are obtained by scaling the normal distance from the wall. If $N_e(Y_{13})$ is the electron density at distance Y_{13} from the wall, for a station 13" from the tip of the cone, then $N_e(Y_{13})$ is the electron density at distance Y_x from the wall, at a station x" from the tip of the cone, where

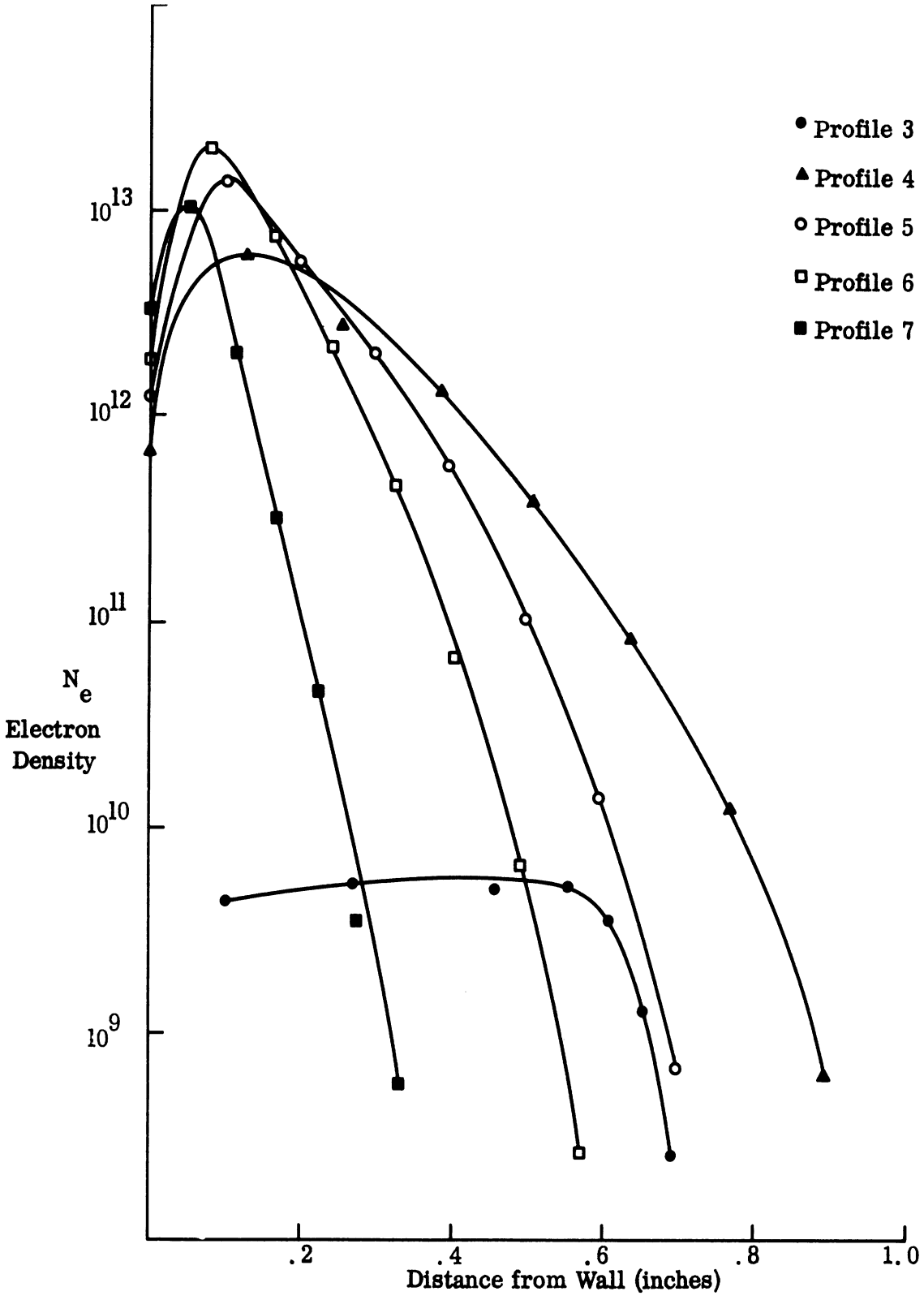

FIG. 4-1: ELECTRON DENSITY PROFILES AT A DISTANCE OF 13" FROM THE TIP.

$$Y_x = (x/13)^{\gamma} Y_{13} ,$$

and the constant $\gamma = .5$ for profile 3 and .8 for the remaining profiles.

(S) The physical optics integral representation of the scattered field (given in the Second Quarterly Report) is based on the evaluation of the local reflection coefficients. Calculations have been carried out for the local reflection coefficients at the following frequencies: 10^8, 5×10^8, 10^9, 5×10^9 and 10^{10} Hz, and two angles of incidence, 0^o and 79^o, measured from the normal to the surface. The former angle of incidence is applicable to the nose-on case, whereas the latter is applicable to the case of broadside scattering. These reflection coefficients were first calculated using the differential equation approach, and some results were given in the Third Quarterly Report. However, it was discovered that certain instabilities occurred in the program, and the results for the higher frequencies were incorrect. In particular, Figs. 3-31(e), 3-32(e) and 3-33(e) in the Third Quarterly, corresponding to a frequency of 10 GHz, display a resonance. This should not occur.

(U) To remove such errors, an alternative approach to the numerical calculation of the local reflection coefficients associated with a plane wave incident upon an inhomogeneous dielectric slab was developed and is outlined below.

4.2 Computational Procedure for Computing Reflection Coefficients

(U) An optimum approach from the standpoint of numerical procedure is given for evaluating the reflection coefficients associated with a plane wave incident upon an inhomogeneous dielectric slab. The fundamental geometry is indicated in Fig. 4-2, where h is the thickness of the slab and θ is the angle of incidence. The following three particular classes of materials backing the slab (the domain $z \leqslant -h$) will be considered: a perfect conductor, free space, and absorber-type material characterized by the impedance boundary condition

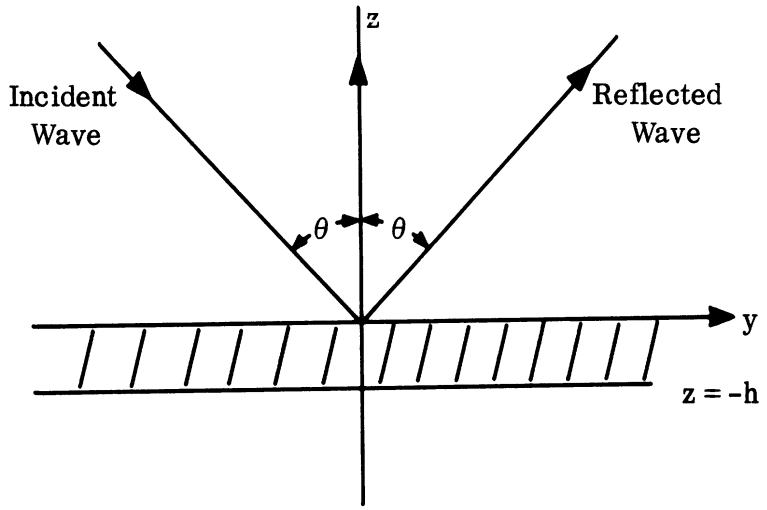

FIG. 4-2: SLAB GEOMETRY

$$\underline{E} - (\underline{E} \cdot \underline{n})\underline{n} = \sqrt{\mu_o/\epsilon_o}\, \eta\, \underline{n} \times \underline{H}$$

where $\underline{n}$ is the unit outward normal to the surface. In particular the case $\eta = 1$ will be treated, which corresponds to an absorber which gives a zero voltage reflection coefficient for normal incidence. The slab itself will have a permittivity which varies in the z-direction.

(U) The numerical approach is based upon the approximation of the non-homogeneous dielectric slab by a set of stratified layers. The resulting computational procedure can then be simply expressed in terms of a set of recurrence relations.

(U) The slab will be decomposed into N layers, numbered from the back of the slab given by the plane $z = -h$. For consistency in notation the region below the slab ($z < -h$) will be noted as the zeroth layer, and the free space region ($z > 0$) will be denoted as the (N+1)th layer.

(U) The distance of the top face of the nth slab from the free space boundary $z = 0$, will be given as z_n, and the thickness of the slab by δ_n. This is illustrated in Fig. 4-3.

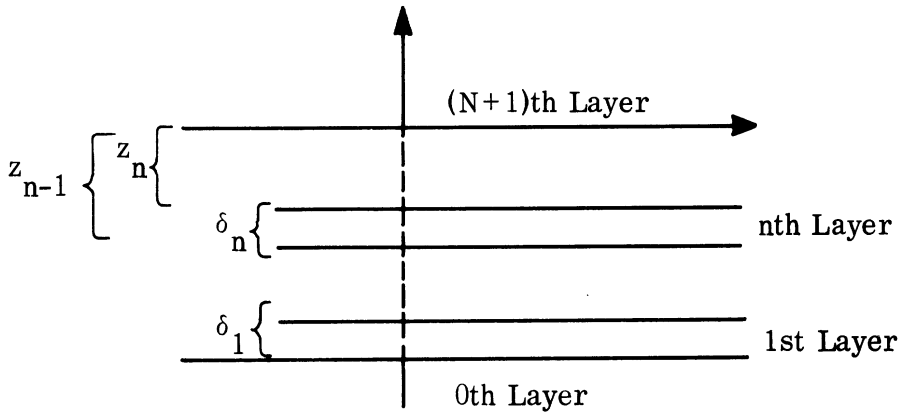

FIG. 4-3: GEOMETRY FOR STRATIFIED LAYERS

(U) We will first consider the derivation of the appropriate expression for $R_{||}$, the reflection coefficient

$$R_{||} = H^r/H^i$$

involving the ratio of the reflected and incident magnetic fields at $z = 0$, and which is associated with the incident wave polarized in the plane of incidence.

(U) In the nth layer, the components of the electric and magnetic fields transverse to the slab can be expressed in the general form

$$H_x = \exp\left\{ik_n \sin\theta_n y\right\}\left[A_n \exp\left\{-ik_n \cos\theta_n z\right\} + B_n \exp\left\{ik_n \cos\theta_n z\right\}\right]$$

$$-E_y = Z_n \exp\left\{ik_n \sin\theta_n y\right\}\left[-A_n \exp\left\{-ik_n \cos\theta_n z\right\} + B_n \exp\left\{ik_n \cos\theta_n z\right\}\right]$$

where

$$Z_n = \frac{1}{N_n}\sqrt{\mu_o/\epsilon_o}\cos\theta_n ,$$

$$k_n = N_n k_o ,$$

where N_n is the index of refraction of the nth layer. The complex angle θ_n is

related to the angle of incidence through the relation

$$N_n \sin\theta_n = \sin\theta \ . \tag{4.1}$$

(U) The coefficients A_n and B_n are found by matching the transverse components H_x and E_y. However, since we require only the reflection coefficient, they will not be explicitly found. Instead, by matching these components across the interfaces, a set of recurrence equations will be derived which will lead to the evaluation of $R_{||}$. This will require the following ratio involving the two components evaluated at the top of the nth layer $(z = z_n)$,

$$Z^{(n)} = -\sqrt{\epsilon_o/\mu_o}\left[E_y/H_x\right]_{z=z_n} \ . \tag{4.2a}$$

It then follows that

$$Z^{(n)} = p_n(S_n - 1)/(S_n + 1) \ ,$$

where

$$p_n = \cos\theta_n/N_n \ ,$$

and

$$S_n = (B_n/A_n)\exp\left[2ik_n\cos\theta_n z_n\right] \ .$$

Similarly it can be shown that

$$Z^{(n-1)} = p_n \frac{S_n e^{-2i\phi_n} - 1}{S_n e^{-2i\phi_n} + 1} \ , \tag{4.2b}$$

where $\phi_n = k_n\cos\theta_n(z_n - z_{n-1}) = k_n\cos\theta_n\delta_n$. It should be noted here that z_n and z_{n-1} are negative numbers, but δ_n is positive.

(U) Eliminating S_n from equations (4.2a, b), one obtains the following recurrence equation

$$Z^{(n)} = p_n \left[\frac{Z^{(n-1)} + ip_n \tan\phi_n}{p_n + iZ^{(n-1)} \tan\phi_n} \right] \quad . \tag{4.3}$$

The reflection coefficient $R_{||}$, given by

$$R_{||} = (H_x^r / H_x^i) = B_{N+1} / A_{N+1}$$

can be expressed in terms of $Z^{(N)}$ as follows

$$R_{||} = \frac{\cos\theta + Z^{(N)}}{\cos\theta - Z^{(N)}} \quad . \tag{4.4}$$

(U) The initial term $Z^{(o)}$ in the recurrence relation, can be found by applying the appropriate boundary conditions at $z = -h$. For the general case of the impedance boundary condition, given by

$$\underline{E} - (\underline{E} \cdot \hat{\underline{i}}_z)\hat{\underline{i}}_z = \eta \sqrt{\mu_o / \epsilon_o}\ \hat{\underline{i}}_z \times \underline{H}$$

we have

$$E_y / H_x = \eta \sqrt{\mu_o / \epsilon_o}$$

yielding the relation

$$Z^{(o)} = -\eta \quad . \tag{4.5a}$$

The special case of perfect conductivity is given by setting $\eta = 0$, yielding

$$Z^{(o)} = 0 \quad . \tag{4.5b}$$

The remaining case, where the slab is backed by free space, can be easily treated. Here the coefficient B_o must vanish, implying that

$$Z^{(o)} = -p_o = -\cos\theta. \tag{4.5c}$$

(U) The set of equations (4.1) - (4.5c) yield the appropriate expressions required to compute $R_{||}$. Dividing the slab into a set of N layers, with an index of refraction N_n associated with each layer, the angles θ_n are first computed from expression (4.1). The set of coefficients p_n are then computed. The application of the required boundary condition (4.5a) - (4.5c) indicative of the material which backs the slab, yields the zeroth order coefficient $Z^{(o)}$. Immediate application of the recurrence relation (4.3) produces the set of numbers $Z^{(n)}$ $(n=1,2,3,\ldots N)$. From this the reflection coefficient is computed using (4.4).

(U) The appropriate recurrence relation, which can be used to compute $R_{\perp}$ associated with polarization perpendicular to the plane of incidence, can be found in a similar manner. In the nth layer, the components of the electric and magnetic field are given by the general expression

$$H_y = \exp\left\{ik_n \sin\theta_n y\right\}\left[A_n \exp\left\{-ik_n\cos\theta_n z\right\} + B_n \exp\left\{ik_n\cos\theta_n z\right\}\right]$$

$$E_x = Z_n \exp\left\{ik_n \sin\theta_n y\right\}\left[-A_n \exp\left\{-ik_n\cos\theta_n z\right\} + B_n \exp\left\{ik_n\cos\theta_n z\right\}\right]$$

where

$$Z_n = \frac{\sqrt{\mu_o/\epsilon_o}}{N_n\cos\theta_n}.$$

Employing the relation

$$Z^{(n)} = \sqrt{\epsilon_o/\mu_o}\,(E_x/H_y)_{z=z_n}$$

one obtains exactly the same relation as is given by (4.3), where in this case

$$p_n = \frac{1}{N_n \cos\theta_n} \quad .$$

The initial value $Z^{(o)}$, for the impedance boundary condition and perfect conductor are given by (4.5a) and (4.5b) respectively, whereas for the free space case it is prescribed by the following relation

$$Z^{(o)} = -1/\cos\theta \quad . \tag{4.5d}$$

The reflection coefficient $R_\perp = E^r/E^i$ is given by

$$-R_\perp = \frac{1+\cos\theta\, Z^{(n)}}{1-\cos\theta\, Z^{(n)}} \quad . \tag{4.4a}$$

(U) The accuracy of the above numerical procedure depends upon N, the number of homogeneous slabs taken, and will be limited by the number of data points for which the dielectric constant is originally specified. The number N required to give sufficient accuracy, increases as the sheath gradient becomes more gradual. This means that for profiles 4 to 7, the number N must increase with frequency and with position along the cone.

(S) Using the above numerical procedure, the local reflection coefficients for the profiles were computed for two cases: where the inner surface was a perfect conductor, and where it was an absorber ($\eta = 1$). The results are given in Figs. 4-4 through 4-13. For the normal incidence case ($\theta = 0$), the impedance boundary condition ($\eta = 1$) is equivalent to the condition that the material backing the sheath is free space. It is noticeable in Figs. 4-4 to 4-6 that at a sufficient distance from the tip of the cone the results are independent of the boundary condition imposed on the inner surface, implying that little energy penetrates the sheath.

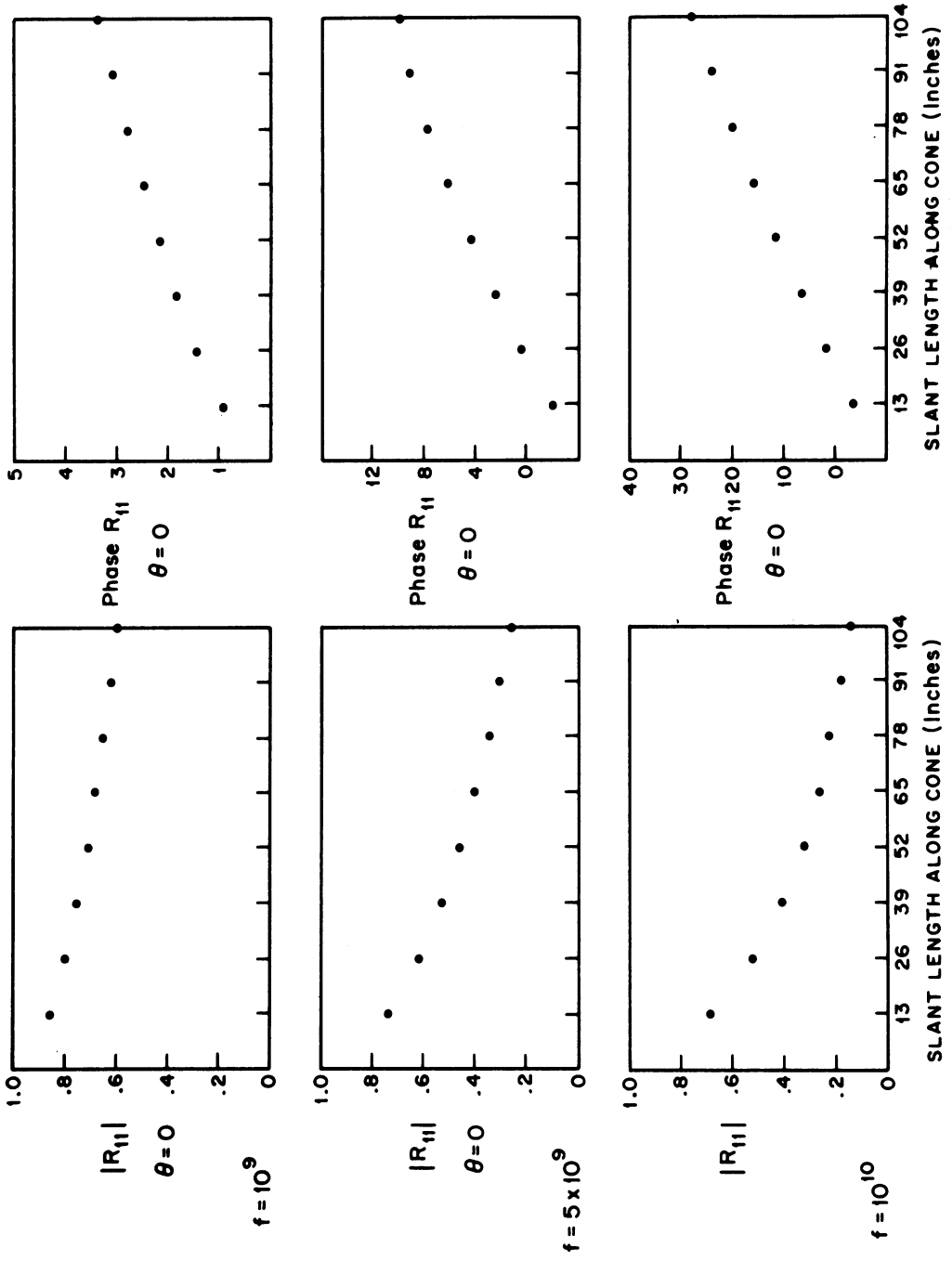

FIG. 4-4: PROFILE 4: AMPLITUDE AND PHASE OF REFLECTION COEFFICIENTS.

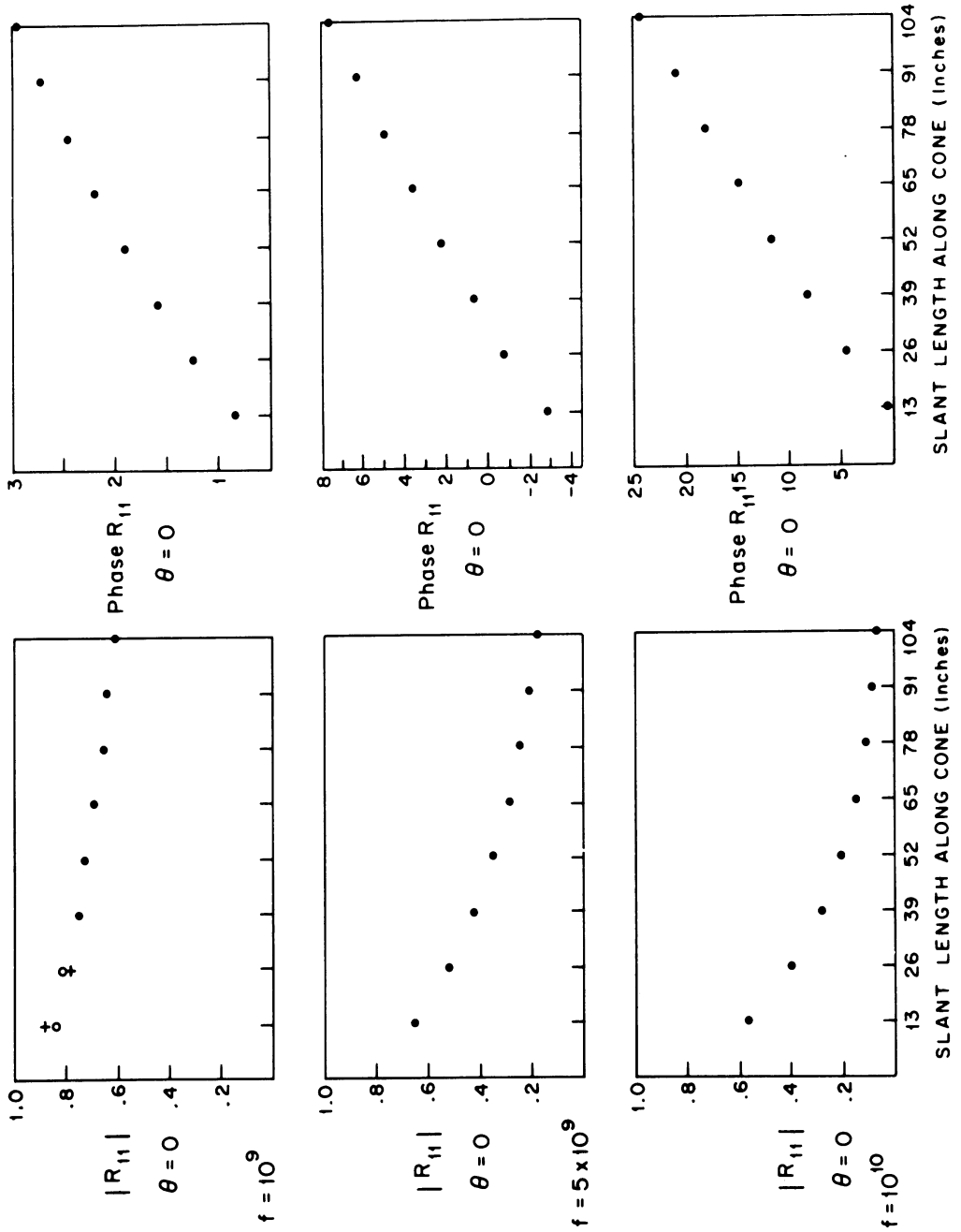

FIG. 4-5: PROFILE 5: AMPLITUDE AND PHASE OF REFLECTION COEFFICIENTS.

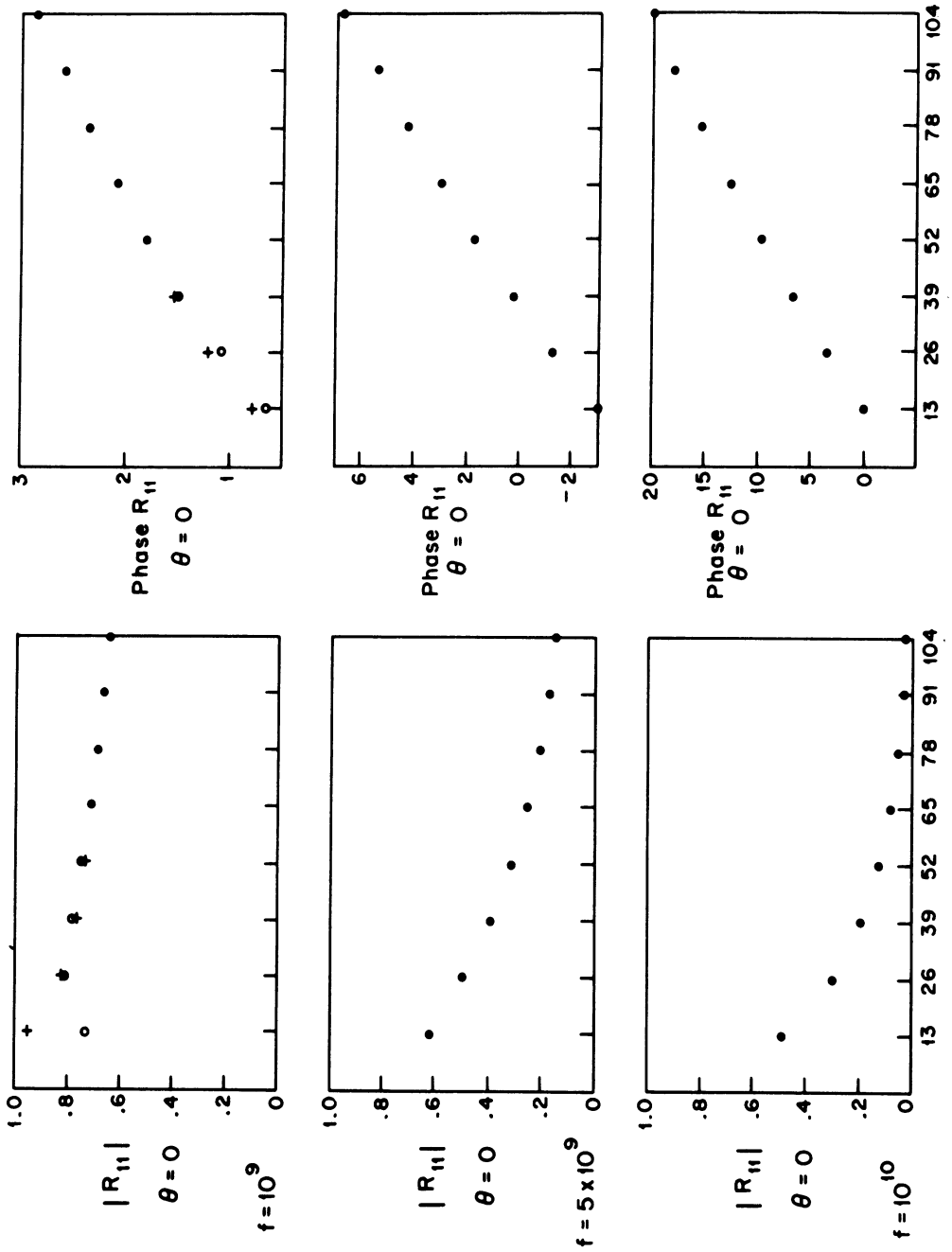

FIG. 4-6: PROFILE 6: AMPLITUDE AND PHASE OF REFLECTION COEFFICIENTS

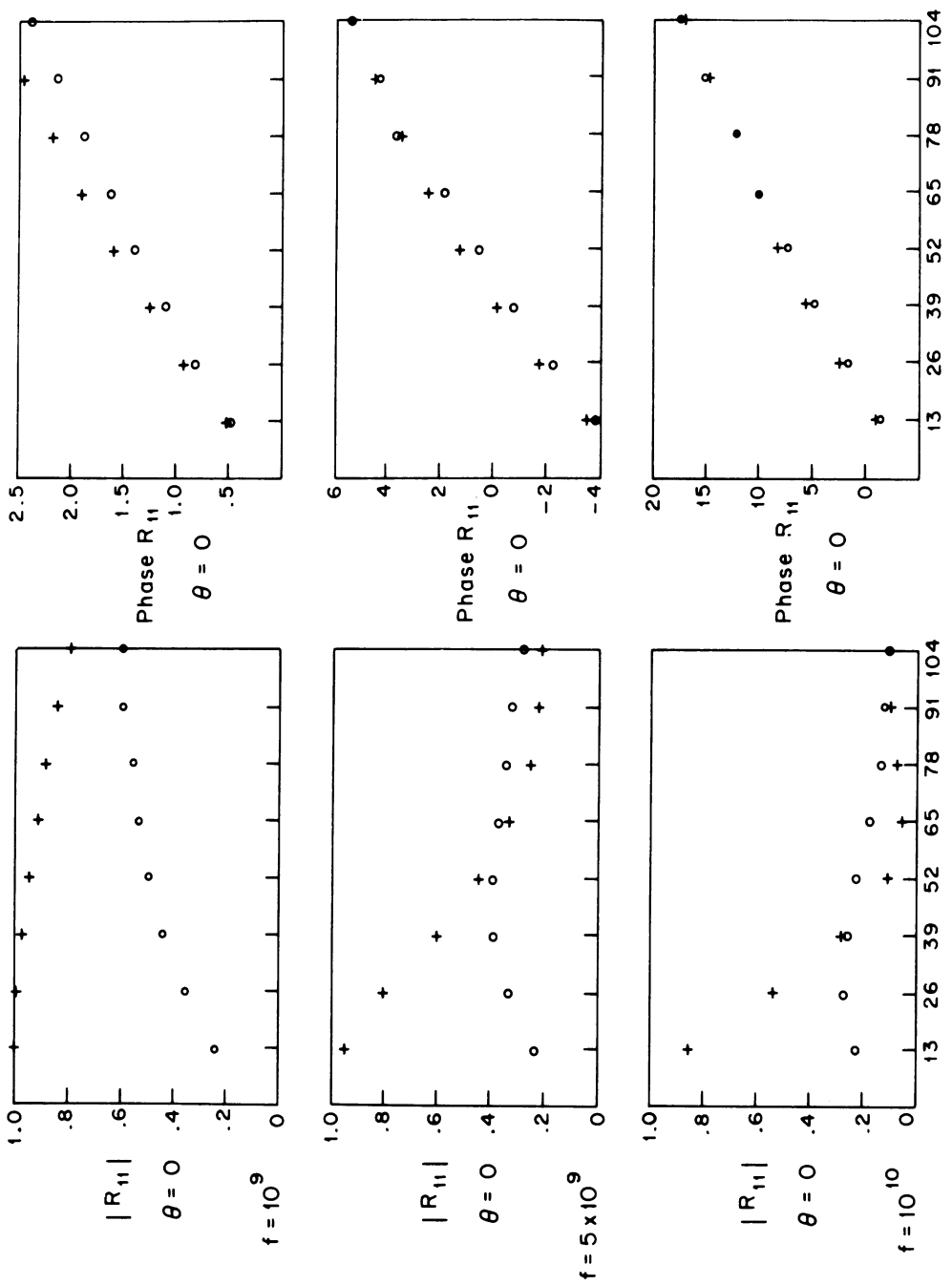

+ = Perfect Conductor, o = Absorber, ● = both.

FIG. 4-7: PROFILE 7: AMPLITUDE AND PHASE OF REFLECTION COEFFICIENTS

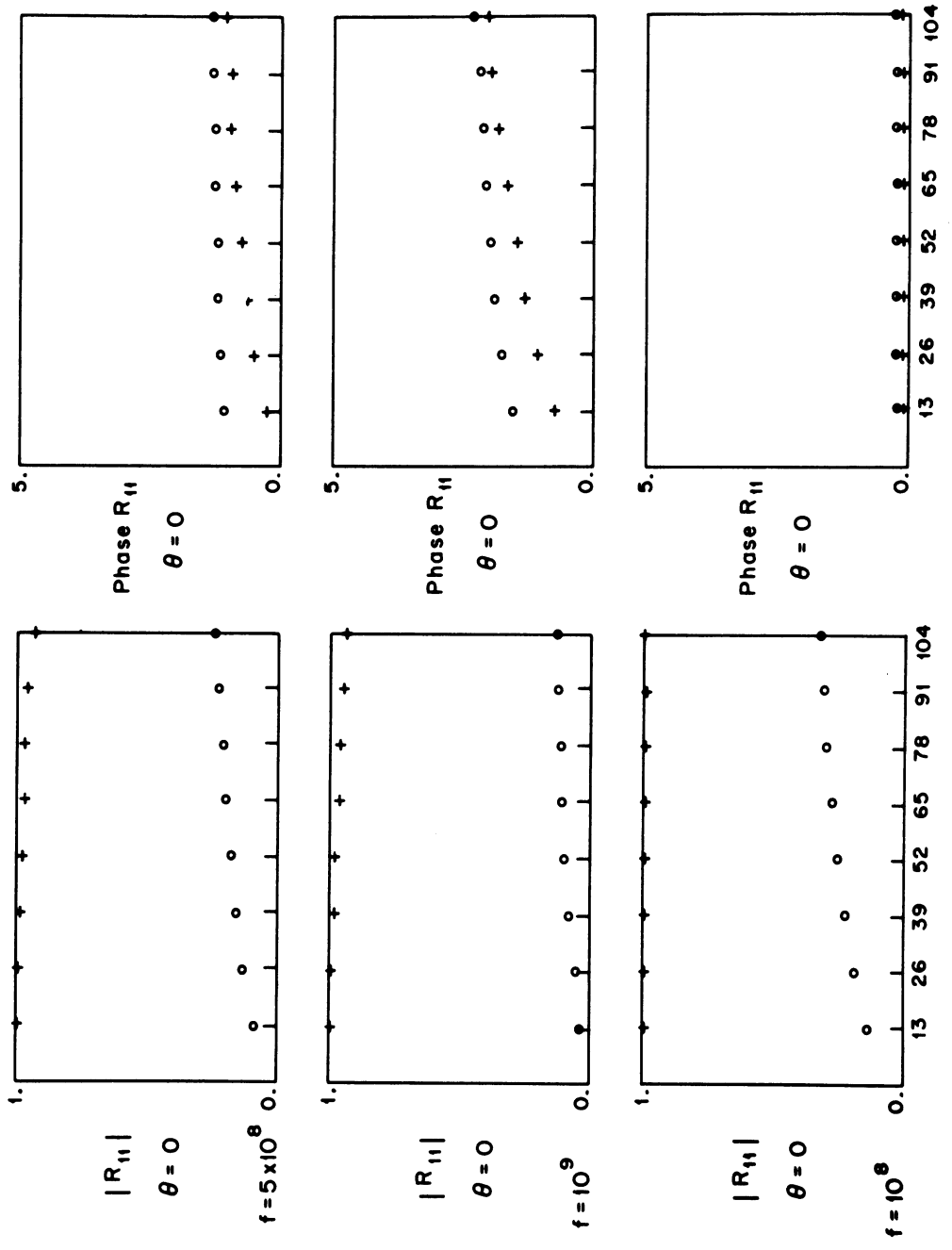

FIG. 4-8: PROFILE 3: AMPLITUDE AND PHASE OF REFLECTION COEFFICIENTS.

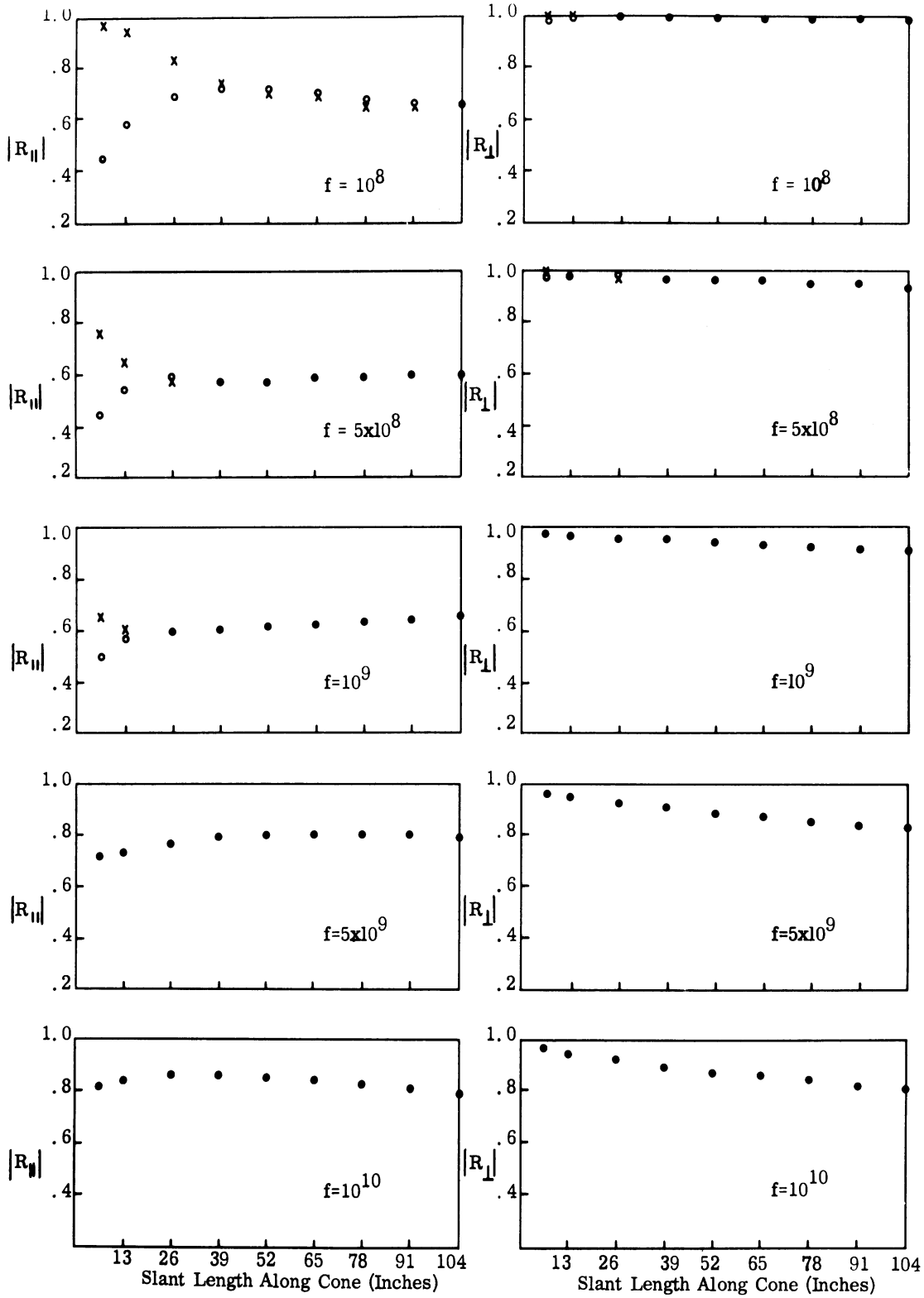

FIG. 4-9: PROFILE 4: MAGNITUDE OF REFLECTION COEFFICIENTS ($\theta = 79^{o}$) AS A FUNCTION OF SLANT DISTANCE ALONG CONE.

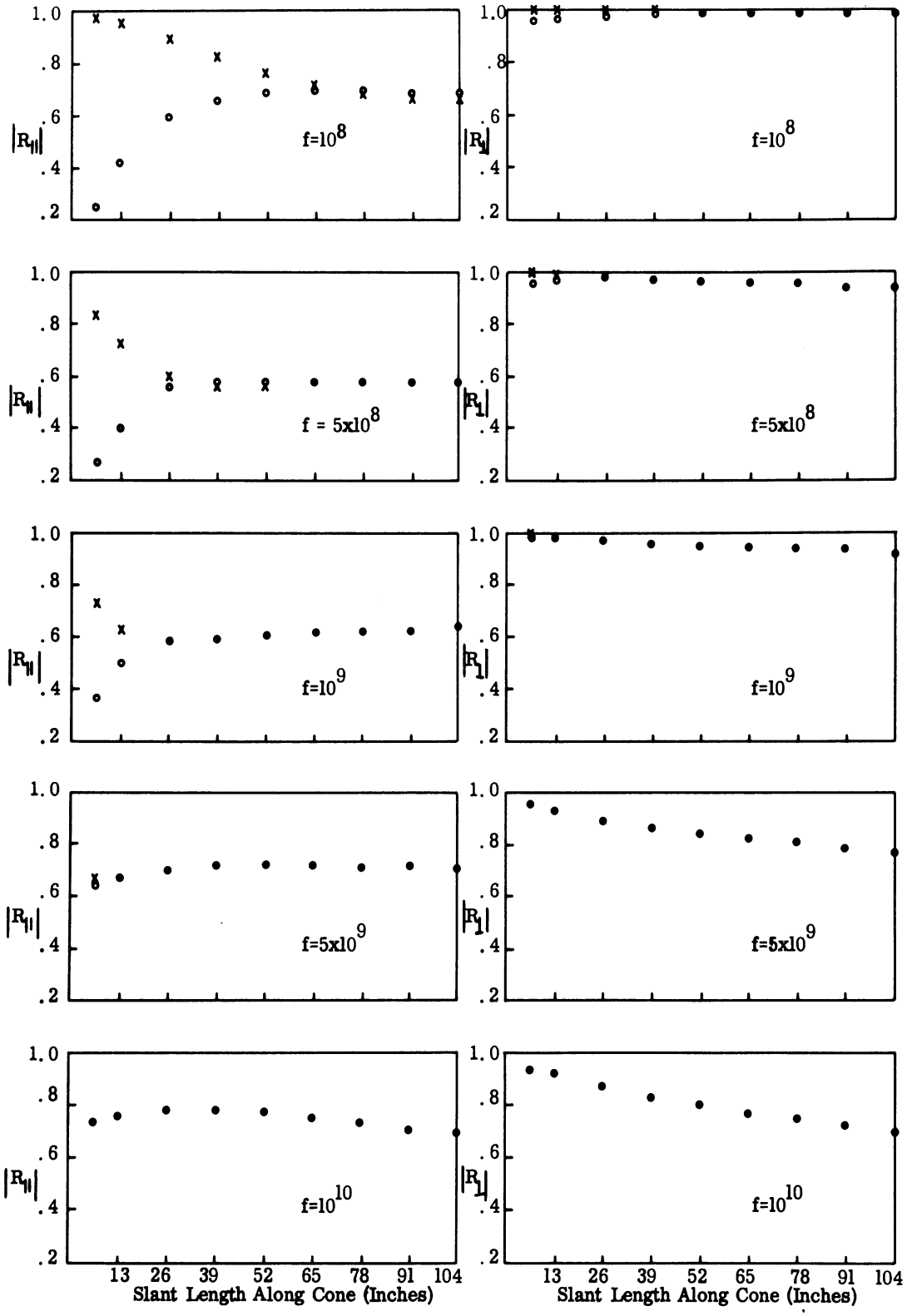

FIG. 4-10: PROFILE 5: MAGNITUDE OF REFLECTION COEFFICIENTS ($\theta = 79^{o}$) AS A FUNCTION OF SLANT DISTANCE ALONG CONE.

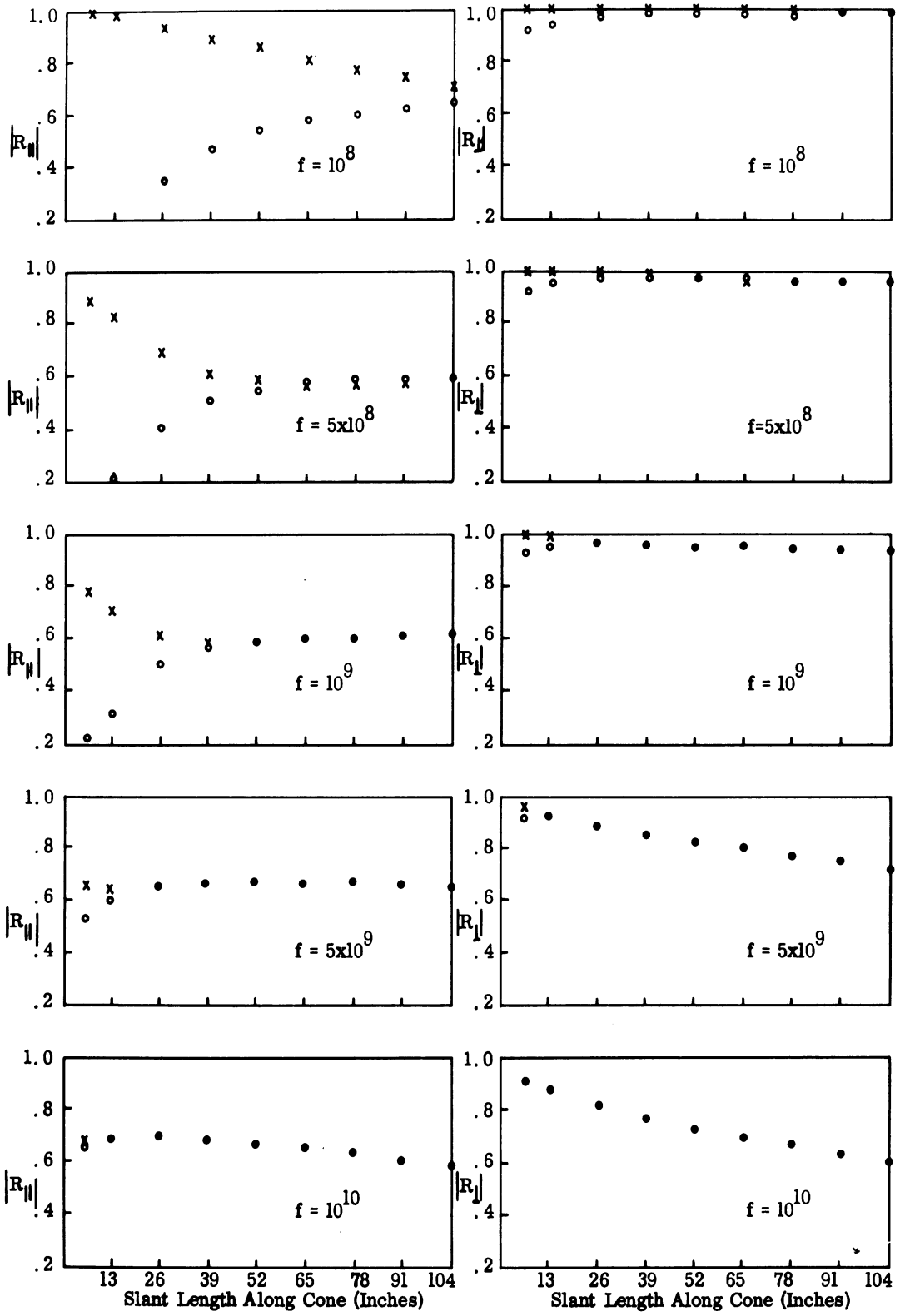

FIG. 4-11: PROFILE 6: MAGNITUDE OF REFLECTION COEFFICIENTS ($\theta = 79^{o}$) AS A FUNCTION OF SLANT DISTANCE ALONG CONE.

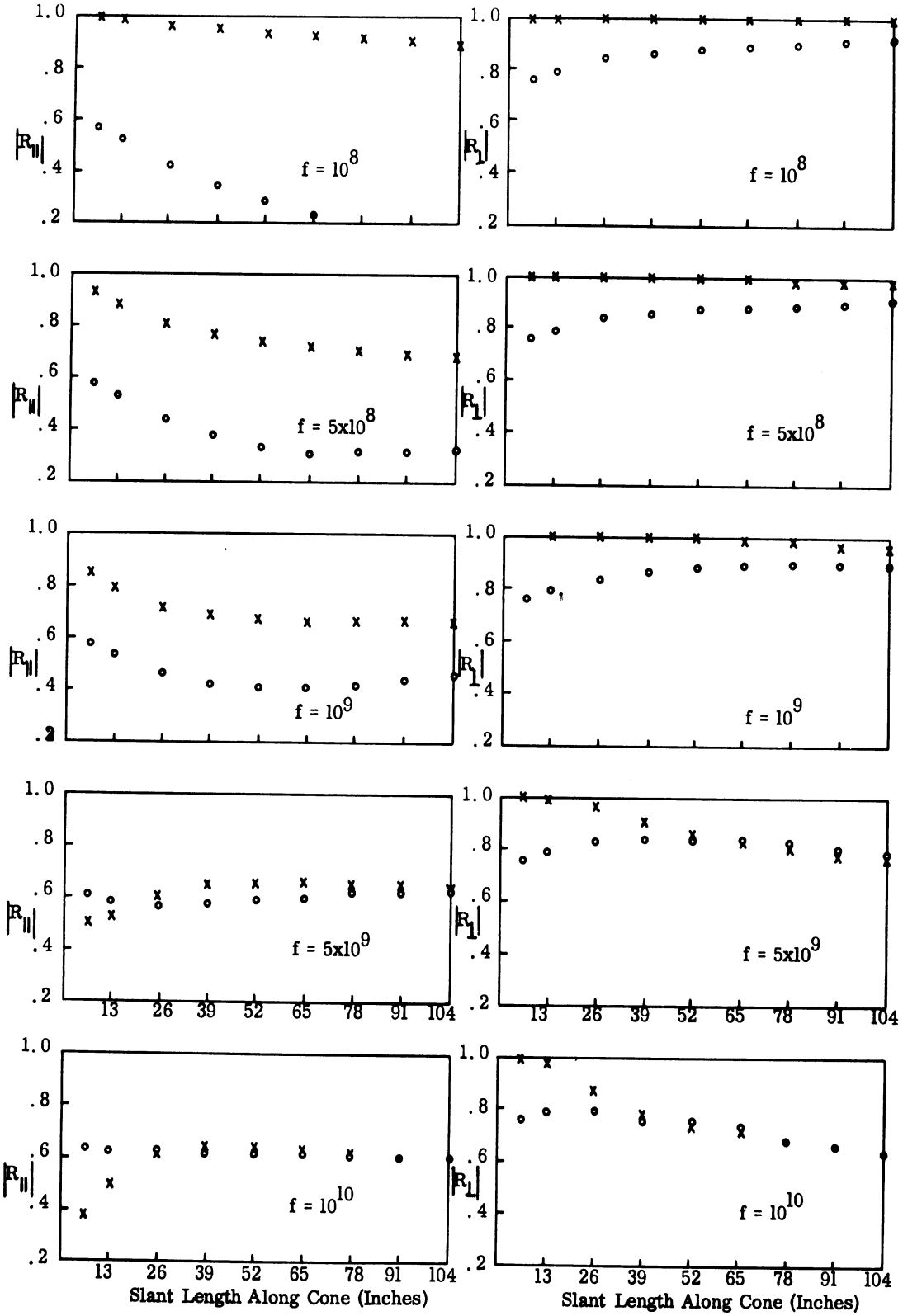

FIG. 4-12: PROFILE 7: MAGNITUDE OF REFLECTION COEFFICIENTS ($\theta = 79^{o}$) AS A FUNCTION OF SLANT DISTANCE ALONG CONE.

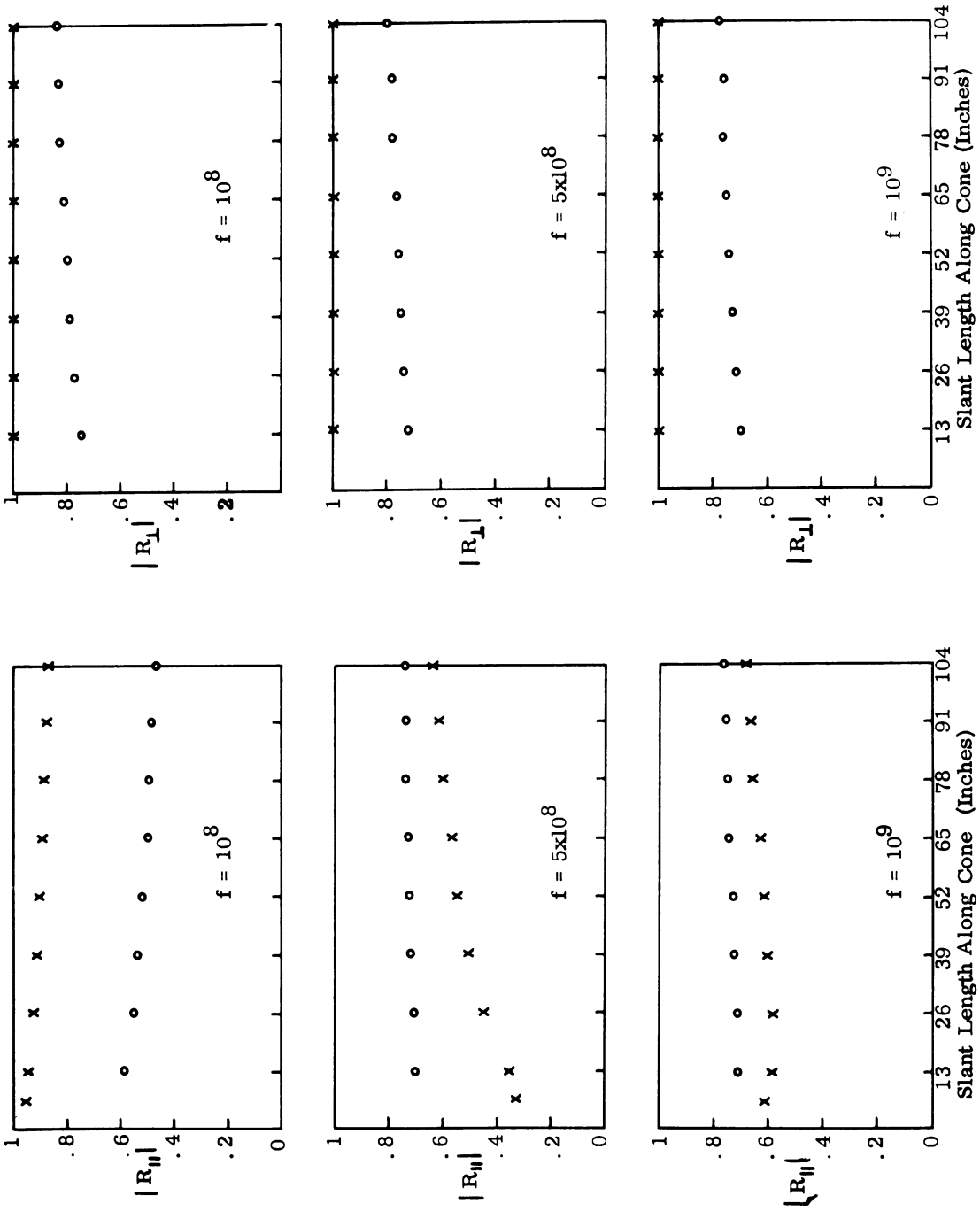

FIG. 4-13: PROFILE 3: MAGNITUDE OF REFLECTION COEFFICIENTS ($\theta = 79^o$).

4.3 Effect of Steep Dielectric Gradients on the Local Reflection Coefficient

(S) As seen in Fig. 4-1, the electron density curves for profiles 4 to 7 have exponential type behavior, the exponent being of parabolic type. In order to check the computations of the reflection coefficients and to study the effect of steep gradients of the electron density upon the reflection coefficient, gradient type sheaths of the form

$$\epsilon(z) = 1+(-\omega+i\nu)A\,e^{-bz}$$

which would correspond to the outer portion of the sheath (outside the maximum density), will be analyzed. The geometry is the same as that given in Fig. 4-2, with the outer edge of the sheath being given by the surface $z=0$. In the above representation of $\epsilon(z)$, ν is the collision frequency, and A is a real constant relative to the electron density at $z=0$. Results from this analysis should approximate the computed results for those frequencies where very little energy penetrates the wall or the maximum electron density point.

(U) For polarization perpendicular to the plane of incidence, the electric field is given by

$$\underline{E} = \hat{\underline{i}}_x\, u(z)e^{iky\sin\theta}$$

where θ is the angle of incidence. The factor u(z) satisfies the differential equation

$$\frac{d^2u}{dz^2} + k^2\,\epsilon(z) - \sin^2\theta\; u = 0 \quad .$$

An exact solution of the above differential equation can be obtained, yielding

$$u = H_{\mu}^{(1)}(Be^{-bz/2})$$

where $H_{\mu}^{(1)}$ is the Hankel function of order

$$\mu = i\frac{2k}{b}\cos\theta \ .$$

The constant B is given by the relation

$$B = \frac{2k}{b}\sqrt{A(-\omega+i\nu)} \ .$$

The reflection coefficient R can be explicitly given as follows:

$$-R_{\perp} = \frac{1+\cos\theta\, Z}{1-\cos\theta\, Z}$$

with

$$Z = \sqrt{\epsilon_o/\mu_o}\ (E_x/H_y)_{z=0} = ik(u/u')_{z=0} \ .$$

It will be assumed that the outer surface of the sheath $(z = 0)$ will be such that

$$\left|\frac{2k}{b}\sqrt{\epsilon(0)-1}\right| \ll 1 \qquad (4.6)$$

implying that the electron density is extremely small there. The argument of the Hankel function is thus extremely small at $z = 0$, and the following is then obtained:

$$Z = \frac{1}{\cos\theta}\,\frac{1-(B/2)^{2\mu}A_{\mu}}{1+(B/2)^{2\mu}A_{\mu}}$$

where

$$A_{\mu} = e^{-i\mu\pi}\,\frac{\Gamma(1-\mu)}{\Gamma(1+\mu)} \ .$$

The reflection coefficient reduces to

$$R_{\perp} = -(B/2)^{-2\mu} e^{i\mu\pi} \frac{\Gamma(1+\mu)}{\Gamma(1-\mu)}$$

and its magnitude is given by

$$\left|R_{\perp}\right| = \exp\left[-\frac{2k}{b}\cos\theta(\pi-\alpha)\right]$$

The angle α lying in the range $\pi/2 \leqslant \alpha \leqslant \pi$, is the argument of $-\omega+i\nu$, and increases with increasing collision frequency. Thus when $\nu \gg \omega$, $\pi-\alpha \sim \pi/2$ and $\nu \ll \omega$, $\pi-\alpha \sim 0$, hence the magnitude of the exponent in the reflection coefficient increases with increasing collision frequency. Because of the scaling laws along the surface of the vehicle, b will decrease with an increase in position along the surface of the cone away from the tip. Thus it can be seen that $\left|R_{\perp}\right|$ decreases with an increase in collision frequency, an increase in position along the cone, or an increase in frequency. The calculations given by Figs. 4-4 through 4-13 illustrate the behavior for the cases where very little energy reaches the wall of the vehicle. It should be pointed out that profiles 4, 5, 6 and 7 (in that order) represent an increase in collision frequency. In addition, the magnitude of the reflection coefficient increases with increasing angle of incidence θ, as is demonstrated by the curves.

(U) To study the effect of large gradients, we will now assume that

$$2k/b \ll 1.$$

This implies that $|\mu| \ll 1$, in which case the following approximation is obtained:

$$Z \sim -\frac{k\pi}{b}\left\{1+\frac{i2}{\pi}\left[.55+\ell n(B/2)\right]\right\} .$$

The real part of Z is extremely small. The imaginary part of Z may be large or small depending upon the magnitude of $\ell n\, B$. In either case, it can be seen that the magnitude of $R_{\perp}$ is approximately unity,

$$\left|R_{\perp}\right| \sim 1 .$$

The sheath will act like a perfect conductor ($R_\perp = -1$) when the term in Z containing $\ell n\, B$ is small, i.e.

$$\left| \frac{2k}{b} \ell n(B/2) \right| \ll 1 .$$

This implies that

$$\left| \frac{k}{b} \left[\epsilon(-1/k) - 1 \right]^{1/2} \right| \gg 1 ,$$

where $\epsilon(-1/k)$ is the value of the relative dielectric constant at a distance $1/k$ from the sheath boundary.

(U)For the other polarization (in the plane of incidence), we shall directly assume the steep gradient case for which $2k/b \ll 1$. The magnetic field is given by

$$\underline{H} = \hat{\underline{i}}_x e^{iky \sin\theta} v(z)$$

where

$$\frac{d^2 v}{dz^2} - \frac{d\epsilon}{\epsilon\, dz} \cdot \frac{dv}{dz} + k^2 \left[\epsilon(z) - \sin^2\theta \right] v = 0 .$$

For steep gradients, the $\sin^2\theta$ term may be dropped, since the dominant behavior is given by $\epsilon(z)$. (The results for the other polarization could have been directly obtained by dropping the $\cos^2\theta$ term in the differential equation.) The solution of the resulting approximate equation, which can be expressed in the form

$$\frac{d}{dz} \left(\frac{1}{\epsilon} \frac{dv}{dz} \right) + k^2 v = 0$$

is easily obtained by setting

$$\frac{dv}{dz} = \epsilon w$$

and differentiating the above equation with respect to z. This yields the following

equation for w

$$\frac{d^2w}{dz^2} + k^2 \epsilon w = 0 ,$$

whose solution is given by

$$w = H_{\bar{\mu}}^{(1)}(Be^{-bz/2})$$

where $\bar{\mu} = i2k/b$.

(U) The original function v(z) is obtained through integration giving

$$v(z) = \zeta \frac{dH_{\bar{\mu}}^{(1)}}{d\zeta}(\zeta) , \qquad \zeta = Be^{-bz/2} .$$

The reflection coefficient R is given by the relation

$$R_{||} = \frac{\cos\theta + Z}{\cos\theta - Z} ,$$

$$Z = -\sqrt{\epsilon_o/\mu_o}\,(E_y/H_x)_{z=0} = -\frac{i}{k\epsilon(0)}\left[\frac{d\ell n\, v}{dz}\right]_{z=0} .$$

Employing the approximations indicated by inequalities (4.6) and (4.7) it follows that

$$Z \sim -\frac{\pi k}{b}\left[1 + i\frac{2}{\pi}(.577 + \ell n\, B/2)\right] .$$

It follows in a similar manner, that when $2k/b \ll \cos\theta$,

$$|R_{||}| \sim 1 .$$

(U) The results for both polarizations can be summed up by pointing out that the effect of the gradient type sheath upon incident radiation can be represented in terms of the impedance boundary condition

$$\underline{E} - (\underline{E} \cdot \underline{n})\underline{n} = \sqrt{\mu_o/\epsilon_o}\ \underline{n} \times \underline{H}$$

where

$$\eta = \frac{k\pi}{b}\left[1 + i\frac{2}{\pi}(.577 + \ell n\, B/2)\right]$$

and $\underline{n}$ is the unit outward normal to the surface, provided that inequalities (4.6) and (4.7) hold.

(U) It should be pointed out however, that the results of the case of polarization in the plane of incidence were derived from an approximate solution to the differential equation. A more accurate solution should be sought, possibly based upon the turning point analysis of Langer where b/k is taken to be a large parameter, to justify the analysis. Then, if possible, the analysis should be extended to curved surfaces, to determine more precisely the conditions for which a sheath with a very steep gradient can be represented by an impedance boundary condition.

4.4 The Radar Cross Section of the Re-entry Vehicle

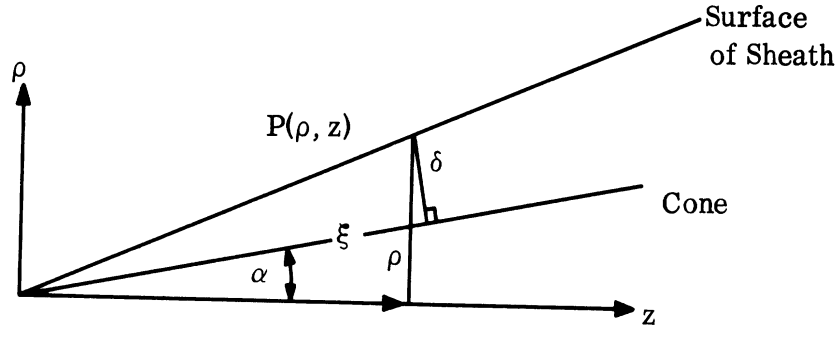

FIG. 4-14: GEOMETRY OF THE SHEATH

(U) Cylindrical polar coordinates (ρ, ϕ, z) will be used, where the z-axis is the axis of the cone of half-angle α. The coordinate ξ will be used for distance

along the cone from the tip. The thickness of the sheath at a distance ξ is given by

$$\delta(\xi) = \delta_1(\xi/13)^{\gamma}$$

where δ_1 is the thickness at a distance of 13 inches from the tip. The constant γ is the appropriate scaling factor, being .5 and .8 for profiles 3 and 4 through 7 respectively. The surface of the sheath specified as a function of ξ is given in the parametric form

$$\rho = \xi \sin\alpha + \cos\alpha\,\delta(\xi)$$

$$z = \xi \cos\alpha - \sin\alpha\,\delta(\xi) \ .$$

The unit outward normal to the surface of the sheath is

$$\underline{n} = \frac{1}{\sqrt{1+\gamma^2\delta^2\xi^{-2}}}\left[\underline{i}_\rho \frac{\partial z}{\partial \xi} - \underline{i}_z \frac{\partial \rho}{\partial \xi}\right] \ .$$

The element of surface dS is given by

$$dS = \rho\left[1+\left(\frac{\partial \rho}{\partial \xi}\right)^2\right]^{1/2} d\phi\, dz \ ,$$

can be expressed in terms of the coordinates (ξ, ϕ) as follows

$$dS = \rho\left[1+\gamma^2\delta^2\xi^{-2}\right]^{1/2} d\phi\, d\xi \ .$$

Physical Optics Integrals

(U) For evaluation of the physical optics integrals, given in the Second Quarterly Report, the direction of propagation of the incident wave $\underline{k}$ will be taken to lie in the $y=0$ plane, such that

$$\underline{\hat{k}} = -\underline{\hat{i}}_x \sin\theta_o + \underline{\hat{i}}_z \cos\theta_o \ .$$

The back scattered cross section for the broadside case ($\theta_o = \frac{\pi}{2} - \alpha$) is given by

$$\sigma(\frac{\pi}{2} - \alpha) = \frac{4\pi}{\lambda^2} \left| \int_{\text{Illuminated Region}} dS \left[\underline{\hat{k}} \cdot \underline{\hat{n}}\right] \left\{ R_\perp - \frac{(R_{||} + R_\perp)(\underline{\hat{n}} \cdot \underline{\hat{a}})^2}{\left[1 - (\underline{\hat{n}} \cdot \underline{\hat{k}})^2\right]} \right\} e^{2i\underline{k} \cdot \underline{r}} \right|^2$$

where $\underline{a}$ is the unit vector in the direction of the incident polarization. The illuminated region is given by the domain $-\pi/2 < \phi < \pi/2$. In the above expression, the cross-polarized term has been neglected, since this term will vanish, when the asymptotic technique, given below, is used to approximately evaluate the integrals.

(U) The integral is of the form

$$I = \iint d\phi \, d\xi \, J(\xi, \phi) \, e^{i2\underline{k} \cdot \underline{r}} \ ,$$

where

$$\underline{k} \cdot \underline{r} = -k\rho(\xi)\cos\alpha \cos\phi + kz(\xi)\sin\alpha \ .$$

For broadside, the dominant contribution to the back scattered field arises from the illuminated area of the sheath, away from the tip, i.e. $k\xi \gg 1$ or $k\rho > 1$. In the region of the tip, the local reflection coefficients obtained from the tangent plane approximation are invalid anyway. Thus neglecting the tip region, the above integral can be partly evaluated by means of the stationary phase technique, where it will be assumed that $J(\xi, \phi)$ is a slowly varying function of ϕ compared to $e^{2i\underline{k} \cdot \underline{r}}$. This implies that the phase of the reflection coefficients must vary slowly as compared to $2k\rho \cos\alpha \cos\phi$, i.e.:

$$\left| \text{Im} \frac{\partial \ell n R}{\partial \phi} \right| \ll 2k\rho \cos\alpha \sin\phi \ .$$

For $\xi > 13$ inches, the unit vector $\hat{\underline{n}}$ normal to the sheath is approximately the same as the unit vector normal to the cone, thus implying that $\phi/2$ is the local angle of incidence for the tangent plane approximation. The above condition thus reduces to

$$\left| \text{Im} \frac{\partial \ell n R}{\partial \cos\theta} \right| \ll k\rho \cos\alpha \cos\theta$$

where θ is the local angle of incidence to the tangent plane at the point $(\xi, 2\theta)$. The local reflection coefficients R are computed as functions of θ.

(U)Employing the stationary phase technique, the integral I is computed as follows:

$$I \sim \int d\xi\, J(\xi, 0) \exp\left\{2ik\left[z \sin\alpha - \rho \cos\alpha\right]\right\} \int_{-\infty}^{\infty} d\phi \exp\left\{ik\rho \cos\alpha \phi^2\right\}$$

$$\sim \int \frac{d\xi\, J(\xi, 0)}{\sqrt{k\rho \cos\alpha/\pi}} \exp\left\{2ik\left[z \sin\alpha - \rho \cos\alpha\right] + \pi/4\right\}$$

$$\sim \int \sqrt{\frac{d\xi}{k\rho \cos\alpha/\pi}}\, J(\xi, 0) \exp\left\{-2ik\,\delta(\xi)\right\} \ .$$

Since the results are not affected by taking either incident polarization, the vector $\hat{\underline{a}}$ will be taken to be $\hat{\underline{i}}_y$. In this case, the value of $J(\xi, 0)$ is

$$J(\xi, 0) = \left\{\rho(\hat{\underline{k}} \cdot \hat{\underline{n}}) R \left[1 + \gamma^2 \delta^2 \xi^{-2}\right]^{1/2}\right\}_{\phi=0} ,$$

which reduces to

$$J(\xi, 0) = -\rho(\xi) R_{\perp}(\xi, 0)$$

where $R_{\perp}$ is the reflection coefficient evaluated for normal incidence to the tangent plane. The cross section expression thus reduces to the form

$$\sigma(\frac{\pi}{2} - \alpha) = \frac{k}{\cos\alpha} \left| \int \sqrt{\rho}\, R_{\perp}(\xi, 0) \exp\left\{-2ik\delta(\xi)\right\} d\xi \right|^2 ,$$

where

$$\rho = \xi \sin\alpha + \cos\alpha\, \delta(\xi) ,$$

and

$$\delta(\xi) = \delta_1 (\xi/13)^{\gamma}$$

Slightly-Off Broadside

(S) More important than the broadside cross section is the cross section slightly off broadside where the angle θ_o is slightly perturbed from $\frac{\pi}{2} - \alpha$ by a small angle ϵ, i.e.:

$$\theta_o = \frac{\pi}{2} - \alpha - \epsilon \quad .$$

In this case

$$\hat{\underline{k}} = -\hat{\underline{i}}_x \cos(\alpha + \epsilon) + \hat{\underline{i}}_z \sin(\alpha + \epsilon) \ .$$

For the specular line on the surface $\phi = 0$,

$$\underline{k} \cdot \underline{r} = -k\rho(\xi)\cos(\alpha+\epsilon) + kz(\xi)\sin(\alpha+\epsilon)$$

$$= k\xi \sin\epsilon - k\delta(\xi)\cos\epsilon \ .$$

The main effect on the cross section for small ϵ is in the phase factor $\underline{k} \cdot \underline{r}$, thus

$$\sigma\left(\frac{\pi}{2} - \alpha - \epsilon\right) = \frac{k}{\cos\alpha}\left| \int \sqrt{\rho}\, R_{\perp}(\xi, 0) \exp\left\{-2ik\left[\delta(\xi)\cos\epsilon - \xi \sin\epsilon\right]\right\} d\xi \right|^2 .$$

For calculation of the cross section, we will neglect the effect of the tip region. The above integral does not hold in the immediate vicinity of the tip. We shall evaluate the integral in the region away from the tip, taking a lower limit on ξ to be $\xi = 13$ inches. Thus considering the contribution from the remaining region $\xi \geq 13$ inches, we can make a number of approximations. First we shall replace ξ by a dimensionless quantity t:

$$\xi/13 = t.$$

Thus the stations $\xi = 13$ inches, 26 inches, etc. correspond to $t = 1, 2, \ldots$, the points for which $R_{\perp}$ was computed. The lower limit of integration is now $t = 1$. To exclude the near wake region, the upper limit will be taken to be ℓ corresponding to a vehicle of slant-length 13ℓ inches.

(S) The following approximations can now be made for $t > 1$:

$$\rho \sim 13 \sin\alpha t$$

$$\delta(\xi) \sim .6\delta_1 [1 + t]$$

where δ_1 is the value of δ at $t = 1$. In this case the phase factor in the integral can be approximated as

$$2k\left[\delta(\xi)\cos\epsilon - \xi \sin\epsilon\right] \sim dt + g ,$$

where

$$d = 2k\left[.6\delta_1 - 13\epsilon\right] ,$$

δ_1 is in inches, and the small angle ϵ is in radians.

(S)For higher frequencies an approximation can be made which simplifies the calculation for a number of cases. For frequencies greater or equal to 1 GHz, it can be seen from Figs. 4-4, 4-5 and 4-6 that in the altitude range 100 K ft to 60 K ft the reflection coefficient

$$R_{\perp}(\xi, 0) = -R_{||}(\xi, 0)$$

is effectively independent of the material composition of the vehicle for values of $\xi > 13$ inches. In addition, the reflection coefficient can be approximated by the following expression for $t > 1$,

$$R_{\perp} = R_{\perp}(1) \exp\left\{(t-1)(-b+ic)\right\}$$

where $R_{\perp}(1)$ is the value of $R_{\perp}(\xi, 0)$ at $\xi = 13$ inches. With this representation, the cross section (in square meters) of the plasma-sheathed vehicle (neglecting the tip region $0 \leqslant t \leqslant 1$) is given by

$$\sigma\left(\frac{\pi}{2} - \alpha - \epsilon\right) = B\left|\int_1^{\ell} t^{1/2} R_{\perp}(1) \exp\left\{-b(t-1) + it(c-d)\right\} dt\right|^2$$

where

$$B = 7.5 f \tan\alpha \, 10^{-10} \quad , \quad f = \text{frequency} .$$

The important case arises when $c = d$, where the angle $\epsilon = \epsilon_o$ satisfies the relation

$$2k\left[.6\delta_1 - 13\epsilon_o\right] = c .$$

As an example, consider profile 4 where $\delta_1 \sim 1$, and at $f = 10^{10}$, $c \sim 4.75$ radians. In this case $\epsilon_o \sim .01$ radians.

(S)The cross section for the plasma-coated vehicle will be considered slightly off broadside at angle $\frac{\pi}{2} - \alpha - \epsilon_o$. In this case, we have

$$\sigma\left(\frac{\pi}{2} - \alpha - \epsilon_o\right) = B\left|\int_1^{\ell} t^{1/2} R_{\perp}(1) \exp\left\{-b(t-1)\right\} dt\right|^2 .$$

For the sake of comparison, we will normalize the cross section by comparing it to the broadside cross section for the perfectly conducting case, given by

$$\sigma_{p.c.}\left(\frac{\pi}{2} - \alpha\right) = B\left|\int_1^{\ell} t^{1/2} dt\right|^2 = B\left\{\frac{2}{3}\left[\ell^{3/2} - 1\right]\right\}^2 .$$

The normalized cross section is thus given by

$$\sigma_n = \left|\int_1^{\ell} t^{1/2} R(1) \exp\left\{-b(t-1)\right\} dt\right|^2 \Big/ \left[\frac{2}{3}\left(\ell^{3/2} - 1\right)\right]^2$$

Table IV-1 shows σ_n for a number of profiles and frequencies. The slant length of the vehicle is 13ℓ inches.

(S) The constant of normalization is given by

$$7.5 f \tan\alpha \, 10^{-10} \frac{4}{9} \ell^3$$

and has the following values for $\ell = 4$ and a cone half-angle of 11^o: 40 for 10 GHz, 20 for 5 GHz, and 4 for 1 GHz. The actual cross section in square meters is obtained by multiplying the normalized values (for $\ell = 4$) in the table by the appropriate normalization constant.

(S) For 150 K ft (profile 3), the change in the local reflection coefficient due to the sheath, for normal incidence, is very small, thus indicating that the broadside cross section is not significantly changed.

TABLE IV-1: σ_n NORMALIZED CROSS SECTION

(Slightly Off Broadside)

Altitude	Profile	Frequency	σ_n $\ell = 4$	σ_n $\ell = 9$
100 K ft	4	10^{10}	.23	.07
	4	5×10^9	.35	.16
	4	10^9	.58	.47
80 K ft	5	10^{10}	.12	.03
	5	5×10^9	.24	.09
	5	10^9	.6	.49
60 K ft	6	10^{10}	.04	.005
	6	5×10^9	.22	.08

The Nose-on Case

(S) The back scattered cross section for the nose-on case ($\theta_o = 0$) is given by

$$\sigma(\theta_o = 0) = \pi k^2 \left| \int \rho(\xi)\rho'(\xi)\left[-R_\perp(\xi) + R_{||}(\xi)\right] e^{2ikz}\, d\xi \right|^2 .$$

Approximate values of $R_\perp(\xi)$ and $R_{||}(\xi)$, the local reflection coefficients, are obtained from the results for the slab geometry, with the angle of incidence taken to be 79^o, and are given in Figs. 4-9 through 4-13. This is a good approximation except very near the tip, when the local angle of incidence will differ appreciably from 79^o. The precise value of the local angle of incidence is prescribed by the formula

$$\cos\theta = -\underline{n} \cdot \hat{\underline{i}}_z = \frac{\partial \rho}{\partial \xi} \left[1 + \gamma^2 \delta^2 \xi^{-2}\right]^{-1/2} \qquad (4.8)$$

where $\underline{n}$ is the unit outward normal to the sheath. For ξ greater than 1 inch the expression can be approximated by

$$\cos\theta \sim \sin\alpha + \gamma\cos\alpha(\delta_1/\xi)(\xi/13)^{\gamma} \quad .$$

For altitudes of 100 K ft and below, $\gamma = .8$ and δ_1 (thickness of sheath at $\xi = 13''$) is at most about 1 inch, decreasing with a decrease in altitude. For a cone half-angle of 11^{o} and with $\delta_1 = 1$ inch, θ is approximately 76^{o} at $\xi = 13$ inches increasing to the value of 79^{o} as ξ increases.

(S)Because of lack of sufficient knowledge (namely the behavior of the sheath at the rear of the vehicle), and because of the approximations involved, precise estimates of the nose-on cross section cannot be given. However, very important sheath effects are immediately evident upon the interpretation of the results for the local reflection coefficients. The amplitude of the local reflection coefficients are slowly varying functions of ξ, except near the tip. The variation in their phases (the calculated results are not presented here) are very small compared to the phase $2kz(\xi)$ in the physical optics integral. This means that the integrand of the physical optics integral is a rapidly oscillating function, and the dominant contribution arises from the end points. The contribution from the end point $\xi = 0$, would yield the tip scattered field. To obtain a physical optics estimate of this, the reflection coefficients $R_{\perp}(\xi)$ and $R_{||}(\xi)$ would have to be computed in the range $0 \leqslant \xi \leqslant 13''$, for the value of local angle of incidence given by (4.8). However, at the present time it is doubtful whether this would yield a good answer since physical optics really is involved near the tip. A more precise technique is required.

(S) More important is the observation that for a number of cases (100 K ft and below) the local reflection coefficient at a sufficient distance from the tip is independent of the material properties of the vehicle. This means that the rear of the vehicle is shielded by the sheath, and thus the sheath will significantly reduce the cross section (especially for flat-backed cones). The return from the rear vicinity of the vehicle will only depend upon the behavior of the sheath: whether it expands, bends inward to the neck of the near wake, or has a discontinuity in the vicinity of

the rear of the vehicle. The shielding effect displayed as a function of altitude and frequency is given in Fig. 4-15. The curves are obtained from Figs. 4-9 through 4-13 by estimating the minimum slant distance from the tip, for which the reflection coefficients corresponding to the two different cone materials, perfect conductor and absorber, coincide for a particular frequency and altitude. Figure 4-15 can be used to estimate when the nose-on cross section of a re-entry vehicle is significantly reduced by the sheath shielding the rear, which effectively kills what is usually the dominant return, be it the creeping wave return for a cone-sphere, or the edge return from a flat-backed cone. For a fixed frequency and altitude, any vehicle of slant length greater than or equal to the length denoted by the appropriate point on the curve will have significant nose-on cross section reduction.

4.5 Comments and Recommendations

(S) The physical optics approach, although a crude first-order tool, has yielded some general results. However, to obtain precise results, not only should the physical optics approach be improved by taking into account the local curvature effects in the computation of the local reflection coefficients, but of more importance, other phenomena should be included which are not contained in the physical optics cold plasma approximation. Among these phenomena are surface waves, creeping waves, temperature effects of the plasma, and turbulent velocity effects of the sheath. A brief review of the phenomena that should be immediately looked into, and the approach to be taken is given below.

Surface Waves

(S) Under certain cases (especially for sheaths like the 150 K ft contaminated case) surface waves can be launched on dielectric structures, which for nose-on back scattering can produce a significant return. A theoretical and experimental approach to the surface wave phenomena should be undertaken. The theoretical analysis will be limited to investigations of the properties (phase velocity etc.) of

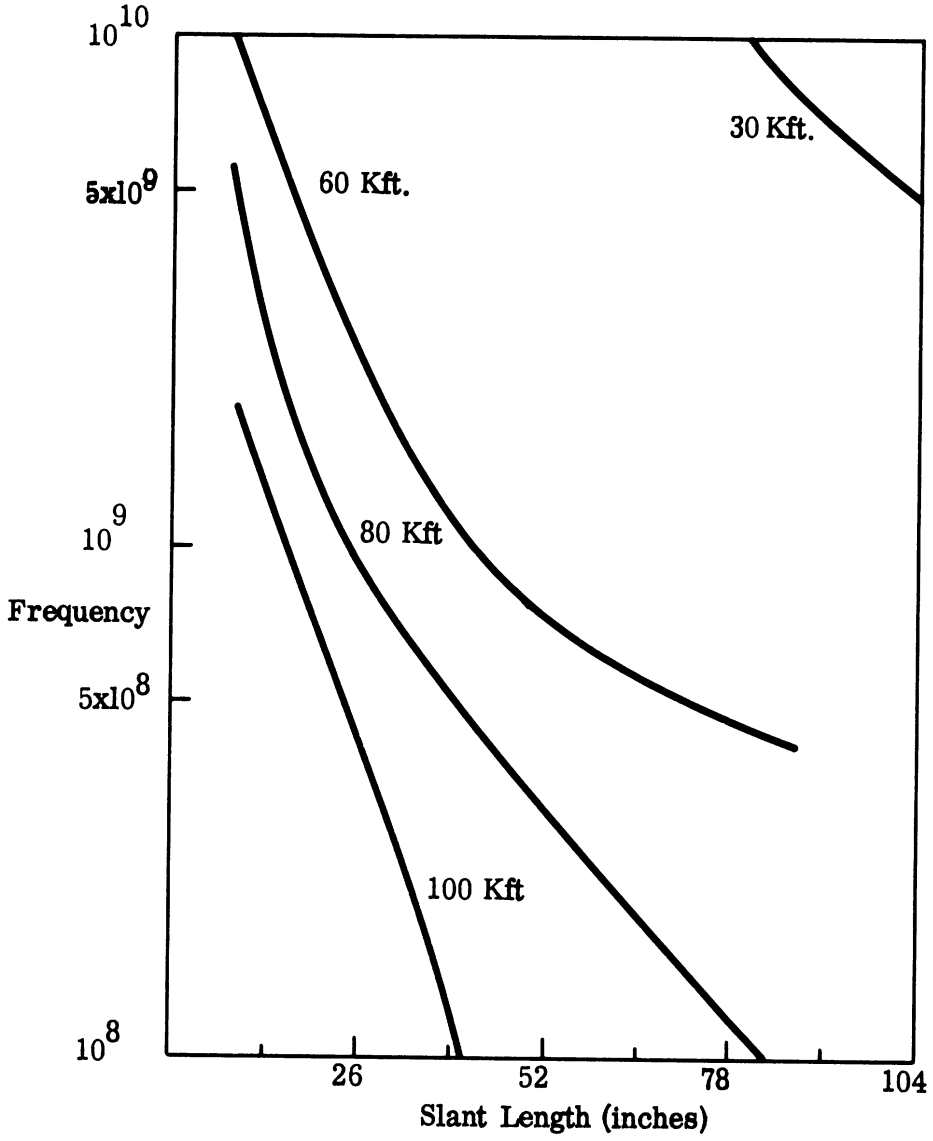

FIG. 4-15: PLASMA SHIELDING EFFECT OF REAR OF VEHICLE

the modes that can propagate on plasma-coated circular cylinders. To obtain the appropriate launch factors, and to assist in the extrapolation of the results derived for a cylinder to a conical surface, an experimental program should be undertaken. The experimental program should employ measurements of the surface field on a cone covered by a simulated plasma sheath (non-lossy). Effects of collisions on the attenuated portions of the surface waves should be included.

Tip Region

(S) The physical optics approximation is not valid in the tip region of the cone. To obtain a better estimate of cross section, more precise evaluation of the surface fields is required. Because of the state of the present art, concentration should be limited to plasma sheaths that can be represented by an impedance boundary condition. There are two types, (i) homogeneous layer (high index of refraction), and (ii) large gradient type. The large gradient types require additional analysis, and additional study (of a more accurate nature than has been done) should be performed, taking into account (if possible) the geometry of the surface.

(U) The computer program described in Appendix B may be extended to handle coated bodies and used at a later date to generate surface field data on the conical surface.

Effects of Rear-end Termination

(S)Because of lack of knowledge of the characteristics of the sheath just beyond the rear of the vehicle, the analysis that is first performed should be more of a qualitative nature. Comparison should be made of the effect on the back scattered field caused by different longitudinal sheath geometries in the rear of the vehicle, types of geometry being characterized by a smooth convex surface, or a wedge type discontinuity.

Temperature Effects

(S)For sheaths with small collision frequency and similar electron density profiles such as that of 150K ft contaminated case (profile 3), temperature effects

should be included to determine if there is significant energy launched into the plasma wave. Both the exact approach based on the coupled Vlasov-Maxwell equations and the hydrodynamical approach should be used.

V
THEORETICAL STUDIES

5.1 Introduction

(S) The prediction of radar scattering by a coated re-entry shape requires classification by the electrical properties of the coatings as well as by the frequency regime. These two classifications are related, leading to computational, if not conceptual, complexity in solving the scattering problem. Because of this complexity we present a brief conceptual description of the problem as an introduction to the use of the methods of calculation which follow.

(S) The coating problem is simplest whenever the continuity condition at the interface can be approximated as an impedance boundary condition, that is, the requirement that the tangential electric and magnetic fields be continuous at the interface

$$H_t,\ E_t \text{ continuous} \tag{5.1}$$

becomes to some approximation

$$E_t = Z H_t \tag{5.2}$$

at the boundary. Provided Z is a global quantity, the same for the entire diffracting surface, (5.2) leads to a description of the scattering which is a direct generalization of the treatment used for the perfectly conducting case. Before we consider this impedance boundary value problem we will discuss the origin and limitations of (5.2).

(S) The boundary condition (5.2) is exact for the reflection of electromagnetic waves from the boundary of a half-space, that is, if the region $z \geqslant 0$ is characterized by the electric quantities ϵ and μ and the region $z \leqslant 0$ is free space, $\epsilon = \mu = 1$, then on the boundary $z = 0$

$$E_t = \eta H_t \; ; \qquad \eta = \sqrt{\mu/\epsilon} \; . \tag{5.3}$$

From this we give the physical interpretation that if the energy penetrating the boundary can be assumed to not return to the boundary, the condition (5.3) is valid. In considering the other "solvable" coating problems we will see that this requirement is approximately met provided the coating absorbs sufficient of the energy that penetrates the boundary and provided the radius of curvature of the boundary is sufficiently large.

5.2 Creeping Waves on Coated Shapes

(S) In the high frequency to resonance region the field scattered from a coated cone-sphere can be decomposed in the same way as that from a perfectly conducting cone-sphere. That is, the contribution to the scattered field can be taken as arising from:

1) the tip,
2) the join,
3) creeping waves,

and 4) specular reflection.

Provided the coating is such as to justify using an impedance boundary condition, all but the creeping wave contribution can be represented simply as the perfectly conducting contribution modified by an appropriate factor, a reflection coefficient. However, the creeping wave is essentially different. The tip, join and specular returns are local phenomena since only the surface field induced at positions of the tip, join and specular regions are required to determine the contributions.

(S) The creeping wave is a global phenomenon since the wave is entrained and travels over the coated surface. For this reason the determination of the creeping wave contribution is more difficult and unlike the perfectly conducting case cannot be described in terms of a single function of ka alone. In fact, we are faced with a new problem for each change in frequency or electrical properties.

(S) The creeping wave analysis is formally similar to that for the perfectly conducting case. We start with an analysis of creeping waves on a coated sphere rather than a conducting sphere, determine the form and validity of an impedance boundary condition and then find a representation by means of the Watson transform. The differences between the two cases lie in the determination of the poles of the Watson representation; they depend on the frequency and electrical properties, and in the appearance of a tangential electrical field which can be the dominant contributor for magnetic materials.

(S) We suppose a plane wave

$$\vec{E}_o = \hat{x} e^{ikz} \tag{5.4}$$

incident on a coated sphere of outer radius b coated with a material of complex relative indices ϵ, μ of thickness b - a, with the inner sphere of radius a perfectly conducting. By a straightforward analysis we find the single circuit creeping wave contribution to the back scattered amplitude to be

$$S^c(0) = -\pi \sum_n \left[\frac{\nu \left(\zeta^{(2)'}_{\nu-1/2}(kb) - Z_e \zeta^{(2)}_{\nu-1/2}(kb) \right)}{\frac{\partial}{\partial \nu} \left(\zeta^{(1)'}_{\nu-1/2}(kb) - Z_e \zeta^{(1)}_{\nu-1/2}(kb) \right)} \right]_{\nu=\nu_n} e^{i\nu_n \pi}$$

$$+ \pi \sum_\ell \left[\frac{\nu \left(\zeta^{(2)'}_{\nu-1/2}(kb) - Z_m \zeta^{(2)}_{\nu-1/2}(kb) \right)}{\frac{\partial}{\partial \nu} \left(\zeta^{(1)'}_{\nu-1/2}(kb) - Z_m \zeta^{(1)}_{\nu-1/2}(kb) \right)} \right]_{\nu=\nu_\ell} e^{i\nu_\ell \pi} \tag{5.5}$$

where the ν_n are the roots of

$$\xi^{(1)'}_{\nu-1/2}(kb) - Z_e \xi^{(1)}_{\nu-1/2}(kb) = 0 \tag{5.6}$$

and the ν_ℓ are roots of

$$\xi^{(1)'}_{\nu-1/2}(kb) - Z_m \xi^{(1)}_{\nu-1/2}(kb) = 0 \tag{5.7}$$

The Z's are the modal impedances

$$Z_e = \eta \frac{\psi'_{\nu-1/2}(k_1 b) - \frac{\psi'_{\nu-1/2}(k_1 a)}{\xi^{(1)'}_{\nu-1/2}(k_1 a)} \xi^{(1)'}_{\nu-1/2}(k_1 b)}{\psi_{\nu-1/2}(k_1 b) - \frac{\psi'_{\nu-1/2}(k_1 a)}{\xi^{(1)'}_{\nu-1/2}(k_1 a)} \xi^{(1)}_{\nu-1/2}(k_1 b)} \tag{5.8}$$

$$Z_m = \frac{1}{\eta} \frac{\psi'_{\nu-1/2}(k_1 b) - \frac{\psi_{\nu-1/2}(k_1 a)}{\xi^{(1)}_{\nu-1/2}(k_1 a)} \xi^{(1)'}_{\nu-1/2}(k_1 b)}{\psi_{\nu-1/2}(k_1 b) - \frac{\psi_{\nu-1/2}(k_1 a)}{\xi^{(1)}_{\nu-1/2}(k_1 a)} \xi^{(1)}_{\nu-1/2}(k_1 b)} \tag{5.9}$$

where $k_1 = \sqrt{\mu\epsilon}$.

If $k_1 a$ is sufficiently large we may use the asymptotic forms for the functions in (5.8) and (5.9) and find

$$Z_e \cong -\eta \tan\left[k_1(b-a)\right] \tag{5.10}$$

$$Z_m \cong +\frac{1}{\eta} \cot\left[k_1(b-a)\right] = -\frac{1}{Z_e} \tag{5.11}$$

where we note these are independent of ν so the root equation is of the form

$$\zeta^{(1)'}_{\nu-1/2}(kb)+\eta\tan k_1(b-a)\,\zeta^{(1)}_{\nu-1/2}(kb) = 0 \tag{5.12a}$$

$$\zeta^{(1)'}_{\nu-1/2}(kb)+\frac{1}{\eta}\cot k_1(b-a)\zeta^{(1)}_{\nu-1/2}(kb) = 0 \ . \tag{5.12b}$$

The justification of the approximations (5.10) and (5.11) can now be tested since it is known that the first roots of (5.12a) are of the form

$$\nu = kb+O\left((kb)^{1/3}\right) \tag{5.13}$$

and the use of the asymptotic forms is valid for $\nu^2/k_1a<1$, hence we require

$$\left|\frac{k^2b^2}{k_1a}\right|<1 \qquad \text{or} \qquad \frac{kb^2}{a}<\left|\sqrt{\mu\epsilon}\right| \ . \tag{5.14}$$

(S) We now suppose the condition that the Z's be independent of ν is met. We then expand the functions $\zeta^{(1)}$ and $\zeta^{(1)'}$ in the Airy functions $w_1(t)$, $w_1'(t)$ where

$$t = (2/kb)^{1/3}(\nu-kb) = \frac{1}{m}(\nu-kb) \tag{5.15}$$

$$\zeta^{(1)}_{\nu-1/2}(kb) = -im^{1/2}w_1(t)\left[1-\frac{t}{15}\frac{1}{m^2}+\left(\frac{t^5}{7200}+\frac{13t^2}{1260}\right)\frac{1}{m^4}\right]$$

$$-im^{1/2}w_1'(t)\left[-\frac{t^2}{60}\frac{1}{m^2}+\left(\frac{t^3}{420}+\frac{1}{140}\right)\frac{1}{m^4}\right]+O\left(\frac{1}{m^6}\right) \tag{5.16}$$

$$\zeta^{(1)'}_{\nu-1/2}(kb) = \frac{i}{m^{1/2}} w_1'(t)\left[1+\frac{t}{15}\frac{1}{m^2}+\left(\frac{t^5}{7200}-\frac{17t^2}{5040}\right)\frac{1}{m^4}\right]$$

$$+\frac{i}{m^{1/2}} w_1(t)\left[-\left(\frac{t^3}{60}+\frac{3}{20}\right)\frac{1}{m}+\frac{t^4}{3360}\frac{1}{m^4}\right]+O\left(\frac{1}{m^6}\right) . \quad (5.17)$$

Keeping only the first terms on substituting in (5.12a) we find the root equations are approximated by

$$w_1'(t)-q_e w_1(t) = 0 \quad (5.18)$$

$$w_1'(t)-q_m w_1(t) = 0 \quad (5.19)$$

where

$$q_e = m\eta \tan k_1(k-a)$$

$$q_m = m\frac{1}{\eta}\cot k_1(b-a) . \quad (5.20)$$

The equations (5.18) and (5.19) are of the form given by Fock (1945) using the Leontovich boundary condition and extensively studied by Logan (1965). To obtain a better approximation, say for approaching the resonance region, the procedure is to expand the expressions (5.16) and (5.17) about the roots of (5.18) or (5.19) so that on substituting in (5.12b) we have an algebraic equation for the difference between the roots of (5.12a) and (5.18); (5.12b) and (5.19).

(S) On returning to (5.6) we observe that at the value $\nu = \nu_n$ or $\nu = \nu_\ell$ the denominator can be written as

$$\xi^{(2)'}_{\nu-1/2}(kb) - Z\,\xi^{(2)}_{\nu-1/2}(kb) = \frac{W\left(\xi^{(1)}_{\nu-1/2}, \xi^{(2)}_{\nu-1/2}\right)}{\xi^{(1)}_{\nu-1/2}(kb)} \tag{5.21}$$

where W is the Wronskian

$$W\left(\xi^{(1)}_{\nu}, \xi^{(2)}_{\nu}\right) = -2i \tag{5.22}$$

hence equation (5.6) becomes

$$S^c(0) = 2\pi i \sum_n \frac{\nu_n e^{i\nu_n \pi}}{\xi^{(1)}_{\nu_n-1/2}(kb)\,\frac{\partial}{\partial\nu}\left[\xi^{(1)'}_{\nu-1/2}(kb) - Z_e \xi^{(1)}_{\nu-1/2}(kb)\right]_{\nu=\nu_n}}$$

$$- 2\pi i \sum_\ell \frac{\nu_\ell e^{i\nu_n \pi}}{\xi^{(1)}_{\nu_\ell-1/2}(kb)\,\frac{\partial}{\partial\nu}\left[\xi^{(1)'}_{\nu-1/2}(kb) - Z_m \xi^{(1)}_{\nu-1/2}(kb)\right]_{\nu=\nu_\ell}} . \tag{5.23}$$

(S) On substituting the expansions (5.16) and (5.17) and retaining only the leading terms in (5.23)

$$S^e(0) = m^4 e^{ika\pi - i\frac{\pi}{6}} \left\{ \sum_n \frac{1}{(\beta_n - e^{-i\frac{\pi}{3}} q_e^2) Ai^2(-\beta_n)} \right.$$

$$\left. - \sum_\ell \frac{q_m^2}{(q_m^2 - e^{i\frac{\pi}{3}} \beta_\ell) Ai'^2(-\beta_\ell)} \right\} \tag{5.24}$$

where the Ai are Airy integrals and β_n satisfies

$$Ai'(-\beta_n) - q_e Ai(-\beta_n) = 0$$

$$q_e = -Z_e m \tag{5.25}$$

while β_ℓ satisfies

$$Ai'(-\beta_\ell) - q_m Ai(-\beta_\ell) = 0$$

$$q_m = -Z_m m \tag{5.26}$$

and $$m = (kb/2)^{1/3} .$$

(S) Equation (5.24) is in a form which is reasonably amenable to numerical methods (Logan, 1965) but any finer approximation leads to an exceedingly more difficult numerical problem in using this creeping wave formalism. Because of this we repeat the assumptions that we have made in arriving at (5.24). The first was that the impedance boundary condition was valid so that Z_m and Z_e do not depend on the order ν. Equivalently

$$\frac{kb^2}{a} < \sqrt{\mu\epsilon} .$$

The second was that kb is large enough that we may neglect all but the first terms in (5.16) and (5.17), that is, approximately, $kb \gtrsim 6$.

(S) Because of the dilemma presented by these requirements we will turn again to behavior of the impedances as functions of the radii, thicknesses and electrical properties.

(S) Equation (5.24) is in a form natural for going to the perfectly conducting limit

$$q_e \to 0 , \qquad q_m \to \infty \tag{5.27}$$

so that

$$S^c_{p.c.}(0) = m^4 e^{ika\pi - i\frac{\pi}{6}} \left\{ \sum_n \frac{1}{\beta_n Ai^2(-\beta_n)} - \sum_\ell \frac{1}{Ai'^2(-\beta_\ell)} \right\} \tag{5.28}$$

where the β_n are the roots

$$Ai'(-\beta) = 0$$

and the β_ℓ are the roots

$$Ai(-\beta_\ell) = 0 .$$

If the contrary limit is taken

$$q_e \to \infty , \qquad q_m \to 0 \tag{5.29}$$

we have a perfect magnetic material and the scattering amplitude is also in fact given by (5.28).

(S) We note that in both the above cases the criteria are met and in fact we can take the solution into the resonance region by a more careful handling of the root equation and the approximation to the spherical Hankel functions (Goodrich et al, 1965). By this we also conclude that materials which are "good" electric or magnetic conductors will satisfy our criteria and the simpler formalism may be used for $ka > 6$.

(S) The use of the simpler creeping wave representation is not restricted to lossy materials; in fact, we only require $|\sqrt{\mu\epsilon}| > kb^2/a$. In this case Logan (1965) has shown the magnetic wave contribution increases, the electric wave contribution decreases as the intrinsic impedance $\eta = \sqrt{\mu/\epsilon}$ increases.

(S) We now examine the behavior of the root equation including the next higher order term in the modal impedances. We find

$$Z_e = Z_e^{(0)} \left(1 - \frac{\nu^2}{4k_1 a} \frac{b-a}{b} \frac{1}{\sin 2k_1(b-a)}\right) . \tag{5.30}$$

Taking $\nu \sim kb$, $k_1 = k_R + ik_I$. The behavior of the second term in the parentheses can be shown to be bounded in absolute value by

$$e^{-2k_I(b-a)} \frac{k(b-a)}{k_1 a} (kb/2) \tag{5.31}$$

provided $k_I(b-a) > 2$. From this estimate we conclude that the simple theory can be used provided the parameters k_I, k_1, b, a, and k are such as to make (5.31) less than 0.1. In this case we estimate the error in the creeping wave return to be approximately 2 db. For the magnetic type field we obtain a different expression in place of (5.30) but precisely the same estimate (5.31) and hence the same criterion for applying the simple theory.

(S) In conclusion, we note that the restriction (5.14) on the use of (5.24) is overly restrictive for lossy coatings, whereas we require the looser restriction

$$e^{-2k_I(b-a)} \frac{k(b-a)}{|k_1 a|} (kb/2) < 0.1 , \tag{5.32}$$

leading to an error in the creeping wave cross section of less than 2.0 db.

5.3 Creeping Wave Enhancement

(S) The counterpart of the creeping wave enhancement problem is further complicated by the behavior of the surface fields on the conical portion of the coated cone-sphere. We observed experimentally a seemingly anomalous behavior of the coated cone surface field in that near the tip the field rose from its expected value to near the perfectly conducting value and then fell off approaching the value corresponding to the high frequency limit for the electrical properties of the coating. We give a qualitative picture of this in Fig. 5-1.

(S) If now the cone is terminated beyond the decay region the enhancement problem is analogous to that for the perfectly conducting case. We develop the method of treatment in Appendix A. On the other hand, if the termination is made in the decay region, the enhancement problem is essentially complicated in two ways. First, we need some method of predicting the field in the decay region. Second, we need a new enhancement treatment since the field on the conical portion is not now a constant.

(S) The first problem is met by the use of a simple model of the coated cone. We assume at each point of the cone that the field induced is that which would be induced on an infinite cylinder having the same coating and having the transverse radius of the cone at that point. This model leads to surprisingly good agreement.

(S) The second problem is not solved but avoided by observing that for all cases of interest the cone field is essentially constant at the cone-base join. Since the greater part of the decay occurs within a wavelength of the tip, the contrary case would not lead to the creeping wave phenomenon anyway.

(S) In passing, we note that the cone field anomaly will be of significance if any perturbations such as antennas are located in the large field region.

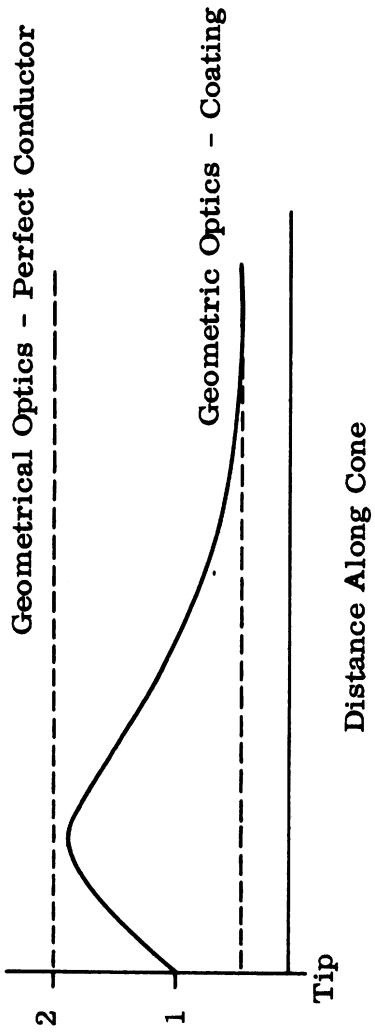

FIG. 5-1: SURFACE FIELD ON A COATED CONE (QUALITATIVE).

5.4 Scattering from a Shape with Rear Indentation

(S) We now consider the scattering from a cone with a smooth, axially symmetric concave base as in Fig. 5-2. This shape typifies the Mark-12 re-entry vehicle.

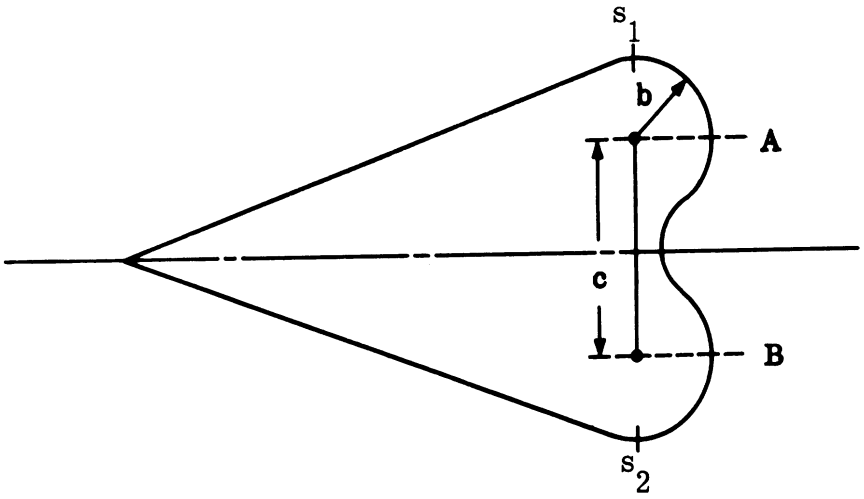

FIG. 5-2: RE-ENTRY VEHICLE WITH INDENTED TERMINATION.

(S) For the sake of a physical discussion we first confine ourselves to the case of symmetric illumination, that is, incidence along the cone axis with the indented base in the shadow. If the radius b is such that the rear bulge can support a creeping wave, $kb > 1$, we would expect the main creeping wave contribution to arise from energy that creeps from the shadow boundary s_1 to the point A. Then that energy which comes off tangentially at A leaps to B, then creeps to the shadow boundary s_2. The energy that follows the surface into the concavity will be much more strongly attenuated, exponentially as a creeping wave until the curvature changes, then geometrically as a whispering gallery wave on the negative curvature portion, than that which leaps across.

(S) The problem then is broken up into determining the amount of energy reaching A from s_1, determining the amount entrained at B, and finally the amount reaching s_2. For the first part of the problem we note that the transverse radius of curvature in going from s_1 to A is much larger than that in the direction of the

wave. This suggests that we can suitably modify the expression for the creeping waves on a cylinder in order to describe the behavior going from s_1 to A.

(S) Since we wish here to investigate a creeping wave phenomenon we will start with the asymptotic analysis of Fock which has found its most careful and complete explication in the work of Logan (1959). We restrict the range of application to $kR_{min} > 6$ where R_{min} is the minimum radius of curvature at s_1 or A.

(S) We assume an incident plane wave at s_1 polarized normal to the surface at s_1. This wave creeps to the point A and the emergent magnetic field in the direction of the tangent at A is given by

$$\vec{H}_A = \hat{\tau} \frac{e^{ikr}}{\sqrt{kr}} \sqrt{2}\, e^{i\frac{\pi}{4}} \hat{q}(\xi_A) \tag{5.33}$$

where $\hat{\tau}$ is a unit vector perpendicular to the tangent at A and the normal at A, r is the distance from A, and $\hat{q}$ is the function

$$\hat{q}(\xi) = \frac{1}{\sqrt{\pi}} \int_{-\infty}^{\infty} e^{i\xi t} \frac{v'(t)}{w_1'(t)}\, dt \tag{5.34}$$

where v and w_1 are the Airy functions

$$\begin{aligned} v(t) &= \sqrt{\pi}\, Ai(t) \\ w_1(t) &= \sqrt{\pi} \left\{ Bi(t) - iAi(t) \right\} \\ w'(t) &= \frac{d}{dt} w(t) \end{aligned} \tag{5.35}$$

and ξ is the line integral

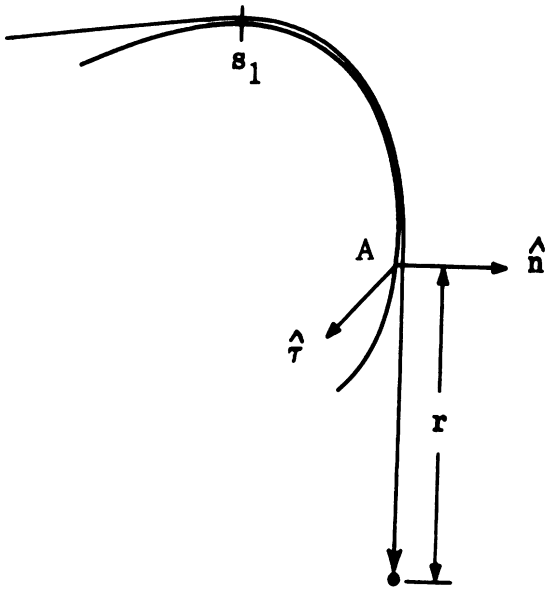

FIG. 5-3: CREEPING WAVE GEOMETRY

$$\xi = \int_{s_1}^{A} \frac{ds}{R} (kR/2)^{1/3} \tag{5.36}$$

where R is the radius of curvature at the point on the surface a distance s from s_1. This wave in turn is entrained at B and by the same argument leaves the point s_2 with the amplitude

$$\vec{H}_\perp = \hat{\tau}_f \frac{e^{ikr}}{kr} \sqrt{2\pi}\, i\hat{q}(\xi_A)\hat{q}(\xi_B) \frac{e^{ikc}}{\sqrt{kc}} \tag{5.37}$$

where

$$\xi_B = \int_{B}^{s_2} \frac{ds}{R} (kR/2)^{1/3} .$$

(S) This is a similar argument leading to the behavior of an incident wave of the orthogonal polarization. In this case the expression for the field involves the function

$$\hat{p}(\xi) = \frac{1}{\sqrt{\pi}} \int_{-\infty}^{\infty} dt\, e^{i\xi t} \frac{v(t)}{w(t)} \tag{5.38}$$

so that

$$\vec{H}_{||} = \hat{\tau}'_f \frac{e^{ikr}}{kr} \sqrt{2\pi}\, i\hat{p}(\xi_A)\hat{p}(\xi_B) \frac{e^{ikc}}{\sqrt{kc}} \tag{5.39}$$

(S) The $H_\perp$ term is much larger than the $H_{||}$ term so for the case of symmetric illumination we approximate the scattering amplitude by

$$s_c^{\perp}(0) = \pi a i \sqrt{2\pi}\, \hat{q}(\xi_A)\hat{q}(\xi_B)\frac{e^{ikc}}{\sqrt{kc}} \quad . \tag{5.40}$$

(S) If the illumination is not symmetric the fact that the base is not a sphere leads to the diffuse caustic phenomenon so that the return is highly polarization dependent. In this case there is a single symmetric creeping wave path so the polarization of the wave entrained on this path will determine the size of the return.

(U) The functions $\hat{p}$ and $\hat{q}$ have been extensively tabulated by Logan (1959).

(S) To refine this description, that is, to reduce the restriction on the frequency, we are faced with the problems of first, finding a refinement of the creeping wave formalism; secondly, discovering a method of making the transition from creeping waves to traveling waves as the frequency is increased. The first problem has been solved by Hong (1966) using local geodesic coordinates, the second problem is to be studied in the coming year.

(S) To apply the Hong correction it is necessary to express $\hat{p}$ and $\hat{q}$ as residue series. These are, for $\xi > 0$,

$$\hat{p}(\xi) = \frac{1}{2\sqrt{\pi}} e^{i\frac{5\pi}{6}} \sum_{s=1}^{\infty} \exp\left\{ie^{i\frac{\pi}{3}}\xi\beta_s\right\} \frac{1}{\left[Ai'(-\beta_s)\right]^2} \tag{5.41}$$

where $Ai(-\beta_s) = 0$;

$$\hat{q}(\xi) = \frac{1}{2\sqrt{\pi}} e^{i\frac{5\pi}{6}} \sum_{s=1}^{\infty} \exp\left\{ie^{i\frac{\pi}{3}}\xi\alpha_s\right\} \frac{1}{\alpha_s\left[Ai(-\alpha_s)\right]^2} \tag{5.42}$$

where $Ai'(-\alpha_s) = 0$.

(S) To make the corrections to $\hat{p}$ and $\hat{q}$ we use the quantity

$$M(s) = \left(\frac{kR(s)}{2}\right)^{1/3} \tag{5.43}$$

where R is the radius of curvature at the point s on the boundary (measured from s_1 to A and from B to s_2 in our case). We obtain the new expressions

$$\hat{P}(\xi) = \left(\frac{M(0)}{M(s)}\right)^{1/2} \hat{p}(\xi)\left[1+O\left(\frac{1}{M^3}\right)\right] \tag{5.44}$$

$$\hat{Q}(\xi) = \left(\frac{M(0)}{M(s)}\right)^{1/2} \left\{\hat{q}(\xi)+\frac{1}{2\sqrt{\pi}}\, e^{i\frac{5\pi}{6}} \sum_{s=1}^{\infty} \exp\left\{ie^{i\frac{\pi}{3}}\xi\alpha_2\right\} \frac{1}{\alpha_s\left[Ai(-\alpha_s)\right]^2} \cdot \right.$$

$$\left. \cdot \frac{e^{i\frac{\pi}{3}} 2^{2/3}}{M^2(0)} \left[-\frac{\beta_s}{30} - \frac{1}{10\beta_s^2}\right] + O\left(\frac{1}{M^3}\right)\right\} . \tag{5.45}$$

5.5 Creeping Waves on Coated Non-Spherical Surfaces

(S) The prediction of creeping waves on a coated surface of varying curvature is essentially complicated by the fact that the asymptotic analysis leads to a boundary condition that is a function of the varying curvature. Using the asymptotic theory of Fock we are faced with the problem of determining the function giving the surface field

$$V(\xi, q) = \frac{1}{\sqrt{\pi}} \int_{-\infty}^{\infty} \frac{e^{i\xi t}}{\omega_1'(t) - q\omega_1(t)}\, dt \tag{5.46}$$

where

$$\omega_1(t) = \sqrt{\pi}\left[Ai(t)+iBi(t)\right]$$

and

$$q = \alpha\ (kR/2)^{1/3},$$

$R = R(\xi)$, the radius of curvature at ξ ,

and where α depends upon the electrical properties of the coating. For any segment of the surface for which the variation in R is negligible, say on $\xi_1 \leq \xi \leq \xi_2$, the field can be found in terms of the initial value $V_1(\xi_1, q)$ and the evaluation of equation (5.46). We will use this approach assuming the frequency is sufficiently large that the asymptotic theory is valid and the residue series representation of (5.46) may be used, that is, for a fixed q

$$V(\xi, q) = 2i\sqrt{\pi} \sum \frac{e^{i\xi t_s}}{\left[\frac{d}{dt}\left(\omega_1'(t) - q\omega_1(t)\right)\right]_{t_s}} \tag{5.47}$$

where t_s is a root of

$$\omega_1'(t) - q\omega_1(t) = 0 \ . \tag{5.48}$$

(S) We now repeatedly apply the creeping wave analysis of Fock (1945) to small segments of the surface on which the curvature is sensibly constant. To do this we take as the canonical problem the diffraction by a parabolic cylinder. Let the parabola be given by

$$x = -\frac{y^2}{2R_o} \tag{5.49}$$

with the incident wave

$$\psi_o = e^{iky} \tag{5.50}$$

as in Fig. 5-4.

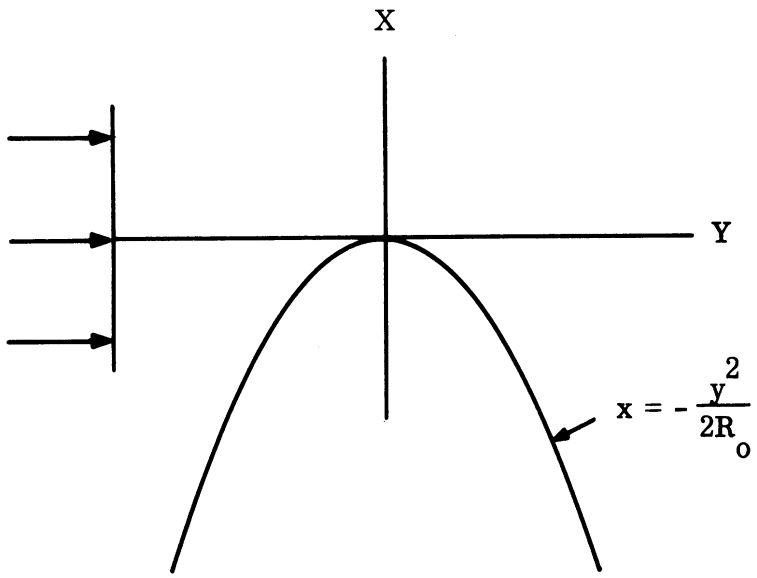

FIG. 5-4: PARABOLA GEOMETRY.

(S) We parameterize the problem in the usual way defining

$$\xi = \int_0^s \frac{ds}{R} \left(\frac{kR}{2}\right)^{1/3} , \tag{5.51}$$

where s is the arc length measured from the shadow boundary and R is the radius of curvature at the point s;

$$\left(\frac{kR}{2}\right)^{1/3} \equiv m = m_o \cosh \frac{\xi}{m_o} , \tag{5.52}$$

where

$$m_o = (kR_o/2)^{1/3} ;$$

and

$$ks = m_o^3 \left[\sinh \frac{\xi}{m_o} \cosh \frac{\xi}{m_o} + \frac{\xi}{m_o}\right] . \tag{5.53}$$

(S) We divide the shadow region into segments $(0, \xi_1)$, (ξ_1, ξ_2), ... such that R and hence m or q may be taken as constant on each segment. Then by requiring continuity at the segment boundaries we argue that the surface field is given by

$$V(\xi, q) = V_o(\xi_1, q) \frac{V_1(\xi_2 - \xi_1, q_1)}{V_1(0, q_1)} \frac{V_2(\xi_3 - \xi_2, q_2)}{V_2(0, q_2)} \cdots \tag{5.54}$$

where

$$V_n(\xi - \xi_n, q_n) = \sqrt{\pi} \int_{-\infty}^{\infty} \frac{e^{i(\xi - \xi_n)t}}{\omega_1'(t) - q_n \omega_1(t)} dt \tag{5.55}$$

with

$$q_n = q(\xi_n)$$

and

$$\xi_n \leq \xi \leq \xi_{n+1} \ .$$

This unwieldy representation can be simplified provided we take only the first term in the residue series representation of the V_n's. We have in this case

$$V(\xi, q) = 2i\sqrt{\pi}\ \frac{1}{(t_o - q_o^2)\omega_1(t_o)} \cdot e^{-i\xi_1(t_1-0)}\ e^{-i\xi_2(t_2-t_1)} \ldots e^{i\xi t_n} \qquad (5.56)$$

where the t_n are the first roots of

$$\omega_1'(t) - q_n\omega_1(t) = 0 \ . \qquad (5.57)$$

The exponential in (5.56) is of the form $e^{i\phi}$ with

$$\phi = -\sum \xi_n(t_n - t_{n-1}) \ .$$

If we define $\xi(t)$ as the value of ξ corresponding to the value of q such that for a given t the root equation (5.57) is satisfied then, by reducing the segment size,

$$\phi = -\int_{t_o}^{t} \xi(t')dt' \ . \qquad (5.58)$$

To evaluate (5.58) we integrate by parts and note that

$$\frac{d\xi}{dt} = \frac{d\xi}{ds}\,\frac{ds}{dq}\,\frac{dq}{dt} \quad .$$

Hence

$$\phi = -\xi(t')t' \Big|_{t_o}^{t} + \frac{1}{\alpha}\int_{t_o}^{t} \frac{t}{\sqrt{\frac{q^2}{q_o^2} - 1}}\,\frac{dq}{dt}\,dt$$

$$= -\xi t + \frac{1}{\alpha}\int_{q_o}^{q} \frac{t}{\sqrt{\frac{q^2}{q_o^2} - 1}}\,dq \qquad (5.59)$$

where we use the fact

$$\xi(t_o) = 0 \quad .$$

(S) To evaluate the q-integral we expand t about some value $\tilde{t}$ corresponding to

$$\left[\omega_1'(t) - \tilde{q}\,\omega(t)\right]_{\tilde{t}} = 0 \qquad (5.60)$$

making use of the Riccatti equation relating t and q,

$$\frac{dt}{dq} = \frac{1}{t - q^2} \quad . \qquad (5.61)$$

For example, taking $q = q_o$ we have

$$t = t_o + \frac{1}{t_o + q_o^2}(q - q_o) + \ldots \tag{5.62}$$

and

$$\phi = -\xi t + m_o t_o \cosh^{-1}\frac{q}{q_o} + \ldots$$

$$= -\xi t + \xi t_o + \ldots \quad . \tag{5.63}$$

To this order

$$V(\xi, q) = V(\xi, q_o) \tag{5.64}$$

as we would expect.

(S) Finally, in order to find the scattered field we include the "launching factor" which, using the form (5.56), gives

$$V_1(\xi) \cong V(\xi, q)\frac{1}{\omega_1[t(\xi)]} \quad , \tag{5.65}$$

Hence, we propose the heuristic formula

$$V_1(\xi) = V(\xi, q)\,\frac{V(\xi, q_o)}{V(\xi, q(\xi))} \quad . \tag{5.66}$$

5.6 Scattering from a Coated Cone-Sphere

(S) We consider a cone-sphere of angle α and base radius a coated with a material of complex relative permittivity and permeability ϵ and μ of thickness d. The underlying surface we take to be perfectly conducting (see Fig. 5-5). For an incident plane wave, at an angle θ from the axis and polarization $\hat{p}$, we consider the contributors to the back scattered return.

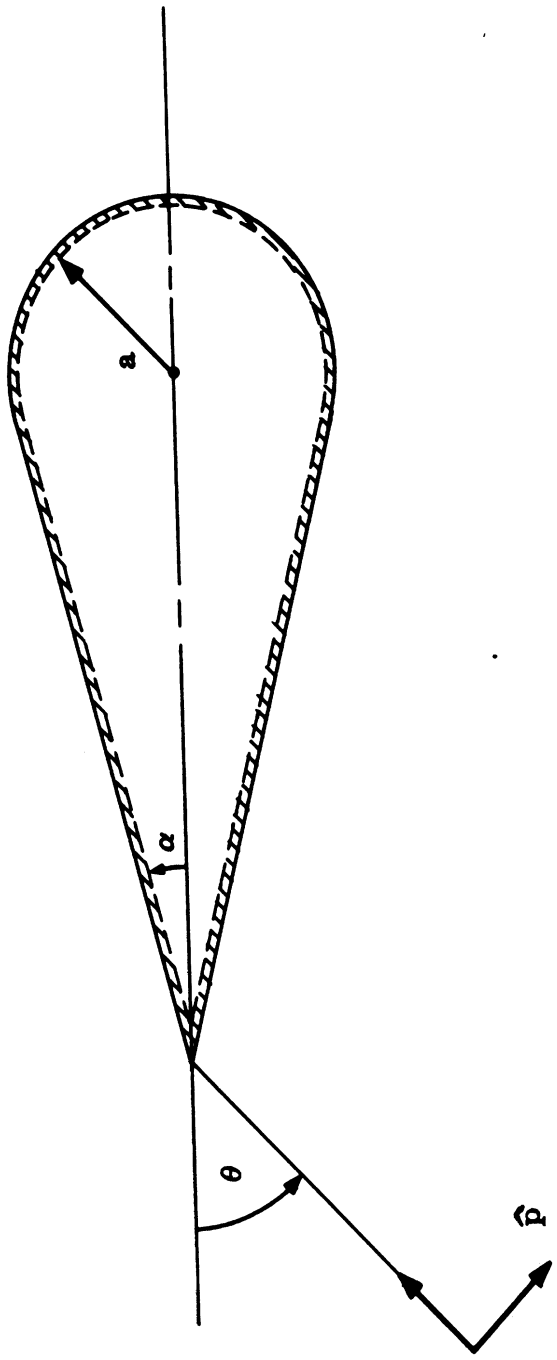

FIG. 5-5: COATED CONE-SPHERE

(S) As in the perfectly conducting case the return from a coated cone-sphere arises from four sources: 1) tip return, 2) join return, 3) creeping waves, and 4) specular reflection.

(S) The tip, join, and specular returns are essentially local phenomena and can be directly related to the corresponding perfectly reflecting case. We have to show within the accuracy of the experimental checks that the perfectly conducting tip return approximates the coated tip return. The join and specular returns are approximated by the perfectly conducting returns multiplied by the appropriate reflection coefficient. Specifically,

Tip Return: $S_T = S_T^{p.c.}$

Join Return: $S_J = S_J^{p.c.}$, R_J

Specular Return: $S_{SP} = S_{SP}^{p.c.}$, R_{SP} .

In the last two, the reflection coefficients depend upon the electrical properties of the coating and are given by

$$R_J = \frac{\sin\alpha}{\sin\alpha+\eta} \tag{5.67}$$

$$R_{SP} = \frac{1}{1+\eta} \tag{5.68}$$

where $\eta = \sqrt{\mu/\epsilon}$.

(S) The creeping wave return is not so easily represented since it is not a local phenomenon. We base our description of this on the analysis of creeping waves on a coated sphere given in Section 5.2 above.

(S) From the sphere creeping wave contribution (5.23) we write

$$S_c = S_c^{(e)} + S_c^{(m)} \quad . \tag{5.69}$$

The contribution from a coated cone-sphere illuminated at an angle θ from the axis with incident polarization $\hat{p} = (\cos\beta, \sin\beta, 0)$, is given by

$$S_c(\theta,\beta) = S_c^{(e)} \frac{1}{\pi} \int_L (\hat{p}\cdot\hat{n})^2 A_e(\phi)d\phi + S_c^{(m)} \frac{1}{\pi} \int_L \left[1-(\hat{p}\cdot\hat{n})^2\right] A_m(\phi)\, d\phi \tag{5.70}$$

where $L = (\phi_1, \phi_2)$ is that part of the shadow boundary for which there is an unobstructed creeping wave path and $\hat{n}$ is the normal, $\hat{n} = (\cos\phi, \sin\phi, 0)$. The functions A_e and A_m are the enhancement terms corresponding to the two types of waves. For example, if $\theta < \alpha$, where α is the cone angle and the functions A are unity, then (5.70) reverts to (5.69).

(S) The determination of the scattering functions and the enhancement factor depends on the coating properties as follows.

(S) CASE I: The coating is not such as to justify the use of an impedance boundary condition. Specifically, neither of the inequalities

$$k_1/k > k(b-d)$$

nor

$$\mathrm{Im}\, k_1 > \frac{1}{2d} \ell n \left[\frac{|k_1| a}{5k^2 d(a+d)}\right]$$

obtains. Then

$$S_c^e = -\pi \sum_n \frac{\nu_n\left(\xi^{(2)'}_{\nu_n-1/2}(ka) - Z_e \xi^{(2)}_{\nu_n-1/2}(ka)\right)}{\left[\frac{\partial}{\partial\nu}\left(\xi^{(1)'}_{\nu-1/2}(ka) - Z_e \xi^{(1)}_{\nu-1/2}(ka)\right)\right]_{\nu=\nu_n}} e^{i\nu_n\pi} \tag{5.71}$$

where

$$Z_e = -\eta \tan k_1 d\ , \qquad \eta = \sqrt{\mu/\epsilon} \tag{5.72}$$

and the ν_n's are the roots of

$$\xi^{(1)'}_{\nu-1/2}(ka) - Z_e \xi^{(1)}_{\nu-1/2}(ka) = 0 \tag{5.73}$$

$$S_c^m = \pi \sum_\ell \frac{\nu_\ell\left(\xi^{(2)'}_{\nu_\ell-1/2}(ka) - Z_m \xi^{(2)}_{\nu_\ell-1/2}(ka)\right)}{\left[\frac{\partial}{\partial\nu}\left(\xi^{(1)'}_{\nu-1/2}(ka) - Z_m \xi^{(1)}_{\nu-1/2}(ka)\right)\right]_{\nu=\nu_\ell}} e^{i\nu_\ell\pi} \tag{5.74}$$

where

$$Z_m = \frac{1}{\eta}\cot k_1 d = -\frac{1}{Z_\ell}\ , \qquad \eta = \sqrt{\mu/\epsilon} \tag{5.75}$$

and the ν_ℓ are roots of

$$\xi^{(1)'}_{\nu-1/2}(ka) - Z_m \xi^{(1)}_{\nu-1/2}(ka) = 0\ . \tag{5.76}$$

Depending upon the proximity of the roots to those of $\xi^{(1)'}_{\nu-1/2}(kb)$ or $\xi^{(1)}_{\nu-1/2}(kb)$ the numerators in (5.69) and (5.72) can be simplified by observing that at the roots of (5.73) or (5.76)

$$\xi^{(2)'}_{\nu-1/2}(kb) - Z\xi^{(2)}_{\nu-1/2}(kb) = \frac{-2i}{\xi^{(1)}_{\nu-1/2}(kb)} = \frac{-2iZ}{\xi^{(1)'}_{\nu-1/2}(kb)} \quad . \tag{5.77}$$

(S) The above is the most general formulation of creeping waves for a single circuit on a coated sphere. The labor involved in determining these is prohibitive but the failure of the inequalities on k_1 is a case of little practical interest.

(S) CASE II: The coating is such as to justify an impedance boundary condition, but is not lossy, that is

$$\frac{k_1}{k} > k(b-d) \ , \qquad \operatorname{Im} k_1 < \frac{1}{2d} \ln \frac{|k_1|a}{5k^2 d(a+d)} \quad .$$

In this case we may use the asymptotic form of the functions in (5.73) and (5.75) and find

$$Z_e = -\eta \tan k_1 d \tag{5.78}$$

$$A_m = \frac{1}{\eta} \cot k_1 d = -\frac{1}{Z_e} \tag{5.79}$$

where $\eta = \sqrt{\mu/\epsilon}$ and d is the thickness of the coating. The scattering amplitudes are computed just as above using the simplified root equations

$$\xi^{(1)'}_{\nu-1/2}(ka) + \eta \tan k_1 d \, \xi^{(1)}_{\nu-1/2}(ka) = 0 \tag{5.80}$$

$$\xi^{(1)'}_{\nu-1/2}(ka) - \frac{1}{\eta} \cot k_1 d \, \xi^{(1)}_{\nu-1/2}(ka) = 0 \tag{5.81}$$

The solutions of these root equations are most easily found by expanding about the roots of the Airy function equations

$$w_1'(t) - q_e w_1(t) = 0$$

$$w_1'(t) - q_m w_1(t) = 0 \qquad (5.82)$$

where

$$q_e = (ka/2)^{1/3} \eta \tan k_1 d$$

$$q_m = (ka/2)^{1/3} \frac{1}{\eta} \cot k_1 d \quad . \qquad (5.83)$$

The procedure is to: 1) approximate the spherical Hankel functions by using the forms (5.82) and (5.83)

$$\zeta^{(1)}_{\nu-1/2}(ka) = -i(ka/2)^{1/6} w_1(t)\left[1 - \frac{t}{15}(ka/2)^{-2/3} + \left(\frac{t^5}{7200} + \frac{13t^2}{1260}\right)(ka/2)^{-4/3} + \ldots\right]$$

$$- i(ka/2)^{1/6} w_1'(t)\left[-\frac{t^2}{60}(ka/2)^{-2/3} + \left(\frac{t^3}{420} + \frac{1}{140}\right)(ka/2)^{-4/3} + \ldots\right] \qquad (5.84)$$

where

$$t = (ka/2)^{-1/3}(\nu - ka)$$

$$w_1(t) = \sqrt{\pi}\left[Bi(t) + iAi(t)\right] = 2\sqrt{\pi}\, e^{i\frac{\pi}{6}} Ai(t e^{i\frac{2\pi}{3}})$$

$$\zeta^{(1)'}_{\nu-1/2}(ka) = i(ka/2)^{-1/6} w_1'(t)\left[1 + \frac{t}{15}(ka/2)^{-2/3} + \left(\frac{t^5}{7200} - \frac{17t^2}{5040}\right)(ka/2)^{-4/3}\right]$$

$$+ i(ka/2)^{-1/2} w_1(t)\left[-\left(\frac{t^3}{60} + \frac{3}{20}\right)(ka/2)^{-2/3} + \frac{t^4}{3360}(ka/2)^{-4/3}\right] ; \qquad (5.85)$$

2) expand $w_1(t)$ and $w_1'(t)$ about the roots of (5.82) and (5.83) using the fact that

$$w''(t) = t\,w(t) \ ; \tag{5.86}$$

3) solve the resulting algebraic equations for the difference in roots.

(S) The solution under the conditions of Case II is very much simplified in the high frequency region, $ka \geqslant 8$, where the expansions (5.84) and (5.85) may be terminated after the first term, that is,

$$\zeta^{(1)}_{\nu-1/2}(ka) \cong -i(ka/2)^{1/6} w_1(t) \tag{5.87}$$

$$\zeta^{(1)'}_{\nu-1/2}(ka) \cong i(ka/2)^{-1/6} w_1'(t) \tag{5.88}$$

and the difference in roots neglected. In this case we have

$$S_c^{(e)} = (ka/2)^{4/3} e^{i\pi ka - i\frac{\pi}{6}} \sum_s \frac{1}{Ai^2(-\beta_s)\left[\beta_s - e^{-i\pi/3} q_e^2\right]} \tag{5.89}$$

where the β_s are roots of

$$Ai'(-\beta) - q_e Ai(-\beta) = 0 \ ; \tag{5.90}$$

and

$$S_c^{(m)} = (ka/2)^{4/3} e^{i\pi ka - i\frac{\pi}{6}} \sum_s \frac{q_m^2}{Ai'(-\alpha_s)\left[e^{i\pi/3}\alpha_s - q_m^2\right]} \tag{5.91}$$

where the α_s are roots of

$$Ai'(-\alpha) - q_m Ai(-\alpha) = 0 \ . \tag{5.92}$$

(S) To determine the roots of (5.90) and (5.92) we refer to the work of Logan (1965) where many cases have been computed and the methods and programs for computation are given in great detail.

(S) CASE III: The coating is such as to justify an impedance boundary condition and the coating is lossy. Specifically

$$\mathrm{Im}\, k_1 > \frac{1}{2d} \ln\left[\frac{|k_1|a}{5k^2 d(a+d)}\right] \quad . \tag{5.93}$$

(S) In this case we make the approximation

$$\tan k_1 d \cong i \tag{5.94}$$

so that

$$Z_e \cong -i\eta \tag{5.95}$$

$$Z_m \cong \frac{i}{\eta} \quad , \tag{5.96}$$

and corresponding to this

$$q_e \cong -i(ka/2)^{1/3}\eta \tag{5.97}$$

$$q_m \cong i(ka/2)^{1/3}\frac{1}{\eta} \quad . \tag{5.98}$$

With these parameters we now use the methods of Case II to determine the creeping wave contribution.

(S) In using the methods of Cases I and II the series for the creeping wave scattering amplitudes must be terminated before the asymptotic approximation to Z_e and Z_m fails. This depends upon the size of the roots α_s and β_s and occurs

at

$$|\alpha_s| \ , \ |\beta_s| = (2/ka)^{1/3}\left(\sqrt{|k_1 a|} - ka\right) \quad . \tag{5.99}$$

5.7 Non-Spherical Termination: Coated Cone-Sphere

(S) Because of the lack of an adequate model we must turn to the heuristic form (5.66) in order to obtain the creeping wave contribution from a non-spherical cone termination. The application of (5.66) is restricted to the region

$$kR_{min} > 8$$

where R_{min} is the minimum radius of curvature of the base. This restriction is in addition to the requirement that the coating be such that the use of an impedance boundary condition is justified.

(S) Because of these restrictions and in particular the restriction on the frequency, we will argue that a physically plausible approximation to the creeping wave return can be made by using the spherical termination results where we choose the average radius

$$a = \frac{1}{2}(R_{max} + R_{min})$$

over the creeping wave path. We estimate the error to be within 3 db for the higher frequencies.

(S) As in the conducting case the creeping wave contribution to the back scattering is significant only near nose-on since in any other region the creeping waves are skewed. For spheroids, the "diffuse caustic" factor should be used to obtain the near-nose-on pattern.

5.8 Concave Termination: Perfectly Conducting Cone

(S) We consider the geometry in Fig. 5-6, where the base is a smooth concave surface. The nose-on creeping wave amplitude is given by

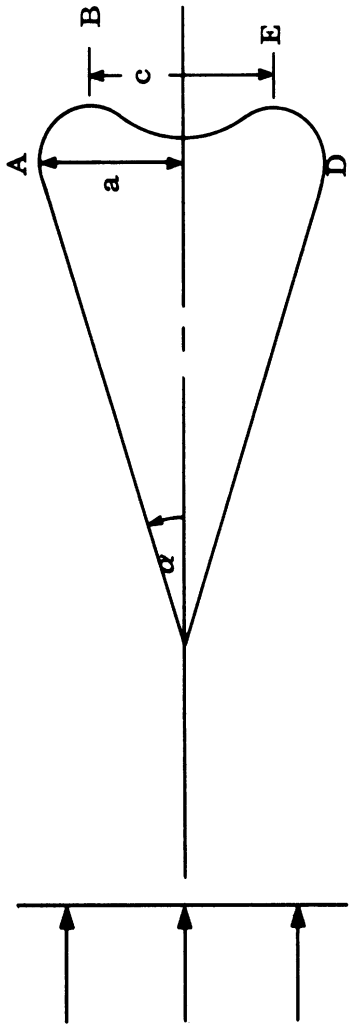

FIG. 5-6: CONE WITH CONCAVE TERMINATION.

$$S_{cw}^{con} = \frac{e^{ik(2s+c)}}{\sqrt{kc}} e^{i\frac{\pi}{2}} \pi a \cdot \left[\hat{q}(\xi_{AB})\right]^2 \tag{5.100}$$

where s is the arc length $\overline{AB}$ and ξ the reduced length

$$\xi_{AB} = (k/2)^{1/3} \int_A^B \frac{dS}{R^{2/3}} \quad . \tag{5.101}$$

$R = R(s)$ is the radius of curvature at s, and

$$\hat{q}(\xi) = \frac{1}{2\sqrt{\pi}} e^{i\frac{5\pi}{6}} \sum \exp\left\{ie^{i\frac{\pi}{3}}\xi\alpha_s\right\} \frac{1}{\alpha_s\left[Ai(-\alpha_s)\right]^2} \tag{5.102}$$

with the α_s roots of

$$Ai'(-\alpha) = 0 \quad . \tag{5.103}$$

(S) This expression is to be used in the creeping wave contribution. In general the far off nose-on contribution will be negligible because the lack of spherical symmetry leads to skewed creeping wave paths. In the near nose-on region we use a shape factor derived from the diffuse caustic approach.

(S) The expression (5.100) is applicable for the frequency region defined by

$$kR_{min} \geqslant 4 \quad . \tag{5.104}$$

For lower frequencies we require the substitution

$$\hat{q}(\xi_{AB}) \rightarrow \hat{Q}(\xi_{AB})$$

$$= \left(\frac{R(A)}{R(B)}\right)^{1/6} \left\{ \left[\hat{q}(\xi_{AB}) + \frac{1}{\sqrt{\pi}} e^{i\frac{\pi}{6}} \left(kR(A)\right)^{2/3} \sum_{s} \exp\left\{ \left[i e^{i\frac{\pi}{3}} \xi\alpha_s \right] \right\} \cdot \right. \right.$$

$$\left. \left. \cdot \frac{1}{\alpha_s \left[Ai(-\alpha_s) \right]^2} \left(\frac{\alpha_s}{30} + \frac{1}{10\alpha_s^2} \right) \right] \right\} \qquad (5.105)$$

where the α_s are the roots of

$$Ai'(-\alpha) = 0 \ . \qquad (5.106)$$

(S) For the cross section, we have for nose-on

$$\sigma(0) = \left| S_T + S_J + S_{cw}^{con} \right|^2 \qquad (5.107)$$

$$\frac{\sigma(0)}{\lambda^2} = \frac{1}{\pi} \left| -\frac{i}{4} \tan^2\alpha \, e^{-i2ka\csc\alpha} + \frac{i}{4} \sec^2\alpha \, e^{-i2ka\sin\alpha} \right.$$

$$\left. + i\pi ka \frac{e^{ikS_{AD}}}{\sqrt{kc}} \left[\hat{q}(\xi_{AB}) \right]^2 \right|^2 . \qquad (5.108)$$

For near nose-on, $\theta < \alpha$,

$$\frac{\sigma(\theta)}{\lambda^2} = \frac{1}{\pi} \left| -\frac{i}{4} \tan^2\alpha \, \frac{1}{(1 - \sin^2\theta \sec^2\alpha)^{3/2}} \, e^{-i2ka\csc\alpha} \right.$$

$$+ \frac{i}{4} \sec^2\alpha \, J_o(2ka\sin\theta) \, e^{-i2ka\sin\alpha} + i\pi ka \frac{e^{ikS_{AD}}}{\sqrt{kc}} \left[\hat{q}(\xi_{AB}) \right]^2 \cdot$$

$$\left. \cdot J_o\left[k\left(a - R(A)\right) \sin\theta \right] \right|^2 \qquad (5.109)$$

where $q(\xi_{AB})$ is given by (5.102) or (5.105), ξ_{AB} is the reduced length (5.101), c is the distance between the points B and E, S_{AD} is the path length from A to D,

$$S_{AD} = 2\int_A^B ds + c \tag{5.110}$$

and J_o is the zeroth order Bessel function.

5.9 Formulas for Coated Cone-Sphere

(S) Nose on, $\theta = 0$:

$$\frac{\sigma(0)}{\lambda^2} = \frac{1}{\pi}\left|-\frac{i}{4}\tan^2\alpha\, e^{-i2ka\csc\alpha} + \frac{i}{4}\sec^2\alpha\,\frac{1}{1+\eta}\, e^{-i2ka\sin\alpha} + S_c^{(e)} + S_c^{(m)}\right|^2 \tag{5.111}$$

(S) Near nose-on, $\theta < \pi/2ka$:

$$\frac{\sigma(\theta)}{\lambda^2} = \frac{1}{\pi}\left|-\frac{i}{4}\,\frac{\tan^2\alpha\, e^{-i2ka\csc\alpha}}{(1-\sin^2\theta\sec^2\alpha)^{3/2}} + \frac{i}{4}\sec^2\alpha\, J_o(2ka\sin\theta)\, e^{-i2ka\sin\alpha}\,\frac{1}{1+\eta} + S_c^{(e)} + S_c^{(m)}\right|^2 \tag{5.112}$$

(S) Forward cone, $\pi/2ka < \theta < \alpha$:

$$\frac{\sigma(\theta)}{\lambda^2} = \frac{1}{\pi}\left|-\frac{i}{4}\,\frac{\tan^2\alpha\, e^{-i2ka\csc\alpha}}{(1-\sin^2\theta\sec^2\alpha)^{3/2}} + \frac{i}{8}\sec^2\alpha\, e^{-i2ka\sin\alpha}\cdot\left[\frac{\cos^3\alpha}{\cos^3(\alpha-\theta)}\, H_o^{(1)}(2ka\sin\theta) + \frac{\cos^3\alpha}{\cos^3(\alpha+\theta)}\, H_o^{(2)}(2ka\sin\theta)\right] + S_c^{(e)} + S_c^{(m)}\right|^2 \tag{5.113}$$

(S) Shadowed cone, $\alpha < \theta < \frac{\pi}{2} - \alpha$:

$$\frac{\sigma(\theta)}{\lambda^2} = \frac{1}{\pi} \left| R(\gamma) S_c^{(e)} + r(\gamma) S_c^{(m)} \right|^2 \tag{5.114}$$

In the above $S_c^{(e)}$ is given by the appropriate form (5.71) or (5.89) and $S_c^{(m)}$ is given by (5.74) or (5.91). The intrinsic surface impedance is given for complex relative permittivity and permeability by $\eta = \sqrt{\mu/\epsilon}$. The factors $R(\gamma)$ and $r(\gamma)$ are shadowing factors and for an incident electric field of polarization $\hat{p}$ such that the horizontal component is $\sin\gamma$ we have

$$R(\gamma) = \frac{2}{\pi} \left\{ \sin^{-1}\left(\frac{\sin\alpha}{\sin\theta}\right) - \frac{\sin\alpha}{\sin\theta} \sqrt{1 - \frac{\sin^2\alpha}{\sin^2\theta} \cos^2\gamma} \right\} \tag{5.115}$$

$$r(\gamma) = \frac{2}{\pi} \left\{ \sin^{-1}\left(\frac{\sin\alpha}{\sin\theta}\right) + \frac{\sin\alpha}{\sin\theta} \sqrt{1 - \frac{\sin^2\alpha}{\sin^2\theta} \cos^2\gamma} \right\} \tag{5.116}$$

(S) Specular flash, $\theta = \frac{\pi}{2} - \alpha$:

$$\frac{\sigma}{\lambda^2}\left(\frac{\pi}{2} - \alpha\right) = \left(\frac{1}{1+\eta}\right)^2 \frac{(ka)^3}{9\pi^2} \sec\alpha \csc^2\alpha \tag{5.117}$$

(S) Sphere return, $\theta > \frac{\pi}{2} - \alpha$:

$$\frac{\sigma}{\lambda^2}(\theta) = \frac{1}{1+\eta} \frac{(ka)^2}{4\pi} \tag{5.118}$$

5.10 Formulas for the Sphere-Cone-Sphere, Coated

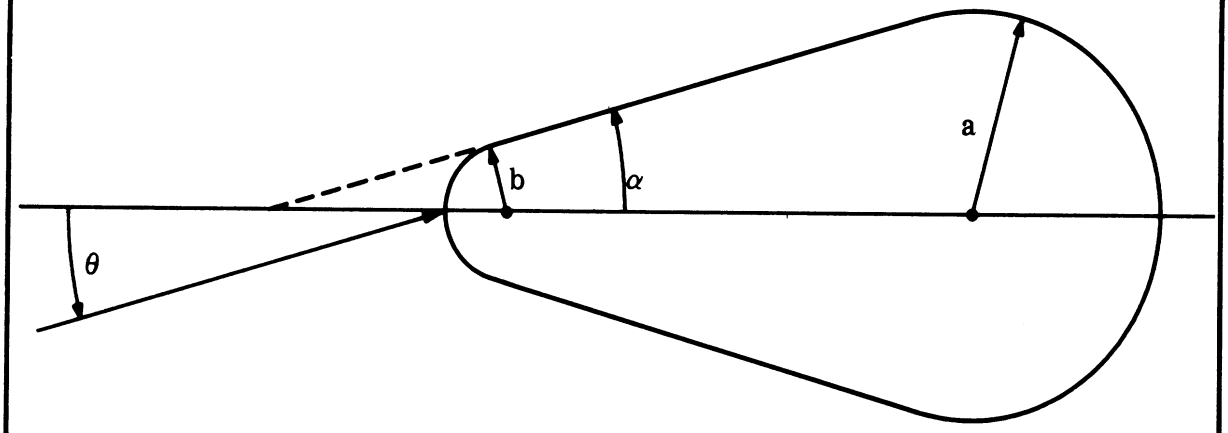

FIG. 5-7: GEOMETRY OF SPHERE-CONE-SPHERE.

(S) We define the parameters

δ = thickness of coating

μ, ϵ = relative permeability and permittivity of coating

$$k_1 = \sqrt{\mu\epsilon} \; ; \qquad N = k_1/k \; ; \qquad k = 2\pi/\lambda$$

$$\eta = \sqrt{\mu/\epsilon} \; .$$

The radar cross section, $\theta < \frac{\pi}{2} - \alpha$, is given by

$$\sigma = \frac{\lambda^2}{\pi} \left| S_1 + S_2 + S_3 \right|^2 \tag{5.119}$$

where

S_1 = tip contribution

S_2 = join contribution

S_3 = creeping wave contribution .

REGION I: Backward cone, $0 \leqslant \theta \leqslant \alpha$

(S) For $kb \ll 1$, define

$$R_t^{(0)} = -\frac{1}{Nkb} + Nkb\,\frac{Nk(b-\delta)+\left[1-N^2k^2(b-\delta)^2\right]\tan Nk\delta}{N^3k^3b(b-\delta)^2+\left[1+N^2b^2\delta(b-\delta)\right]\tan Nk\delta} \tag{5.120}$$

then in equation (5.119)

$$S_1 = R_t^{(0)}\left[-\frac{kb}{2}\,\frac{1}{\cos^2\theta-\tan^2\alpha\sin^2\theta}-\frac{i}{4}\,\frac{\tan^2\alpha}{(1-\sin^2\theta\sec^2\alpha)^{3/2}}\right] \tag{5.121}$$

$$S_2 = \frac{1}{1+\eta}\,\frac{i}{4}\sec^2\alpha\,J_o(2ka\sin\theta)\,e^{-2ika\sin\alpha} \tag{5.122}$$

$$S_3 = S_c^{(e)}+S_c^{(m)} \tag{5.123}$$

where $S_c^{(e)}$ is given by (5.71) or (5.89) and $S_c^{(m)}$ is given by (5.74) or (5.91).

(S) For $kb > 1$

$$S_1 = \frac{1}{1+\eta}\left[-\frac{kb}{2}\left(1-\frac{i}{2kb}\right)-\frac{i}{8}\sec^2\alpha\,e^{2ikb(1-\sin\alpha)\cos\theta}\cdot\right.$$

$$\left.\cdot\left\{\frac{\cos^3\alpha}{\cos^3(\alpha+\theta)}\,H_o^{(1)}\Big(2kb(1-\sin\alpha)\sin\theta\tan\alpha\Big)+\frac{\cos^3\alpha}{\cos^3(\alpha+\theta)}\,H_o^{(2)}\Big(2kb(1-\sin\alpha)\sin\theta\tan\alpha\Big)\right\}\right] \tag{5.124}$$

and the same expressions, (5.122) and (5.123) are to be used for S_2 and S_3 in (5.119).

REGION II: Shadowed cone, $\alpha < \theta < \frac{\pi}{2} - \alpha$.

The cross section is given by (5.114) as it stands.

REGION III: Specular flash, $\theta \sim \frac{\pi}{2} - \alpha$.

Use equation (5.117) as it stands.

REGION IV: Sphere return, $\theta > \frac{\pi}{2} - \alpha$.

Use equation (5.118) as it stands.

5.11 Formulas for the Cone-Prolate Spheroid, Coated

(S) Let a and b be the semi-major and semi-minor axes, $a > b$.

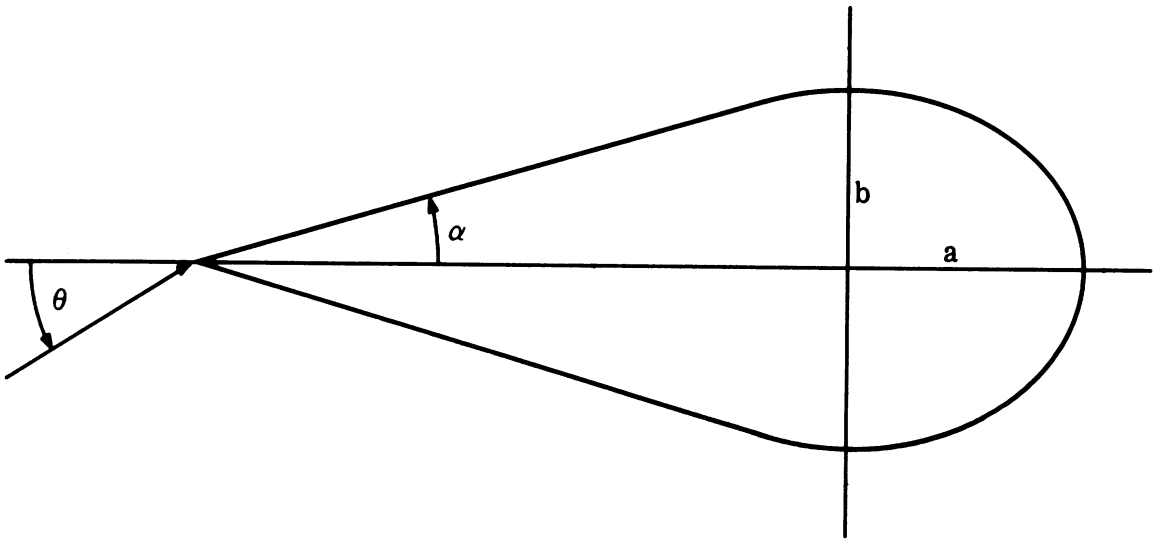

FIG. 5-8: GEOMETRY OF CONE-PROLATE SPHEROID

(S) For $0 \leqslant \theta \leqslant \alpha$, backward cone, both polarizations,

$$\sigma = \frac{\lambda^2}{\pi} \left| S_1 + S_2 + S_3 \right|^2 \qquad (5.125)$$

where

$$S_1 = S_{tip} = -\frac{i}{4}\frac{\tan^2\alpha}{(1-\sin^2\theta\sec^2\alpha)^{3/2}} \tag{5.126}$$

$$S_2 = S_{join} = \frac{i}{4}\sec^2\alpha\, J_o(2ka\sin\alpha)\, e^{-2ika\sin\alpha}\frac{1}{1+\eta} \tag{5.127}$$

$$S_3 = S_{cw} = 2\sqrt{\pi}\,\frac{m_o^4}{w_1(t_o)}\,V(0,q_o)\,e^{-i\phi}\,e^{2ikb\cot\alpha+iks}\,J_o\left(2k\frac{a^2-b^2}{a}\sin\theta\right) \tag{5.128}$$

where

$$\eta = \sqrt{\mu/\epsilon}$$

$$m_o = \left(\frac{ka^2}{2b}\right)^{1/3}, \qquad q_o = -i\eta m_o$$

$$s = 2a\int_0^{\pi/2}\sqrt{1-\epsilon^2\sin^2\theta}\;d\theta$$

$$\epsilon = \frac{\sqrt{a^2-b^2}}{a}$$

$w_1(t) = \sqrt{\pi}\left(Bi(t)+Ai(t)\right)$, the Airy integrals

t_o is the first root of $w_1'(t) - q_o w_1(t) = 0$

$$V(0,q_o) = \frac{1}{\sqrt{\pi}}\int_{-\infty}^{\infty}\frac{dt}{w_1'(t)-q_o w_1(t)}$$

$$\phi = 2\xi t_o - 2\frac{b}{a} m_o \int_0^{\pi/2} t \frac{d\theta}{\sqrt{1-\epsilon^2 \sin^2\theta}}$$

where $$\xi = \frac{b}{a} m_o \int_0^{\pi/2} \frac{d\theta}{\sqrt{1-\epsilon^2 \sin^2\theta}}$$

and $t = t(\theta)$ is the first root of

$$w'(t) - qw(t) = 0$$

$$q = -i\eta m_o \sqrt{1-\epsilon^2 \sin^2\theta} \quad .$$

(S) For $\alpha < \theta \leqslant \frac{\pi}{2} - \alpha$, shadowed cone, the return is primarily the specular flash for

$$\frac{\pi}{2} - \alpha - \frac{\lambda \sin\alpha}{2b} \leqslant \theta \leqslant \frac{\pi}{2} - \alpha + \frac{\lambda \sin\alpha}{4b} \quad ,$$

$$\sigma = \frac{\lambda^2}{\pi} \left(\frac{1}{1+\eta}\right)^2 \frac{(kb)^3}{9\pi^2} \sec\alpha \csc^2\alpha \quad . \tag{5.129}$$

(S) For $\theta > \frac{\pi}{2} - \alpha$, base return,

$$\sigma = \frac{\lambda^2}{4\pi} \left(\frac{1}{1+\eta}\right)^2 \frac{\left(k\frac{b^2}{a}\right)^2}{(1-\epsilon^2 \sin^2\theta)^2} \tag{5.130}$$

5.12 Formulas for the Cone-Oblate Spheroid, Coated

(S) Let B and A be the semi-major and semi-minor axes, $B > A$.

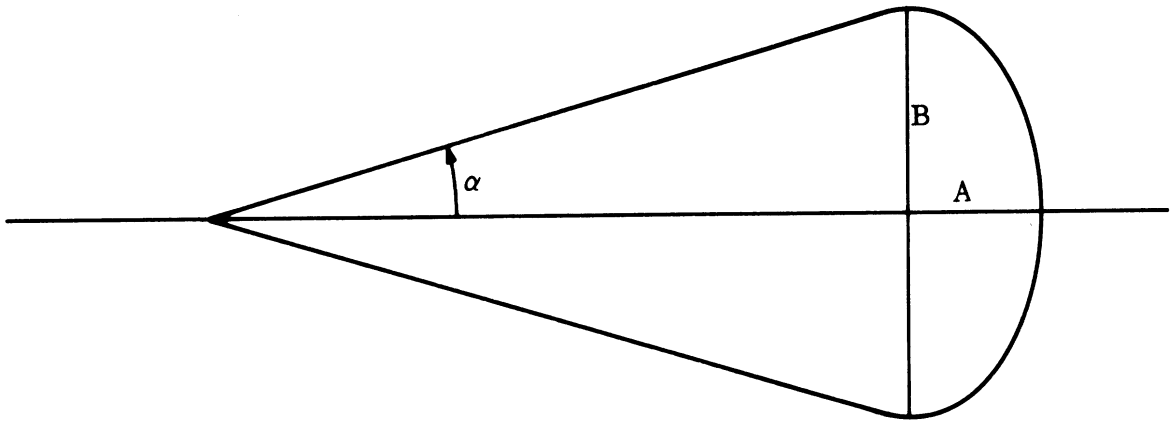

FIG. 5-9: GEOMETRY OF CONE-OBLATE SPHEROID.

(S) For $0 \leqslant \theta \leqslant \alpha$, backward cone, both polarizations,

$$\sigma = \frac{\lambda^2}{\pi} \left| S_1 + S_2 + S_3 \right|^2 \tag{5.131}$$

$$S_1 = S_{tip} = \text{equation (5.126) for the prolate spheroid,} \tag{5.132}$$

$$S_2 = S_{join} = \text{equation (5.127) for the prolate spheroid,} \tag{5.133}$$

$$S_3 = S_{cw} = \text{equation (5.128) for the prolate spheroid ,} \tag{5.134}$$

with the replacement

$$a \rightarrow A\,, \qquad b \rightarrow B\,, \qquad \text{and} \quad \epsilon \rightarrow \frac{\sqrt{B^2 - A^2}}{B}\,.$$

(S) For $\alpha < \theta < \frac{\pi}{2} - \alpha$, specular flash region,

$$\sigma = \frac{\lambda^2}{\pi}\left(\frac{1}{1+\eta}\right)^2 \frac{(kB)^3}{9\pi^2} \sec\alpha \csc^2\alpha \quad . \tag{5.135}$$

(S) For $\theta > \frac{\pi}{2} - \alpha$, base return,

$$\sigma = \frac{\lambda^2}{4\pi}\left(\frac{1}{1+\eta}\right)^2 \frac{\left(k\frac{B^2}{A}\right)^2}{(1-\epsilon^2\sin^2\theta)^2} \tag{5.136}$$

where

$$\epsilon = \frac{\sqrt{B^2 - A^2}}{B} \quad .$$

5.13 Formulas for the Cone-Sphere with Indented Base

(S) Let the base radius be a, the radius of curvature of the protuberance be approximately R, the radius of curvature of the concavity approximately r.

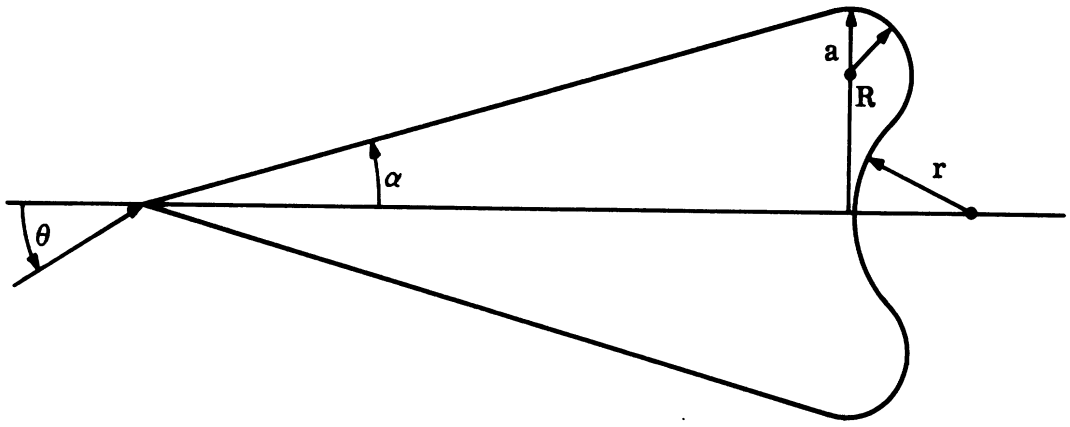

FIG. 5-10: GEOMETRY OF CONE-SPHERE WITH INDENTED BASE.

(S) For $\theta < \alpha$ use formula (5.109).

(S) For $\frac{\pi}{2} - \alpha < \theta \ll \frac{\pi}{2} - \alpha$, the return is primarily the specular flash. Use formula (5.117) for $\theta = \frac{\pi}{2} - \alpha \pm \frac{\lambda \sin\alpha}{4a}$.

(S) For $\theta > \frac{\pi}{2} - \alpha$, base return,

$$\sigma = \frac{\lambda^2}{\pi}\left(k^3 Ra^2 + \frac{kr^2}{4}\right) J_o^2(2ka\sin\theta) \tag{5.137}$$

5.14 Perturbations on Cone-Sphere Shapes

(S) The effect of perturbations such as slot antennas and rocket nozzles on the scattering from perfectly conducting re-entry shapes is practically negligible except for annular slots located on either the conical portion or the base of the shape. We argue that the other types of perturbations have a small effect since in every case in which the scattering from these could be significant, the return from the body itself is clearly dominant. For example, rocket nozzles on the base scatter very little unless they are directly illuminated. When they are directly illuminated, the base return is the specular sphere return and completely swamps the nozzle return. Similarly, the return from slots along the cone generator will be lost in the specular flash. For this reason we concentrate on the annular slot problem.

(S) The procedure we use is that of Plonus (1966) so we give only a brief qualitative description of the procedure. We assume the slot small enough so that the voltage across it at any point is a measure of the electric field in the slot. From this assumed voltage we can compute the field radiated from the slot. To determine the voltage in terms of the electrical parameters of the slot we compute the radiation admittance density

$$y_r = \frac{\text{complex power radiated/unit length}}{(\text{voltage})^2} \tag{5.138}$$

and the total radiation admittance

$$Y_r = \int_{slot} y_r d\ell \quad ; \tag{5.139}$$

in addition, the load admittance density

$$y_\ell = \frac{\text{total complex power/unit length}}{(\text{voltage})^2} \tag{5.140}$$

and the total load admittance

$$Y_\ell = \int_{slot} y_\ell \, d\ell \quad . \tag{5.141}$$

(S) From the expressions for Y_ℓ and Y_r we can find an expression for the voltage in terms of Y_ℓ, Y_r and the field which would be induced at the slot position in the absence of the slot.

(S) We suppose a cone-sphere having annular slots at either $r=b$ on the cone or at $\theta=\theta_o$ on the base (Fig. 5-11). Given an incident plane wave the scattering amplitude of the radiation from a symmetrically illuminated annular slot on the spherical portion of a cone-sphere is given by

$$S^r_{sph}(0) = \pi(ka)^3 \sin\theta_o (H_\phi)^2 \frac{1}{Y_r + Y_\ell} \tag{5.142}$$

where the slot is located at $\theta=\theta_o$, is of width $\Delta \ll \lambda$ and Y_r and Y_ℓ are the radiation and load admittance respectively. H_ϕ is the surface magnetic field which would be induced on $\theta=\theta_o$, $\phi=0$ in the absence of the slot

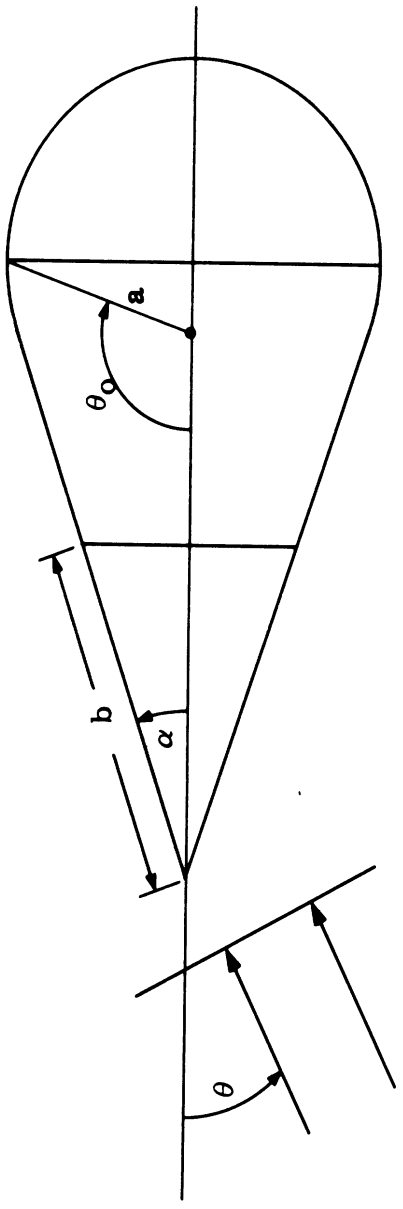

FIG. 5-11: CONE-SPHERE GEOMETRY.

$$H_\phi = \frac{i}{\sqrt{\sin\theta_o}} e^{ika(\theta_o - \frac{\pi}{2})} g\left((ka/2)^{1/3}\left(\theta_o - \frac{\pi}{2}\right)\right) \tag{5.143}$$

where

$$g(\xi) = \frac{1}{\sqrt{\pi}} \int_{-\infty}^{\infty} \frac{e^{i\xi t}}{w'(t)} dt$$

is the Fock universal functions tabulated by Logan (1959). Similarly we can obtain the radiation from an annular slot on the conical portion and find

$$S^r_{cone}(0) = \frac{2\pi b \sin\alpha}{Y_\ell + Y_r} H_\phi \cdot S_1$$

where the slot is located at $r = b$ on a cone of half-angle α, Y_r and Y_ℓ are the radiation and load admittances, and H_ϕ is the magnetic field which would be induced at the slot position in the absence of the slot. S_1 is a function similar to H_ϕ but not the same due to reflections from the cone tip. To a good approximation for $b > \lambda/4$,

$$H_\phi = 2e^{ikb\cos\alpha} \tag{5.144}$$

while S_1 must be computed using conical harmonics:

$$S_1 = e^{ikb\cos\alpha}\left\{k\sum_n (2\nu_n+1)\,e^{i\nu_n\frac{\pi}{2}}\,\frac{1}{\left[\frac{\partial}{\partial\nu}P^1_\nu(\cos\alpha)\right]_{\nu_n}}\,\psi_{\nu_n}(kb)\right.$$

$$\left. -ik\sum_m (2\mu_m+1)\,e^{i\mu_m\frac{\pi}{2}}\,\frac{1}{\sin^2\alpha\left[\frac{\partial}{\partial\mu}\frac{\partial P^1_\mu}{\partial\alpha}\right]_{\mu_m}}\,\frac{\psi_{\mu_m}(kb)\zeta'_{\mu_m}(kb)}{\zeta_{\mu_m}(kb)}\right\} \quad (5.145)$$

where the ν_n are roots of

$$P'_{\nu_n}(\cos\alpha) = 0 \quad ,$$

the μ_n are roots of

$$\frac{\partial}{\partial\alpha}P'_{\mu_m}(\cos\alpha) = 0$$

and

$$\psi_\nu(x) = \sqrt{\pi x/2}\;J_{\nu+1/2}(x)$$

$$\zeta_\nu(x) = \sqrt{\pi x/2}\;H^{(1)}_{\nu+1/2}(x) \quad .$$

(S) For incidence near the axis of symmetry we have

$$S^r_{sph}(\theta) = S^r_{sph}(0)\,J_o(ka\sin\theta_o\sin 2\theta) \quad (5.146)$$

where $\theta \leqslant \lambda/4a$;

and

$$S^r_{cone}(\theta) = S^r_{cone}(0)\, J_o(kb \sin\alpha \sin 2\theta) \qquad (5.147)$$

where $\theta \leqslant \lambda/4b\sin\alpha$.

(S) The computation of the radar cross section of metallic cone-sphere shapes with annular slot antennas is discussed in the next section. The tip antenna and the antenna near the cone-sphere join are treated separately.

5.15 Formulas for Cone-Spheres with Annular Slot Antennas

(S)CASE I: Annular slot on conical portion, distance b from tip:

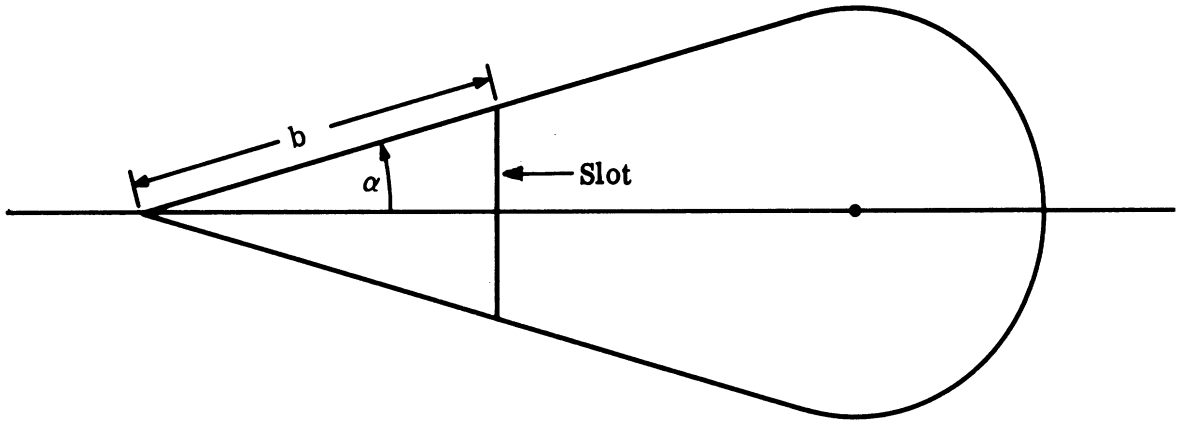

FIG. 5-12: GEOMETRY FOR NOSE-TIP ANNULAR SLOT.

for $\theta < \alpha$:

$$S^c_{slot}(\theta) = \frac{4\pi kb \sin\alpha\, e^{2ikb\cos\alpha}}{Y_\ell + Y_r}\, S(0)\, J_o(kb \sin\alpha \sin 2\theta) \qquad (5.148)$$

where Y_ℓ and Y_r are the load and radiation admittances of the slot and

$$S(0) = \sum_n (2\nu_n + 1)\, e^{i\nu_n \frac{\pi}{2}} \frac{1}{\left[\frac{\partial}{\partial \nu} P_\nu^1(\cos\alpha)\right]_{\nu_n}} \psi_{\nu_n}(kb)$$

$$- i \sum_m (2\mu_m + 1)\, e^{i\mu_m \frac{\pi}{2}} \frac{\psi_{\mu_m}(kb)\zeta'_{\mu_m}(kb)}{\sin^2\alpha \left[\frac{\partial}{\partial \mu}\frac{\partial}{\partial \alpha} P_\mu^1(\cos\alpha)\right]_{\mu_m} \zeta_{\mu_m}(kb)}$$

where the ν_n are roots of

$$P_{\nu_m}^1(\cos\alpha) = 0$$

and the μ_m are roots of

$$\frac{\partial}{\partial \alpha} P_\mu^1(\cos\alpha) = 0 \ .$$

(S) CASE II: Spherical base slot located at an angular distance θ_o measured from the point at which the completion of the sphere meets the cone axis.

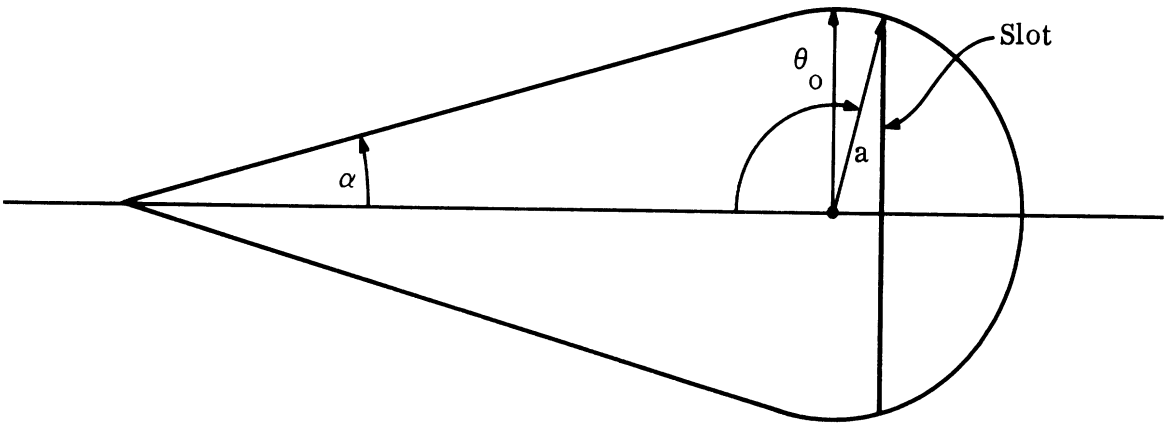

FIG. 5-13: GEOMETRY OF SPHERICAL BASE ANNULAR SLOT.

$$S_{slot}^{sph} = e^{2ika(\cot\alpha + \frac{\pi}{2} - \theta_o)} \frac{\pi(ka)^3}{\sin\theta_o} \frac{1}{Y_\ell + Y_r} \left[g\left((ka/2)^{1/3} \left(\frac{\pi}{2} - \theta_o \right) \right) \right]^2 \cdot$$

$$\cdot J_o(ka \sin\theta_o \sin 2\theta) \qquad (5.149)$$

where Y_ℓ and Y_r are the load and radiation admittances of the slot and

$$g(\xi) = \frac{1}{\sqrt{\pi}} \int_{-\infty}^{\infty} \frac{e^{i\xi t}}{w'(t)} dt$$

is the Fock function (Logan, 1959) and w(t) is the Airy function

$$w(t) = \sqrt{\pi} \left[Bi(t) + iAi(t) \right] .$$

(S) The radar cross section of metallic cone-sphere shapes with annular antennas may be computed by selecting the tip, join, and creeping wave contributions appropriate to the shape being considered and adding the slot contribution to them as follows:

$$\sigma = \frac{\lambda^2}{\pi} \left| S_1 + S_2 + S_3 + S_{slot} \right|^2$$

where, as before,

S_1 = tip contribution

S_2 = join contribution

S_3 = creeping wave contribution,

and S_{slot} = annular slot contribution.

VI
SUPPORTING STUDIES

(U) The technical detail of the work performed under Contract AF 04(694)-834 has been reported in three Quarterly Reports and in three Technical Reports. The Technical Reports are as follows:

7741-1-T "Notes on Electromagnetic Scattering from Rotationally Symmetric Bodies with an Impedance Boundary Condition", Dario Castellanos.

(U) This report details the complex mathematics for extending the IBM computer program which is being developed for metallic shapes to rotationally symmetric shapes which are coated with absorber materials.

7741-2-T "Asymptotic Theory of Diffraction by Smooth Convex Surfaces of Nonconstant Curvature", Soonsung Hong.

(U) This report gives the theoretical foundation for handling the creeping wave contribution to the radar cross section when the cone is terminated by a spheroid or when the shape is illuminated obliquely.

7741-3-T "Scattering by Small Obstacles Mounted on a Perfectly Conducting Plane", M.A. Plonus.

(U) A simplification in time and cost is achieved if the flush-mounted slot antenna can be studied experimentally by simple dipoles and loops mounted on the cone-sphere at appropriate locations and thus representing the same electromagnetic situation as slot antennas at the same locations. This report treats the theoretical justification for making such a simplification and shows the equivalence between slots and combinations of dipoles and loops.

VII
ACKNOWLEDGMENTS

(U)Experiments, analysis, interpretation and theorization are necessarily interrelated in a program of this complexity. It is possible, therefore, to indicate the gross categories of specialization only for the individuals who took part in these studies.

(U) The program was under the supervision of Prof. Ralph E. Hiatt, Head of the Radiation Laboratory. Dr. Raymond F. Goodrich was the Principal Investigator. Burton A. Harrison was the Program Manager. Dr. Thomas B.A. Senior was responsible for the analysis and interpretation of the surface field data, assisted by Leon P. Zukowski. Eugene F. Knott was responsible for the experimental program. He was assisted by Ernest C. Bublitz who carried out the surface field measurements and developed procedures for coating metallic models, and by Theodore E. Hon who carried out the back scatter measurements. Dr. Vaughan H. Weston was responsible for the research on re-entry vehicles in a plasma environment. The mathematical analysis for the continuing development of a generalized computer program was based upon work by Dr. Dario Castellanos. The computer programming is being carried forward by Thomas L. Boynton and Peter H. Wilcox. Computer programming in support of the plasma re-entry environment studies and creeping wave analysis was carried out by Dallas R. Hodgins. Harold E. Hunter was responsible for supporting computational studies and the hand check of the computer program. The above named investigators were assisted by technicians and students. The preparation of memoranda, reports and manuscripts was carried out under the supervision of Mrs. Claire F. White.

(U) We would like to express our appreciation for the additional cone-sphere models made available by Dr. John Rheinstein and James H. Pannell of MIT-Lincoln Laboratory for use on this program, and for the suggestions of Dr. Sidney L. Borison of the same organization. We wish to acknowledge the assistance and

suggestions of Major Aharonian and Lt. James Wheatley, Contract Monitors for the Ballistic Systems Division and of H.J. Katzman and his associates, Dr. William Botch, Dr. Fred F. Meyer, Edward N. Skomal and Dr. Morris Weisfeld of the Aerospace Corporation.

REFERENCES

Bowman, J.J. and T.B.A. Senior (1966), "Half Plane," Scattering by Simple Shapes, (to be edited by R.E. Kleinman, P.L.E. Uslenghi and T.B.A. Senior), to be published by North-Holland Publishing Company, Amsterdam, The Netherlands.

Bowman, J.J. and V.H. Weston (1966), "The Effect of Curvature on the Reflection Coefficient of Layered Absorbers," IEEE Trans. G-AP, AP-14, pp. 760-767.

Castellanos, D. (1966), "Notes on Electromagnetic Scattering from Rotationally Symmetric Bodies with an Impedance Boundary Condition," The University of Michigan Radiation Laboratory Report 7741-1-T, AD 804220. UNCLASSIFIED

Ducmanis, J.A. and V.V. Liepa (1965), "Surface Field Components for a Perfectly Conducting Sphere," The University of Michigan Radiation Laboratory Report 5548-3-T, AD615368. UNCLASSIFIED

Fock, V.A. (1945), "Diffraction of Radio Waves around the Earth's Surface," J. of Physics, 9, No. 4, 255-256.

Goodrich, R.F., et al (1965), "Radar Cross Section of the Metallic Cone-Sphere: Final Report," The University of Michigan Radiation Laboratory Report No. 7030-5-T, BSD-TR-66-112. SECRET

Goodrich, R.F., et al (1967), "08525 Program Plan No. 1" The University of Michigan Radiation Laboratory. SECRET

Hong, S. and V.H. Weston (1965), "A Modified Fock Function," The University of Michigan Radiation Laboratory Report No. 7030-2-T, AD477155. UNCLASSIFIED

Hong, S. (1966), "Asymptotic Theory of Diffraction by Smooth Convex Surfaces of Variable Curvature," The University of Michigan Radiation Laboratory Report 7741-2-T, AD 804916. UNCLASSIFIED

Knott, E.F. (1965), "Design and Operation of a Surface Field Measurement Facility," The University of Michigan Radiation Laboratory Report No. 7030-7-T, AD 482481. UNCLASSIFIED

References (continued)

Liepa, V.V. and T.B.A. Senior (1965), "Modification to the Scattering Behavior of a Sphere by Reactive Loading," Proc. IEEE, Vol. 53, pp. 1004-1011.

Logan, N.A. (1959), "General Research in Diffraction Theory," Lockheed Missiles and Space Division Report LMSD 288088, Vol. II, AD243182. UNCLASSIFIED.

Logan, N.A. (1965), "Numerical Investigation of Electromagnetic Scattering and Diffraction by Convex Objects," Lockheed Missiles and Space Company Final Report AFCRL-66-153. UNCLASSIFIED. M-76-66-1, 707pp.

Maue, A.W. (1949), "On the Formulation of a General Diffraction Problem through an Integral Equation," Zeit. f. Physik, 126, pp. 601--618.

Plonus, M.A. (1966), "Scattering from Small Obstacles on an Infinite Conducting Plane," The University of Michigan Radiation Laboratory Report 7741-3-T. UNCLASSIFIED

Rytov, S.M. (1940), J. Exp. Theor. Phys. USSR, Vol. 10, p. 120.

Schweitzer, P. (1965), "Electromagnetic Scattering from Rotationally Symmetric Perfect Conductors," MIT-Lincoln Laboratory Report PA-88 (BMRS) UNCLASSIFIED

Senior, T.B.A. (1952), "Diffraction by a Semi-Infinite Metallic Sheet," Proc. Roy. Soc., A, 213, 436-458.

Senior, T.B.A. (1959a), "Diffraction by an Imperfectly Conducting Half-Plane at Oblique Incidence," Appl. Sci. Res., Sect. V, 8, 35-61.

Senior, T.B.A. (1959b), "Diffraction by an Imperfectly Conducting Wedge," Comm. Pure and Appl. Math., XII, 337-372.

Senior, T.B.A. (1960), "Impedance Boundary Conditions for Imperfectly Conducting Surfaces," Appl. Sci. Res., Sect. B, Vol. 8, 418-436.

Senior, T.B.A. (1962), "A Note on Impedance Boundary Conditions," Can. J. Phys., 40, 663-665.

References (continued)

Senior, T. B. A. (1965), "Physical Optics Applied to Cone-Sphere-Like Objects," unpublished notes.

Senior, T. B. A. and L. P. Zukowski (1965), "The Interpretation of Some Surface Field Data," The University of Michigan Radiation Laboratory Report No. 7030-8-T, AD 374993. CONFIDENTIAL, 107 pp.

Senior, T. B. A. and P. H. Wilcox (1967), "Traveling Waves in Relation to the Surface Fields on a Semi-Infinite Cone," Radio Science, Vol. 2, No. 5, pp. 479-487.

Streifer, W. (1964), "Creeping Wave Propagation Constants for Impedance Boundary Conditions," IEEE Trans. G-AP, AP-12, 764-766.

Weston, V. H. (1963), "Theory of Absorbers in Scattering," IEEE Trans. G-AP, AP-11, pp. 578-584.

Weston, V. H. (1965), "Extension of Fock Theory for Currents in the Penumbra Region," Radio Science J., 69D, No. 9, pp. 1257-1270.

APPENDIX A
THE ENHANCEMENT OF CREEPING WAVES ON A COATED PLANE-PARABOLA

(S) In analyzing high frequency scattering by a cone-sphere we must take into account the modification of the creeping wave field whenever the cone-sphere join lies in the penumbra region. The phenomenon has been described by Hong and Weston (1965) in terms of a modified Fock function. In deriving this modified Fock function Hong and Weston modeled the penumbra region by a smoothly joined flat plane and parabolic cylinder. We parallel their treatment for a surface on which the field satisfies an impedance boundary condition.

(U) The approach we use after Hong and Weston is to find the asymptotic solution of the integral equation governing the surface field.

A.1 Formulation

(U) We suppose a plane wave

$$\psi_o = e^{iky} \tag{A.1}$$

incident on the cylinder

$$x = -\frac{y^2}{2R} \quad ; \qquad y \geqslant -R\tan\alpha$$

$$x = \tan\alpha\left(y + \frac{R}{2}\tan\alpha\right) \quad ; \qquad y \leqslant -R\tan\alpha \tag{A.2}$$

as in Fig. A-1.

(U) The field, ψ, satisfies the equation

$$(\nabla^2 + k^2)\psi = 0 \tag{A.3}$$

and the boundary conditions

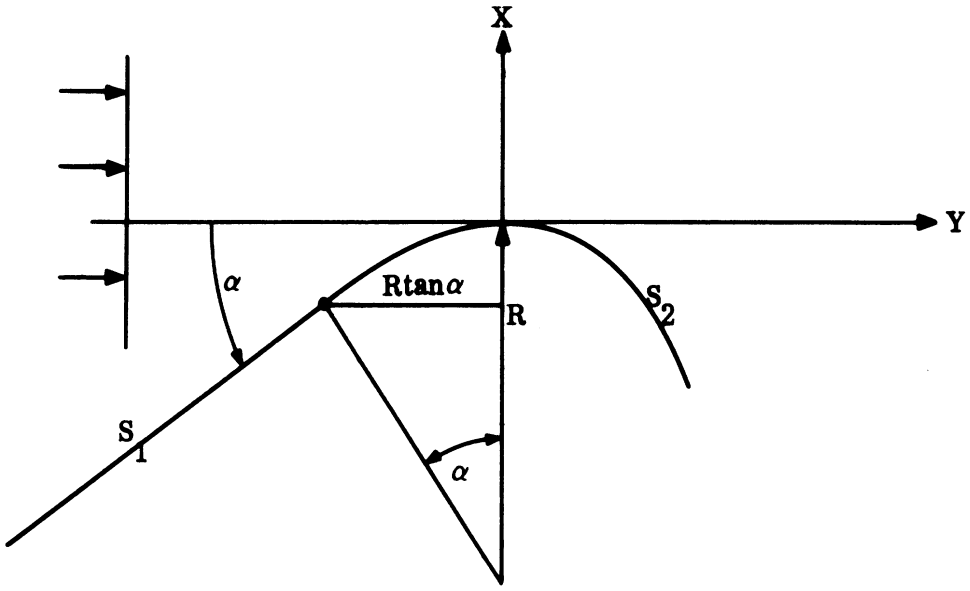

FIG. A-1: GEOMETRY OF THE PLANE-PARABOLIC CYLINDER

$$\frac{\partial \psi}{\partial n} + ik\eta\psi = 0 \qquad \text{on the surface ,} \tag{A.4}$$

where η is the surface impedance. After Maue (1949) the surface field satisfies the integral equation

$$\psi_{(\vec{r}_p)} = 2\psi_o(\vec{r}_p) + 2 \int_{\text{Surface}} \left(\frac{\partial G}{\partial n_1} + i\eta k G \right) \psi(\vec{r}_q) dS_q \tag{A.5}$$

where

$$G = \frac{i}{4} H_o^{(1)}(kr) \; ; \quad r = \left| \vec{r}_p - \vec{r}_q \right| \tag{A.6}$$

and

$$\frac{\partial G}{\partial n_1} = \frac{ik}{4} \hat{n}_1 \cdot \hat{r} H_1^{(1)}(kr) \tag{A.7}$$

with $\hat{n}_1$ the outward unit normal vector at the integration point. Substituting (A.6) and (A.7) in (A.5) we have that

$$\psi = 2\psi_o + \frac{ik}{4} \int_{\text{Surface}} \left[\hat{n}_1 \cdot \hat{r}\, H_1^{(1)}(kr) + i\eta H_o^{(1)}(kr)\right] \psi dS_q \ . \qquad \text{(A.8)}$$

(U)We now prepare for the asymptotic solution of (A.8) by considering the integration in two parts: S_1 over the plane, and S_2 over the parabolic cylinder. We let y and t by the y-coordinates of the field and integration points respectively. Then on noting that the field on the plane must be the geometric optics field

$$\psi = \frac{2\sin\alpha}{\sin\alpha + \eta}\, \psi_o \ ; \quad y \leqslant -R\tan\alpha \qquad \text{(A.9)}$$

and writing

$$\psi = I(y)\, e^{iks(y)} \ ; \ y \geqslant -R\tan\alpha \ , \qquad \text{(A.10)}$$

$$s = \int_0^y \sqrt{1 + \frac{t^2}{R^2}}\ dt \quad ,$$

equation (A.8) becomes

$$I(y) = 2e^{ik\left(y - s(y)\right)} + \frac{ik\sin\alpha}{\sin\alpha + \eta} \int_{-\infty}^{-R\tan\alpha} \frac{dt}{\cos\alpha} \left[\hat{n}_1 \cdot \hat{r}_1 H_1^{(1)}(kr_1) + i\eta H_o^{(1)}(kr_1)\right] \cdot$$

$$\cdot\, e^{ik\left(t - s(y)\right)} + \frac{ik}{2} \int_{-R\tan\alpha}^{\infty} dt \sqrt{1 + \frac{t^2}{R^2}}\ I(t)\left[\hat{n}_2 \cdot \hat{r}_2 H_1^{(1)}(kr_2) + i\eta H_o^{(1)}(kr_1)\right] \cdot$$

$$\cdot\, e^{ik\left(s(t) - s(y)\right)} \qquad \text{(A.11)}$$

where

$$\vec{r}_1 = \left(\tan\alpha(y-t) - \frac{(y+R\tan\alpha)^2}{2R}\ ,\ y-t\right)$$

$$r_2 = (y-t)\left(-\frac{y+t}{2R}\ ,\ 1\right) \qquad \text{(A.12)}$$

and

$$\hat{n}_1 = (\cos\alpha, -\sin\alpha)$$

$$\hat{n}_2 = \frac{1}{\sqrt{1+\frac{t^2}{R^2}}}\,(1, t/R) \qquad \text{(A.13)}$$

To facilitate the asymptotic analysis we put

$$\left.\begin{array}{ll} (kR)^{1/3} = m & \xi + m\alpha = \theta \\ ky = m^2\xi & \zeta + m\alpha = \phi \\ kt = m^2\zeta & I(y) = J(\xi) \end{array}\right\} \qquad \text{(A.14)}$$

(U) We now go to the asymptotic analysis of (A.11). We assume for this purpose

$$\left.\begin{array}{l} (kR)^{1/3} = m \gg 1 \\ m\tan\alpha \cong m\alpha \ll 1 \end{array}\right\} \qquad \text{(A.15)}$$

and make the change of variable

$$\left.\begin{aligned} ky &= m^2\xi & \xi + m\alpha &= \theta \\ kt &= m^2\zeta & \zeta + m\alpha &= \phi \\ I(y) &= J(\xi) & \xi - \zeta &= x \end{aligned}\right\} \qquad (A.16)$$

Using (A.15) and (A.16) we find for $\xi \gtrless -m\alpha$

$$J(\xi) = 2e^{-i\frac{\xi^3}{6}} - \frac{e^{-i\frac{\pi}{4}}}{\sqrt{2\pi}} \frac{\alpha}{\alpha+\eta} \exp\left\{-i\frac{\xi^3}{6} - \frac{i}{2}\alpha m(\xi+m\alpha)^2\right\} \cdot$$

$$\cdot \int_{-\infty}^{-m\alpha} d\zeta \left[\frac{(\xi+m\alpha)^2}{(\xi-\zeta)^{3/2}} + \frac{2\eta m}{(\xi-\zeta)^{1/2}}\right] \exp\left\{\frac{i}{2}\alpha^2 m^2(\xi-\zeta) + \frac{i}{8}\frac{(\xi+m\alpha)^4}{\xi-\zeta}\right\} \cdot$$

$$- \frac{e^{-i\frac{\pi}{4}}}{2\sqrt{2\pi}} \int_{-m\alpha}^{\xi} d\zeta \left[(\xi-\zeta)^{1/2} + \frac{2\eta m}{(\xi-\zeta)^{1/2}}\right] \exp\left\{-i\frac{(\xi-\zeta)^3}{24}\right\} J(\zeta) \qquad (A.17)$$

or on putting $x = \xi - \zeta$, $\theta = \xi + m\alpha$

$$J(\xi) = 2e^{-i\frac{\xi^3}{6}} - \frac{e^{-i\frac{\pi}{4}}}{\sqrt{2\pi}} \frac{\alpha}{\alpha+\eta} \exp\left\{-i\frac{\xi^3}{6} - \frac{i}{2}\alpha m\theta^2\right\} \cdot$$

$$\cdot \int_{\theta}^{\infty} dx \left[\frac{\theta^2}{x^{3/2}} + \frac{2\eta m}{x^{1/2}}\right] \exp\left\{i\left(\frac{\theta^4}{8x} + \frac{m^2\alpha^2}{2}x\right)\right\} -$$

$$- \frac{e^{-i\frac{\pi}{4}}}{2\sqrt{2\pi}} \int_{0}^{\theta} dx \left[x^{1/2} + \frac{2\eta m}{x^{1/2}}\right] e^{-i\frac{x^3}{24}} J(\xi - x) \qquad (A.17a)$$

We now rewrite the integral in the second term of (A.17a) as

$$\int_{\theta}^{\infty} dx\ldots = \int_{o}^{\infty} dx\ldots - \int_{o}^{\theta} dx\ldots$$

and consider the integral

$$I = \int_{o}^{\infty} dx \left(\frac{\theta^2}{x^{3/2}} + \frac{2\eta m}{x^{1/2}} \right) \exp\left\{ i \left(\frac{\theta^4}{8x} + \frac{m^2\alpha^2}{2} x \right) \right\} .$$

We have after Weston (1965) that

$$\int_{o}^{\infty} dx \frac{\theta^2}{x^{3/2}} \exp\left\{ i \left(\frac{\theta^4}{8x} + \frac{m^2\alpha^2}{2} x \right) \right\} = 2\sqrt{2\pi}\, e^{i\frac{\pi}{4}}\, e^{i\frac{m\alpha}{2}\theta^2} ,$$

hence,

$$I = 2\sqrt{2\pi}\, e^{i\frac{\pi}{4}}\, e^{i\frac{m\alpha}{2}\theta^2} \left(1 + \frac{\eta}{\alpha}\right) .$$

This part of the second term is just the negative of the first term and (A.17) becomes for $\xi > 0$

$$J(\xi) = \frac{1}{\sqrt{2\pi}} \frac{\alpha}{\alpha+\eta} e^{-i\frac{\pi}{4}} \exp\left\{ -i \left(\frac{\xi^3}{6} + \frac{m\alpha}{2}\theta^2 \right) \right\} \cdot$$

$$\cdot \int_{o}^{\theta} dx \left(\frac{\theta^2}{x^{3/2}} + \frac{2\eta m}{x^{1/2}} \right) \exp\left\{ i \left(\frac{\theta^4}{8x} + \frac{m^2\alpha^2}{2} x \right) \right\}$$

$$- \frac{1}{2\sqrt{2\pi}} e^{-i\frac{\pi}{4}} \int_{-m\alpha}^{\xi} d\zeta \sqrt{\xi - \zeta} \left(1 + \frac{2\eta m}{\xi - \zeta} \right) \exp\left\{ -i \frac{(\xi - \zeta)^3}{24} \right\} J(\zeta) \qquad (A.18)$$

On defining

$$j(\theta) = J(\xi)$$

where

$$\theta = \xi + m\alpha$$

$$\phi = \zeta + m\alpha$$

equation (A.18) can be written as

$$j(\theta) = \frac{1}{\sqrt{2\pi}} \frac{\alpha}{\alpha+\eta} e^{-i\frac{\pi}{4}} \exp\left\{i\left(\frac{m^3\alpha^3}{6}\right) - i\frac{\theta^3}{6}\right\} \int_0^\theta dx \left(\frac{\theta^2}{x^{3/2}} + \frac{2\eta m}{x^{1/2}}\right) \cdot$$

$$\cdot \exp\left\{i\left(\frac{\theta^4}{8x} + \frac{m^2\alpha^2}{2}(x-\theta)\right)\right\} - \frac{1}{2\sqrt{2\pi}} e^{-i\frac{\pi}{4}} \int_0^\theta d\phi \sqrt{\theta-\phi}\left(1+\frac{2\eta m}{\theta-\phi}\right) e^{-i\frac{(\theta-\phi)^3}{24}} j(\theta). \tag{A.19}$$

Since (A.19) is of the form

$$j(\theta) = j_o(\theta) + \int_0^\theta K(\theta-\phi)\, j(\phi) d\phi \tag{A.20}$$

we take the Laplace transform of (A.20) and solve for the transform of $j(\theta)$

$$\bar{j}(p) = \frac{\bar{j}_o(p)}{1-\bar{K}(p)} \tag{A.21}$$

where

$$\bar{j}(p) = \int_0^\infty d\theta\, e^{-p\theta} j(\theta) \tag{A.22}$$

$$\bar{j}_o(p) = \frac{1}{\sqrt{2\pi}} e^{-i\frac{\pi}{4}} \int_o^\theta d\theta\, e^{-p\theta - i\frac{\theta^3}{6}} \int_o^\theta dx \left(\frac{\theta^2}{x^{3/2}} + \frac{2\eta m}{x^{1/2}} \right) \cdot$$

$$\cdot \exp\left\{ i \left(\frac{\theta^4}{8x} + \frac{m^2\alpha^2}{2}(x-\theta) \right) \right\} \qquad \text{(A.23)}$$

$$\bar{K}(p) = -\frac{1}{2\sqrt{2\pi}} e^{-i\frac{\pi}{4}} \int_o^\infty d\theta\, e^{-p\theta} \sqrt{\theta} \left(1 + \frac{2\eta m}{\theta} \right) e^{-i\frac{\theta^3}{24}} \quad . \qquad \text{(A.24)}$$

(U) On taking the inverse transform of (A.21) we obtain the solution which can be expressed as a residue series. However, for numerical solutions it is much more convenient to use the integral (A.17) directly. We write (A.17) as

$$J(\xi) = H(\xi) + \int K(\xi, \zeta) J(\zeta) d\zeta$$

and define

$$J_n = J(\xi_n)$$

$$H_n = H(\xi_n)$$

$$K_{n,n1} = K(\xi_n, \xi_{n1})$$

where

$$\xi_n = n\Delta - m\alpha$$

Hence, we find

$$J_n = H_n + \frac{\Delta}{3} \left[K_{no} J_o + 4K_{n1} J_1 + 2K_{n2} J_2 + \ldots + 2K_{n,n-2} J_{n-2} + 4K_{n,n-1} J_{n-1} \right] .$$

APPENDIX B
COMPUTER PROGRAM FOR ROTATIONALLY SYMMETRIC BODY

B.1 Relation of Problem to Overall SURF Objectives

(S) The SURF undertaking, a development of adequate and effective methods for predicting the back scattering cross section of any of a class of targets typical of a nose-cone at those aspects for which a re-entry body might normally be viewed, is a fairly restricted one. It is, for example, only concerned with bodies of a generally pointed shape which have been selected for their low cross sections in a range of aspect angles and, as a result tends to possess a less complex type of scattering behavior than would be true for an arbitrary body. Attention is also restricted to back scattering, and the aspects of interest cover only the angular range about nose-on where the cross section control is effective. Such a range is certainly bounded by the direction of the broadside (specular) flash. Note the inclusion of the words "adequate and effective" in reference to the cross section estimates. It is neither desirable nor practical to provide exact values for the scattering for each and every situation of interest, but it is essential to produce results which are "adequate and effective" as a basis of target design, and which are sufficiently precise to serve in place of time-consuming and expensive range measurements in the course of the design process.

(S) These restrictions, allied with the unique surface field experimental facility at our disposal, give grounds for believing that the objective is achievable, but at the same time the magnitude of the task should not be underestimated. The class of targets to be covered is still a very wide one, embracing a large variety of base surfaces obtained by parametric modification of a cone-sphere, surface perturbations in the form of slots or other indentations, surface protuberances representative of brackets, nozzles, antennas etc., and, last but not least, gross modifications that may result when the targets are non-metallic, i.e. when the surface is

covered wholly or partially with one or more coatings of appropriately-chosen materials. It is because of this variety that a step-by-step program, in which the effects of each successive complication could be studied with full knowledge of the scattering behavior at the previous stage, was regarded as essential for the successful fulfillment of the undertaking. And thus it was that each year of the program had specific but ever more complex surface modification as its subject matter.

(S)As originally conceived, the program was made up of certain basic lines of investigation, each of which is inadequate in itself, but which, in total, were felt capable of providing the necessary information. These approaches are essential to each year's effort, and are as follows:

1.a) The detailed analytical solution of certain boundary value problems. The problems to be selected with the aim of revealing the mechanisms governing specific features of the surface and back scattering behavior, and the solutions to be found with the utmost accuracy achievable within the time alloted.

1.b) The decomposition of these "canonical" solutions to provide the elements out of which the scattering picture for a more general body might be constructed.

2.a) Detailed measurements of the surface fields for a small sample of the total (combined) ranges of the various parameters and perturbations inherent in the class of objects appropriate to the year's study, the cases chosen for such measurements to be selected primarily to illuminate specific features of the surface field behavior.

2.b) The study and interpretation of the measured data to pinpoint the sources and mechanisms governing the surface fields.

3) The mating of the information derived from 1) and 2) to produce an adequate understanding of the surface field and, hence, quantitative estimates of both the surface and far field values.

4) A very limited number of back scatter measurements to confirm the predictions, which measurements are to be performed only when equivalent data is not available from other sources.

(S)Several features of this breakdown should be noted. First, there is considerable interplay between items 1) and 2), and whereas in some instances the measurements will "lead" the theory in the sense that an examination of the experimental surface field data indicates an appropriate theoretical model to be investigated, in other cases the analyses that have been carried out pinpoint the effects that must be looked for in the data. The ultimate product is, however, a set of theoretical expressions, and if these are to be other than empirical in nature, they must be an outgrowth of the theoretical studies based on the physical picture of the scattering that has been developed. Secondly, because of the laborious and time-consuming process of acquiring surface field data, particularly at oblique angles of incidence and/or in the presence of non-metallic surfaces (where up to four components of the surface field may be required), the measurements must be limited to only a sampling of the various combinations of parametric values of interest. The intervention of theory is therefore necessary in order to furnish complete coverage of the ranges of each parameter, and this does leave the possibility that effects important for specific values of some parameter may be overlooked. It also makes doubly important the possession of very precise values for the surface fields on the basic metal shapes, since effects which are of no significance with these shapes (and might therefore be overlooked) may well be significant when slots or antennas are present. It is further true that the formulae for oblique incidence are less accurate than those for nose-on, and though the uncertainties are of no real concern with the basic metallic shapes, unexpected deficiencies could show up when the picture is extended to embrace coatings or other perturbations.

(S) To guard against these possibilities, however remote, an item as added to the SURF program. This item called for the direct digital solution of the integral equation for the fields excited on a metallic body of revolution illuminated by a plane wave at arbitrary incidence. This computer program would be used to supplement the surface field measurements, particularly at oblique angles of incidence, and to provide the detailed quantitative continuity referred to above. The availability (and use) of such a program would be of considerable value in the perfection of the surface field picture, as an adjunct and check on combined theoretical, experimental and interpretational studies. It was not, however, visualized as a tool to be widely used by us, or by Air Force agencies, as a means of computing the scattering from each and every shape, and is not so visualized now. In the first place, the running time of the program would mitigate against its being used except in a limited number of cases, and since the time increases with the electrical size of the target, it hardly represents a method for assessing the effect of each and every possible perturbation to the shape. Secondly, it is limited to bodies of revolution, which necessitates that if the surface is modified in any way (e.g. by the insertion of a slot or the addition of an antenna), the resulting structure must still be symmetric as a function of rotation of the body about its axis; and thirdly, the body must be perfectly conducting (i.e. metallic), though it was anticipated that with the successful conclusion of this phase of the programming, the extension to surfaces with an impedance boundary condition would be carried through.

(U)Being convinced of the value of this tool as an aid in the development of an adequate picture of the scattering and, hence, of valid formulae for the prediction of the scattering, we found it desirable to undertake the programming of this highly complex problem ourselves because:

1) Alternative, but doubtless effective, programs were not accessible to us;

2) We felt it desirable that the program be available for instant use as the occasion demanded; and

3) A novel analytical and computational procedure has been described in an MIT report (Schweitzer, 1965), and though this had not been put into practice, we believed it to be sufficiently superior to those adopted elsewhere to justify the effort required to make it operational.

(U)The nature of this highly involved programming task is summarized in Section B.2.

B.2 Discussion of Analytic Problem

(S)The computer program for the current on a rotationally symmetric body is a numerical method for solving the so-called Maue integral equation. This is the fundamental integral equation for the current density on a scatterer. The computer program is designed to solve this equation and make the results specific to whatever metallic body of revolution (e.g. a cone-sphere) is being considered.

(U) The analytical development on which the program is based has been described in a Radiation Laboratory technical report (Castellanos, 1966). It is an adaptation of a numerical method of solution proposed by Paul Schweitzer at Lincoln Laboratory. It approximates the Maue integral equation with a system of simultaneous linear equations. Since the kernel (i.e. known part of the integrand) of the integral equation is a Green's function it has a singularity within the range of integration used to generate the matrix elements (coefficients). Thus analytic methods must be employed to handle the neighborhood of the singularity. In solving the system of simultaneous equations, a matrix and a matrix inversion were programmed. The matrix inversion followed the method suggested by Schweitzer and the results of the programming show that the method(applied initially to a 20 by 20 matrix) is remarkably accurate, uses very little storage facility, and requires only ten percent of the total machine time. However, as described in the following discussion,

it was discovered that the first treatment of the neighborhood of the singularity of the Green's function was inadequate and a refinement of Schweitzer's method was needed.

(S)This did not become apparent until the computer program was run for a test object for which not only the final result, i.e. the surface current, but also intermediate values of the computation were known. The test body was a sphere. A question which has been put to the analyst in connection with the choice of a test object is, "Why the sphere instead of the cone-sphere?". It appears to the questioner an unnecessary intermediate step to devise a program for a sphere when the shape for which the program will be useful in the SURF investigation is the cone-sphere. However, the analytic problem is entirely independent of the shape just as the program itself will be independent of a particular shape and must be workable for all rotationally symmetric bodies. But for purposes of checking out the analysis, the sphere is the one rotationally symmetric body for which an analysis already exists and which is available for a point-by-point check of the programming. It is comparable, in a gross sense, to using a sphere or a corner reflector for the calibration of a radar set. One could use a more complicated shape but would not get comparable information or accuracy from it. In using the sphere to check out the program, advantage was taken of the fact that the rotational properties of the sphere are such that image points on its surface have equal values of surface current (except for sign) and the equality of the values is reflected in the symmetry of the matrix elements. For example, in the sketch below, at points A and B where the current is equal, the F functions, K functions and Green's functions are equal with the possible exception of sign. The matrix can therefore be examined cell-by-cell to determine whether this symmetry has been realized numerically. When, through analytic refinements, this has been accomplished with the desired accuracy, the matrix is analytically operational. The program can then be run for any other desired shape with rotational symmetry. The discussion which follows describes the analysis mathematically.

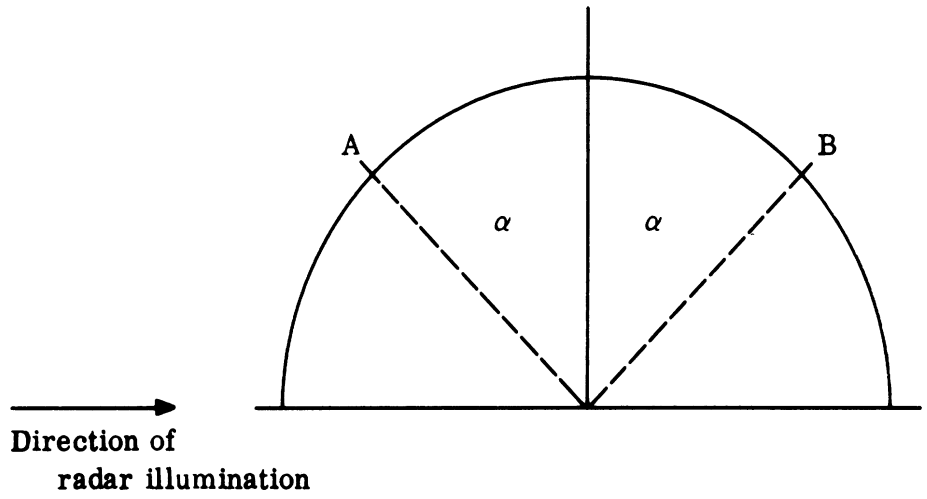

B.3 Mathematical Representation of Diagnostic Technique

(U)In testing the numerical analysis on a sphere we were able to make use of certain symmetries in the matrix T to correct both analytic and programming errors. The matrix elements are made up of integrals of the form

$$I_{ij} = \int_0^1 F_1(t')K_i(t')dt' \int_0^1 F_2(t)K_j(t)G_m(t,t')dt \ . \qquad \text{(B.1)}$$

We observed that for the sphere under the change of the variables of integration

$$t' = 1 - \tau'$$

$$t = 1 - \tau \qquad \text{(B.2)}$$

that

$$G_m(t,t') \rightarrow G_m(t,\tau')$$

$$F_1(t') \rightarrow \pm F_1(\tau')$$

$$F_2(t) \rightarrow \pm F_2(\tau)$$

and $$K_i(t) \rightarrow K_{11-i}(\tau) = K_J(\tau) \tag{B.3}$$

Hence

$$I_{ij} = \pm I_{IJ} \tag{B.4}$$

so for the matrix element

$$\begin{aligned} T_{2i,\,2j} &= T_{2I,\,2J} \\ T_{2i-1,\,2j} &= -T_{2I-1,\,2J} \\ T_{2i-1,\,2j-1} &= T_{2I-1,\,2J-1} \end{aligned} \tag{B.5}$$

(U) We observed after the first trial that the symmetry did not obtain. The discrepancy was immediately resolved for the off-diagonal element, $T_{ij}(i \neq j, i \neq \pm 1)$, by noting an indexing inconsistency in the numerical integration routine.

(U) However, for the diagonal and near-diagonal elements we found the difficulty lay in the required analytic integrations. To illustrate this we consider a typical integration for a diagonal element

$$\int_{t_i}^{t_{i+1}} F_1(t')K_i(t')dt' \int_{t_i}^{t_{i+1}} F_2(t)K_i(t)G_m(t,t')dt \quad . \tag{B.6}$$

Since the Green's function has an integrable singularity, one of the above integrations must be done analytically. Making use of the fact that $s = t - t'$ is small, we expand the second integrand

$$F_2(t)K_i(t) = F_2(t')K_i(t') + \left[F_2(t')K_i(t')\right]' s \tag{B.7}$$

and write

$$G_m(t,t') = \int_0^{\eta_m} G\cos m\theta\, d\theta + \int_{\eta_m}^{\pi} G\cos m\theta\, d\theta \qquad (B.8)$$

and note that G is singular only for both $\theta = 0$ and $s = 0$. This leads then to the analytic integral over s and θ

$$\int_0^{\eta_m} d\theta \cos m\theta \int_{t_i - t'}^{t_{i+1} - t'} ds\, s^n G \; ; \quad n = 0, 1 \quad . \qquad (B.9)$$

Initially these integrations were approximated making an expansion in powers of $\eta_m/t_i - t'$ and $\eta_m/t_{i+1} - t'$, that is, in ratios of small quantities. The earlier discrepancy again showed up in a departure from the expected symmetry for the sphere matrix. This difficulty was resolved by observing that the integrations can be performed in finite terms.

(U) There was one final problem for the near-diagonal elements. We see from (B.7) that a derivative of the function $K_i(t)$ is to be taken. In performing the numerical integration subsequent to the analytic integration, the value of $\frac{d}{dt} K_i(t)$ needs to be found for various points. Since the K_i are triangular

$$K_i(t) = \begin{cases} \alpha(t - t_{i-1}) & t_{i-1} \leqslant t < t_i \\ -\alpha(t - t_{i+1}) & t_i < t \leqslant t_{i+1} \\ 0 \quad \text{otherwise} \end{cases} \qquad (B.10)$$

we must adopt some convention for

$$\frac{d}{dt} K_i(t)\Big|_{t=t_i} \quad . \qquad (B.11)$$

We have taken

$$\frac{d}{dt} K_i(t)\Big|_{t=t_i} = 0 \qquad (B.12)$$

arguing from the fact that changing the order of integration in (B.6) for these near-diagonal elements must be allowed and given the same result.

(S) With this re-analysis completed, a test run with the sphere will be made and then the cone-sphere. The function which describes the cone-sphere has been programmed. This is not a substantial programming task. Therefore, very little time should elapse until the cone-sphere can be run, once these analytical difficulties are overcome and the program is successfully checked out on the test object. In Section B.3 the schematic representation of the program is given.

B.4 Computer Flow Diagram

(U) A computer flow diagram is given in Fig. B-1 and is expanded and detailed in Figs. B-2a through B-2g. With the exception of the additional symbols defined below, the symbols which are used are those of the two reports referenced in the previous sections of this Appendix, Castellanos (1966) and Schweitzer (1965). All of the operations shown in the diagrams have been programmed. The entire program has been run through a check sequence. Analytic, as opposed to programming, modifications are being studied to bring the computed values into line with the check values.

$$I_n^m \equiv \frac{1}{\Gamma}\int_0^{\pi} d\theta \cos m\theta\, e^{i\Omega}\int_{\beta_i}^{\beta_{i+1}} ds\, \frac{s^n}{\sqrt{s^2+\lambda s+\omega^2}}$$

$$+\frac{if_1'(t')}{\Gamma}\int_0^{\pi} d\theta \sin\frac{\theta}{2}\cos m\theta\, e^{i\Omega}\int_{\beta_i}^{\beta_{i+1}} ds\, \frac{s^{n+1}}{\sqrt{s^2+\lambda s+\omega^2}}$$

where

$$\Gamma = kC$$

$$\Omega = 2f_1(t')\sin\frac{\theta}{2} = \Gamma\omega$$

$$\Gamma^2\lambda = \Lambda = 4f_1(t')f_1'(t')\sin^2\frac{\theta}{2}$$

$$I_o^m = \int_{\eta_m}^{\pi} d\theta \cos m\theta\, e^{i\Omega}\psi_o + if_1'(t')\int_0^{\pi} d\theta \cos m\theta \sin\frac{\theta}{2}\, e^{i\Omega}\tilde{\psi}_1$$

$$-\frac{2i}{\Gamma^2}\left[f_1'(t')\right]^2 f_1(t')\int_{\eta_m}^{\pi} d\theta \cos m\theta \sin^3\frac{\theta}{2}\, e^{i\Omega}\psi_o + \frac{1}{\Gamma}\left(\mathcal{L}_o^o(\beta_{i+1}) - \mathcal{L}_o^o(\beta_i)\right)$$

$$+\frac{1}{\Gamma}\int ds\left[if_1(t')\phi_1 - \frac{m^2}{2}\phi_2 - \frac{i}{2}f_1(t')\left(m^2 + \frac{\left[f_1'(t')\right]^2}{2\Gamma^2}\right)\phi_3\right]$$

$$\psi_o = \frac{1}{\Gamma}\ell n\left\{\frac{2\sqrt{\Gamma^2\beta_{i+1}^2 + \Lambda\beta_{i+1} + \Omega^2} + 2\Gamma\beta_{i+1} + \frac{\Lambda}{\Gamma}}{2\sqrt{\Gamma^2\beta_i^2 + \Lambda\beta_i + \Omega^2} + 2\Gamma\beta_i + \frac{\Lambda}{\Gamma}}\right\}$$

$$\psi_1 = \frac{1}{\Gamma^2}\left\{\sqrt{\Gamma^2\beta_{i+1}^2 + \Lambda\beta_{i+1} + \Omega^2} - \sqrt{\Gamma^2\beta_i^2 + \Lambda\beta_i + \Omega^2}\right\}$$

$$\mathcal{L}_o^o(\beta) = \frac{2\gamma^{1/2}}{\xi}\ell n\left(\frac{\gamma^{1/2}\eta_m + b}{|\beta|}\right) + \eta_m\ell n\left(b + \beta + \frac{\xi}{2}\eta_m^2\right)$$

$$-\frac{2\zeta}{\xi}\ell n\left\{\frac{b + \zeta\eta_m + \frac{\xi}{2\zeta}\eta_m\beta}{|\beta|}\right\}$$

Note for $\beta = 0$ this goes to

$$\mathcal{L}_o^o(0) = \eta_m \ell n\left(\xi\eta_m + \frac{1}{2}\xi\eta_m^2\right)$$

where

$$\xi = \frac{f_1(t')f_1'(t')}{\Gamma^2}$$

$$\zeta = \frac{f_1(t')}{\Gamma}$$

$$\gamma = \xi\beta + \zeta^2$$

$$b = \sqrt{\beta^2 + \gamma\eta_m^2} = \sqrt{\beta^2 + \lambda\beta + \omega^2}$$

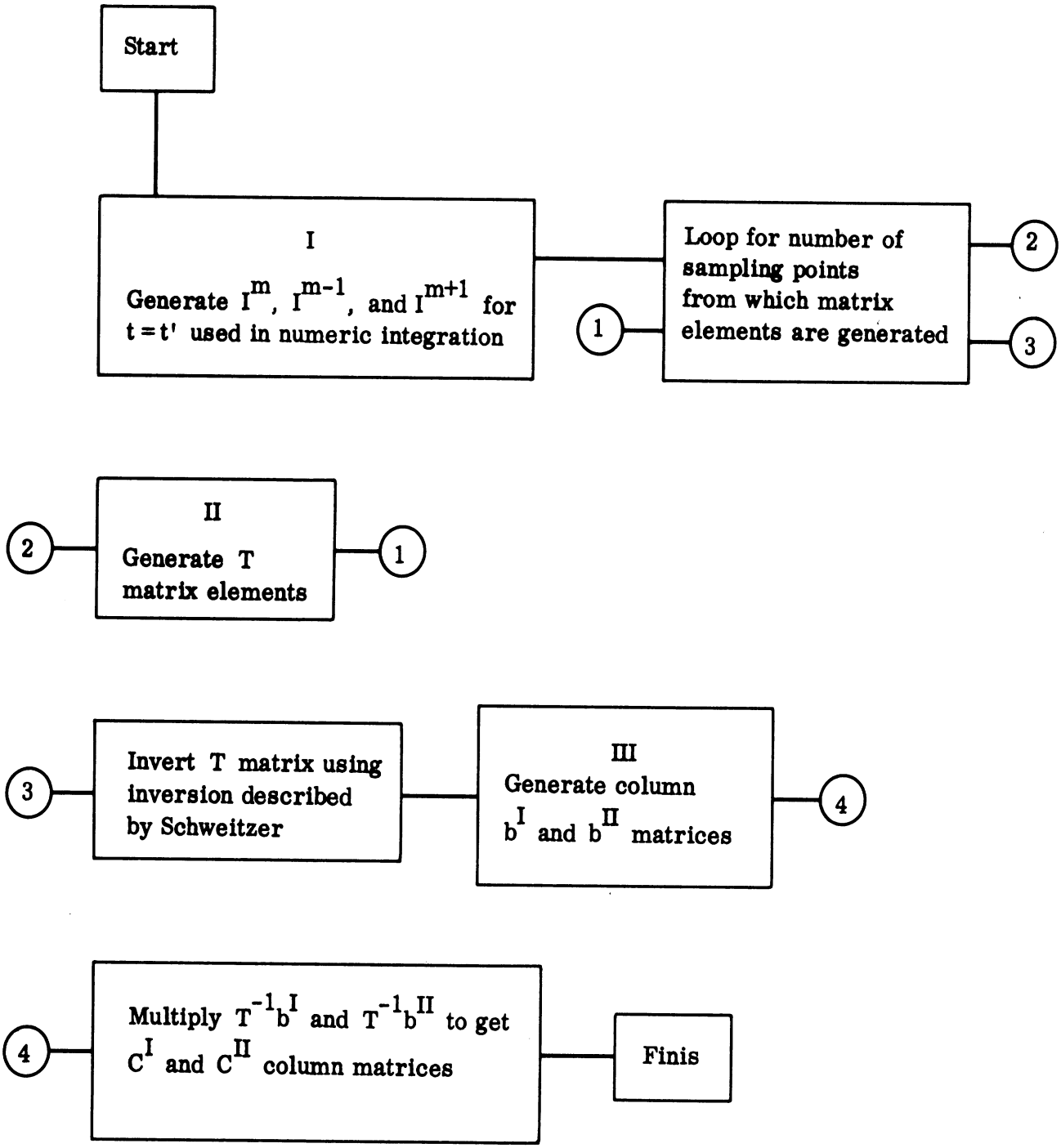

FIG. B-1: COMPUTER FLOW DIAGRAM

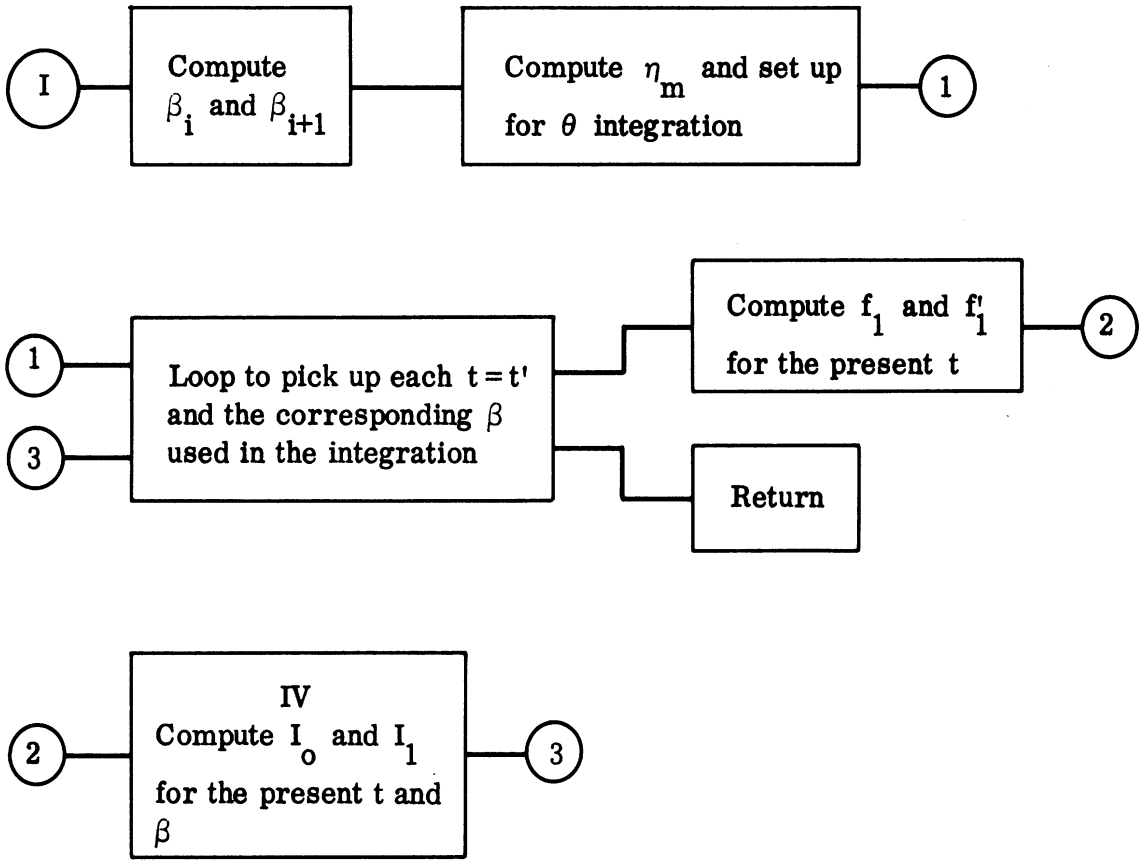

FIG. B-2a: COMPUTER FLOW DIAGRAM

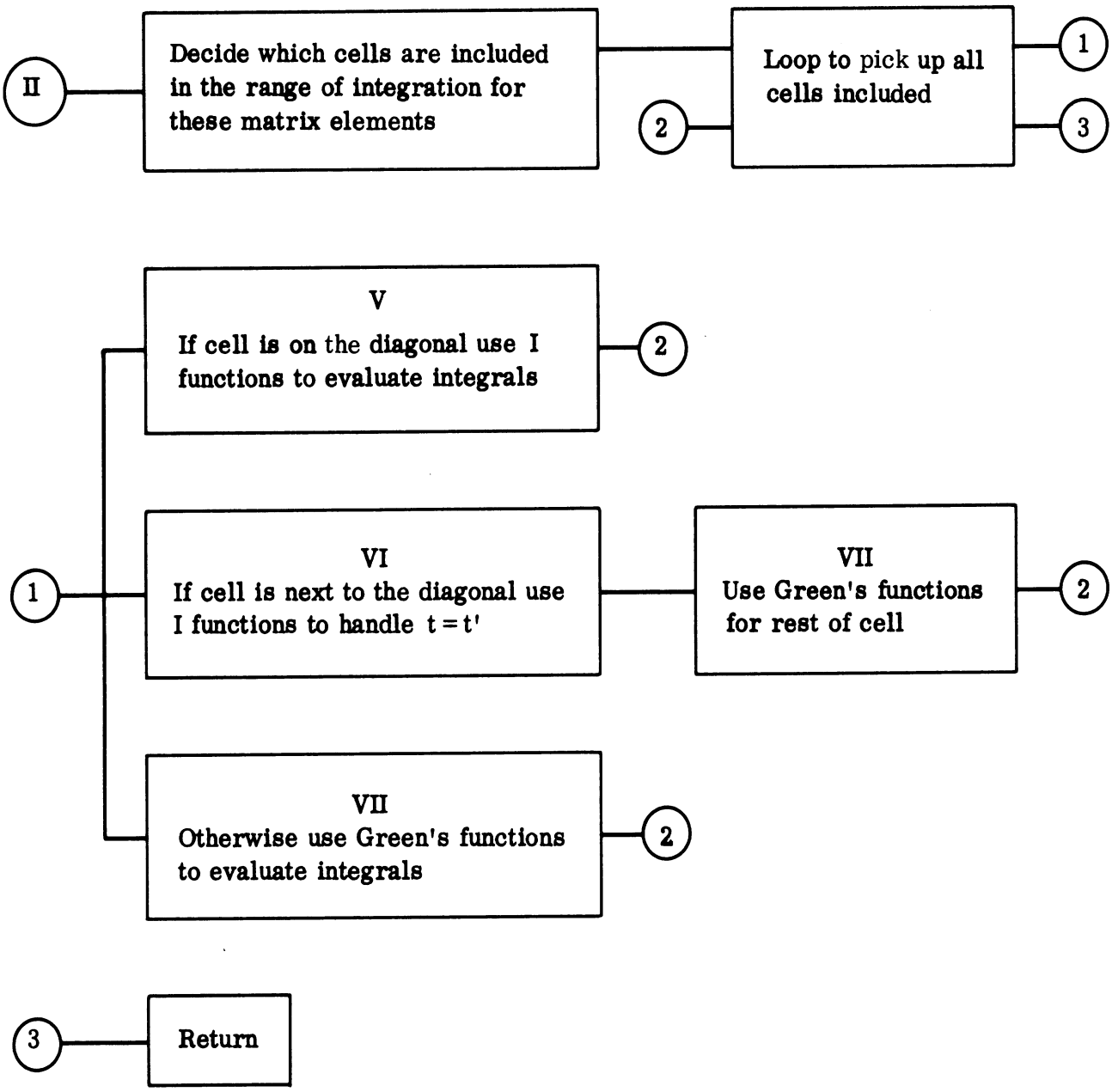

FIG. B-2b: COMPUTER FLOW DIAGRAM

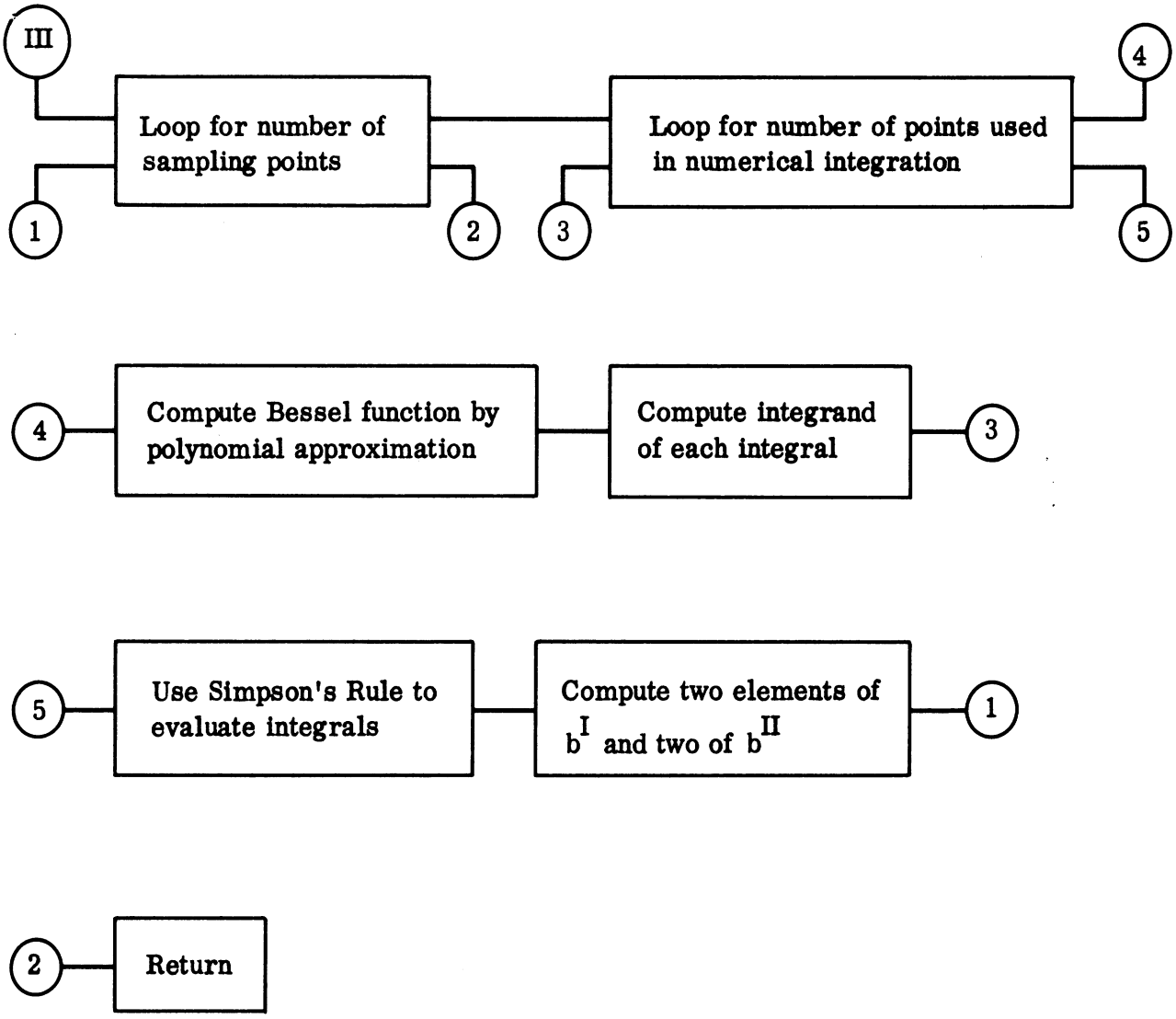

FIG. B-2c: COMPUTER FLOW DIAGRAM

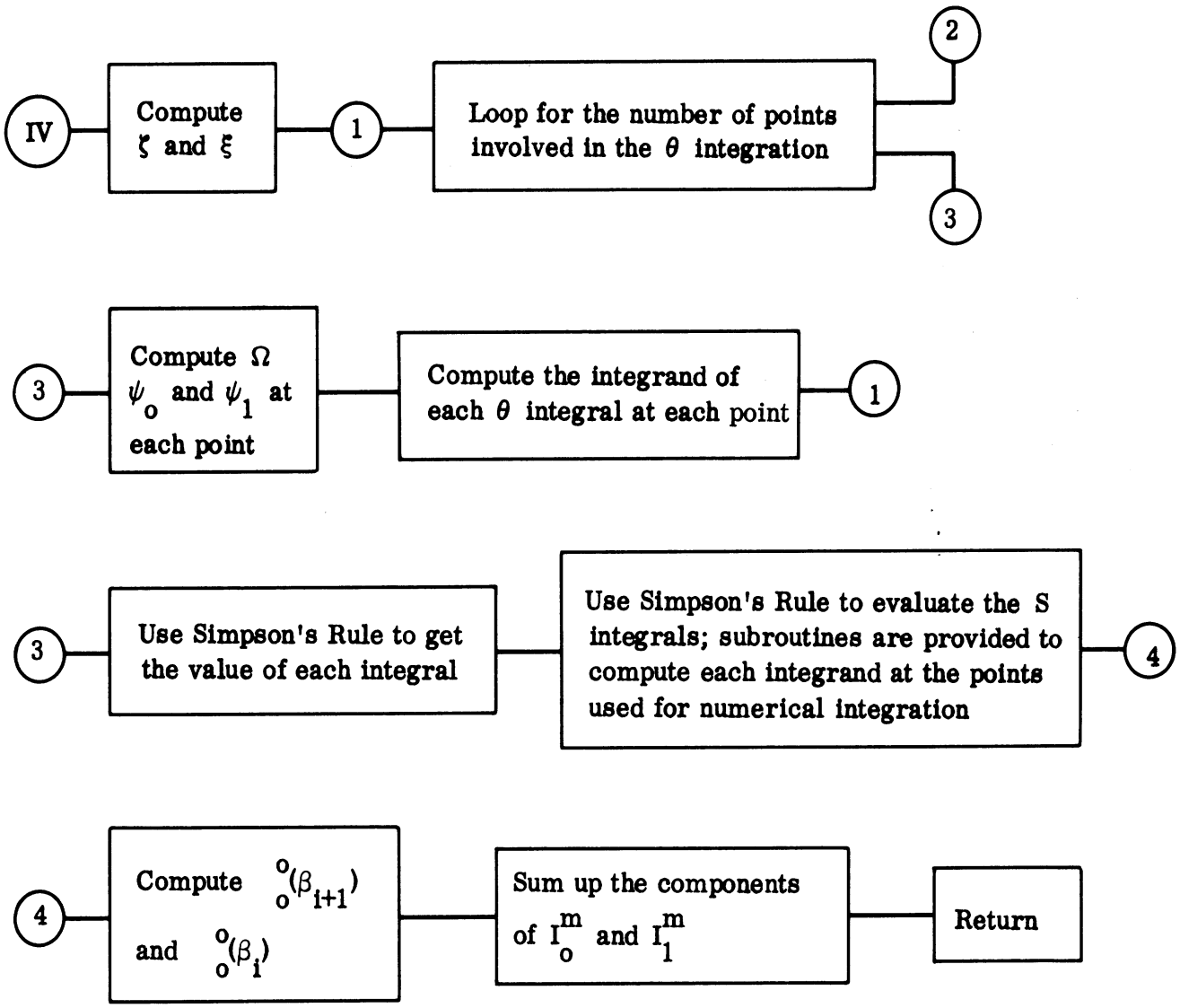

FIG. B-2d: COMPUTER FLOW DIAGRAM

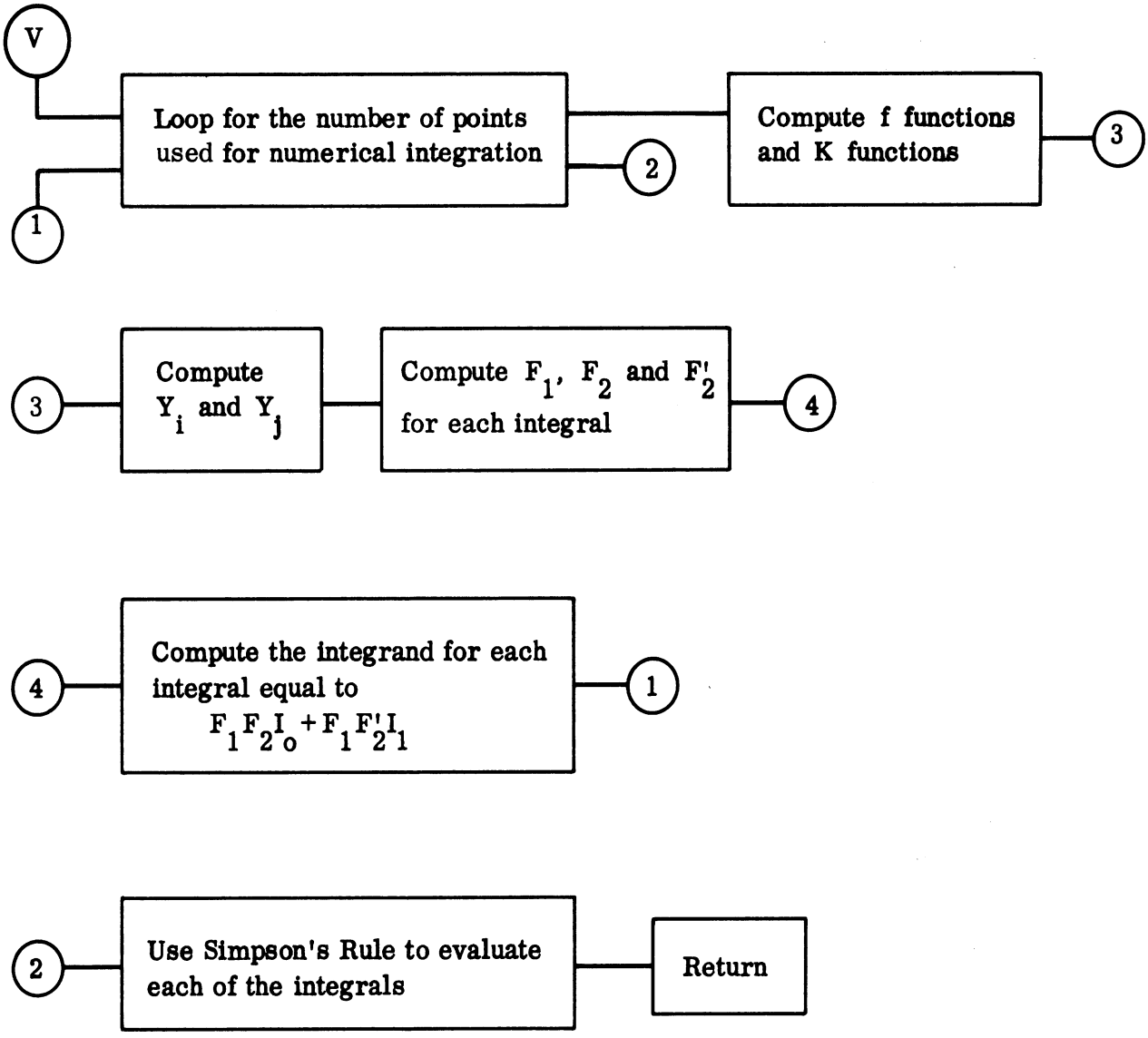

FIG. B-2e: COMPUTER FLOW DIAGRAM

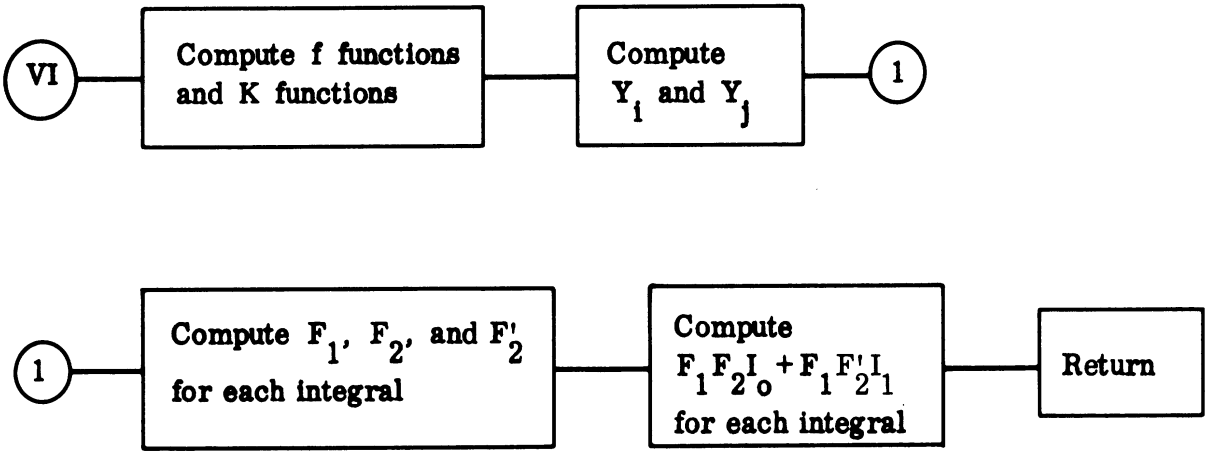

FIG. B-2f: COMPUTER FLOW DIAGRAM

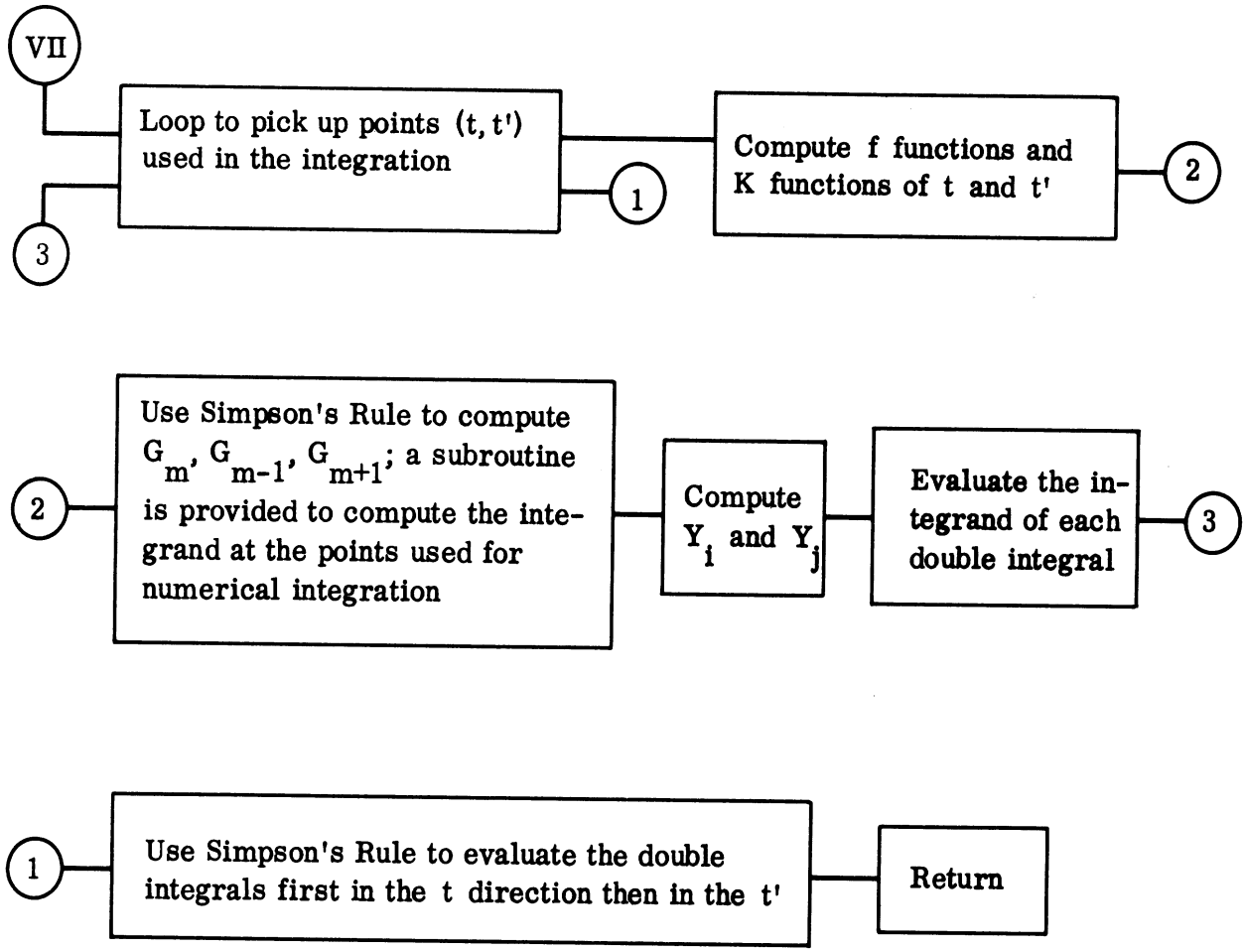

FIG. B-2g: COMPUTER FLOW DIAGRAM

THE UNIVERSITY OF MICHIGAN

7741-4-T

DISTRIBUTION

Destination	Copy No(s)
Aerospace Corporation, San Bernardino Operations Building 537, Room 1007 ATTN: H.J. Katzman Post Office Box 1308 San Bernardino, California 92402	1 through 10
Air Force Cambridge Research Laboratories ATTN: R. Mack CRDG L.G. Hanscom Field Bedford, Massachusetts 01730	11, 12
Advanced Research Projects Agency ATTN: W. Van Zeeland The Pentagon Washington, D.C. 20301	13, 14
Air University Library AU Maxwell AFB, Alabama 36112	15
Air Force Avionics Laboratory ATTN: W.F. Bahret AVWE-2 Wright-Patterson AFB, Ohio 45433	16
Ballistic Systems Division ATTN: Lt. J. Wheatley BSYDP Norton AFB, California 92409	17, 18
Ballistic Systems Division ATTN: BSYLD Norton AFB, California 92409	19, 20
Electronic Systems Division (AFSC) ATTN: Lt. H.R. Betz ESSXS L.G. Hanscom Field Bedford, Massachusetts 01730	21
Institute for Defense Analyses ATTN: Classified Library 400 Army-Navy Drive Alexandria, Virginia 22202	22

Destination	Copy No(s)
MIT-Lincoln Laboratory Representative Post Office Box 4188 Norton AFB, California 92409	23
MIT-Lincoln Laboratory ATTN: BMRS Project Office Post Office Box 73 Lexington, Massachusetts 02173	24
MIT-Lincoln Laboratory ATTN: S. Borison Post Office Box 73 Lexington, Massachusetts 02173	25
MIT-Lincoln Laboratory ATTN: J. Rheinstein Post Office Box 73 Lexington, Massachusetts 02173	26
The MITRE Corporation ATTN: Dr. P. Waterman Bedford, Massachusetts 01730	27
North American Aviation Space and Information Systems Division ATTN: Mr. S. Wozniak Tulsa, Oklahoma 73100	28
Special Projects Office Bureau of Weapons ATTN: M. Blum Washington, D.C. 20301	29, 30, 31
Northrop - Norair Division ATTN: F.K. Oshiro 3901 West Broadway Hawthorne, California 90250	32
Defense Documentation Center Cameron Station Alexandria, Virginia 22314	33 through 52
DRC, Incorporated Box 3587 Santa Barbara, California 93105	53

END

SECRET

Security Classification

DOCUMENT CONTROL DATA - R&D

(Security classification of title, body of abstract and indexing annotation must be entered when the overall report is classified)

1. ORIGINATING ACTIVITY (Corporate author) The University of Michigan Radiation Laboratory Department of Electrical Engineering Ann Arbor, Michigan 48108	2a. REPORT SECURITY CLASSIFICATION SECRET 2b. GROUP 4

3. REPORT TITLE
Investigation of Re-entry Vehicle Surface Fields (U)

4. DESCRIPTIVE NOTES (Type of report and inclusive dates)
Final Report 18 December 1965 - 18 December 1966

5. AUTHOR(S) (Last name, first name, initial)
Goodrich, Raymond F., Harrison, Burton A., Knott, Eugene F., Senior, Thomas B.A., Weston, Vaughan H. and Zukowski, Leon P.

6. REPORT DATE	7a. TOTAL NO. OF PAGES	7b. NO. OF REFS
January 1967	286	28

8a. CONTRACT OR GRANT NO.	9a. ORIGINATOR'S REPORT NUMBER(S)
AF 04(694)-834 b. PROJECT NO. c. d.	7741-4-T 9b. OTHER REPORT NO(S) (Any other numbers that may be assigned this report) BSD-TR-67-140

10. AVAILABILITY/LIMITATION NOTICES In addition to security requirements which apply to this document and must be met, it may be further distributed by the holder only with specific prior approval of BSD/BSOMS, Norton AFB, California 92409.

11. SUPPLEMENTARY NOTES	12. SPONSORING MILITARY ACTIVITY
	Ballistic Systems Division Deputy for Ballistic Missile Re-entry Systems AFSC, Norton AFB, California 92409

13. ABSTRACT (Secret) This is the final report on Contract AF04(694)-834, an investigation of re-entry vehicle radar cross section, the second phase of a program designated Project SURF. The objective of the SURF program is to achieve the capability to determine the radar cross section of metallic and coated re-entry vehicles which are sphere-capped-cones in shape, or modifications of that basic shape. The investigation reported here includes a determination of the effect on radar cross section of the plasma re-entry environment and of such perturbations as slot antennas, annular antennas, rocket motors and non-spherical terminations at the rear of the vehicle. The study is based upon the interpretation of surface field data obtained on models illuminated by radar in a specially designed experimental facility. Radar backscatter data and computer programs are used to check theoretical conclusions. The unperturbed metallic cone-sphere was investigated in the previous phase of the project. In this second phase, the metallic cone-sphere with antenna and termination perturbations and the coated unperturbed cone-sphere were studied. A report is given of the results of the experimental work, the interpretation of the measurement data, the theoretical work on plasma environment and such formulas for cross section as were developed and which extend the results previously reported.

DD FORM 1 JAN 64 1473

SECRET

Security Classification

SECRET
Security Classification

14. KEY WORDS	LINK A		LINK B		LINK C	
	ROLE	WT	ROLE	WT	ROLE	WT
Radar Cross Sections						
Re-entry Vehicles						
Cone-Sphere Shapes						
Coated and Metallic Bodies						
Flush Mounted Slot Antennas						
Surface Field Measurements						
Backscatter Measurements						
Theoretical Analysis						

INSTRUCTIONS

1. ORIGINATING ACTIVITY: Enter the name and address of the contractor, subcontractor, grantee, Department of Defense activity or other organization *(corporate author)* issuing the report.

2a. REPORT SECURITY CLASSIFICATION: Enter the overall security classification of the report. Indicate whether "Restricted Data" is included. Marking is to be in accordance with appropriate security regulations.

2b. GROUP: Automatic downgrading is specified in DoD Directive 5200.10 and Armed Forces Industrial Manual. Enter the group number. Also, when applicable, show that optional markings have been used for Group 3 and Group 4 as authorized.

3. REPORT TITLE: Enter the complete report title in all capital letters. Titles in all cases should be unclassified. If a meaningful title cannot be selected without classification, show title classification in all capitals in parenthesis immediately following the title.

4. DESCRIPTIVE NOTES: If appropriate, enter the type of report, e.g., interim, progress, summary, annual, or final. Give the inclusive dates when a specific reporting period is covered.

5. AUTHOR(S): Enter the name(s) of author(s) as shown on or in the report. Enter last name, first name, middle initial. If military, show rank and branch of service. The name of the principal author is an absolute minimum requirement.

6. REPORT DATE: Enter the date of the report as day, month, year; or month, year. If more than one date appears on the report, use date of publication.

7a. TOTAL NUMBER OF PAGES: The total page count should follow normal pagination procedures, i.e., enter the number of pages containing information.

7b. NUMBER OF REFERENCES: Enter the total number of references cited in the report.

8a. CONTRACT OR GRANT NUMBER: If appropriate, enter the applicable number of the contract or grant under which the report was written.

8b, 8c, & 8d. PROJECT NUMBER: Enter the appropriate military department identification, such as project number, subproject number, system numbers, task number, etc.

9a. ORIGINATOR'S REPORT NUMBER(S): Enter the official report number by which the document will be identified and controlled by the originating activity. This number must be unique to this report.

9b. OTHER REPORT NUMBER(S): If the report has been assigned any other report numbers *(either by the originator or by the sponsor)*, also enter this number(s).

10. AVAILABILITY/LIMITATION NOTICES: Enter any limitations on further dissemination of the report, other than those imposed by security classification, using standard statements such as:

(1) "Qualified requesters may obtain copies of this report from DDC."

(2) "Foreign announcement and dissemination of this report by DDC is not authorized."

(3) "U. S. Government agencies may obtain copies of this report directly from DDC. Other qualified DDC users shall request through

_____."

(4) "U. S. military agencies may obtain copies of this report directly from DDC. Other qualified users shall request through

_____."

(5) "All distribution of this report is controlled. Qualified DDC users shall request through

_____."

If the report has been furnished to the Office of Technical Services, Department of Commerce, for sale to the public, indicate this fact and enter the price, if known.

11. SUPPLEMENTARY NOTES: Use for additional explanatory notes.

12. SPONSORING MILITARY ACTIVITY: Enter the name of the departmental project office or laboratory sponsoring *(paying for)* the research and development. Include address.

13. ABSTRACT: Enter an abstract giving a brief and factual summary of the document indicative of the report, even though it may also appear elsewhere in the body of the technical report. If additional space is required, a continuation sheet shall be attached.

It is highly desirable that the abstract of classified reports be unclassified. Each paragraph of the abstract shall end with an indication of the military security classification of the information in the paragraph, represented as *(TS), (S), (C), or (U)*.

There is no limitation on the length of the abstract. However, the suggested length is from 150 to 225 words.

14. KEY WORDS: Key words are technically meaningful terms or short phrases that characterize a report and may be used as index entries for cataloging the report. Key words must be selected so that no security classification is required. Identifiers, such as equipment model designation, trade name, military project code name, geographic location, may be used as key words but will be followed by an indication of technical context. The assignment of links, rules, and weights is optional.

SECRET
Security Classification